The Dissertation Committee for Madeline Reinke Lucey
certifies that this is the approved version of the following dissertation:

Ancient Stars and the Inner Galaxy as tracers of the Milky Way's Early Evolution

Committee:

Keith Hawkins, Supervisor

Mike Boylan-Kolchin

Volker Bromm

Harriet Dinerstein

Paula Jofré

Chris Sneden

Ancient Stars and the Inner Galaxy as tracers of the Milky Way's Early Evolution

by

Madeline Reinke Lucey

DISSERTATION

Presented to the Faculty of the Graduate School of

The University of Texas at Austin

in Partial Fulfillment

of the Requirements

for the Degree of

DOCTOR OF PHILOSOPHY

THE UNIVERSITY OF TEXAS AT AUSTIN

August 2023

Dedicated to my mom, my grandmothers and all the women who made me.

Acknowledgments

I would like to take this opportunity to express my deepest gratitude to all those who have supported and encouraged me. I am grateful to so many people who have helped me get to where I am today, including so many who are not explicitly acknowledged here. From teachers who have directly encouraged my interest in science to all the barrier breakers who left paths for others to follow, I am eternally grateful.

First and foremost, I am indebted to my supervisor, Keith Hawkins, for his invaluable guidance. I feel so lucky that he took a chance on me and recruited me to come to work with him. His excitement about science is infectious and kept me motivated through difficult times. Keith not only taught me so much, but also always pushed me to become more independent, including how to craft my own research questions. I am grateful for the freedom Keith gave me to chose my own path, including giving me the opportunities to travel and work with other collaborators. Most importantly, Keith built my confidence in my abilities. By encouraging, celebrating and trusting me, Keith helped me to build my self-esteem as an astronomer. I cannot thank him enough for his support throughout my research journey.

I would also like to extend my gratitude to the members of my dissertation committee, Volker Bromm, Mike Boylan-Kolchin, Harriet Dinerstein,

Paula Jofré and Chris Sneden, for their constructive feedback and valuable input, which have greatly enriched the quality of this work. Furthermore, their encouragement and advice have and will continue to be helpful for navigating my career.

I feel very lucky to have had the opportunity to work with so many amazing mentors. I cannot express how grateful I am to my undergraduate research advisor, Natalie Gosnell, without whom I would never have even imagined this future for myself. Natalie not only gave me the opportunity to go to graduate school, but also prepared me incredibly well for all of the difficulties I would face. I am so thankful for her continued support and encouragement. I'd also like to thank Yuan-Sen Ting, and Melissa Ness. My collaborations with them taught me many skills that made me a better scientist. I'm also very grateful for my mentors at the Flatiron Institute, Sarah Pearson, Jason Hunt, Adrian Price-Whelan and David Hogg. Being able to work with and learn from them in New York was so beneficial to my career, my science and my life as well. I'm forever grateful for the resources and support they shared with me.

I certainly would not have made it through grad school without my fellow grad students who brought me so much joy and fun. I am especially grateful for Dreia Carrillo, Jackie Champagne, Patty Cho, Danny Krolikowski, Emily Lubar and Catherine Manea. Being able to go to your offices and talk through issues I was facing or just be goofy really made grad school such a supportive place for me. I am so grateful you all came into my life and made

grad school so much more enjoyable.

I'd also like to thank many people in the department who have helped me over the years, including Lara Eakins, Kelly Quinney, Kalyn Williams, Josephine Foster, and Terry Bruegging. From helping me with paperwork and my wild travel plans, all of these people helped make a chaotic time in my life more seamless. Furthermore, I'd like to thank the McDonald observatory staff, especially Coyne Gibson and Dave Doss. I've loved having the opportunity to go out to the Observatory and use the Harlan J. Smith telescope. I very much appreciate all of their hard work keeping things functioning out there, and supporting my observing runs. Lastly, I'd like to thank Danielle Berg, John Chisholm and Arianna Long who took time out of their days to help me prepare job applications and navigate the academic job market. The advice you all gave me will continue to help me as I go forward in my career.

Last but not least, I thank my family for their continued support throughout this journey. I'm especially grateful for my parents who took me to the Hayden Planetarium as a kid and encouraged my curiosity about the universe. I'd like to also thank my mom for allowing me to move back home during the pandemic and for taking care of my cat during my busy travels. Speaking of, I'm grateful to my cat, Pork, for being the world's most perfect cat. Finally, I'd like to express my gratitude to my partner, Tona, for his patience and support during the chaos that is experiencing the academic job market for the first time.

Ancient Stars and the Inner Galaxy as tracers of the Milky Way's Early Evolution

Madeline Reinke Lucey, Ph.D.
The University of Texas at Austin, 2023

Supervisor: Keith Hawkins

The oldest stars in our Galaxy contain crucial information about its formation and the early Universe. Simulations predict that the oldest stars are likely to be located in the central regions of galaxies. Furthermore, nucleosynthetic predictions for the first stars indicate large yields of carbon, suggesting that the oldest stars may be Carbon-Enhanced Metal-Poor (CEMP) stars. Studying the chemo-dynamical properties of metal-poor inner Galaxy stars and CEMP stars can illuminate their origins and, in turn, inform our models of first star formation and galaxy evolution. In this dissertation, I complete a three-part survey entitled Chemical Origins of Metal-poor Bulge Stars (COMBS). COMBS I and COMBS III focused on the chemical abundance analysis of 600 metal-poor stars using VLT/FLAMES spectra, while COMBS II focused on the dynamics of these stars. These studies show evidence that the population that enriched the old metal-poor inner Galaxy stars had a more top-heavy IMF than the typical Milky Way population. Furthermore, my results indicate that secular disk evolution may be more important in

early galaxy evolution than previously thought. However, the COMBS survey did not detect any CEMP stars in the inner Galaxy. To investigate this further, I used machine learning to identify an all-sky sample of millions of CEMP stars using Gaia DR3. In addition, my dissertation puts new constraints on the length and pattern speed of the Milky Way's bar by developing a novel orbit integration method which, in turn, improves the precision and accuracy of inner Galaxy dynamical analysis. In total, my dissertation brings new insights into the formation of the Galaxy, especially the bulge, and provided constraints on the formation of the first stars through the chemo-dynamics of ancient stars.

Table of Contents

List of Tables

List of Figures

Chapter 1

Introduction

One of the main goals of astrophysics is to uncover how our Universe formed and evolved over cosmic time. What is the physics that created our planet, our Sun, our Galaxy, and our Local Group? How did the Universe evolve from Hydrogen, Helium and Lithium gas to the diverse range of galaxies, stars, planets and elements that we see in the Universe today? In this dissertation, I work towards answering these questions and contribute to our knowledge of galaxy formation and chemical evolution by using the wealth of information within the Milky Way's stellar populations. First, in this introduction, I cover the current leading theories of cosmology and galaxy formation, focusing on first star formation and the proto-Milky Way. Next, I introduce near-field cosmology and the importance of studying of ancient stars and the inner Galaxy. Last, I present an overview of the following chapters of this dissertation and how they contribute to our knowledge of our cosmic origins.

1.1 Cosmology and Galaxy Formation

The Big Bang is the leading model for the formation of the universe. In the Big Bang model, the universe was created from a cosmic singularity.

Shortly after the Big Bang, the universe is a hot, dense, extremely small primordial fireball. Density fluctuations are created as the Universe expands and cools. The epoch of recombination begins as the universe cools below 3,000 K and neutral hydrogen can form. At $z \approx 1000$, or $\approx 10^6$ years after the Big Bang, the mean free path of a photon becomes larger than a Hubble length and the cosmic microwave background is released. This begins the dark ages which end with the formation of the first star (Rees, 1999).

1.1.1 First Star Formation and Nucleosynthetic Yields

Very little is known about the formation of the first stars given that they have never been directly observed. In the Big Bang cosmological model, these stars (also known as Population III stars) would form entirely out of H/He gas as heavier elements are yet to be made in stellar interiors and supernovae. As metals and dust are essential cooling agents in models of present-day star formation, it is thought that the formation of the first stars would be quite different as it would rely on molecular hydrogen for cooling (Saslaw & Zipoy, 1967; Peebles & Dicke, 1968). Furthermore, in ΛCDM cosmology, the first molecular hydrogen clouds form in dark matter minihalos and therefore the properties of the first stars are sensitive to dark matter models.

Numerical cosmological simulations of metal-free star formation have provided predictions for the formation time and location of the first stars along with predictions for their masses and nucleosynthetic yields. Specifically, the first stars are thought to form at $z \approx 20$-30 in dark matter minihalos which had

masses of $\approx 10^6 M_\odot$ (Couchman & Rees, 1986; Tegmark et al., 1997; Yoshida et al., 2003). Furthermore, numerical simulations indicated that the first stars would be predominantly very massive with M$\geq$1000 $M_\odot$ (Bromm et al., 1999, 2002; Nakamura & Umemura, 2001; Abel et al., 2000, 2002). Although it is generally agreed that the initial mass function (IMF) of the first stars is likely top-heavy, the slope and range of masses is highly debated (Yoshii & Saio, 1986; Larson, 1998; Nakamura & Umemura, 2001, 2002; Omukai & Palla, 2003; Susa et al., 2014; Hirano et al., 2014). The low-mass end is of particular interest given that some simulations predict that stars with masses ≤ 0.8 $M_\odot$ may have formed and would survive to this day (Bromm, 2013).

As the lifetime of a star is inversely related to its mass, the first stars to supernova will be the most massive first stars. Generally, stars with masses ≥ 8 $M_\odot$ will explode in a core-collapse supernova. If the stars has a mass $\geq$ 40 $M_\odot$, the stellar remnant will be a black hole which will trap most of the newly synthesized metals, preventing significant chemical enrichment of the interstellar medium (ISM). However, if a star has a mass within $140 M_\odot \leq M_* \leq 260 M_\odot$, it will explode as a pair-instability supernova (PISN; Fryer et al., 2001; Heger et al., 2003).

PISNe completely disrupt the progenitor (no stellar remnant), and therefore contribute all of their newly synthesized metals to the ISM. Therefore, it is thought that PISNe would be the first events to enrich the universe with elements heavier than lithium. Predictions for the nucleosynthetic yields of PISNe give a strong odd/even effect in that elements with even atomic

numbers are more enhanced than elements with odd atomic numbers (Heger & Woosley, 2002). It is also predicted that the explosive α elements, calcium and silicon, would be especially enhanced with [Ca/Mg]$\approx$1 (Takahashi et al., 2018). However, the signature of a PISN has yet to be conclusively detected in the chemical abundances of metal-poor stars.

Driven by the observed chemical abundances of metal-poor stars in the Milky Way (see Section 1.2.1), there have been a number of developments in numerical simulations and theoretical yields of core-collapse supernovae with metal-free progenitors in the mass range $25M_{\odot} \leq M_{*} \leq 60M_{\odot}$. Specifically, the impact of fast stellar rotation and the possibility of spinstars as first stars has been investigated with indications that the carbon, nitrogen and oxygen yields may be significantly enhanced in this case (Fryer et al., 2001; Meynet et al., 2006, 2010). Furthermore, work on the detailed hydrodynamics of core-collapse supernova, has shown that the transfer of energy to ejecta (hypernovae), mixing and fallback (faint supernovae) can all impact the theoretical yields (Nomoto et al., 2013).

1.1.2 First Galaxies and the Proto-Milky Way

The formation of the first galaxies is a crucial step in the evolution of the universe, about which very little is known given that they have never been directly observed. One of the major and most complex physical processes that would impact the formation of the first galaxies is the stellar feedback from the first generation of stars.

Given that the first stars are generally thought to be massive, they would provide an abundance of radiation that would ionize the inter-galactic medium (IGM; Kitayama et al., 2004; Whalen et al., 2004). With the additional abundance of free elections, initially ionized primordial gas can cool to lower temperatures ($\approx 100\,K$) through hydrogen deuteride (HD; Johnson & Bromm, 2006). Out of this cool gas, a generation of metal-free less massive stars could form with M$\approx$10M$_\odot$ (Johnson & Bromm, 2006; Yoshida et al., 2007; Clark et al., 2011).

In order to retain the gas heated by stellar radiation, the potential wells of the first galaxies were likely more massive than the minihalos where the first stars formed. Specifically, it is thought that they would form in dark matter halos of $\approx 10^8$M$_\odot$ that would collapse at $z \approx$10 (Wise & Abel, 2007, 2008; Greif et al., 2008, 2010). These halos are special in that their virial temperature exceeds the threshold to allow for atomic hydrogen cooling ($\approx 10^4$ K) and are thus called atomic-cooling halos (Oh & Haiman, 2002).

It is debated whether or not the first galaxies would contain the first stars. It is possible that their supernova explosions and/or stellar feedback would prevent further star formation in the minihalos. However, if $\approx$10 minihalos with Population III stars merge to form an atomic cooling halo, then it would be massive enough to withstand the disruptions and retain the metals synthesized by the first stars (Wise & Abel, 2008; Greif et al., 2008). On the other hand, if lower mass Population III stars that formed in minihalos are sufficient low mass ($<$40 M$_\odot$), then the supernova explosions would be weak

enough to allow for a subsequent generation of star formation in those halos after ≈10 Myr (Jeon et al., 2014; Cooke & Madau, 2014). Even in the case that the first galaxies did not contain Population III stars, it is still possible that they would have formed out of gas that was enriched by Population III stars in neighboring minihalos, given that galactic scale outflows can transport metals into the IGM (Madau et al., 2001; Mori et al., 2002; Wada & Venkatesan, 2003).

Simulations of the first galaxies predict that they would be enriched by Population III to $Z > 10^{-3}\mathrm{Z}_{\odot}$ (Greif et al., 2010; Safranek-Shrader et al., 2014). Therefore, metal cooling, dust formation, and dust cooling all become possible (Todini & Ferrara, 2001; Nozawa et al., 2003; Schneider et al., 2004; Omukai et al., 2005; Cherchneff & Dwek, 2010; Schneider et al., 2012). For metal line cooling, it is predicted that if the gas reaches the critical metallicity of $Z_{crit} = 10^{-3.5}\,\mathrm{Z}_{\odot}$, then sufficient fragmentation can occur in order to form stars with masses $\leq$1 $\mathrm{M}_{\odot}$ (Bromm & Loeb, 2003). For dust cooling, this metallicity is lower with $Z_{crit} = 10^{-5}\,\mathrm{Z}_{\odot}$ (Schneider et al., 2003, 2012; Omukai et al., 2005). By studying the metallicity and chemical abundance distributions of low-mass Population II stars that have survived to the present day, we can learn about the elements created by Population III stars and the star formation in the early universe.

In the ΛCDM cosmological model, galaxies are formed by the hierarchical mergers of smaller systems to create larger galaxies (White & Rees, 1978). The previous leading model of galaxy formation was the rapid monolithic col-

lapse of a large gas cloud (Eggen et al., 1962, hereafter ELS). In this model, it would be easy to define and study the proto-Milky Way. However, in the bottom-up hierarchical accretion paradigm, there are many "proto-galaxies" that merged to form the Milky Way (Searle & Zinn, 1978) and it is difficult to define a single main progenitor (Santistevan et al., 2020a). With the first data from the James Webb Space Telscope (JWST) now being analyzed, we will get new insights into the earliest epochs of galaxy formation by studying galaxy properties at $z > 10$. Combining these results with near-field cosmology will provide a detailed picture of galaxy formation and evolution across cosmic time.

1.2 Near-Field Cosmology

Near-field cosmology is the study of the history of the universe through the properties of stars in the Milky Way (Freeman & Bland-Hawthorn, 2002). Stars are powerful tools for studying the universe as it was billions of years ago, because they have witnessed it all and have kept near perfect records. The first low-mass ($\leq$1 $M_\odot$) that formed in the universe would still survive to this day given that a star's lifetime is inversely proportional to its mass ($\approx 10\ (M/M_\odot)^{-2.5}$ Gyr).

The kinematics/dynamics, chemical composition and age of a star are key properties for decoding its history and the cosmic history that its witnessed. However, the age of a star is one of the more difficult properties to measure with typical uncertainties on the order of 1-5 Gyr. The kinematics for

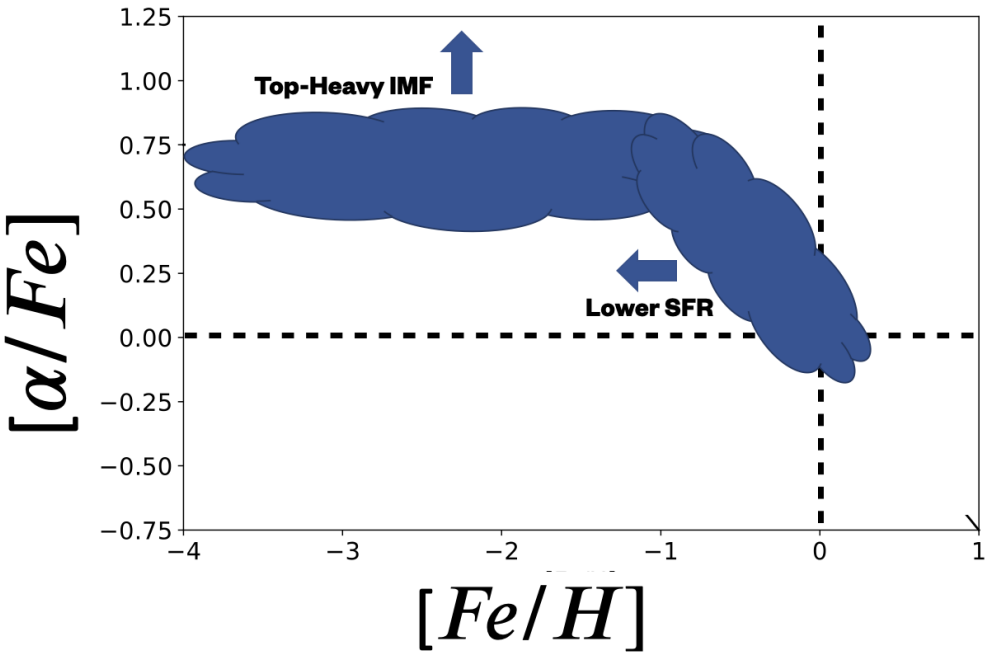

Figure 1.1: A cartoon of [α/Fe] as a function of [Fe/H] for a Milky Way-like stellar population. The black dashed lines indicated the solar values of [α/Fe] and [Fe/H]. For [Fe/H]$\lesssim$-1, only Type II supernovae have contributed to the chemical abundances of these stars. Therefore, the [α/Fe] value is roughly constant and dependent on the IMF of the enriching population, with higher [α/Fe] indicating a more top-heavy IMF. At [Fe/H]$\approx$-1, the [α/Fe] ratio begins to decrease with the onset of Type I supernovae. The [Fe/H] at which this decrease begins is sensitive to the star formation rate of the stellar population, with lower [Fe/H] indicating less star formation.

billions of stars have become readily available in the *Gaia* era (Gaia Collaboration et al., 2016b,a, 2018b, 2021a), but the Galaxy's gravitational potential is uncertain, and time-dependent. Therefore, the energy and momentum of stellar orbits are not conserved. On the other hand, a star's surface chemical abundances generally will not change over its lifetime. Thus, they can act as a fossil record of the ISM at the star's formation time. In the Big Bang cosmological model, the elements in the ISM that are heavier than Lithium were all released into the ISM during the deaths of previous generations of stars. Therefore, the chemistry of a star can inform our understanding of the stellar populations that came before the given star's formation.

As an example, the abundance of α-elements (O, Mg, Si, and Ca) and Fe in a stellar population are some of the most well-understood and commonly used diagnostics for the population's star formation history. α-elements are thus named because they form by the successive addition of α-particles (i.e., helium nuclei) (Burbidge et al., 1957). These elements are primarily released into the ISM by massive stars ($M \geq 20 M_{\odot}$) through Type II supernovae (Tinsley, 1979). The yield of [α/Fe] from these supernovae increases with initial stellar mass (Arnett, 1978). Therefore, the [α/Fe] ratio of a stellar population that was solely enriched by Type II supernovae will be dependent on the IMF of the enriching stellar population, with a top-heavy IMF giving a higher [α/Fe] ratio (see Figure 1.1). Fe is contributed to the ISM by both low and high mass stars ($M \geq 3 M_{\odot}$) through Type II and Type I supernovae (Matteucci & Greggio, 1986). As substantial amounts of Fe are contributed to the ISM

by Type I supernovae, they cause the [α/Fe] ratio to decrease as metallicity increases (Nomoto, 1984). However, as Type I systems take longer to evolve than Type II, they are not expected to dominate the Fe production of a stellar population until $\approx 10^9$ yr after formation (Gilmore et al., 1989). Therefore, the metallicity at which the decrease in the [α/Fe] ratio begins is sensitive to the star formation rate of a stellar population, in that it indicates how much Fe was produced in Type II supernovae before the onset of Type I supernovae in $\approx 10^9$ yr.

We demonstrate this foundational concept in Figure 1.1. Specifically, we show a cartoon version of the [α/Fe] ratio as a function of [Fe/H] for a Milky Way-like stellar population. The black dashed lines indicate the solar values for [α/Fe] and [Fe/H]. At [Fe/H]$\lesssim$-1, the [α/Fe] ratio is constant at [α/Fe]$\approx$0.6, as typical for observations of the Milky Way (Yong et al., 2013; Roederer et al., 2014). We use a cloud to represent the abundances of a stellar population rather than a line in order to demonstrate the typical observed scatter, but it is yet to be seen if the observed scatter is intrinsic or due to measurement uncertainties (Griffith et al., 2023). With an arrow, we indicate that the [α/Fe] ratio would increase for a more top-heavy IMF. The converse is also true, although we did not include an arrow for simplicity. Furthermore, the [α/Fe] ratio begins to decrease at [Fe/H]$\approx$-1 as observed for the Milky Way (Bensby et al., 2014; Adibekyan et al., 2012; Battistini & Bensby, 2015). The arrow indicates that the [Fe/H] value of this turnover would decrease for a stellar population with a lower star formation rate. Again, the converse is

also true. In Chapters 2 and 4, we analyze and discuss similar figures, but created with observed data in order to better understand the star formation history of particular high-impact stellar populations.

1.2.1 Ancient Stars

As JWST is not expected to directly observe the first stars (Schauer et al., 2020), our best observational constraints for their properties come from the study of ancient stars within the Milky Way. However, it is difficult to measure the age of a star and uncertainties can be as high as 5 Gyr. Frequently, lower metallicity is used as an indicator of older age, but this can frequently be misleading.

Whether a relation exists between the age and metallicity of a star has long been debated (Twarog, 1980; Meusinger et al., 1991; Carlberg et al., 1985; Edvardsson et al., 1993; Friel, 1995). It has be come clear that a universal relation that applies to all stars independent of location and age does not exist. However, when some parameters are constricted a relation can be found. For example, a relationship has been found for stars in the solar neighborhood that are younger than 2 Gyr and have $\log T_{\rm eff} > 3.8$ (Feltzing et al., 2001). Although the existence of old, metal-rich star has been known for a long time (Arp, 1962; Eggen, 1969; Hirshfeld et al., 1978), it is still generally thought that the best constraints on Population III stars will come from the most metal-poor stars in the Galaxy, given that Population III stars are expected to have only enriched the ISM to $Z \gtrsim 10^{-3}\,Z_{\odot}$ (Greif et al., 2010; Safranek-Shrader et al., 2014).

The study of the chemical nature of metal-poor stars has been hindered by their rarity in the local neighborhood. Specifically, in the solar neighborhood, stars with [Fe/H] <–3 are one in 100,000 (Frebel & Norris, 2015). On the other hand, the Galactic halo is more metal-poor with mean [Fe/H]=-1.2, and a strong metal-poor tail with $\gtrsim$1 in 500 stars having [Fe/H]<–3 (Conroy et al., 2019). In addition to using proper motions to target halo stars, there have also been efforts to use photometry to locate candidate very metal-poor stars. For example, the SkyMapper (Keller et al., 2007; Casagrande et al., 2019) and the Pristine (Starkenburg et al., 2017c) surveys have both developed photometric filters with the goal of optimizing the sensitive to metallicity. This efforts have been widely successful, including the discovery of the most metal-poor star known to date with [Fe/H]=–7 (Keller et al., 2014).

One of the strongest results from studying the chemistry of metal-poor stars is the prevalence of stars with enhanced carbon abundances, as first recognized by Beers et al. (1992). The occurrence rate of these stars, which have been dubbed CEMP (Carbon-Enhanced Metal-Poor) stars, increases with decreasing [Fe/H] in that they make-up 10-20% of stars with [Fe/H]<–2, but $\approx$80% of stars with [Fe/H]<–4 (Lucatello et al., 2006; Lee et al., 2013; Placco et al., 2014; Yoon et al., 2018). Furthermore, a number of subclasses of CEMP stars have been identified, based on the abundance of heavy neutron-capture elements. The two most common classes are CEMP-*s* stars, which exhibit an enhancement in slow neutron-capture (i.e., *s*-process) elements, and CEMP-no stars which do not show an enhancement in any heavy neutron-capture

elements (Beers & Christlieb, 2005; Norris et al., 2013). Given that CEMP-s stars are more common at [Fe/H]>-3 and have a high binarity rate, it is thought their enhanced carbon and s-process abundances are due to a mass transfer events with a (post-)AGB star (Lugaro et al., 2012; Placco et al., 2013; McClure & Woodsworth, 1990; Preston & Sneden, 2001; Lucatello et al., 2005; Bisterzo et al., 2010; Abate et al., 2015; Hansen et al., 2016b; Jorissen et al., 2016). On the other hand, CEMP-no stars are thought to have formed from an ISM that was carbon-enhanced. This has led to theories that the first generation of stars may have had high rotation rates or exploded in faint supernovae, given that both of these possibilities would lead to overproduction of carbon (Chiappini et al., 2006; Meynet et al., 2006; Umeda & Nomoto, 2003; Nomoto et al., 2013; Tominaga et al., 2014). However, many open questions about the origins of CEMP stars remain, including their occurrence rate as a function of location (e.g., Carollo et al., 2012; Frebel et al., 2006; Lee et al., 2017; Yoon et al., 2018; Carollo et al., 2014; Lee et al., 2019). For further reading, CEMP stars are discussed in detail in Chapter 6.

Furthermore, simulations suggest that the search for and discovery of very metal-poor stars can have varying impacts depending on the Galactic location. For example, it is predicted that stars of a given metallicity are more likely to be older if they are found closer to the center of the Galaxy (Salvadori et al., 2010; Kobayashi & Nakasato, 2011; Tumlinson, 2010). Moreover, the fraction of ancient stars is highest in the inner Galaxy once metal-poor stars are isolated (Starkenburg et al., 2017a; El-Badry et al., 2018b). This is consistent

with predictions that if low-mass Population III stars formed, then they are most likely to be found in the inner regions of the Galaxy (White & Springel, 2000; Brook et al., 2007; Diemand et al., 2008). However, the inner region is the most difficult part of the Galaxy to search for the most metal-poor stars given that it is the densest region with primarily metal-rich stars and high levels of dust extinction.

1.2.2 The Inner Galaxy

Early studies of the inner Galaxy quickly discovered it has a distinct structure, specifically a bulge, which is a massive, major component of many spiral galaxies (Baade, 1946; Stebbins & Whitford, 1947; Gadotti, 2009). Evidence quickly built up that the stars in the bulge are primarily old and metal-rich (Nassau & Blanco, 1958; Whitford & Rich, 1983; Terndrup, 1988; Frogel & Whitford, 1987; Zoccali et al., 2003; Clarkson et al., 2008). Furthermore, detailed abundance studies revealed significant enhancement in the α-elements, indicating a fast chemical enrichment (McWilliam & Rich, 1994; Zoccali et al., 2006; Fulbright et al., 2007; Lecureur et al., 2007).

As observational capabilities increased, large spectroscopic surveys such as the Bulge Radial Velocity Assay (BRAVA; Rich et al., 2007), the Abundances and Radial velocity Galactic Origins Survey (ARGOS; Freeman et al., 2013), the GIRAFFE Inner Bulge Survey (GIBS; Zoccali et al., 2014), the HERMES Bulge Survey (HERBS; Duong et al., 2019a), and the Apache Point Observatory Galactic Evolution Experiment (APOGEE; García Pérez et al.,

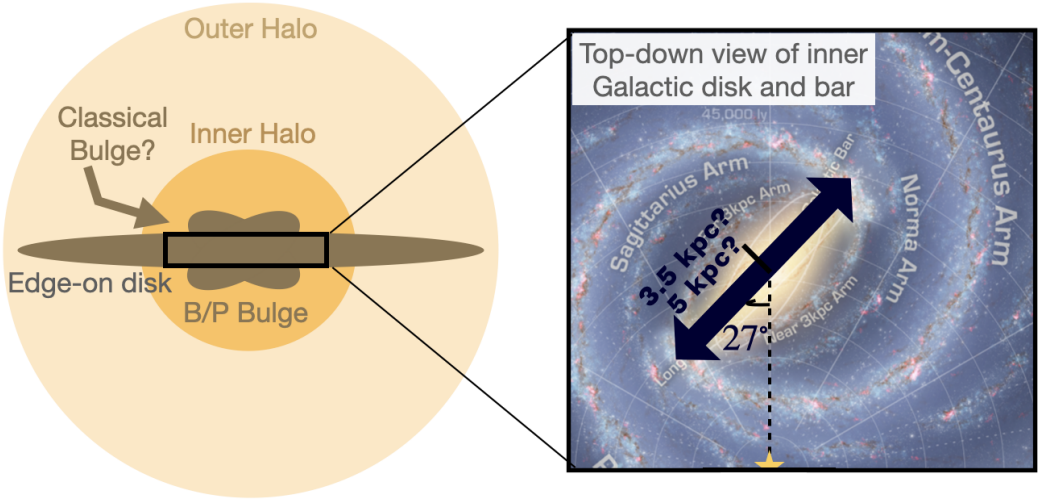

Figure 1.2: A cartoon of the structure of the Milky Way Galaxy. On the left is a edge-on view of the Milky Way's disk with the inner and outer halo shown as yellow circles. In the inner galaxy is a B/P bulge. There is also an arrow pointing to a hypothetical classical bulge as it is currently an open question as to whether or not the Milky Way has one. On the right side we show a face-on zoom-in of the inner disk (Image Credit: NASA/JPL-Caltech/R. Hurt). In this image, the Galactic bar is highlighted at an angle of 27° from the line connecting the Sun to the Galactic center. The half-length of the Galactic bar is uncertain and is labeled here with both leading estimates of 3.5 kpc and 5 kpc.

2018; Rojas-Arriagada et al., 2020) discovered deeper complexity in the chemical distributions of the inner Galaxy. Specifically, the ARGOS survey found that the metallicity distribution function (MDF) of the inner Galaxy is multidimensional and best described with five components (Ness et al., 2013a). Furthermore, the relative strength of the components changes along different lines-of-sight toward the inner Galaxy (Babusiaux et al., 2010; Gonzalez et al., 2013; Rojas-Arriagada et al., 2014a; Massari et al., 2014; Babusiaux et al., 2014; Zoccali et al., 2017; Rojas-Arriagada et al., 2017; Schultheis et al., 2017). In total, results from these surveys indicate that the bulge is composed of multiple stellar populations.

From observations of other nearby spiral galaxies, bulges have been classified into two categories: classical bulges and pseudobulges (Kormendy & Kennicutt, 2004; Athanassoula, 2005; Fisher & Drory, 2016). A classical bulge is a spheroidal, pressure-supported structure while a pseudobulge is flattened, rotation-supported and commonly found to have a boxy/peanut (B/P) or X shape when observed edge-on (Kormendy & Illingworth, 1982). Classical bulges are thought to form from accretion in the hierarchical growth of galaxies model (Kauffmann et al., 1993; Guedes et al., 2013; Kobayashi & Nakasato, 2011). On the other hand, psuedobulges form from secular evolution of a disk which first forms a bar and then bulge from buckling instabilities or orbit trapping (Raha et al., 1991; Merritt & Sellwood, 1994; Bureau & Athanassoula, 2005; Debattista et al., 2006; Combes & Sanders, 1981; Combes et al., 1990; Quillen, 2002; Quillen et al., 2014; Sellwood & Gerhard, 2020). External galax-

ies have also been observed to have both a classical bulge and pseudobulge, which has been dubbed a compound bulge (Athanassoula, 2005; Erwin et al., 2015).

The first evidence that the Milky Way hosts a galactic bar came from high gas velocity in the inner region (de Vaucouleurs, 1964). By the 1990's the Galactic bar's existence was irrefutably confirmed from further gas and stellar density observations (Binney et al., 1991; Englmaier & Gerhard, 1999; Fux, 1999; Blitz & Spergel, 1991; Weiland et al., 1994; Binney et al., 1997; Stanek et al., 1994). It is now clear that the bar formed a B/P bulge in the inner Galaxy, in which most of the stellar mass participates (Howard et al., 2009; Shen et al., 2010; Ness et al., 2013b; Debattista et al., 2017). However, it has also been suggested that the Milky Way may have a compound bulge where the less-massive, metal-poor component is a classical bulge structure (Babusiaux et al., 2010; Hill et al., 2011; Zoccali et al., 2014).

A cartoon of the current theory of the Milky Way's structure is shown in Figure 1.2. Specifically, on the left is an edge-on view of the Milky Way disk. The outer and inner halo are shown as yellow circles. In the center, a B/P bulge is shown, but the classical bulge is not visible and only suggested as a possibility with an arrow. On the left is a face-on view of the inner region of the disk, highlighting the Galactic bar. The exact length, angle, and pattern speed of the Galactic bar is currently uncertain. Estimates of the angle range from (25-33)°, although 27° is most commonly assumed (Wegg & Gerhard, 2013; Wegg et al., 2015; Bovy et al., 2019). The pattern speed of the bar

is thought to be between 39-40 km/s/kpc (Wang et al., 2013; Binney, 2020; Portail et al., 2017; Sanders et al., 2019; Bovy et al., 2019; Leung et al., 2023; Wang et al., 2012). Measurements of the half-length of the bar range from 3.5-5 kpc (Wegg & Gerhard, 2013; Wegg et al., 2015). As the Galactic bar is a major component of the mass of the inner Milky Way, it is essential to further constrain its properties.

1.3 Overview of this Dissertation

The primary focus of this dissertation is near-field cosmology in the inner Galaxy. Specifically, I use ancient stars in and out of the inner Galaxy to study the nucleosynthetic yields of the first stars. I also constrain the structure of the inner Galaxy with the goal of further illuminating the Milky Way's early formation history. This dissertation is composed of seven chapters, including this introduction (Chapter 1) and a final chapter (Chapter 7) which summarizes the results and discusses plans for future work. Four of the chapters are published articles and one is currently in revision. Chapters 2, 3 and 4 comprise the Chemo-dynamical Origins of Metal-Poor Bulge Stars (COMBS) survey. Chapter 5 focuses on the length of the Galactic bar, while Chapter 6 focuses on CEMP stars.

The COMBS survey aims to chemodynamically characterize the metal-poor stars in the inner Galaxy and constrain their origins. These metal-poor stars are thought to be especially informative for the nature of the first stars and early Milky Way given that they are predicted to be some of the oldest

stars in the Galaxy. The first installment of the COMBS survey is Chapter 2 of this dissertation. Here, I perform detailed chemical abundance analysis of 26 stars observed with VLT/UVES (Lucey et al., 2019). With this data, I answer the following question: **What does the chemistry of metal-poor stars in the inner Galaxy tell us about star formation in the early universe?** Chapter 3 of this dissertation and the second installment of the COMBS survey focuses on the dynamics of these and ≈500 more metal-poor inner Galaxy stars (Lucey et al., 2021). This chapter answers, **what fraction of metal-poor stars in the inner Galaxy stay confined to it and to what Galactic structure do they belong?** The third and final installment of the COMBS survey is Chapter 4 of this dissertation. It presents chemodynamical analysis of all ≈500 stars observed with VLT/GIRAFFE (Lucey et al., 2022). In the final chapter of the COMBS survey we investigate, **how does comparative analysis of the different dynamical populations of metal-poor inner Galaxy stars inform chemical evolution of the early universe?**

In order to better understand the structure and mass distribution of the inner Galaxy, Chapter 5 of this dissertation aims to constrain the length of the Galactic bar. Specifically, this chapter answers the question: **Is the length of the Milky Way's bar shorter when measured from the maximal extent of the last trapped bar star than from stellar number density?** To answer this question, I develop a new method to dynamically constrain the length of a galactic bar and apply the method to APOGEE DR17 (Abdurro'uf et al., 2022) and *Gaia* DR3 (Gaia Collaboration et al., 2021a). This works

was published in Lucey et al. (2023).

Chapter 6 of this dissertation focuses on detecting the largest sample of CEMP stars known to date. As these stars are hypothesized to be enriched by Population III stars, I begin to answer the crucial question, **What is the distribution of CEMP stars throughout the Galaxy?** Using *Gaia* DR3 BP/RP spectra, I develop a new method to detect and map CEMP stars. This work is submitted to MNRAS.

Chapter 2

The COMBS survey I: Chemical Origins of Metal-Poor Stars in the Galactic Bulge

Abstract: Chemistry and kinematic studies can determine the origins of stellar population across the Milky Way. The metallicity distribution function of the bulge indicates that it comprises multiple populations, the more metal-poor end of which is particularly poorly understood. It is currently unknown if metal-poor bulge stars ([Fe/H] $<$ -1 dex) are part of the stellar halo in the inner most region, or a distinct bulge population or a combination of these. Cosmological simulations also indicate that the metal-poor bulge stars may be the oldest stars in the Galaxy. In this study, we successfully target metal-poor bulge stars selected using SkyMapper photometry. We determine the stellar parameters of 26 stars and their elemental abundances for 22 elements using R$\sim$ 47,000 VLT/UVES spectra and contrast their elemental properties with that of other Galactic stellar populations. We find that the elemental

[1] This chapter is based on Lucey M., Hawkins K., Ness M., Asplund M., Bensby T., Casagrande L., Feltzing S., Freeman K.C., Kobayashi C., Marino A.F., 2019, MNRAS, 488, 2283. The author of this document, Madeline Reinke Lucey, completed all of the analysis and wrote the publication. M. Ness led the proposal to obtain the observations necessary to achieve this work. K. Hawkins supervised and directed my work on this project.

abundances we derive for our metal-poor bulge stars have lower overall scatter than typically found in the halo. This indicates that these stars may be a distinct population confined to the bulge. If these stars are, alternatively, part of the inner-most distribution of the halo, this indicates that the halo is more chemically homogeneous at small Galactic radii than at large radii. We also find two stars whose chemistry is consistent with second-generation globular cluster stars. This paper is the first part of the Chemical Origins of Metal-poor Bulge Stars (COMBS) survey that will chemo-dynamically characterize the metal-poor bulge population.

2.1 Introduction

Understanding galaxy formation and evolution is now a realizable objective of astrophysics given the ensemble of data and tools in hand. Bulges are major components of most spiral galaxies (e.g., Gadotti, 2009). However, it is not well understood how they form and evolve. By studying the large number of resolved stars in our own Galactic bulge, we can gain new insight into the formation and evolution of bulges. However, historically, this has been difficult. The level of crowding in the bulge makes it difficult to resolve individual stars without very large telescopes. In addition, high levels of dust extinction towards the Galactic center cause dimming, making it hard to achieve high signal-to-noise ratios for observations of resolved bulge stars.

There is now many observations of the Galactic bulge from a multitude of surveys. Imaging surveys such as the Optical Gravitational Lensing

Experiment (OGLE, Udalski et al., 2002), the Two Micron All-Sky Survey (2MASS, Skrutskie et al., 2006), and Vista Variables in the Via Lactea survey (VVV, Minniti et al., 2010; Saito et al., 2012a) have used red clump giant stars (RCGs) to reveal an X-shaped structure (Nataf et al., 2010; McWilliam & Zoccali, 2010; Saito et al., 2012b). This was possible because RCGs can be used as standard candles (Stanek et al., 1998; Hawkins et al., 2017). Spectroscopic surveys such as the Bulge Radial Velocity Assay (BRAVA, Rich et al., 2007), the Abundances and Radial velocity Galactic Origins (ARGOS, Freeman et al., 2013), the GIRAFFE Inner Bulge Survey (GIBS, Zoccali et al., 2014), and the HERMES Bulge Survey (HERBS, Duong et al., 2019a) have measured the radial velocities and chemical abundances of bulge stars. Ness et al. (2012) found that only stars with [Fe/H][2] > -0.5 dex participate in the B/P structure. On the other hand, stars with lower [Fe/H] have been shown to have distinct kinematics and morphological structure (Sharples et al., 1990; Rich, 1990; Zhao et al., 1994; Soto et al., 2007; Hill et al., 2011; Ness & Freeman, 2016; Zoccali et al., 2017).

The metallicity distribution function (MDF) of the bulge provides further evidence for multiple populations. Using 14,150 stars in the bulge, Ness et al. (2013a) found the MDF to have five distinct components with peaks at metallicities of about +0.15, -0.25, -0.7, -1.18, -1.7 dex. They associate these

[2]Chemical abundances are reported in the standard way, as a logarithmic ratio with respect to solar values. Mathematically, $[\mathrm{X/Y}] = \log\left(\frac{\mathrm{N_X}}{\mathrm{N_Y}}\right)_{\mathrm{star}} - \log\left(\frac{\mathrm{N_X}}{\mathrm{N_Y}}\right)_{\odot}$ where N_X and N_Y are the number of each element X and Y per unit volume, respectively.

peaks with the B/P bulge (+0.15 and -0.25 dex peaks), the thick disk (-0.7 dex peak), the metal-weak thick disk (-1.18 dex peak) and the stellar halo (-1.7 dex peak). The three higher metallicity peaks dominant with only about 5% of stars with metallicities $<$ -1.0 dex (Ness & Freeman, 2016). Other studies have found similar results, demonstrating the MDF of the bulge has multiple components (e.g., Zoccali et al., 2008; Johnson et al., 2013a; Zoccali et al., 2017; Bensby et al., 2013; Rojas-Arriagada et al., 2014b; Bensby et al., 2017; Rojas-Arriagada et al., 2017; Duong et al., 2019a).

The low metallicity end of the MDF has recently become of interest. State of the art simulations have shown low-mass Population III stars could still exist today (e.g., Clark et al., 2011; Greif et al., 2012; Bromm, 2013). It has become increasingly clear that if these Population III stars exist in our galaxy, they will be found in the central regions (White & Springel, 2000; Brook et al., 2007; Diemand et al., 2008). Further work has shown the metal-poor stars in the bulge are more likely to be older than equally metal-poor stars located elsewhere in the Galaxy (Salvadori et al., 2010; Tumlinson, 2010).

Given the predicted initial mass function (IMF) from simulations of metal-free star formation, it is thought that a significant fraction of the first stars would explode as pair-instability supernovae (PISNe) (Heger & Woosley, 2010). Simulated yields from PISNe show over 90% stars primarily enriched from PISNe and formed in atomic cooling halos have metallicities around $\sim$ -2.5 dex (Karlsson et al., 2008). Given that most of the oldest stars are thought to have formed ex-situ (e.g., in atomic cooling halos) and end up in the center of

the Galaxy (Nakasato & Nomoto, 2003; El-Badry et al., 2018b), it is possible that the oldest stars in the Galaxy are in the bulge with metallicities $\leq$ -2 dex (Chiappini et al., 2011; Wise et al., 2012; Cescutti et al., 2018). The progenitors in which the oldest stars formed are too faint to be detected, even with the James Webb Space Telescope (Gardner et al., 2006). So these Galactic stars, concentrated to the inner regions, provide the only window into the formation and evolution of these small galaxies at high redshift. We note that prior efforts to study the most metal-poor and first stars have largely focused on the Galactic halo, and dwarf satellites, far from the centre of the Galaxy (e.g., Frebel et al., 2006; Norris et al., 2007; Christlieb et al., 2008; Keller et al., 2014; Starkenburg et al., 2017c).

The discovery of low mass ($\sim 0.7\ M_{\odot}$) stars from a first-star population could provide a vital constraint on the initial mass function (IMF) in the first galaxies. Although this would not give insight into the IMF for metal-free stars it would be very relevant to the evolution of the earliest stars to form in the universe. Additionally, this potentially oldest stars population can test different models of early enrichment.

There has been a recent effort to search for the most metal-poor and Population III stars in the bulge. These searches have made significant progress despite the large distance, crowding and high dust extinction in the bulge. The bulge is also the most metal-rich component of the Galaxy, leaving only 1 in 20 stars to have [Fe/H] <-1 dex (Fulbright et al., 2006; Ness & Freeman, 2016). Although they cannot definitively determine if their target stars are located

in the bulge, García Pérez et al. (2013) used infrared spectroscopy of $\sim$ 2,400 stars toward the bulge and found five stars with -2.1 dex $\leq$ [Fe/H] $\leq$ -1.6 dex. Schlaufman & Casey (2014) found three stars with -3.0 dex $<$ [Fe/H] $<$ -2.7 dex. The Extremely Metal-poor BuLge stars with AAOMega spectroscopic survey (EMBLA, Howes et al., 2014) was the first survey to successfully target metal-poor bulge stars. Howes et al. (2014) found four bulge stars with -2.72 dex $\leq$ [Fe/H] $\leq$ -2.48 dex and Howes et al. (2015) found 23 bulge stars with [Fe/H] $<$-2.3 dex with the most metal-poor star at [Fe/H] = -3.94 dex. Finally, Howes et al. (2016) added 10 more stars with -3.0 dex $\leq$ [Fe/H] $\leq$ -1.6 dex. Koch et al. (2016) analyzed 3 Bulge stars within 4 kpc of the Galactic center with -2.56 dex $\leq$ [Fe/H] $\leq$ -2.31 dex. In total, there are on the order of 50 studied metal-poor stars in the bulge.

It is important to note that these studies of metal-poor bulge stars could be contaminated. In other words, it is yet to be determined if the detected metal-poor stars in the bulge are truly the oldest stars or if they have other origins. For example, it is possible that these stars are simply halo stars with eccentric orbits that pass through the bulge. Howes et al. (2015) measured the orbits of 10 metal-poor bulge stars and found only seven of the stars to have tightly-bound bulge-like orbits. Another possible origin scenario is accreted material from a dwarf galaxy such as Gaia-Enceladus (Belokurov et al., 2018; Helmi, 2008) or massive disrupted globular clusters (Kruijssen, 2015; Shapiro et al., 2010; Bournaud, 2016). Siqueira-Mello et al. (2016) found 3 of the 5 metal-poor bulge stars they studied had chemical abundances similar to the

metal-poor bulge globular clusters, NGC 6522 and M62. These stars could be from protogalactic clusters (e.g., Diemand et al., 2005; Moore et al., 2006) and therefore still some of the oldest stars in the Galaxy.

The goal of this paper is to explore the chemistry of the most metal-poor stars in the Galactic bulge in order to determine their origin. In particular, we want to search for clues as to if these stars are distinct from the Milky Way populations of the thick disk and stellar halo, which have well described chemical properties (e.g., Reddy et al., 2003; Adibekyan et al., 2012; Yong et al., 2013; Roederer et al., 2014; Bensby et al., 2014; Battistini & Bensby, 2015, 2016). Chemical markers that would differentiate the oldest stars from stars of the Galactic halo include sodium, aluminum, copper and manganese, which are expected to be much lower in the oldest stars given the metallicity dependence of the yields (Kobayashi et al., 2011a). If a star is predominantly enriched from PISNe, as some of the oldest stars are thought to be, it would have almost no elements heavier than Fe (e.g., Karlsson et al., 2008; Kobayashi et al., 2011b; Takahashi et al., 2018). Given the first stars have a top-heavy IMF (Tumlinson, 2006; Bromm, 2013), the stars enriched from the first stars would have higher levels of α-enhancement than the thick disk or halo. The theoretical yields of α elements from a non-rotating PISNe are on the order of $[\alpha/\mathrm{Fe}] \sim 2$ dex (Takahashi et al., 2018) while the lowest metallicity stars in the local disk have $[\alpha/\mathrm{Fe}] \sim 0.4$ dex.

We present the discovery of 22 metal-poor bulge stars and additional analysis of 4 ARGOS stars. In total, we perform abundance analysis of 26 stars

Table 2.1: ARGOS targets with the ARGOS stellar parameters

2MASS ID	ID	RA (deg)	DEC (deg)	T_{eff} (K)	log(g)	[Fe/H]
J18240990-3341561	7383.0	276.04140	-33.69890	5179	2.50	-2.22
J18182580-3739409	25782.0	274.60750	-37.66138	5038	2.05	-2.56
J18550481-1949206	12931.0	283.77004	-19.82239	5296	2.64	-2.36
J18531035-2050078	5262.0	283.29310	-20.83540	5193	2.86	-2.46
J18153438-2727353	42011.0	273.89320	-27.45980	5393	3.15	-2.46

Column 1 and 2 gives the 2MASS ID and the ID from this study, respectively. Column 3 and 4 gives the coordinates of these targets. The stellar parameters (T_{eff}, log g, and [Fe/H], respectively) determined for these stars in the ARGOS survey are given columns 5, 6, and 7.

for 22 elements. In section 2.2 we describe the selection of metal-poor bulge stars and in section 6.2 we describe the observations. As described in section 2.4, the data is reduced using standard techniques and the FLAMES/UVES reduction pipelines. For the stellar parameter and abundance analysis we use the Brussels Automatic Code for Characterizing High accUracy Spectra (BACCHUS, Masseron et al., 2016) which is further described in section 2.4. Finally, in section 4.7 we present and discuss the results.

2.2 Selection of Metal-Poor Bulge Stars

To date, it has been extremely difficult to select the most metal-poor stars in the Galactic bulge region, due to crowding and high extinction in the centre of the Galaxy and the large fraction of relatively metal-rich stars in the bulge. The metal-poor population represents only a tiny fraction of the overall stellar population in the inner Galaxy. The combination of large

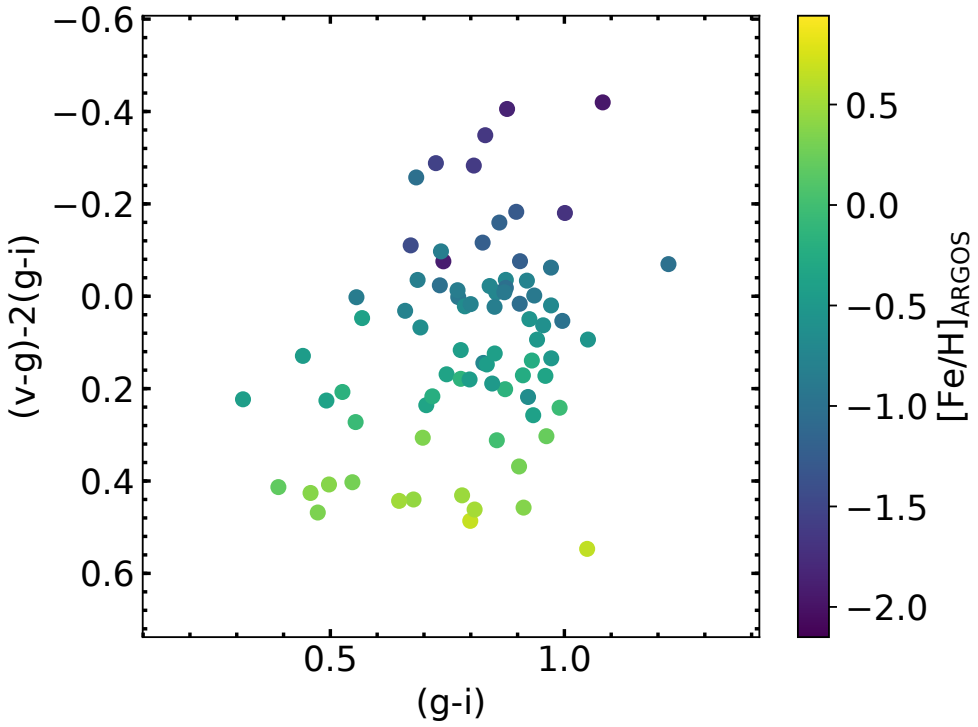

Figure 2.1: Shows the relationship between SkyMapper colors and metallicity. The x-axis is (g-i) photometry and the y-axis (v-g)-2(g-i). Each point is colored by its spectroscopically derived metallicity from the ARGOS survey. The most metal-poor stars have the most negative (v-g)-2(g-i) colour index and largest (g-i) values.

spectroscopic surveys such as ARGOS, GIBS and APOGEE (Freeman et al., 2013; Zoccali et al., 2014; Majewski et al., 2017), which each observe up to tens of thousands of bulge stars, and which determine an [Fe/H] measurement for each star, and the photometric SkyMapper survey, which provides metallicity sensitive colours for orders of magnitude more stars across the Galaxy and into the bulge, are absolutely essential to pre-select metal-poor candidates in order to make progress.

Our program represents a specific targeted set of observations of metal-poor stars with [Fe/H] $<$ -2.0 dex and lying within 3.5 kpc of the Galactic centre. We used a combination of ARGOS spectroscopic and SkyMapper photometry to make our target selection. ARGOS measured stellar parameters for about 28,000 stars in the inner regions of the Galaxy. The ARGOS fields span latitudes of $b = -5°, -7.5°$ and $-10°$ and longitudes extending out into the thin and thick disks of $l = +26°$ to $-31°$. From the ARGOS medium resolution (R=$\lambda/\Delta\lambda \sim$ 11,000) spectra across the Ca-triplet region stellar parameters, $T_{\rm eff}$, log g, [Fe/H], [α/Fe] were determined, and distances were calculated for all stars. In total, the metal-poor ARGOS sample includes 17 stars with -2.8 dex $\leq$ [Fe/H] $\leq$ -2.2 dex with Galactocentric radii between 1 and 3 kpc. From these 17 primary ARGOS targets ($14.5 < V < 17.5$), we selected for our high resolution UVES observations, 5 ARGOS targets with magnitudes $14.5 < V < 15.5$, which ARGOS measured metallicities between -2.5 to -2.25 ($\pm$ 0.15) dex and α enhancement all at $\sim$ 0.7 ($\pm$0.15) dex and within 3.5 kpc from the Galactic center.

These primary 5 targets are listed in Table 2.1. These targets are supplemented with a larger sample of metal-poor stars selected from our SkyMapper[3] photometry within each 25 arcminute UVES/FLAMES field (similarly to Howes et al., 2014), with SkyMapper photometry calibrated using the ARGOS [Fe/H] determinations. This approach represents a highly efficient survey for metal-poor stars within the inner Milky Way. As outlined in Howes et al. (2014), the SkyMapper survey features a filter set optimized for stellar astrophysics. In particular it provides excellent resolution of stellar metallicity (Keller et al., 2007): the rare metal-poor stars can be isolated from the bulk of bulge stars by their UV excess with a low level of contamination. The photometric selection was made, however, using the preliminary (and uncalibrated) commissioning SkyMapper photometry. Individual cuts were made on each field using the colour sensitivity as shown in Figure 2.1. The use of commissioning data suffices for our purpose of identifying metal-poor stars. Current SkyMapper data has shown to perform well at mapping stellar metallicities (Casagrande et al., 2019) although this does not include regions close to the Galactic plane where the current pipeline is not optimized to deal with high stellar crowding (Wolf et al., 2018).

Our UVES/FLAMES fields are at longitudes of $0°, +5°, +15°$ and $-10°$; all within the region predicted by simulations to be populated with the highest

[3]Located at Siding Spring Observatory in Australia, SkyMapper is a 1.35m automated wide-field survey telescope with the goal of mapping the entire southern sky down to $\sim$ 20-21 mag with photometry in six filters, *uv* (unique to SkyMapper) and *griz* (Sloan Digital Sky Survey like, Fukugita et al., 1996). For further description of the SkyMapper photometric system we refer the reader to Bessell et al. (2011).

density of the oldest stars in the Galaxy. We used the photometric sensitivity to make a selection of targets to fill all FLAMES and remaining UVES fibers (beyond our 5 primary targets), and have a sample of a total of 40 UVES (R$\sim$ 47,000) stars and 640 FLAMES stars (R $\sim$ 20,000) and in this work, we examine our high resolution UVES targets.

We required between 3 to 9.5 hours on each primary ARGOS target to obtain a signal-to-noise, S/N $\sim$ 50. This SNR requirement is linked to the requirement to reach a precision <0.2 dex in our elemental abundance measurements, which is sufficient to distinguish between different stellar populations.

2.3 Data

2.3.1 UVES Spectroscopic Data

Spectroscopic data for the 40 bulge targets, selected as described in Section 2.2, were obtained with the UVES instrument on the European Southern Observatory's (ESO) Very Large Telescope (VLT). UVES is a high resolution optical spectrograph with wavelength coverage 3000-11000 Å. The spectrograph has two arms, the RED arm and the BLUE arm. The BLUE arm is for the ultraviolet wavelengths (3000-5000 Å) and the RED arm is for the visual wavelengths (4200-11000 Å). The RED arm has two CCDs, lower/blue and upper/red. Observations for this work were taken in the standard RED580 setup. This setup has a wavelength coverage of 4726-6835 Å with a gap (5804-5817 Å) between the lower/blue and upper/red chips and R $\sim$ 47,000. For

more details about UVES we refer the reader to Dekker et al. (2000).

The data for this project were taken in the 'MOS' mode for the FLAMES/UVES instrument. Raw data can be found within the ESO archive[4] (Program ID: 089.B-0694). As noted within the ESO archive, reduced Phase 3 data products are not provided for UVES spectra observed in the 'MOS' mode. Therefore, we have reduced the data using version 2.9.1 of the EsoReflex interface[5]. Within the EsoReflex interface we made use of the FLAMES-UVES workflow for the data reduction.

In short, the EsoReflex package performs a traditional data reduction workflow. Namely, it completes a bias subtraction, fiber order trace, computation and correction for both the detector pixel-to-pixel gain variations and the blaze function. After which it extracts the spectrum and performs the wavelength calibration for each fiber. For more details we refer the reader to Section 9 of the UVES-fibre pipeline manual. Descriptions on how to download EsoReflex, its use, and the exact calibration steps we refer the reader to the UVES-FIBRE instrument pipeline package[6], and the accompanying tutorial[7].

Each bulge star in this work has been observed multiple times. Therefore, once the data had been reduced, extracted and wavelength calibrated from the EsoReflex interface, we co-added the spectra from unique bulge tar-

[4] http://archive.eso.org/eso/eso_archive_main.html

[5] https://www.eso.org/sci/software/esoreflex/

[6] ftp://ftp.eso.org/pub/dfs/pipelines/uves/uves-fibre-pipeline-manual-18.11.pdf

[7] ftp://ftp.eso.org/pub/dfs/pipelines/uves/uves-fibre-reflex-tutorial-1.11.pdf

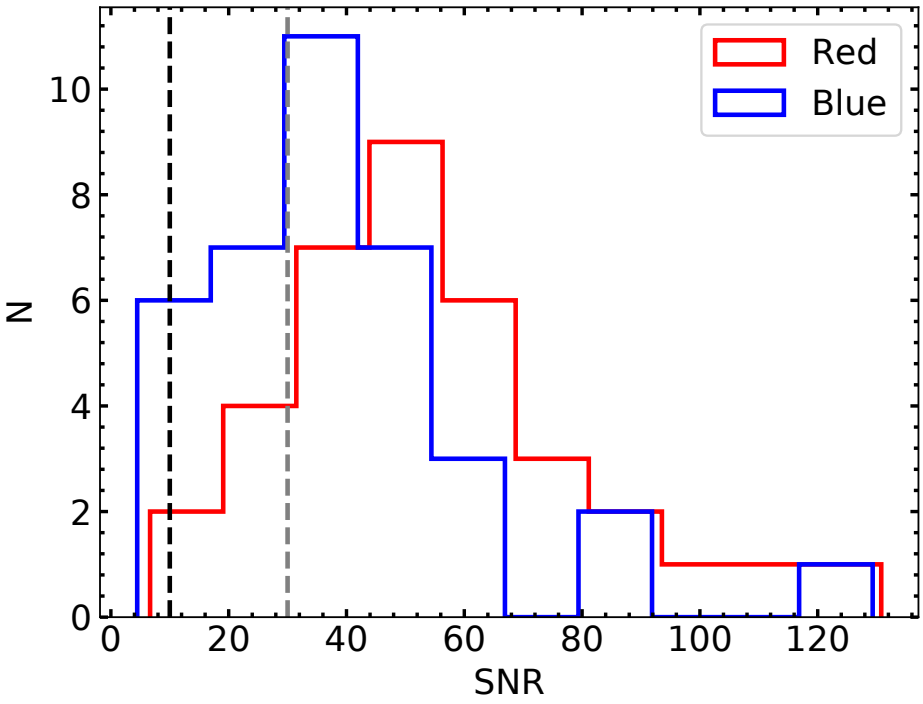

Figure 2.2: Shows the distribution of the signal-to-noise ratio (SNR) per pixel in the final bulge sample in both the UVES blue/lower (blue line) and red/upper (red line) chips. The SNR for the blue/lower chip is measured at wavelengths 5353 to 5354.2 Å, 5449.6 to 5450.49 Å, and 5464.6 to 5465.4 Å. The SNR for the red/upper chip is measured at wavelengths 6328.1 to 6329.7 Å, 6446.7 to 6447.5 Å, and 6705.5 to 6706.1 Å. The black dashed line shows the SNR cut of 10 pixel^{-1}. The grey dashed line shows the low SNR cut of 30 pixel^{-1}. Although we report the results, we flag stars with 10 pixel^{-1} $<$ SNR $<$ 30 pixel^{-1} in our abundance analysis.

gets. To do this, we start by using iSpec (Blanco-Cuaresma et al., 2014) to fit a continuum to each spectra using a third order spline. We note that it is significantly easier to find the continuum in metal-poor stars. Once the continuum is fit, the spectra are radial velocity (RV) corrected. RVs are determined using a cross-correlation with respect to Arcturus. Finally, spectra for the same object which had signal-to-noise ratio (SNR) larger than >10 pixel^{-1} were co-added. One star is removed from the analysis because none of its spectra had SNR > 10 pixel^{-1}. Stars were rejected if the scatter in radial velocity between the individual visits was larger than a few km s^{-1}. This is done because it is not clear if the wrong star made its way into the fiber or if the star has radial velocity variability. This criteria removed three stars. We also removed another 3 stars that have a final SNR in the red/lower chip < 10 pixel^{-1}. The SNR for the blue/lower chip is measured at wavelengths 5353 to 5354.2 Å, 5449.6 to 5450.49 Å, and 5464.6 to 5465.4 Å while the SNR for the red/upper chip is measured at wavelengths 6328.1 to 6329.7 Å, 6446.7 to 6447.5 Å, and 6705.5 to 6706.1 Å. We have a final sample of 33 stars for spectral analysis. The distribution of the final SNR per pixel for the final sample in both the blue/lower and red/upper chip can be found in Fig. 2.2. We note that the typical SNR for spectra in this study is SNR ∼50 pixel^{-1} in the red chip. For reference, we also show in Fig. 6.1 the final reduced, extracted 1-D, continuum and RV corrected spectra for 3 bulge targets. These spectra are what will be used to derive stellar parameters and elemental abundances.

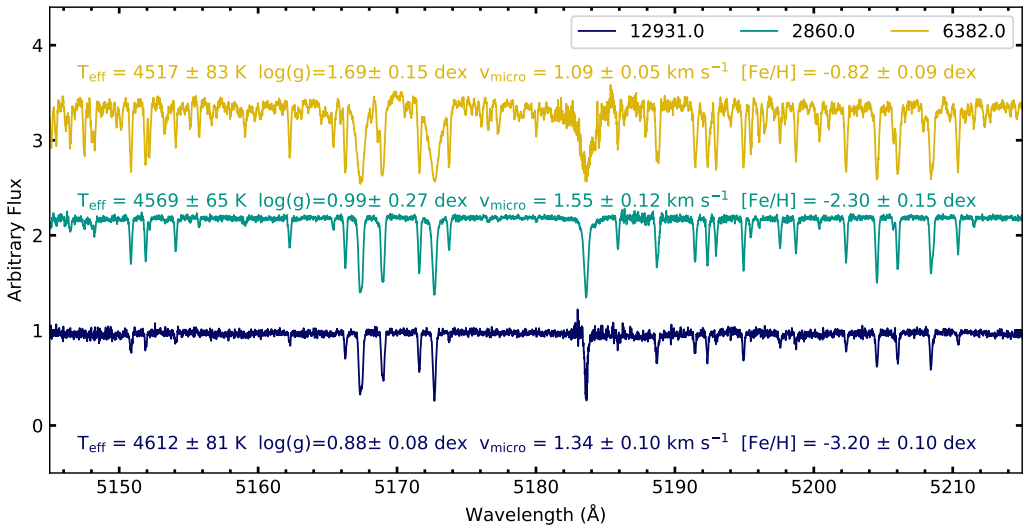

Figure 2.3: The observed spectra in the Mg triplet region (5145-5215 Å) of a few target stars, specifically 6577.0 (dark blue solid line), 2860.0 (green solid line), and 6805.0 (yellow solid line).

2.3.2 Gaia

In this study, we use *Gaia* DR2 data to confirm that our target stars are located in the bulge. Combining the Galactic coordinates of our stars with distances derived from *Gaia* DR2 parallaxes, gives us the location of our stars with respect to the Galactic center. However, most of our stars have fractional parallax errors $> 20\%$ in *Gaia* DR2. Therefore, estimating the distance by inverting the parallax will give unreliable results. The distance catalog from Bailer-Jones et al. (2018) uses more sophisticated methods, namely Bayesian inference with a weak distance prior, to accurately take the large parallax errors into account when determining the distances. Therefore, these distances are more reliable than a simple inverted parallax method and we use them when determining the Galactic positions of the stars in our, and other, samples.

The distances from Bailer-Jones et al. (2018) combined with the Galactic coordinates show that our sample is comprised of bulge stars. Figure 2.4 shows the Galactocentric radius of our target stars. The error bars are calculated by determining the Galactocentric radius for lower and upper bound of the 68 % confidence interval given in Bailer-Jones et al. (2018). In addition, we show a local disk study

(Bensby et al., 2014, light blue open squares), a halo study (Roederer et al., 2014, green triangles) and two bulge studies (Howes et al., 2016; Gonzalez et al., 2015, yellow open squares and yellow triangles, respectively). The distances for each study are taken from the distance catalog in Bailer-Jones et al. (2018). Compared to the local disk study and the halo study our stars are

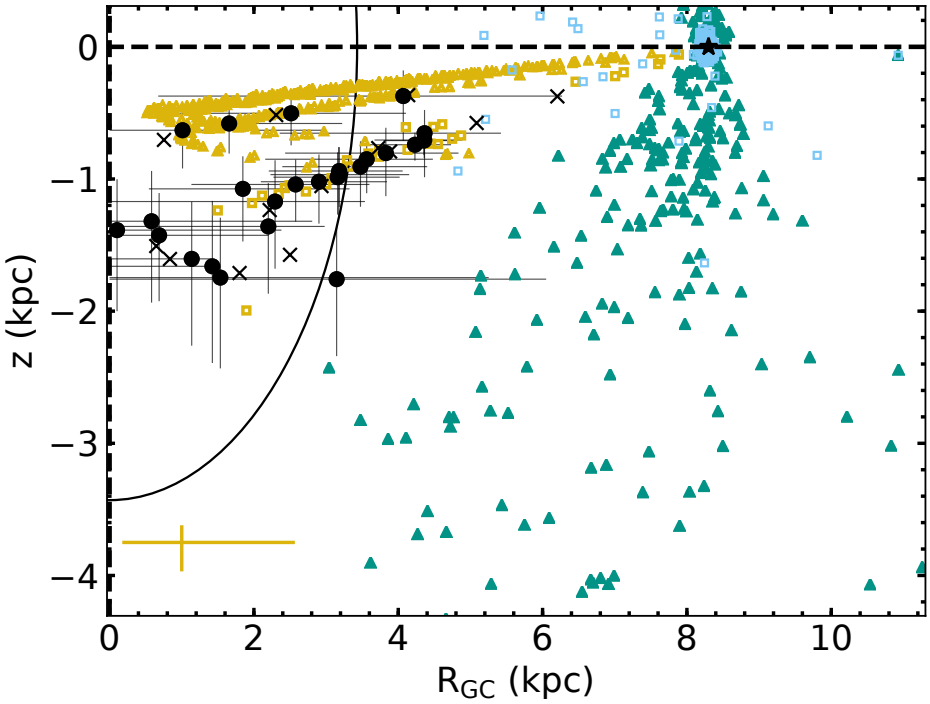

Figure 2.4: Demonstrating the Galactic position of our target bulge stars compared to a few of the literature samples used in this study. Stars for which we successfully derived abundances are shown as black filled circles, while stars we observed but for which we do not report abundances are shown as black xs. Previous bulge studies are shown in yellow, halo studies are shown in green and disk studies are shown in light blue. The bulge studies included in this figure are Howes et al. (2016, yellow open squares) and Gonzalez et al. (2015, yellow triangles). For comparison, a median error bar for these studies is shown in the yellow in the bottom right corner. The disk study shown is Bensby et al. (2014, light blue open squares) and the halo study is Roederer et al. (2014, green triangles). Distances for each sample are taken from the Bailer-Jones et al. (2018) distance catalog. The Sun is shown as a black star. The solid line denotes a spherical radius of 3.43 kpc. The typical error in R_{GC} for our sample is 2.57 kpc while the typical error in z is 0.40 kpc.

much closer to the Galactic center. As shown in Figure 2.4, the samples from both Howes et al. (2016) and Gonzalez et al. (2015) are contaminated with stars with a Galactocentric radius > 5 kpc. The majority of our stars are within 3.43 kpc which Robin et al. (2012) defines as the simplest criteria for a bulge star. Despite the large parallax errors in *Gaia* DR2 for our sample, we find that the Galactocentric radius of our sample is similar to Howes et al. (2016), which is expected given the similar selection method. Therefore, we conclude our sample is spatially consistent with bulge stars and may be more representative of the bulge than the previous studies. We note that the Galactocentric velocity distribution is consistent with previous bulge studies Howard et al. (e.g., 2008). In the next part of this survey, we will perform a detailed study of the kinematics of these stars to determine if they are confined to the bulge.

2.4 Stellar Parameter and Elemental Abundance Analysis

Stellar parameters and elemental abundance analysis was done using Brussels Automatic Code for Characterizing High accUracy Spectra (BACCHUS, Masseron et al., 2016). The current released version generates synthetic spectra using the MARCS model atmosphere grid (Gustafsson et al., 2008) and the TURBOSPECTRUM radiative transfer code (Alvarez & Plez, 1998; Plez, 2012). Also used are the fifth version of the Gaia-ESO linelist for atomic lines which includes hyperfine structure (Heiter at al., in preparation),

and molecular lines for CH (Masseron et al., 2014), CN, NH, OH, MgH, C_2 (T. Masseron, private communication), SiH (Kurucz linelists), and TiO, ZrO, FeH, CaH (B. Plez, private communication).

In short, BACCHUS derives the effective temperature (T_{eff}), surface gravity (log g), iron abundance ([Fe/H]), and microturbulent velocity (v_{micro}) using the standard Fe-Ionization-Excitation equilibrium technique (see Figure 2.5) under the assumption of local thermodynamic equilibrium (LTE). Abundances are determined from a χ^2 minimization to synthesized spectra.

To determine the stellar parameters, BACCHUS first determines the convolution (accounts for instrumental and rotational broadening) and v_{micro}, while fixing the T_{eff} and log g to the initial guesses. The v_{micro} and convolution are solved when the Fe abundances derived from the core line intensity and the equivalent width are in agreement for each line. This ensures there is no correlation between the Fe abundance and the reduced equivalent width (EW/λ, defined as the equivalent width divided by the wavelength of the line). The equivalent width is calculated by taking the integral of the synthesized spectrum over an automatically selected window, as in Masseron et al. (2016). Next, BACCHUS fixes the v_{micro} and convolution and solves for the T_{eff} and log g. The T_{eff} is solved when there is no correlation between the Fe abundance and the excitation potential of the lines and log g is solved when there is no significant offset between the neutral Fe (Fe I) and singly ionized Fe (Fe II) abundances. Here, the Fe abundance is calculated by a χ^2 minimization between the observed spectrum and the synthesized spectrum. Last, BAC-

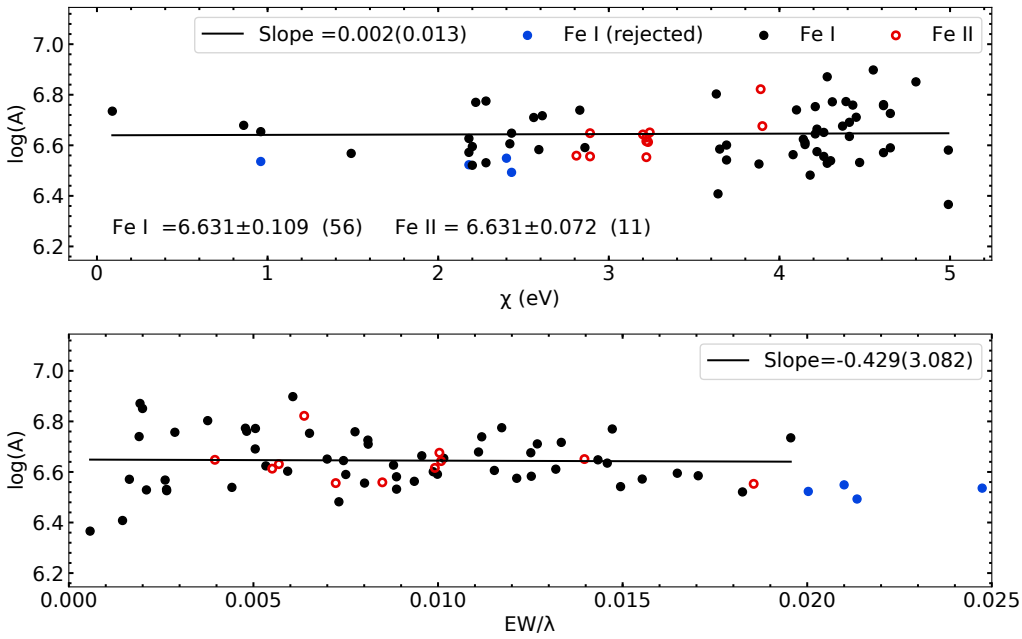

Figure 2.5: Demonstrates the Fe-Ionization-Excitation equilibrium technique for star 7064.3. The upper panel shows the log of the Fe abundance as a function of excitation potential for Fe I lines (black filled circles) and Fe II lines (red open circles). The lower panel shows the log of the Fe abundances as a function of the reduced equivalent width (EW/λ). For each panel, the blue filled circles show lines that have a reduced equivalent > 0.02 and are consequently rejected from the analysis. The black lines show the best fit lines to the Fe I abundances for each panel. The text in the upper panel shows the abundance determined using Fe I and Fe II lines, the standard deviation in those abundances and in parentheses, the number of lines used to calculate them.

CHUS uses the previous results to create a grid of 27 model atmospheres and interpolating between them to find the solution where all the criteria for the Fe-Excitation-Ionization equilibrium are met. Each of these steps use up to 80 Fe I lines and 15 Fe II lines. We refer the reader to Section 2.2 of Hawkins et al. (2015) for more information about BACCHUS.

The error in the $T_{\rm eff}$ is roughly related to the error in the slope of the best fit line for the excitation potential versus Fe abundance plot. The error in log g is roughly related to the error in the Fe I and Fe II abundances. The error in [Fe/H] is the standard deviation in the Fe I abundances. Finally, the error in $v_{\rm micro}$ is related to the error in the slope of the best fit line for the Fe abundance versus reduced equivalent width plot. We refer the reader to Masseron et al. (2016) for more information on BACCHUS error analysis.

We attempted spectral analysis for 33 stars. The stellar parameters were successfully derived for 26 stars in our sample. BACCHUS failed to derive precise stellar parameters for a total of 7 stars. Four of these stars have low SNR (< 30 pixel^{-1}). We flag any star with SNR < 30 pixel^{-1} that BACCHUS successfully derives parameters. Another star whose calculated SNR is 34 pixel^{-1} also failed. Upon further visual inspection of its spectrum, we find it has regions where it is much noisier which causes a large dispersion in the derived Fe II abundances. For the last two stars, BACCHUS was only able to find a solution when it fixes the microturbulence to a set value. However, we do not report these abundances because of the large errors in the derived parameters. In summary, we observed a total of 474 spectra of 40 stars. Seven

of these 40 stars are removed during the data reduction process (see Section 2.3.1). Another seven stars are removed during the spectral analysis for the reasons stated above. This leaves a total of 26 stars for which we derived abundances.

The abundances for each element, X, and absorption feature are determined by using the derived stellar parameters to create synthetic spectra with different values of [X/H]. A χ^2 minimization is then performed between the observed spectrum and the synthesized spectra to determine the abundance. BACCHUS automatically rejects lines that are strongly blended. Further, we visually inspect the lines to ensure quality fits to the synthesized spectra. The final elemental abundance is determined by taking the median of the elemental abundances for individual accepted lines. The elemental abundances are scaled relative to solar values from Asplund et al. (2005). This process was completed for 22 different elements in addition to Fe.

The uncertainties in the elemental abundances are derived by adding the typical sensitivities of the abundance and the internal error in quadrature. The typical sensitivities for each stellar parameter are found by calculating the change in the abundance after adjusting the parameter by the average error in that parameter. The average error in the $T_{\rm eff}$, log g, [Fe/H] and $v_{\rm micro}$ of our sample is 127 K, 0.46 dex, 0.16 dex and 0.12 km s^{-1}, respectively. This process is completed for one star (5126.2) whose parameters are in the center of our parameter space ($T_{\rm eff}$ = 4785 K, log g = 2.27 dex, [Fe/H] = -0.86 dex, and $v_{\rm micro}$= 1.22 km s^{-1}). The internal error is the line-by-line dispersion in

Table 2.2: Typical Sensitivities of the [X/H] Abundances on Stellar Parameters

[X/H]	$\sigma_{T_{eff}}$ ($\pm$ 127 K)	$\sigma_{log(g)}$ ($\pm$ 0.46)	$\sigma_{[Fe/H]}$ ($\pm$ 0.16)	$\sigma_{v_{micro}}$ ($\pm$ 0.12 km s^{-1})
Fe	$\pm$0.10	$\pm$0.09	$\pm$0.03	$\mp$0.05
Mg	$\mp$0.05	$\mp$ 0.08	$\pm$0.02	$\pm$0.05
Si	$\mp$0.14	$\pm$0.10	$\mp$0.02	$\pm$ 0.04
Ca	$\pm$0.11	$\mp$0.12	$\mp$ 0.09	$\mp$0.07
Ti	$\pm$0.09	$\mp$ 0.04	$\mp$0.04	$\pm$0.03
Mn	$\pm$0.13	$\mp$0.06	$\mp$0.09	$\pm$ 0.04
Co	$\pm$0.04	$\mp$ 0.02	$\pm$0.01	$\pm$0.05
O	$\mp$0.09	$\pm$0.16	$\pm$0.08	$\pm$0.05
Cr	$\pm$0.11	$\mp$0.07	$\mp$0.05	$\mp$0.04
Cu	$\pm$ 0.12	$\mp$0.10	$\pm$0.10	$\pm$0.04
La	$\mp$ 0.05	$\pm$0.11	$\pm$ 0.06	$\pm$0.05
Al	$\mp$0.26	$\mp$ 0.09	$\pm$ 0.29	$\pm$0.05
Na	$\mp$0.01	$\mp$0.09	$\pm$0.02	$\pm$0.05
Ni	$\pm$0.04	$\pm$0.03	$\mp$0.00	$\pm$ 0.01
Ba	$\pm$0.13	$\pm$0.12	$\mp$0.01	$\mp$0.14
Sr	$\pm$0.37	$\mp$0.28	$\pm$0.28	$\pm$0.11
Y	$\mp$0.08	$\pm$0.12	$\pm$0.04	$\pm$0.01
Eu	$\mp$0.11	$\pm$0.25	$\pm$ 0.10	$\pm$0.05
V	$\pm$0.12	$\mp$0.08	$\mp$0.03	$\pm$0.05
Sc	$\mp$0.10	$\pm$0.11	$\pm$0.06	$\pm$0.02
Zr	$\pm$0.12	$\mp$0.09	$\pm$0.08	$\pm$0.05
Nd	$\mp$0.04	$\pm$0.13	$\pm$ 0.04	$\pm$0.05

The typical sensitivities are calculated by measuring the change in abundance [X/H] when the stellar parameters are adjusted by the average error. Columns 2, 3, 4, and 5 shows the change in [X/H] for a change in T_{eff} of $\pm$127 K, in log g of $\pm$0.46 dex, in metallicity of $\pm$0.16 dex and in v_{micro} of $\pm$0.12 km s^{-1}, respectively. This is completed for one star (5126.3) in the median of our parameter space (T_{eff} = 4785 K, log g = 2.27 dex, [Fe/H] = -0.86 dex, and v_{micro}= 1.22 km s^{-1}), and has measured abundances in all of our 22 elements besides Li.

the abundance divide by the square root of the number of lines used. If only one line is used, an internal error of 0.1 dex is assigned, as in Hawkins & Wyse (2018); Howes et al. (2016).

The differences in atomic data, adopted solar abundances, and analysis methods cause systematic offsets in abundances between surveys. In order to determine the impact of systematic offsets and accurately compare abundances, a comparative analysis with metal-poor stars from Bensby et al. (2014) and Yong et al. (2013) is performed. We take reduced spectra from the ESO Archive for stars in these samples that are observed with VLT/UVES and have [Fe/H] $<$ -0.5 dex. They are analyzed in BACCHUS and the stellar parameters and elemental abundances are derived as described above. The difference between the reported results in Yong et al. (2013) and Bensby et al. (2013), and our analysis are calculated and shown in Figures 2.6 and 2.7. The median of the differences for the 12 stars from Bensby et al. (2014) are applied to shift our results to the same scale as the Bensby et al. (2014) results in the figures. The average shift across all elements is -0.05 dex. The elemental abundances from Yong et al. (2013) are then shifted according to the differences in Figure 2.6 to match our new scale. The average shift across all elements for the results in Yong et al. (2013) is -0.15 dex.

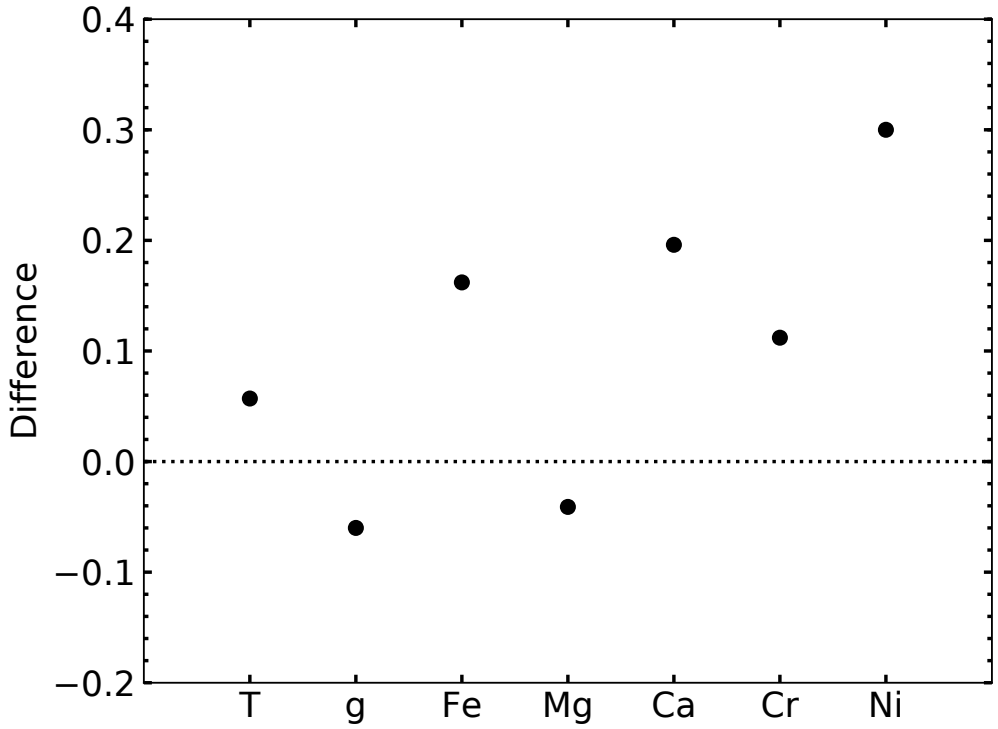

Figure 2.6: The differences in the derived parameters and elemental abundances between our analysis and the analysis in Yong et al. (2013) for star HE 1506-0113. For each element, the difference reported is $[X/H]_{Yong} - [X/H]_{BACCHUS}$. The two leftmost values show the T_{eff} (T) and log g. The value for T_{eff} is scaled down by a factor of 1000. The elemental abundance differences are used to scale the reported abundances in Yong et al. (2013) to our results.

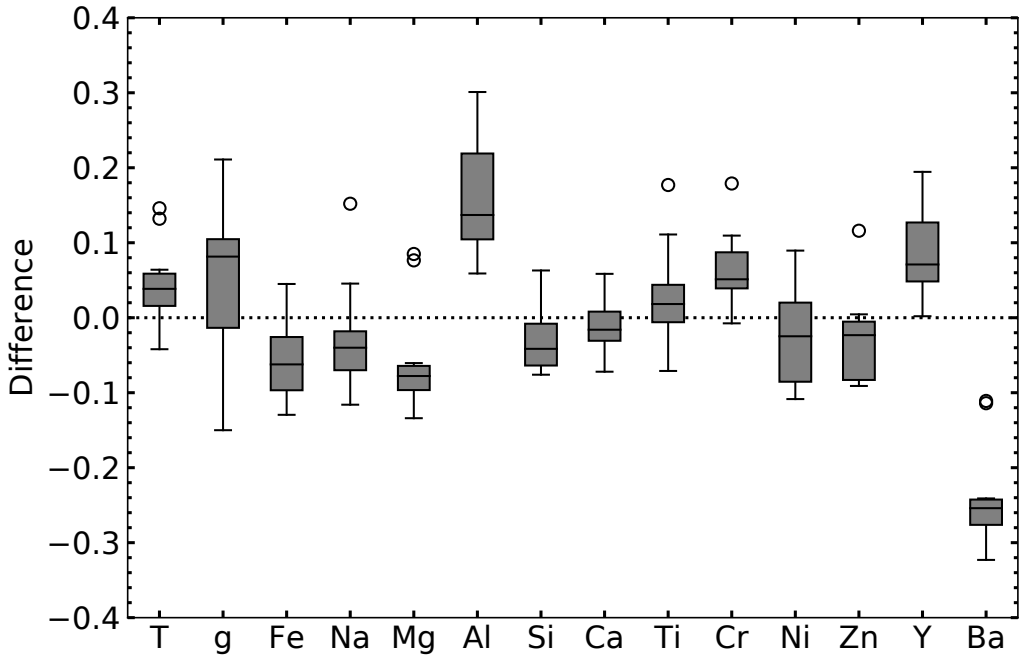

Figure 2.7: The differences in the derived parameters and elemental abundances between our analysis and the analysis in Bensby et al. (2014) for 12 metal-poor stars observed by VLT/UVES. For each element, the difference reported is $[X/H]_{Bensby} - [X/H]_{BACHHUS}$. The two leftmost values show the T_{eff} (T) and log g. The value for T_{eff} is scaled down by a factor of 1000. The elemental abundance differences are used to scale our elemental abundances to the results in Bensby et al. (2014).

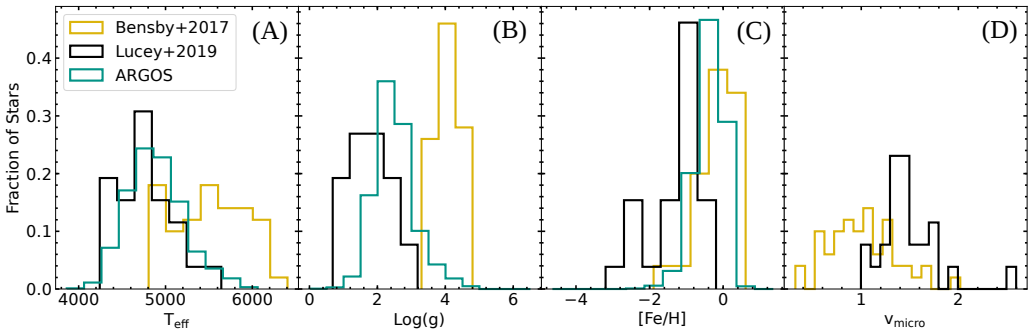

Figure 2.8: The distribution of stellar parameters for our sample of bulge giant stars compared to the micro-lensed bulge dwarf and subgiant stars from Bensby et al. (2017) and the bulge giant stars in the ARGOS survey (Freeman et al., 2013). Our sample is shown as a black line while the Bensby et al. (2017) sample is shown in gold and the ARGOS survey is shown in green. Our sample focuses on the low-end of the metallicity distribution of the bulge.

2.5 Results

2.5.1 Metallicity and Stellar Parameters

The results of the derived stellar parameters are shown in Figure 2.8. The average uncertainties are 127 K, 0.46 dex, 0.16 dex and 0.12 km s^{-1} for T_{eff}, log g, [Fe/H] and v_{micro}, respectively. The results shown in Panel C of Figure 2.8 confirm our SkyMapper selection method has been sufficient to isolate a sample of metal-poor stars in the inner region. We note here that we have derived parameters that are not consistent with the parameters found in the ARGOS survey (Ness & Freeman, 2016) for two of our stars (12931.0 and 42011.0). In total, we have four star in common with ARGOS. The average and standard deviation in the differences in the ARGOS parameters and our results are as follows: $\Delta T_{eff} = 527 \pm 238$K, Δlog(g) $= 1.23 \pm 0.76$ dex, and

Δ[Fe/H] = 0.28$\pm$0.33 dex. We conclude that our parameters are more accurate given the much higher resolution of our spectra.

The MDF of the bulge has a mean metallicity of around [Fe/H] = 0 dex. In ARGOS, only about 5% of stars have metallicities < -1.0 dex (Ness & Freeman, 2016).

The average metallicity of our sample is -1.29 dex with a dispersion of 0.74 dex. We find five stars with [Fe/H] < -2.0 dex. The observed metallicity distribution indicates that our sample contains stars that come from the populations associated with the metal-weak thick disk, and the stellar halo.

2.5.2 The α elements

Elements that are formed by successive addition of helium nuclei (α-particles) are called α elements (Burbidge et al., 1957). α elements are further divided into two categories: hydrostatic and explosive. Hydrostatic α elements (oxygen and magnesium) are primarily formed during the hydrostatic phase of massive stars while the explosive α elements (silicon, calcium, and titanium) are primarily formed during explosive nucleosynthesis of core-collapse supernovae (SNII) (Woosley & Weaver, 1995; Woosley et al., 2002).

2.5.2.1 O and Mg

The hydrostatic α elements (O and Mg) are formed during the hydrostatic burning phase of massive stars and are dispersed through the ISM through SNII events. Therefore, their ratios relative to Fe are sensitive to the

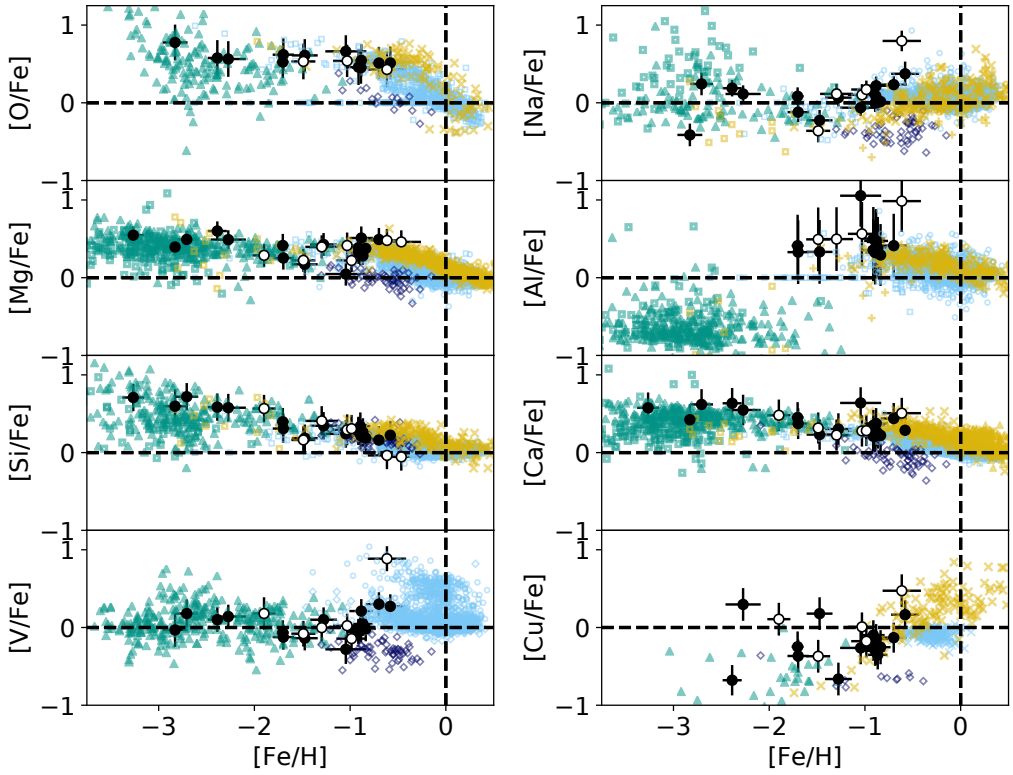

Figure 2.9: [X/Fe] for the program stars as a function of metallicity for O, Mg, Si, and V from top to bottom on the left and Na, Al, Ca, and Cu from top to bottom on the right. These elements are α and odd-Z elements. Also shown are abundances for the halo (green), the Large Magellanic Cloud (LMC; dark blue), the disk (light blue) and the bulge (yellow). The program stars with SNR $\geq$ 30 are shown as black filled circles while program stars with SNR between 10 and 30 are shown as black open circles. The halo abundances are from Roederer et al. (2014, green triangles) and Yong et al. (2013, green open squares). The LMC abundances are from Van der Swaelmen et al. (2013, dark blue open diamonds). The disk abundances are from Bensby et al. (2014, light blue open squares), Adibekyan et al. (2012, light blue open circles), and Battistini & Bensby (2015, light blue open diamonds). The bulge abundances are from Howes et al. (2016, yellow open squares), Gonzalez et al. (2015, yellow triangles), Johnson et al. (2014, yellow xs) and Bensby et al. (2017, yellow open circles).

Type Ia time-delay scenario and star formation history.

Results in the literature show there is a slight Mg enhancement in the bulge at higher metallicities consistent with a shorter star formation timescale. For example, Bensby et al. (2014) found [Mg/Fe] abundances of micro-lensed dwarf stars in the bulge are slightly higher than in the disk as shown in Figure 4.7. Gonzalez et al. (2015) measured similar results in giant bulge stars. Additionally, Howes et al. (2016) found the [Mg/Fe] abundances in the bulge at low metallicity have a large dispersion.

All of our target bulge stars show enhanced values of [Mg/Fe] relative to the Sun, consistent with previous studies (e.g., Gonzalez et al., 2015; Bensby et al., 2017). At the higher metallicity end, our observed stars show enhancement in [Mg/Fe] relative to the disk, indicating that the bulge may have a shorter star formation timescale. It is interesting to note the low-dispersion of [Mg/Fe] abundances at the low-metallicity end for our observed stars. This is contrary to the dispersion observed in Howes et al. (2016). We use Yong et al. (2013) to compare our sample's dispersion to the dispersion of the halo. We choose to use Yong et al. (2013) instead of Roederer et al. (2014) because the error analysis in Yong et al. (2013) is very similar to our analysis while Roederer et al. (2014) uses a different method. Therefore, we can more accurately compare the dispersion and precision of our elemental abundances with Yong et al. (2013). In order to take the difference in sample size into account, we randomly selected stars from Yong et al. (2013) 1000 times and calculated the mean dispersion. For each element, we would select the same number of

stars as we had abundance measurements of stars with [Fe/H] < -1.5 dex. We measure a dispersion in [Mg/Fe] at metallicities below -1.5 dex of 0.11 dex and an average error in [Mg/Fe] of 0.13 dex for our sample. For Yong et al. (2013), we measure an average dispersion of 0.23 dex and an average error of 0.12 dex. Therefore, we do not measure a significant dispersion, while Yong et al. (2013) finds that the halo has significant dispersion in [Mg/Fe]. It is possible that the low dispersion in various elements observed here could partially be attributed to the lack of carbon-enhanced metal-poor (CEMP) stars. However, we note that Howes et al. (2016) observes a large dispersion (possibly from contamination of their bulge sample with halo stars) despite the lack of CEMP stars. In addition, when we remove the CEMP stars from the stellar halo sample from Yong et al. (2013), we still find an average dispersion that is significantly larger in the halo compared to the bulge targets studied here.

In order to address the impact on [Mg/Fe] of non-LTE (NLTE) at low metallicities, we obtained line-by-line NLTE corrections for Mg from Bergemann et al. (2015). When these corrections are applied, the mean abundance trend is still consistent with the literature. Although our scatter in the abundances increases, we cannot accurately compare this NLTE scatter to the observed scatter in the halo because Yong et al. (2013) calculates the abundances in LTE and we do not know how they would behave in NLTE.

Oxygen abundances are thought to be impacted by an additional mechanism given that it declines more steeply with metallicity in the Galactic disk compared to the other α elements. The two mechanisms that have been pro-

posed to account for this steepening include: 1. stellar wind mass-loss which leads to a decrease in O yield and 2. a steeper IMF at the top-end with increasing metallicity (McWilliam, 2016). Johnson et al. (2014) found evidence for a higher [O/Fe] plateau suggesting a top-heavy IMF in the bulge. They also found [O/Fe] enhancement at higher metallicities compared to the disk indicating a shorter star formation timescale that agrees with the results from the other α elements.

As shown in Figure 4.7, our observed O abundances show an agreement with the disk plateau indicating that the bulge and disk may have the same IMF. Interestingly, we do not measure a significant dispersion in [O/Fe] for stars on our sample with [Fe/H] $<$ -1.5 dex. Our measured dispersion is 0.09 dex, while our average error is 0.22 dex.

2.5.2.2 Si and Ca

The α elements Si and Ca are primarily formed during the explosive nucleosynthesis of SNII events. SNII yield more of these α elements than Fe while SNIa yield more Fe than these elements. Therefore, Si and Ca are sensitive to the SNIa time-delay scenario and star formation history.

There is ample evidence for an enhanced [X/Fe] ratio for Si and Ca at roughly solar metallicities in the Galactic bulge, indicating higher rates of star formation than in the disk. For example, Johnson et al. (2014), Howes et al. (2016) and Bensby et al. (2017) all measured Ca and Si abundances for stars in the bulge and found that they are enhanced relative to the disk. This

enhancement starts around metallicities of -1.00 dex. Below those metallicities, Howes et al. (2016) found a large dispersion in [Si/Fe] and [Ca/Fe], and an overall enhancement relative to the Sun.

Our derived elemental abundances for Si and Ca are consistent with the literature and our observed hydrostatic α abundances. However, the dispersion at low metallicities is much lower for our program stars than in the halo and in Howes et al. (2016). The average dispersions of Si in Yong et al. (2013) is more than twice the measured dispersions of our sample. It is possible that the large dispersion in Howes et al. (2016) is due to contamination from halo stars. Though, studying their kinematics will allow us to confirm if that is the case. Figure 2.4 shows there are several stars with Galactic radii $> \sim 6$ kpc, according to the Bailer-Jones et al. (2018) distance catalog. We also note that Fulbright et al. (2007) found similar results and measured a "starkly" small scatter in Si, Ca and Ti abundances in the the bulge compared to the halo.

The level of α enhancement observed in these low metallicity stars provides evidence that these stars are not from an accreted dwarf galaxy. The high level of enhancement in Ca for four of our stars with [Fe/H] $<$ -2 dex relative to the Galactic disk plateau at [Fe/H] $<$ -2 dex is consistent with a flat IMF (e.g., Johnson et al., 2013a). Our Ca abundances are also consistent with Duong et al. (2019a) who also measure high levels of Ca enhancement in metal-poor bulge stars. At the higher metallicity end the [α/Fe] values have similar trends to those seen in the disk, but are more enhanced likely from a shorter star formation timescale.

Line-by-line NLTE corrections for Si were obtained from Bergemann et al. (2013). When these corrections are applied to our Si abundances, the mean abundance trend is still consistent with the literature. Although our scatter in the abundances increases, we cannot accurately compare this NLTE scatter to the observed scatter in the halo because Yong et al. (2013) calculates the abundances in LTE.

2.5.3 The odd-Z elements

Odd-Z elements are any element with an odd atomic number (and therefore could not have been produced by successive addition of α-particles). Of the odd-Z elements, we measured elemental abundances for sodium (Na), aluminum (Al), vanadium (V), copper (Cu) and lithium (Li).

However, we were only able to measure Li abundances for four of our stars. These stars all have A(Li)[8]between 0.5 and 1 dex. These abundances are roughly what are expected for giant stars with the T_{eff} probed here. The uncertainties in the Li abundances are calculated in the same manner as the other elements. However since the selected median star (5126.3) for the typical sensitivities did not have a measured Li abundance, we calculated the typical sensitivities for Li using another star, 42011.0 (T_{eff} = 4559 K, log g = 0.98 dex, [Fe/H] = -2.65 dex, and v_{micro}= 1.45 km s^{-1}). Analysis of this star resulted in the following typical sensitivities: $\sigma_{T_{eff}} = 0.043$ dex, $\sigma_{log(g)} = 0.016$ dex, $\sigma_{[Fe/H]}$

[8]Li abundances are reported in the standard way, where A(Li) = log $\left(\frac{N_{Li}}{N_H}\right)$+12, where N_{Li} and N_H are the number of lithium and hydrogen atoms per unit volume, respectively.

= 0.034 dex, and $\sigma_{\mathrm{v_{micro}}}$ = 0.051 dex. The other odd-Z elements are will be discussed separately below.

2.5.3.1 Na

Results in the literature show that there is no significant difference between the trends in [Na/Fe] as a function of metallicity between the bulge and the disk. The lowest metallicity stars in our sample show enhanced [Na/Fe] relative to the Sun. However, we note the low dispersion and enhancement relative to Howes et al. (2016). Our sample also shows a lower dispersion at [Fe/H] <-1.5 dex (σ_{Na} = 0.22 dex) than the halo sample of Yong et al. (2013) (σ_{Na} = 0.42 dex). This difference in dispersion is significant given the average error of our [Na/Fe] abundances is 0.12 dex and Yong et al. (2013) reports an average error of 0.15 dex. At the higher metallicity end of our sample the [Na/Fe] abundances are disk-like. As shown in Figure 4.7, there is one clear outlier in [Na/Fe]. This star is an outlier in other elements as well and will be discussed further in Section 2.6

2.5.3.2 Al

Results in the literature show Al's α-like abundances in the bulge at metallicities above $\sim$-1 dex. In this range, the bulge shows a slight enhancement of [Al/Fe] with respect to the disk. This is consistent with a shorter star formation timescale. At the low metallicity end ([Fe/H] < $\sim$-1 dex), Howes et al. (2016, yellow squares in Figure 4.7) found the bulge has [Al/Fe] simi-

lar to the halo. Unfortunately, we are unable to measure Al abundances for our lowest metallicity stars due to low SNR. The [Al/Fe] ratios for our higher metallicity stars are consistent with previous results showing slight enhancement compared to the disk. There are two clear outliers with [Al/Fe] $\sim$ 1 dex. Large Al enhancement paired with low [Mg/Fe] is a signature of second generation globular cluster stars (Gratton et al., 2001; Carretta et al., 2004; Ramírez & Cohen, 2002, 2003; Lind et al., 2015). Therefore, we explore the possibility of globular cluster origin for these stars in Section 2.6.

2.5.3.3 V

Unfortunately, there has been very little work measuring V abundances in the Galactic bulge. However, we can still compare our results to literature values in the disk, halo and the LMC. As shown in Figure 4.7, [V/Fe] is roughly flat with metallicity in the halo, while showing an α-like slope in the disk and LMC. Overall, the [V/Fe] abundances of our target stars are consistent with those seen in the halo.

2.5.3.4 Cu

Consistent with a shorter star formation timescale, Johnson et al. (2014) measured [Cu/Fe] enhancement in the bulge relative to the disk at metallicities above $\sim$ -1 dex. Our results support this conclusion. At lower metallicities ([Fe/H] $<$ -1 dex) our bulge stars have a large dispersion in [Cu/Fe]. However, further measurements of Cu abundances for stars throughout the Milky Way

will be needed to constrain its production site.

2.5.4 The Fe-peak elements

The Fe-peak elements (chromium, nickel, scandium, titanium, manganese, zinc and cobalt) are formed in a variety of ways (Iwamoto et al., 1999; Kobayashi et al., 2006; Nomoto et al., 2013) but are largely dispersed into the ISM in ways similar to iron. Therefore, the Fe-peak elements generally trace iron with small variations except for Mn. We discuss each of the Fe-peak elements shown in Figure 4.8 separately.

2.5.4.1 Sc

There has not been much previous work measuring scandium (Sc) abundances in the bulge. Howes et al. (2016) found low metallicity stars in the bulge have [Sc/Fe] abundances similar to the halo. Our results support this conclusion. At [Fe/H] $<\sim$ -1.00 dex, our sample has [Sc/Fe] abundances that are consistent with the halo, and are roughly flat with values around the solar value. At higher metallicities ([Fe/H] $>\sim$-1 dex), Sc appears to have α-like trends in the disk and the LMC. We find that our results have an α-like trend and show a slight enhancement compared to the disk. This enhancement is consistent with a shorter star formation timescale in the bulge.

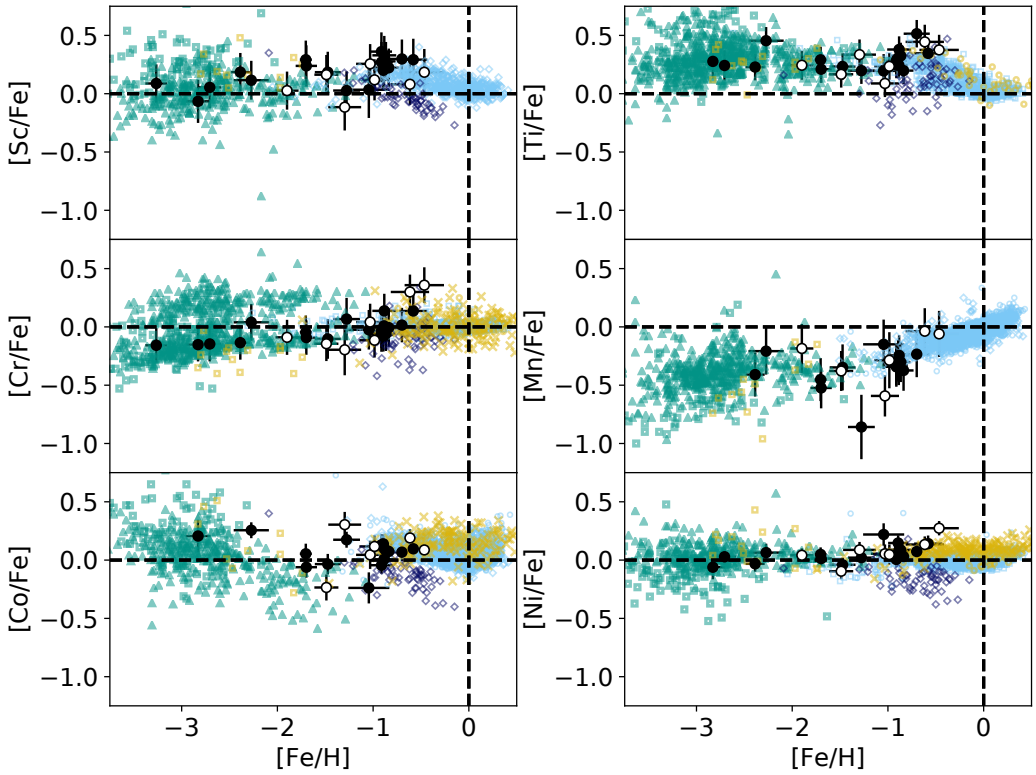

Figure 2.10: [X/Fe] for the program stars as a function of metallicity for Sc, Cr, and Co from top to bottom on the left and Ti, Mn, and Ni from top to bottom on the right. These elements are Fe-peak elements. The symbols are the same as in Figure 4.7 with the addition of copper abundances for the disk from Reddy et al. (2003, light blue xs).

2.5.4.2 Ti

Titanium (Ti) behaves similarly to the α elements. Its yield from SNII is higher than the yield from SNIa with respect to Fe. Therefore, it is sensitive to the SNIa time-delay scenario and star formation history. Often, it is thought of as an α element, however it is not formed through the successive addition of α particles. Therefore, we do not categorize it as an α element.

Bensby et al. (2017) and Howes et al. (2016) successfully measured Ti abundances for bulge stars for a range of metallicities. Their measured [Ti/Fe] abundances are enhanced relative to the disk at [Fe/H] $>$ -1 dex. This indicates a shorter star formation timescale which agrees well with the results for α elements in the bulge.

Our measured [Ti/Fe] abundances are consistent with the literature. For [Fe/H] $>$ -1 dex, we measure [Ti/Fe] that is enhanced relative to the disk, indication a shorter star formation timescale in the bulge. For [Fe/H] $<$ -1.5 dex our Ti abundances show a lower dispersion than the halo. The average dispersions of Ti in Yong et al. (2013) is more than twice the measured dispersions of our sample.

Line-by-line NLTE corrections for Ti were obtained from Bergemann et al. (2011). When the Ti corrections are applied, [Ti/Fe] is enhanced to values $\sim$ 0.75 dex. Because our comparative literature samples all have LTE abundances, we are unable to accurately compare our NLTE abundances to known stellar populations. Therefore, we do not draw conclusions about the

origins of these stars from their NLTE abundances.

2.5.4.3 Cr

Chromium (Cr) abundances roughly track Fe abundances. Therefore, [Cr/Fe] as a function of metallicity is largely flat and centered at the solar value. As shown in Figure 4.8 this is largely what has been seen in the halo and disk populations (Roederer et al., 2014; Yong et al., 2013; Bensby et al., 2014). We find that our sample has elemental abundances consistent with the halo and disk populations. It is interesting to note that our lowest metallicity stars all have [Cr/Fe] deficient relative to the Sun. We also note the low dispersion of our sample relative to the halo. The dispersion in [Cr/Fe] for our stars with [Fe/H] $<$ -1.5 dex is 0.06 dex and the average error is 0.15 dex while the average dispersion for the Yong et al. (2013) sample is 0.16 dex and the average error is 0.12 dex. This indicates these stars are likely from a distinct population, or that the halo is more chemically homogeneous towards the Galactic center. Overall, our results are consistent with the literature in the bulge. The combined results from our study and Howes et al. (2016) indicate possible Cr deficiency in the bulge at low metallicities.

2.5.4.4 Mn

Mn is thought to be produced in SNII and SNIa events. Theoretical work indicates SNII events under-produce [Mn/Fe] at roughly -0.3 to -0.6 dex regardless of metallicity (Kobayashi et al., 2006) while SNIa events produce

yields of Mn that increase with metallicity (Kobayashi et al., 2015). These theoretical results indicate that [Mn/Fe] is sensitive to the SNIa time-delay scenario. Opposite to the α-like trends, [Mn/Fe] as a function of metallicity has a plateau below solar values and it begins to increase at the "knee". This trend has been observed in the Galactic halo and disk (Roederer et al., 2014; Yong et al., 2013; Adibekyan et al., 2012). It is debated whether the observed trend of [Mn/Fe] as a function of metallicity in the Milky Way is astrophysical or due to metal-dependent NLTE effects in stellar atmospheres.

There has been little work measuring Mn abundances in the Galactic bulge. Our elemental abundances measured for the lowest metallicity stars in our sample are consistent with the observed LTE halo abundances. At the higher metallicity end of our sample [Mn/Fe] shows slight deficiency relative to the disk consistent with a shorter star formation timescale. Further work on Mn abundances in the bulge are desired.

Mn NLTE corrections are sourced from Bergemann & Gehren (2008). When the abundance corrections are applied, we see [Mn/Fe] is flat across our metallicity range. This is the same trend seen in the NLTE Mn results from Battistini & Bensby (2015). Because our comparative literature samples all have LTE abundances, we are unable to accurately compare our NLTE abundances to known stellar populations. Therefore, we do not draw conclusions on the origins of these stars from their NLTE abundances.

2.5.4.5 Co

NLTE corrections are also determined for Co from Bergemann et al. (2010). These corrections result in a trend that continues to increase with decreasing metallicity below [Fe/H] $\sim$ -1 dex. However, because our comparative literature samples all have LTE abundances, we are unable to accurately compare our NLTE abundances to known stellar populations. Therefore, we do not draw conclusions on the origins of these stars from their NLTE Co abundances.

2.5.4.6 Ni

Similar to Cr, nickel (Ni) abundances roughly track Fe abundances and we expect [Ni/Fe] as a function of metallicity to be roughly flat. Interestingly, [Ni/Fe] deficiencies have been measured for α-poor systems like the LMC (Van der Swaelmen et al., 2013) and slight [Ni/Fe] enhancements have been observed in the bulge at metallicities above $\sim$ -1 dex (Johnson et al., 2014; Bensby et al., 2017). Our results provide further evidence for this enhancement. Our low metallicity stars have [Ni/Fe] abundances consistent with the halo.

2.5.5 The Neutron-Capture elements

Enhancements of s- and r-process material has frequently been observed in very metal-poor halo stars (e.g., Sneden et al., 2002; Barbuy et al., 2009; Masseron et al., 2010; Chiappini et al., 2011; Sakari et al., 2018). These enhancements are thought to either a result of enrichment from an early gener-

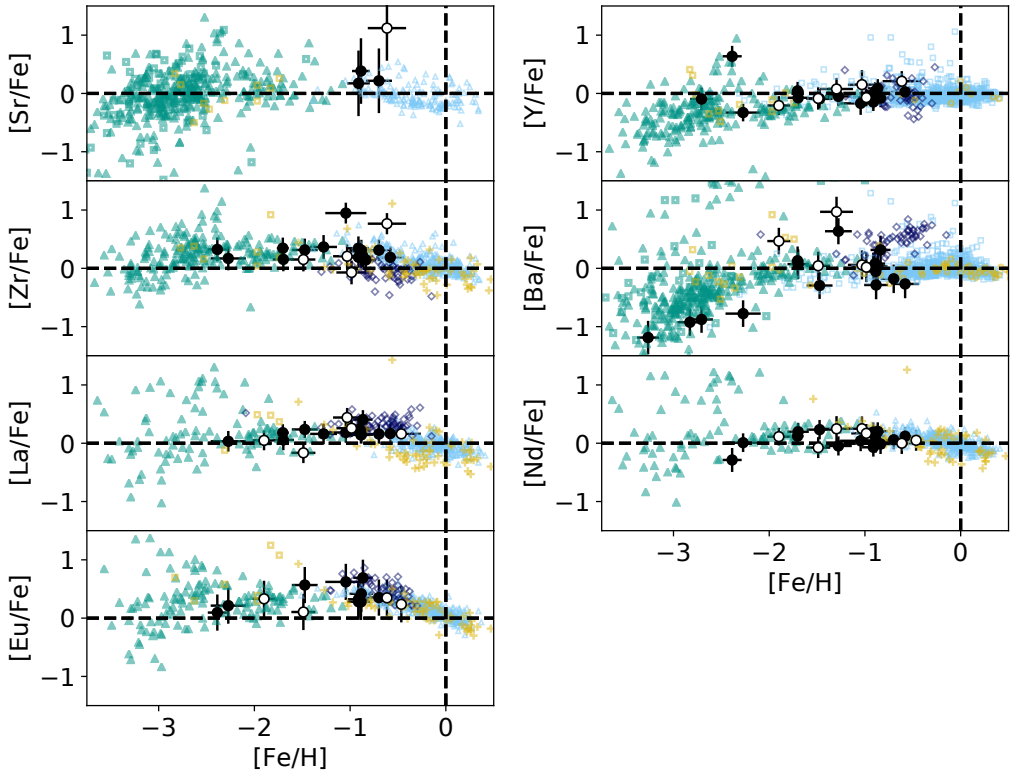

Figure 2.11: [X/Fe] for the program stars as a function of metallicity for Sr, Zr, La and Eu from top to bottom on the left and Y, Ba, and Nd from top to bottom on the right. These elements are neutron-capture elements. The symbols are the same as in Figure 4.7 with the addition of disk abundances from Battistini & Bensby (2016, light blue open triangles) and bulge abundances from Johnson et al. (2012, yellow crosses).

ations of spinstars (Pignatari et al., 2008) or neutron star mergers (Lattimer & Schramm, 1974; Rosswog et al., 2014; Lippuner et al., 2017), or from mass-accretion from an AGB binary companion (Abate et al., 2015). Detections of neutron-capture element enhancements among metal-poor stars in the bulge have been rare, given the rate at which this stars appear in the halo (Koch et al., 2019). Currently, there are only three known metal-poor s- and/or r-process enhanced stars in the bulge (Johnson et al., 2013b; Koch et al., 2019).

2.5.5.1 r-process elements

Europium (Eu) is almost purely produced through r-processes (Burbidge et al., 1957; Bisterzo et al., 2011). The observed decline of [Eu/Fe] with metallicity observed in the disk (see Figure 4.9) is thought to be from the Type Ia time-delay scenario given its α-like appearance. Similar to α elements, the theorized shorter star formation timescale would lead to an enhancement of Eu in the bulge relative to the disk. However, there is no evidence of this enhancement (McWilliam, 2016). At metallicities above $\sim$ -1 dex, our observed [Eu/Fe] as a function of metallicity are consistent with the disk while at lower metallicities, they are consistent with the halo.

2.5.5.2 s-process elements

A significant portion of the production of neodymium (Nd) and zirconium (Zr) are through r-processes even though they are largely thought of as s-process elements. Therefore, the behavior of [X/Fe] of Nd and Zr as a func-

tion of metallicity is similar to Eu. Just as with Eu, Nd and Zr are expected to be slightly enhanced in the bulge if there is α enhancement with respect to the disk. Again, there is no evidence for this enhancement in the bulge (McWilliam, 2016). Our observed [Nd/Fe] and [Zr/Fe] abundances are consistent with the disk at metallicities above $\sim$ -1 dex and with the halo below. The outlying stars with high levels of Zr enhancement also are enhanced in Al and are discussed further in Section 2.6.

Elements thought to be almost solely created through s-processes (Sr, Y, Ba, and La) show roughly flat ratios of [X/Fe] as a function of metallicity. The slight decrease of [X/Fe] as a function of metallicity shown in the disk observations for Sr and La (see Figure 4.9) is not well understood (e.g., Cristallo et al., 2011). Regardless, Figure 4.9 shows that our target stars are consistent with s-process abundances in the halo at low metallicities and the disk at higher metallicities ([Fe/H] >-1 dex). The behavior of [La/Eu] as a function of metallicity for our stars indicates higher levels of r-process material enrichment than s-process material relative to the thin disk. This is consistent with previous results in the bulge (McWilliam et al., 2010; Johnson et al., 2012).

2.6 Discussion and Summary

The MDF of the bulge indicates multiple populations (Ness et al., 2013a; Zoccali et al., 2017; Bensby et al., 2017). The most metal-poor population of the bulge has recently become a focus of interest (e.g., Howes et al.,

2016, 2014, 2015; Schlaufman & Casey, 2014; García Pérez et al., 2013). The origin of these stars are under debate. Whether this population is mostly halo interlopers with eccentric orbits, accreted material or some of the oldest stars in the Universe is still yet to be determined. Howes et al. (2015) found that only 7 out of 10 metal-poor bulge stars have orbits confined to the bulge. It may be possible to determine the origin of these stars by studying their chemical composition. In this study, we successfully targeted metal-poor bulge stars using SkyMapper photometry. We obtained high-resolution spectra of 40 targets using VLT/UVES. These spectra were reduced in the standard way. BACCHUS was used to determine the stellar parameters and abundances of 22 elements for 26 stars.

We find our targets to have an average metallicity of -1.29 dex with dispersion 0.74 dex. To discuss the results, we divide our targets into two groups, high metallicity ([Fe/H] > -1.5 dex) and low metallicity ([Fe/H] <-1.5 dex). In general, the high metallicity stars have elemental abundances consistent with other bulge studies at those metallicities (e.g., Gonzalez et al., 2015; Johnson et al., 2014; Bensby et al., 2017; Johnson et al., 2012). The α abundances for the high metallicity stars are consistent with a high SFR in the bulge relative to the thick disk. We find that two high metallicity stars with unusually high Al abundances which we discuss shortly. In general, we find the elemental abundances of the low-metallicity stars are consistent with halo abundances. The α abundances of these stars are similar to the most α-enhanced stars in the halo. This α enhancement indicates that these

stars are from a more massive system than a typical dwarf spheroidal galaxy and therefore, not likely to be from an accreted dwarf galaxy. We find four stars with [Ca/Fe] enhancement higher than the Galactic disk plateau. This indicates these stars were enhanced from a population with a more top-heavy IMF (e.g., Johnson et al., 2013a). We also find the the dispersion in the α and odd-Z elements is generally lower than the average dispersion in the halo populations from Yong et al. (2013). This indicates the metal-poor bulge is a distinct bulge population, or that the halo is more chemically homogeneous closer to the center of the Galaxy. However, our sample size is relatively small, with only 26 stars, and we caution drawing conclusions from the observed low dispersion.

We also find two stars (6805.0 and 6531.3) that have unusually high Al abundances at around the 2σ level. It is thought that the bulge may be partially built from dissipated globular clusters (Kruijssen, 2015; Shapiro et al., 2010; Bournaud, 2016). Schiavon et al. (2017) found a population of stars in the Galactic bulge whose chemistry is consistent with the known chemical signature of globular cluster stars. These stars are nitrogen rich. Fernández-Trincado et al. (2017) found 5 stars with chemistry consistent with globular cluster stars and have highly eccentric orbits that pass through the bulge. Some second generation (SG) globular clusters (GC) stars are thought to have a unique chemical signature in that they show a Mg-Al anti-correlation. That is to say, they are more enhanced in Al than expected given their Mg abundance. Figure 2.12 demonstrates that the two stars have Mg and Al abun-

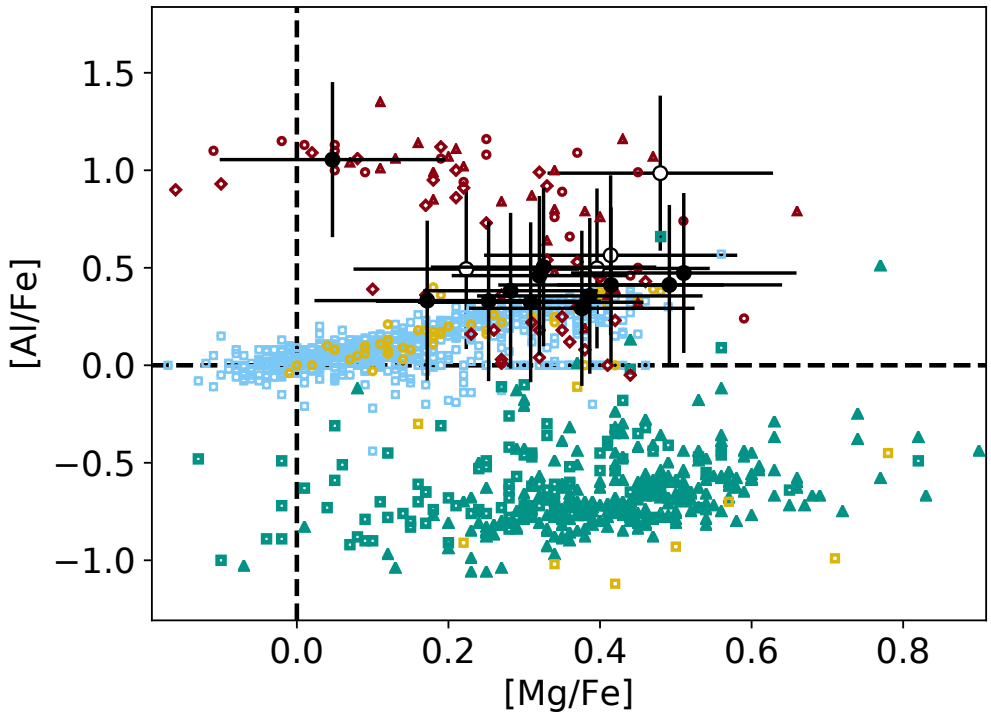

Figure 2.12: The [Al/Fe] abundances as a function of [Mg/Fe] for our target stars. The symbols are the same as in Figure 4.7 with the addition of elemental abundances for star in the globular clusters NGC4833 (red circles), NGC7089 (M2; red triangles) and NGC2808 (red diamonds) from Pancino et al. (2017).

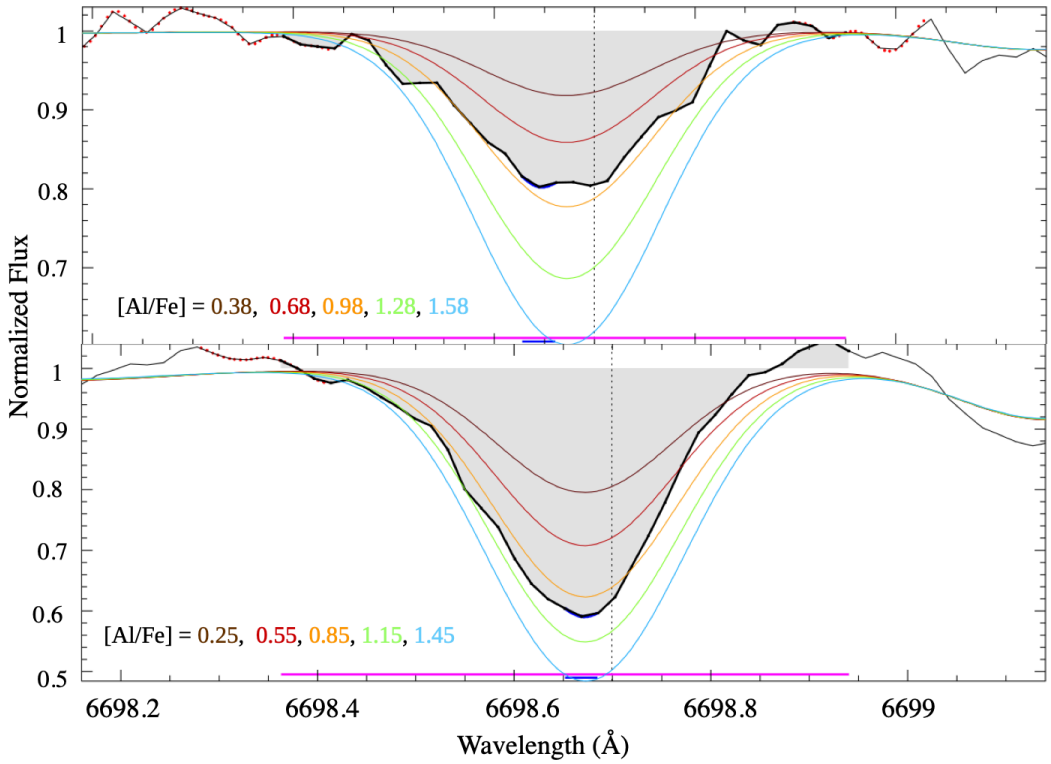

Figure 2.13: The Al line at 6698.67 Å in the spectra of 6531.3 (top) and 6805.0 (bottom) along with synthesized spectra with varying Al abundances. [Al/Fe] for each synthesized spectrum is given in the bottom right, in order of increasing [Al/Fe]. These lines clearly show these stars have enhanced [Al/Fe] $\sim$ 1 dex, consistent with Figure 2.12.

dances consistent with SG GCs[9]. We note that the large errors bars are a result of the strong sensitivity to the stellar parameters (see Table 2.2) and the strength of the Al lines clearly show high levels of Al enhancement (see Figure 2.13). It is also known that GCs frequently show a Na-O anti-correlation (Gratton et al., 2004). 6805.0 has Na and O abundances consistent with those seen in the globular cluster ω Centauri which has stars with -2.0 dex $<$ [Fe/H] $<$ -0.7 dex (Marino et al., 2011). 6531.3 does not show Na enhancement, so we suggest caution with assuming this star is a SG GC star. The chemistry of these two stars indicate that part of the metal-poor population of the bulge could be made up of dissipated globular clusters. There are no known globular clusters within an angular separation of one degree of these stars.

In conclusion, we find evidence that the metal-poor stars in the bulge are not halo interlopers or accreted from a dwarf galaxy. Although these stars have elemental abundances consistent with those seen in the halo, the dispersion of the elemental abundances are not. We also find evidence that a portion of the population of the metal-poor stars in the bulge may have come from globular clusters. More precise orbits with *Gaia* Data Release 3 and an increase in the sample size could definitively rule out halo or accreted origin for the metal-poor population in the bulge. If these stars are not halo-interlopers or accreted, then they are likely to be some of the oldest known stars in our

[9]We note here that the reported abundances for Mg and Al in the online table for Pancino et al. (2017) are mislabeled. The column labeled Mg is actually the Al abundances from the Gaia-ESO survey (Gilmore et al., 2012; Randich et al., 2013) fourth data release and vice versa.

Galaxy and could be used to study the early universe. For the second part of the COMBS survey, we plan to determine the orbits of these stars along with the 640 GIRAFFE spectra in order to determine if the metal-poor bulge population is confined to the bulge.

Chapter 3

The COMBS Survey - II. Distinguishing the Metal-Poor Bulge from the Halo Interlopers

Abstract: The metal-poor stars in the bulge are important relics of the Milky Way's formation history, as simulations predict that they are some of the oldest stars in the Galaxy. In order to determine if they are truly ancient stars, we must understand their origins. Currently, it is unclear if the metal-poor stars in the bulge ([Fe/H] $<$ -1 dex) are merely halo interlopers, a unique accreted population, part of the boxy/peanut-shaped bulge or a classical bulge population. In this work, we use spectra from the VLT/FLAMES spectrograph to obtain metallicity estimates using the Ca-II triplet of 473 bulge stars (187 of which have [Fe/H]$<$-1 dex), targeted using SkyMapper photometry. We also use *Gaia* DR2 data to infer the Galactic positions and velocities along with orbital properties for 523 stars. We employ a probabilistic orbit analysis and

[1] This chapter is based on Lucey M., Hawkins K., Ness M., Debattista V.P., Luna A., Asplund M., Bensby T., Casagrande L., Feltzing S., Freeman K.C., Kobayashi C., Marino A.F., 2021, MNRAS, 501, 5981. The author of this document, Madeline Reinke Lucey, completed most of the analysis and wrote the publication. M. Ness led the proposal to obtain the observations necessary to achieve this work. K. Hawkins supervised my work on this project and A. Luna assisted in part of the analysis. V.P. Debattista provided the simulation data to which the observations are compared.

find that about half of our sample has a $> 50\%$ probability of being bound to the bulge, and half are halo interlopers. We also see that the occurrence rate of halo interlopers increases steadily with decreasing metallicity across the full range of our sample ($-3 <$ [Fe/H] < 0.5). Our examination of the kinematics of the confined compared to the unbound stars indicates the metal-poor bulge comprises at least two populations; those confined to the boxy/peanut bulge and halo stars passing through the inner galaxy. We conclude that an orbital analysis approach, as we have employed, is important to understand the composite nature of the metal-poor stars in the inner region.

3.1 Introduction

Piecing together the history of our Galaxy, the Milky Way (MW), is one of the major objectives of astrophysics and will lead to new insights in our understanding of galaxy evolution in general. The center of our Galaxy is one of the least understood components given that it has historically been difficult to study. High levels of both crowding, which makes it difficult to resolve individual stars, and of extinction, which makes it difficult to achieve high signal-to-noise ratio data have prevented substantial studies of the Galactic bulge until recently.

Large spectroscopic surveys such as Bulge Radial Velocity Assay (BRAVA, Rich et al., 2007), the Abundances and Radial velocity Galactic Origins Survey (ARGOS, Freeman et al., 2013), the GIRAFFE Inner Bulge Survey (GIBS, Zoccali et al., 2014), the HERMES Bulge Survey (HERBS, Duong et al.,

2019a), the Extremely Metal-poor BuLge stars with AAOmega survey (EMBLA, Howes et al., 2015) and the Apache Point Observatory Galactic Evolution Experiment (APOGEE, García Pérez et al., 2018; Rojas-Arriagada et al., 2020) have measured the radial velocities and chemical abundances of bulge stars. One of the major results from these surveys is the measurement of the metallicity distribution function (MDF) of the central part of the MW. The ARGOS survey, which used 14,150 stars, determined that the MDF is made up of five components (Ness et al., 2013a). They associate the five components with different components of the Galaxy. The highest metallicity components (peaks at [Fe/H]= +0.15 and -0.25 dex) they associate with the boxy/peanut-shaped (B/P) bulge. The three most metal-poor components they associate with the thick disk (peak at [Fe/H]=-0.7 dex), the metal-weak thick disk (peak at [Fe/H]=-1.18 dex) and the stellar halo (peak at [Fe/H]=-1.7 dex). However, the higher metallicity components dominate with only 5% of stars having metallicities $<$ -1 dex (Ness & Freeman, 2016). Other studies have found similar results with slight variations (e.g., Zoccali et al., 2008; Johnson et al., 2013a; Zoccali et al., 2017; Bensby et al., 2013; Rojas-Arriagada et al., 2014b; Bensby et al., 2017; Rojas-Arriagada et al., 2017; Duong et al., 2019a). However, Johnson et al. (2020) find that the multi-peak model is only valid for the outer bulge and within a Galactic latitude (b) $\sim 6^{\circ}$ the metallicity distribution is best described by a single peak with a long metal-poor tail, consistent with a closed box model.

Although they only comprise a small fraction of the bulge, the metal-

poor stars have become of particular interest recently. Simulations have shown that the metal-poor stars in the center of the Galaxy may hold critical information about the first stars and early Galaxy evolution. For example, simulations predict that if Population III stars exist in our Galaxy, they are more likely to be found in the bulge (White & Springel, 2000; Brook et al., 2007; Diemand et al., 2008). It has also been predicted that stars of a given metallicity are typically older if they are found in the center of the Galaxy (Salvadori et al., 2010; Tumlinson, 2010; Kobayashi & Nakasato, 2011). Furthermore, simulations show that if one selects metal-poor stars, then the fraction of the oldest stars becomes highest towards the Galactic center (Starkenburg et al., 2017a; El-Badry et al., 2018b). Therefore, targeting metal-poor stars towards the center of the Galaxy is conducive for the discovery of ancient stars.

However, discovering metal-poor stars that are currently in the bulge is not enough to assume they are ancient. These stars have many possible origins which may correspond to different age distributions. For example, it is unclear if these stars are confined metal-poor bulge stars that stay confined to the bulge or if they are halo stars that are just passing through the bulge and actually spend most of their time at large distances from the Galactic center. If they do stay confined to the bulge, it is uncertain if they are a classical bulge population or participate in the B/P bulge. The signature of a classical bulge is a pressure-supported component that is the result accretion in the hierarchical growth of galaxies model (Kauffmann et al., 1993; Guedes et al., 2013) or is the rapid assembly of gas-rich small sub-galaxies (Kobayashi &

Nakasato, 2011). On the other hand, a B/P bulge is rotation-supported and formed through secular evolution of the bar either by buckling instabilities (Raha et al., 1991; Merritt & Sellwood, 1994; Bureau & Athanassoula, 2005; Debattista et al., 2006) or orbit trapping (Combes & Sanders, 1981; Combes et al., 1990; Quillen, 2002; Quillen et al., 2014; Sellwood & Gerhard, 2020). Most of the mass in the bulge has been shown to participate in the B/P bulge (Howard et al., 2009; Shen et al., 2010; Ness et al., 2013b; Debattista et al., 2017). However, it has been suggested that the MW has a compound bulge (a B/P bulge with a classical bulge; Athanassoula, 2005) where the less massive metal-poor component is a classical bulge population (Babusiaux et al., 2010; Hill et al., 2011; Zoccali et al., 2014). As a B/P bulge and a classical bulge are the result of different formation histories, it is essential to distinguish between these scenarios in order to determine if these stars are truly ancient. On the other hand, if these stars do not stay confined to the bulge, then it is possible that they are part of a unique accreted population or the in-situ halo. Consequently, it is essential to study the chemistry and kinematic properties of the metal-poor stars in the bulge in order to distinguish between these possible origin scenarios and determine whether they are truly the oldest stars in the Galaxy.

To this end, there have been a number of studies on the chemistry of metal-poor bulge stars. The first installment of the Chemical Origins of Metal-poor Bulge Stars (COMBS) survey studied the detailed chemical abundances of 26 metal-poor bulge stars (Lucey et al., 2019). One of the main results

from this work is that the metal-poor bulge has higher levels of Calcium (Ca) enhancement compared to the disk and halo. In addition, the metal-poor stars have lower dispersion in the α-element abundances (Ca, Silicon, Magnesium and Oxygen) than halo stars of similar metallicity. These results indicate that either metal-poor bulge stars are not halo stars and are a unique Galactic population or that the halo is more chemically homogeneous towards the Galactic center. The HERBS survey found complementary results (Duong et al., 2019a). They also observed higher levels of Ca-enhancement and lower dispersion in the α-elements for metal-poor bulge stars. In addition, the Carbon and neutron-capture material abundances have shown deviations from the halo distributions. Carbon-Enhanced Metal-Poor (CEMP) stars occur at a rate of 15-20% among halo stars with [Fe/H]<-2 dex (Yong et al., 2013). However, we know of only one that has been observed in the bulge (Koch et al., 2016). After accounting for mixing that occurs during the red giant branch phase, the EMBLA survey found one out of 23 stars with [Fe/H] <-2 dex may have had a natal [C/Fe] >1 dex (Howes et al., 2015). Although, the lack of CEMP stars in the EMBLA survey could at least partially be a selection effect from the SkyMapper photometry (Da Costa et al., 2019). Similarly, neutron-capture enhanced stars have been observed at a lower rate than in the halo (Johnson et al., 2012; Koch et al., 2019; Lucey et al., 2019; Duong et al., 2019a).

Studies of the kinematics of metal-poor bulge stars indicate that they are distinct from the metal-rich population and do not participate in the B/P bulge. Using the line-of-sight velocities, it has been shown that the metal-

poor component of the bulge rotates slower than the metal-rich component and has higher velocity dispersion (Ness et al., 2013b; Kunder et al., 2016; Arentsen et al., 2020a). Furthermore, the vertex deviation, which measures the orientation of the covariance between the radial and tangential motion, approaches zero for metal-poor bulge stars while it is large for metal-rich stars (Soto et al., 2007; Babusiaux et al., 2010). This indicates that the metal-poor stars do not participate in the bar structure since the vertex deviation is large for a triaxial bar and zero for a stationary axisymmetric disk (Zhao et al., 1994). These observations are typically interpreted as evidence for a classical bulge population. However, Debattista et al. (2019) demonstrated that a vertex deviation of zero for metal-poor stars does not necessarily indicate an ex-situ classical bulge population. Furthermore, it is important to be careful when interpreting these previous results on the metal-poor bulge because it is unclear how many of these stars are confined bulge stars or are merely halo interlopers. For example, Howes et al. (2015) found that roughly half of their very metal-poor bulge stars ([Fe/H]<-2) had orbits bound to the bulge. Using RR Lyrae stars, Kunder et al. (2020) separated the halo interlopers from the confined stars and found evidence for a B/P bulge and a classical bulge population.

In this work, we aim to remove the interlopers from our sample using orbit analysis in order to determine the properties of confined metal-poor bulge stars. We present metallicity estimates for 473 stars (187 of which have [Fe/H] <-1 dex) and 3D kinematics for 523 stars, all of which are stars near the

Galactic bulge. In Section 6.2 we present the data we use to accomplish this work. We describe the method for determining the metallicities from the Ca-II triplet (CaT) in Section 3.3. The derivation of the kinematics and orbital properties is outlined in Section 3.4. Last, we discuss the fraction of metal-poor stars in the bulge that stay confined to the bulge in Section 3.5 and the properties of the stars that do stay confined in Section 3.6.

3.2 Data

Historically, observing large numbers of metal-poor bulge stars has been difficult given that they only make up around 5% of stars in the Galactic bulge (Ness & Freeman, 2016). However, photometric surveys, like the SkyMapper survey, which has a filter set designed to provide accurate stellar parameters (Keller et al., 2007; Casagrande et al., 2019), enabling the detection of extremely metal-poor stars for spectroscopic follow-up (e.g., Keller et al., 2014; Howes et al., 2015). Our stars have been selected using SkyMapper photometry along with ARGOS spectra (Freeman et al., 2013) to target metal-poor stars within 3.5 kpc of the Galactic center. Our selection was made using uncalibrated commissioning photometry which is not included in the SkyMapper data releases as the pipeline is not yet optimized to deal with high levels of crowding. However, the use of this photometry suffices for the selection of metal-poor stars. For more details about the selection method, we refer the reader to Section 2 of Lucey et al. (2019).

Our spectroscopic data were obtained using the FLAMES instrument

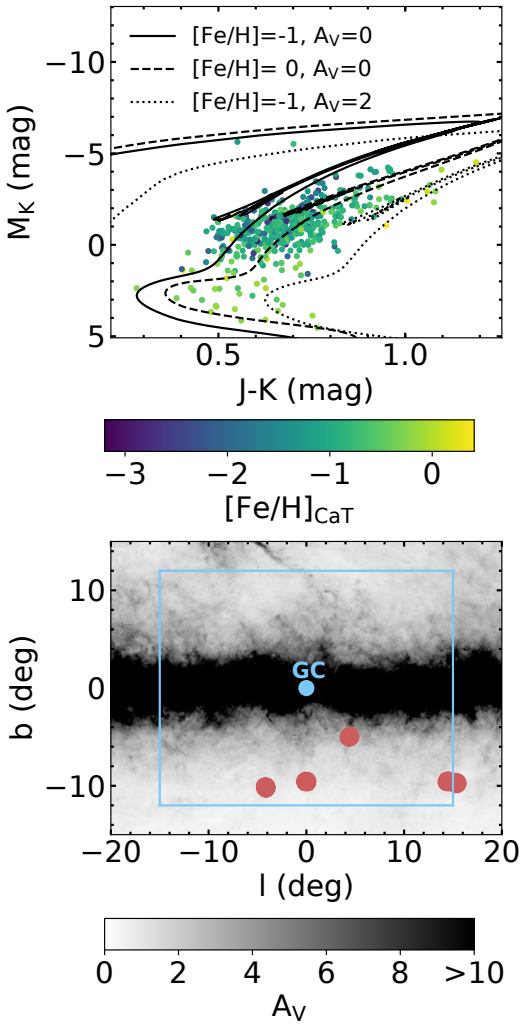

Figure 3.1: In the top plot, we show a color magnitude diagram of our sample colored by metallicity. On the y-axis we show the absolute K-band magnitude which is determined using our derived distance estimates. We only use "A" quality photometry from the 2MASS survey (Skrutskie et al., 2006). For comparison, three isochrones with age 10 Gyr and varying metallicities and extinctions are shown in black. In the bottom plot, we show the Galactic longitudes and latitudes for the fields in our survey as red points. We also show the extinction map from Planck Collaboration et al. (2014) in the background. A box roughly indicating the bulge region and a point indicating the Galactic center (GC) are shown in blue.

(Pasquini et al., 2002) on the European Southern Observatory's (ESO) Very Large Telescope (VLT). We use the MEDUSA fibers, which feed to the GIRAFFE spectrograph along with the UVES spectrograph fibers. Therefore, we have high resolution data (R=$\lambda/\Delta\lambda \sim$ 47,000) from the UVES spectrograph along with medium resolution data (R$\sim$ 20,000) from the GIRAFFE spectrograph. We observed 40 stars with the UVES spectrograph and 555 stars with the GIRAFFE spectrograph, prioritizing the most promising metal-poor targets for the high resolution data.

In top plot of Figure 5.2, we show the color magnitude diagram of our sample. We only use "A" quality photometry from the 2MASS survey (Skrutskie et al., 2006). We color the points by the metallicity that we derive in Section 3.3. The distances we derive in Section 3.4 are used to convert the apparent K-band magnitudes into absolute magnitudes. For comparison, we also show MIST isochrones with age 10 Gyr (Paxton et al., 2011, 2013, 2015; Dotter, 2016; Choi et al., 2016). Specifically, we show an isochrone with [Fe/H]=-1 dex, A_V=0 mag (black solid line), [Fe/H]=0 dex, A_V=0 mag (black dashed line) and [Fe/H]=-1 dex, A_V=2 mag (black dotted line). The majority of our stars have magnitudes consistent with red giant stars, red clump stars, or horizontal branch stars. The spread in color is due to a combination of varying metallicities and levels of extinction. The more metal-rich stars are generally redder than the more metal-poor stars. However, we do not de-redden the photometry. Therefore, the varying levels of extinction causes the metal-poor stars to appear redder and obscure the relation between color and metallicity.

We also have a number of stars whose magnitudes are consistent with sub-giant stars. These stars are generally more metal-rich and are likely contamination from the disk along the line of sight towards the bulge. There are two stars whose magnitudes are consistent with planetary nebula. However, it is likely that these bright absolute magnitudes are the result of overestimated distances. Both of these stars have negative parallaxes and estimated distances > 20 kpc. However, these stars also have large distance errors, with the low error bar putting them within a distance of 11-14 kpc. This corresponds to a magnitude change of $\sim$+1.7-3.0 mag, which puts them reasonably on the giant branch.

In the bottom plot of Figure 5.2, we show the Galactic longitudes and latitudes for the fields in our survey as red points. We also show an extinction map in the background from Planck Collaboration et al. (2014). The light blue box roughly indicates the region of the bulge and the light blue point indicates the Galactic center (GC) at (l, b)=(0°,0°). Our observations have a range of Galactic longitudes that span from the center to one edge of the bulge's major axis. We also have observations from two different Galactic latitudes. However, as the bulge has a vertical metallicity gradient where the larger latitudes are generally more metal-poor (Zoccali et al., 2008; Gonzalez et al., 2011; Johnson et al., 2011, 2013a), most of our observations are concentrated there.

3.2.1 High Resolution UVES Spectra

In this work, we made use of the radial velocities (RVs) and metallicities from COMBS I (Lucey et al., 2019), which reduced and analyzed the

UVES spectra. For a complete description of the UVES spectra and reduction see Section 3.1 of Lucey et al. (2019). In short, the UVES observations were taken in the standard RED580 setup. This setup has R$\sim$ 47,000 and wavelength coverage of 4726-6835 Å with a gap (5804-5817 Å) between the lower/blue and upper/red chips. In Lucey et al. (2019), we reduced the data using the FLAMES-UVES workflow within the EsoReflex interface[2]. We continuum normalized, RV corrected and co-added the spectra using iSpec (Blanco-Cuaresma et al., 2014). After removing stars with signal-to-noise ratio (SNR) $<$ 10 pixel^{-1} in the red part of the spectrum, we are left with 35 stars that we use the RV measurements of in this work.

In Lucey et al. (2019), we also measured the metallicities for 26 of these stars. The metallicities were determined using the standard Fe-Excitation-Ionization balance technique through the Brussels Automatic Code for Characterizing High accUracy Spectra[3] (BACCHUS, Masseron et al., 2016). In short, BACCHUS uses an iterative technique to simultaneously solve for the effective temperature ($T_{\rm eff}$), the surface gravity (log g), microturbulence ($v_{\rm micro}$) and metallicity ([Fe/H]). The $v_{\rm micro}$ is solved when the Fe abundance derived from the core line intensity and equivalent width for each line are consistent. For the $T_{\rm eff}$ and log g determination as well as the final reported [Fe/H], the Fe abundance is computed using a χ^2 minimization between a synthesized spectrum and the observed spectrum for each Fe line. The $T_{\rm eff}$ is solved when

[2]https://www.eso.org/sci/software/esoreflex/
[3]http://ascl.net/1605.004

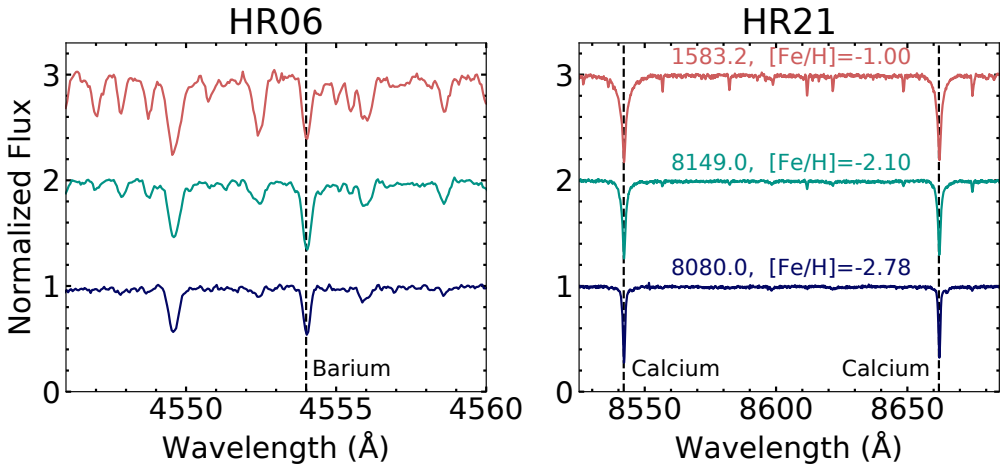

Figure 3.2: Partial regions of three observed spectra with varying metallicities. Specifically we show the spectra of 1583.2 (red), 8149.0 (green) and 8080.0 (dark blue). On the left is part of the HR06 spectra while on the right is part of the HR21 spectra with two of the Ca-II triplet lines shown. On the left side, we inidcate Barium line at 4554 Å.

there is no correlation between the excitation potential and abundance of the line. The log g is solved when there is no offset between the neutral (Fe I) and singly ionized (Fe II) line abundances. Although this process is automated, we visually inspect the line fits and validity of the solution for each star. For more details on how BACCHUS derives the stellar parameters, see Section 4 in Lucey et al. (2019).

3.2.2 Medium Resolution GIRAFFE Spectra

The GIRAFFE spectrograph in MEDUSA mode can range from medium to high resolution (R=5500-38000) with possible, although not complete, wave-

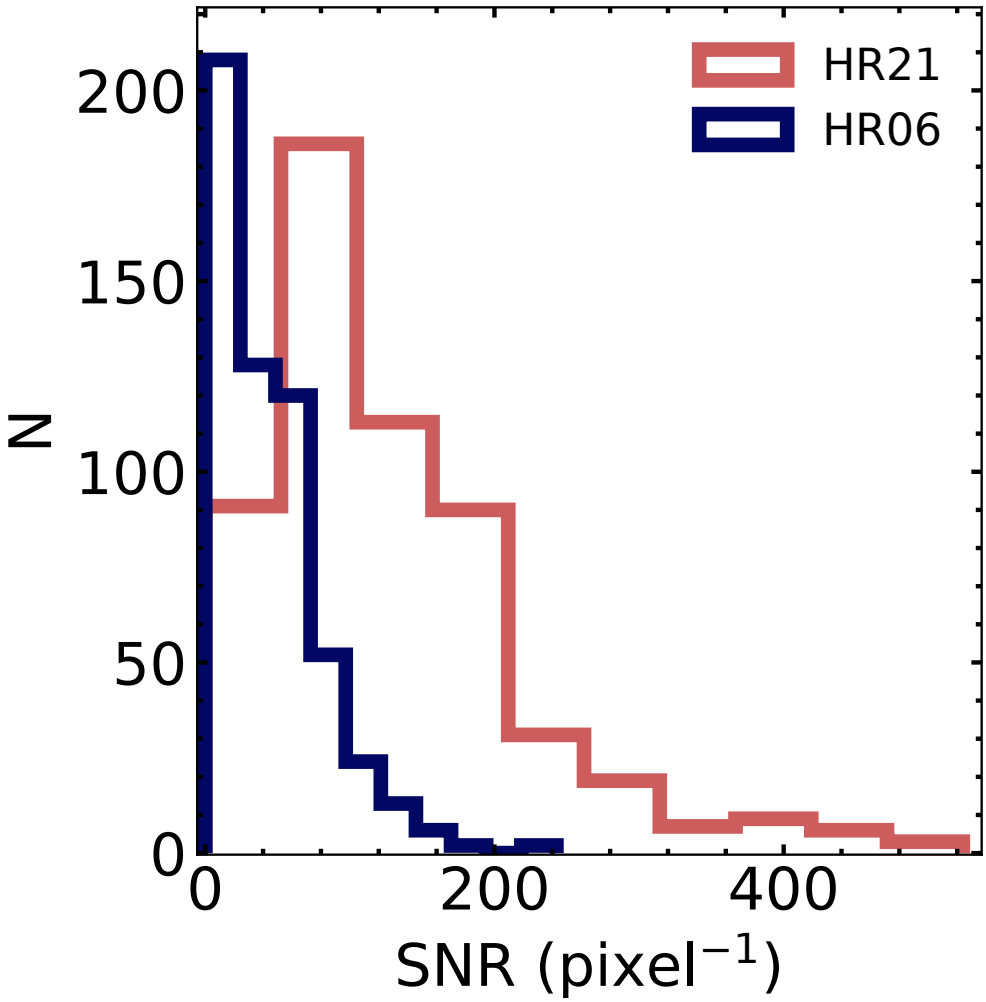

Figure 3.3: Distribution of the signal-to-noise ratios (SNR) per pixel for the HR06 spectra and HR21 spectra. The SNR is determined using the measured flux errors. The HR21 spectra typically have higher SNR because they are redder and are therefore less impacted by extinction.

length coverage from 3700-9000 Å. For the high resolution mode, this wavelength coverage is divided into 22 different possible setups. For this work, we use the high resolution MEDUSA HR06 and HR21 setups. The HR06 setup has R∼24,300 with wavelength coverage from 4538-4759 Å. The HR21 setup has R∼18,000 with wavelength coverage 8484-9001 Å. We chose the HR21 setup because it contains the CaT, which provides precise radial velocities and accurate metallicity estimates (e.g., Steinmetz et al., 2020a,b). The HR06 set up is useful for deriving stellar parameters and elemental abundances because it contains many metal lines including a Barium line (4554 Å). We show three examples of spectra with varying metallicities in Figure 6.1. Specifically, on the left, we show a part of the HR06 spectra with the Barium line at 4554 Å. On the right, we show a part of the HR21 spectra with two of the CaT lines. For more information about the FLAMES/GIRAFFE instrument we refer the reader to Pasquini et al. (2000).

We reduced the GIRAFFE spectra using the workflow[4] in the EsoReflex interface. We downloaded the calibration files from the ESO archive[5] using the CalSelector tool[6]. In short the workflow performs standard bias and flat-field subtraction, fiber-to-fiber corrections, wavelength calibration and extraction. We also turn on the cosmic ray cleaning feature using the package PYCOSMIC[7].

[4] ftp://ftp.eso.org/pub/dfs/pipelines/instruments/giraffe/giraf-reflex-tutorial-1.3.pdf

[5] http://archive.eso.org/eso/eso_archive_main.html

[6] http://www.eso.org/sci/archive/calselectorInfo.html

[7] http://www.bhusemann-astro.org/?q=pycosmic

In addition to the EsoReflex workflow reduction, we also perform sky subtraction. As multiple fibers per pointing observed the sky, we create a master sky spectrum for each of the pointings. We then use the IRAF function SKYTWEAK to perform the sky subtraction for the science spectra. The rest of the reduction is done using iSpec (Blanco-Cuaresma et al., 2014). We RV correct the spectra using a cross-correlation with respect to an Arcturus spectrum. As each target was observed multiple times, we then co-add the spectra of each unique target. We only add spectra whose individual SNR > 10 pixel^{-1}. As the EsoReflex pipeline returns flux error estimates, we determine the SNR by dividing the flux value of each pixel by the flux error and taking the median of all the pixels. We then continuum normalize the co-added spectra using a third-order spline. Figure 3.3 shows the SNR values for HR06 and HR21, respectively. The HR06 spectra generally has lower SNR because the high levels of extinction toward the Galactic center preferentially remove bluer light. There are 5 stars that do not have a single observation with SNR > 10 pixel^{-1} and therefore we only report RVs for 550 stars. In addition, there are 545 stars observed with HR21 that has SNR > 10 pixel^{-1} and only 394 stars observed with HR06 that has SNR > 10 pixel^{-1}.

3.2.3 Parallaxes and Proper Motions from Gaia

We use *Gaia* DR2 data in order to do full 3-D dynamical and orbit analysis for our stars. We perform a sky-crossmatch using the right ascension (RA), declination (DEC) to acquire the parallaxes, proper motions, and full

covariance matrix for each of our stars. As the parallax and proper motions are highly covariant, it is essential that we include the covariances in our analysis to ensure we do not underestimate our final reported errors on the Galactic positions and velocities of our stars. Out of the 550 GIRAFFE spectra with RV measurements, only 541 stars have a match in the *Gaia* DR2 catalog within 1 arcsecond. All 35 stars with RV measurements from the UVES spectra have a match within 1 arcsecond in the *Gaia* DR2 catalog.

Lindegren (2018) demonstrated that only using stars with renormalized unit weight error (ruwe) <1.4 is as, if not more, effective at removing problematic astrometry than the quality cuts recommended by Gaia Collaboration et al. (2018a); Lindegren et al. (2018); Arenou et al. (2018). Therefore, similar to recent literature (e.g., Anders et al., 2019; Lucey et al., 2020), we only use *Gaia* DR2 data with ruwe<1.4. This leaves us with a total of 523 stars, including 31 stars with UVES spectra, with which we can perform 3D dynamical and orbit analysis.

3.3 Metallicity Estimates from Ca-II Triplet

The CaT is frequently used to determine metallicities from moderate resolution spectra (e.g., Armandroff & Zinn, 1988; Olszewski et al., 1991; Armandroff & Da Costa, 1991; Starkenburg et al., 2010; Li et al., 2017). It has been shown that the equivalent widths (EW) of the CaT can provide accurate metallicity estimates within ∼0.1 dex, irrespective of age effects (Cole et al., 2004). However, early work demonstrated it is essential to account for the sen-

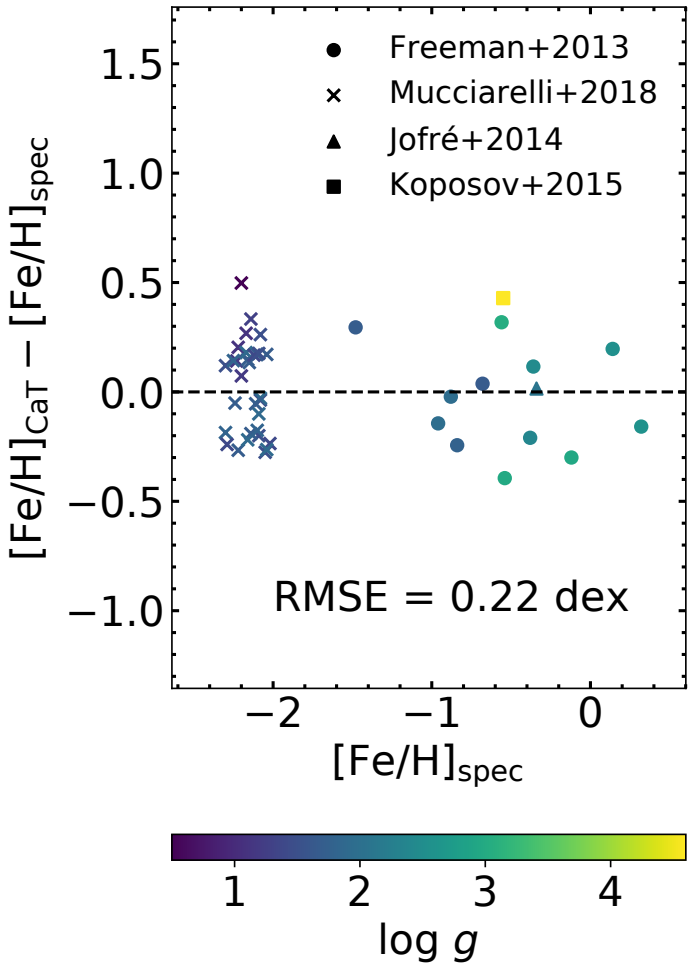

Figure 3.4: Comparison of metallicity estimates from the Ca-II triplet to the values derived from Fe lines using full spectroscopic analysis for the entire validation sample of 45 stars. The spectroscopic values for the validation sample are taken from 4 different studies (Freeman et al., 2013; Mucciarelli et al., 2018; Jofré et al., 2014; Koposov et al., 2015), indicated by the marker shape. We quantify the precision of the estimate using the root-mean-square error (RMSE), which equals 0.22 dex. The points are colored by the surface gravity (log g).

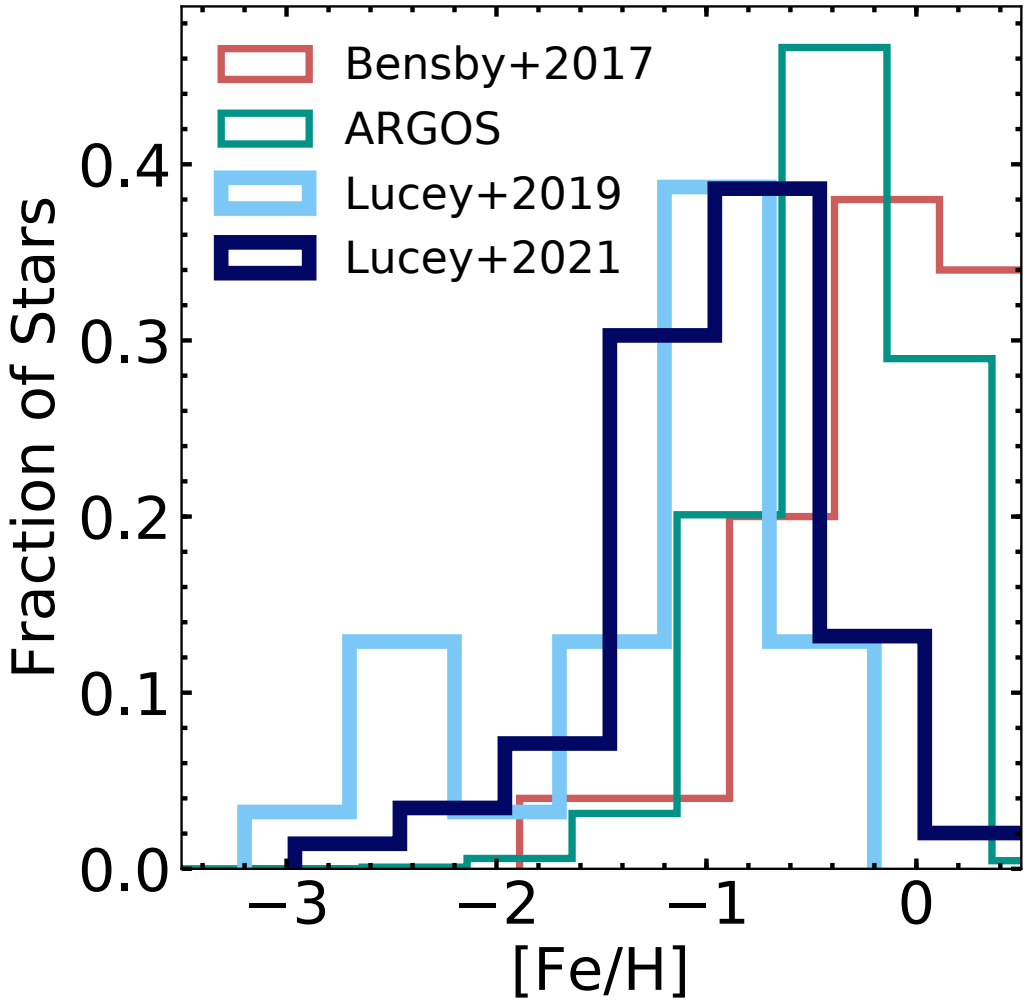

Figure 3.5: Derived metallicity distribution function for the 473 GIRAFFE spectra compared to the results for the 26 UVES spectra (Lucey et al., 2019), the ARGOS survey (Freeman et al., 2013) and Bensby et al. (2017). We have successfully targeted the metal-poor tail of the bulge metallicity distribution function. The distribution for the GIRAFFE spectra are not as metal-poor as the UVES spectra, which is expected given that the most promising metal-poor targets were prioritized for the higher resolution data.

sitivity to surface gravity (log g) (Spinrad & Taylor, 1969, 1971; Cohen, 1978; Jones et al., 1984). The most common method to accomplish this is to use the absolute magnitude of the star in the calibration. Unfortunately, determining the absolute magnitude for our bulge stars is extremely difficult given the high and varying levels of extinction along with the large uncertainties on the distance estimates.

In this work, we develop a new method to estimate the metallicity from the CaT for the GIRAFFE spectra. As some of the stars observed in this program were also observed in the ARGOS survey (Freeman et al., 2013), we use those to calibrate our metallicities. We also supplement these data with other metal-poor samples from the literature that have spectroscopic metallicities and have been observed with the GIRAFFE HR21 setup. These samples are of NGC 5824 (Mucciarelli et al., 2018), Reticulum 2 (Koposov et al., 2015), and a number of *Gaia* benchmark stars (Jofré et al., 2014). These data were downloaded from the ESO archive and reduced using the same methods as our program spectra. Consistent with previous work (e.g., Armandroff & Da Costa, 1991; Battaglia et al., 2008; Starkenburg et al., 2010), we use only the two strongest CaT lines, 8542 Å and 8662 Å, whose equivalent widths can be measured more accurately. We fit a Voigt profile, which is a combination of a Lorentzian and Gaussian profile, to these lines and define the EW as the integral of the fitted function. The wings of the CaT line have proven to be powerful for constraining the log g in addition to the metallicity, of giant stars (Jones et al., 1984; Freeman et al., 2013; Arentsen et al., 2020b). These works

indicate that there should be both log g and metallicity information embedded in the line profiles of the CaT. As such, we include the Voigt profile fit parameters in our calibration in order to calibrate out the impact of log g on our metallicity determination. In this way, we are essentially using the line profile information opposed to reducing this to a single number, the EW, as in previous work. However, it is important to note that we do not determine the log g. We merely are using the line profile information in our calibration to account for the effects of log g on the EW. We perform a regression where the input parameters are the mean amplitude of the Lorentzian components ($A_{Lorentz}$), the mean full-width-half-maximum (FWHM) of the Lorentzian components ($\sigma_{Lorentz}$), the mean FWHM of the Gaussian components (σ_{Gauss}), and the sum of the EWs of the two lines (EW_{Σ}). We also input the square of these parameters in order to allow for a non-linear, second-order relation. For completeness, we also try higher-order relations but found that the increase in precision was negligible. The final relation we derive is:

$$\begin{aligned}[\text{Fe/H}] = &-0.99 - 0.80EW_{\Sigma} + 3.46\sigma_{Lorentz} + 7.12\sigma_{Gauss} \\ &+ 10.07A_{Lorentz} + 0.08EW_{\Sigma}^2 - 0.49\sigma_{Lorentz}^2 \\ &- 42.09\sigma_{Gauss}^2 + 7.72A_{Lorentz}^2\end{aligned} \tag{3.1}$$

We use 70% of our sample with known metallicities to calibrate the model and the remaining 30% to validate. We show the comparison between the literature metallicities to the metallicities we derive for our validation sample in Figure 3.4. Although we are unable to find a reference star in the

literature across all metallicities, we have no reason to expect that the relation does not interpolate well or is unable to extrapolate slightly. We are able to recreate the metallicities to a precision of 0.22 dex over a wide range of log g. It is important to note that the precision is not a function of log g or metallicity. As our method is data-driven, the precision is limited by the precision of the training data with which we calibrate our method. Our calibration sample generally has metallicity uncertainties between ∼0.05-0.15 dex (Freeman et al., 2013; Jofré et al., 2014; Koposov et al., 2015; Mucciarelli et al., 2018). It is also possible that there are systematic offsets in the metallicity scale between the 4 bodies of work from which we source our calibration sample. Offsets in metallicity between bodies of work is typical and can be as high as ∼0.2 dex depending on the lines, atomic data and methods used (Yong et al., 2013; Bensby et al., 2014; Lucey et al., 2019). It is likely that the offsets between the literature values, from which we derive our calibration sample, also decreases our precision. Previous work on the CaT metallicity calibration has achieved a precision of ∼0.1-0.2 dex (Battaglia et al., 2008; Carrera et al., 2013). However, these methods rely on an accurate estimate of the luminosity to account for the impact of the log g on the EW. In this work, we achieve a precision of 0.22 dex, which is competitive to previous studies. In total, our method provides a unique way to derive metallicities from the CaT that achieves similar precision to previous results without depending on an estimate of the luminosity.

We apply this calibration to our entire sample of 492 stars that have a HR21 spectrum with SNR $>$ 10 pixel^{-1} and a match in *Gaia* DR2 with

ruwe<1.4. The majority of our stars are giant stars with log $g > 3.5$ dex (see Figure 5.2). This is consistent with our calibration sample which also primarily consists of giant stars. However, we also likely have some sub-giant stars in our sample (see Figure 5.2). Therefore we include stars with log g as high as 4.5 dex in our calibration sample. In order to avoid extreme extrapolation, we only keep stars with -3 dex $< [\mathrm{Fe/H}]_{\mathrm{CaT}} <$ 0.5 dex given that our calibration sample has -2.74 dex $\leq$[Fe/H]$\leq$ 0.32 dex. This leaves us with 473 out of 492 GIRAFFE spectra with metallicity estimates from the CaT. We show the final metallicity distribution of our sample in Figure 4.6 along with a comparison to the results for the UVES spectra from Lucey et al. (2019), the ARGOS survey (Freeman et al., 2013), and a survey of bulge micro-lensed dwarf stars (Bensby et al., 2017). From Figure 4.6, it is clear we have successfully targeted metal-poor stars compared to the bulge surveys which did not specifically target metal-poor stars (ARGOS; Freeman et al., 2013; Bensby et al., 2017). However, we also do not have as large of a low metallicity tail ([Fe/H] <-2) as seen in Lucey et al. (2019). This is as expected because the most promising metal-poor stars were prioritized to be observed with the higher resolution setup and were therefore included in the UVES sample.

3.4 Dynamical Analysis

One of the main goals of our work is to determine if the metal-poor stars that are currently in the bulge are of the bulge. However, this is difficult given that the majority of our data have *Gaia* DR2 fractional parallax uncertainties

$> 50\%$. With high parallax uncertainties, probabilistic Bayesian inference affords a useful approach for determining stellar distances (e.g., Bailer-Jones et al., 2018) and subsequently their orbital properties.

3.4.1 Galactic Positions and Velocities

To determine the Galactic positions and velocities, we use a Markov Chain Monte Carlo (MCMC) simulation and Bayesian inference, which allows us to incorporate prior information on Galactic structure and the covariances between the positions and velocities. We first infer the distance and proper motions using the parallax and proper motion data from *Gaia* DR2 along with the covariance matrix. Although the proper motions are measured by *Gaia* it is necessary to reinfer them with the distance in the context of the prior and covariances. Our prior on the proper motions is flat, while our prior on the Galactic distance is based on the *Gaia* DR2 mock catalog from Rybizki et al. (2018). Specifically, we use the star counts as a function of distance, which changes as a function of line-of-sight, as an unnormalized probability distribution function. With the use of an MCMC simulation, it is not necessary to normalize this distribution. This is different from the Bailer-Jones et al. (2018) catalog, which uses an exponentially decreasing prior with a scale length that varies as a function of line-of-sight. An exponentially decreasing model does not accurately describe the distribution of stars when looking towards the Galactic center. Therefore, using the mock catalog provides a more realistic prior. Nonetheless, when we compare our results to the catalog from Bailer-

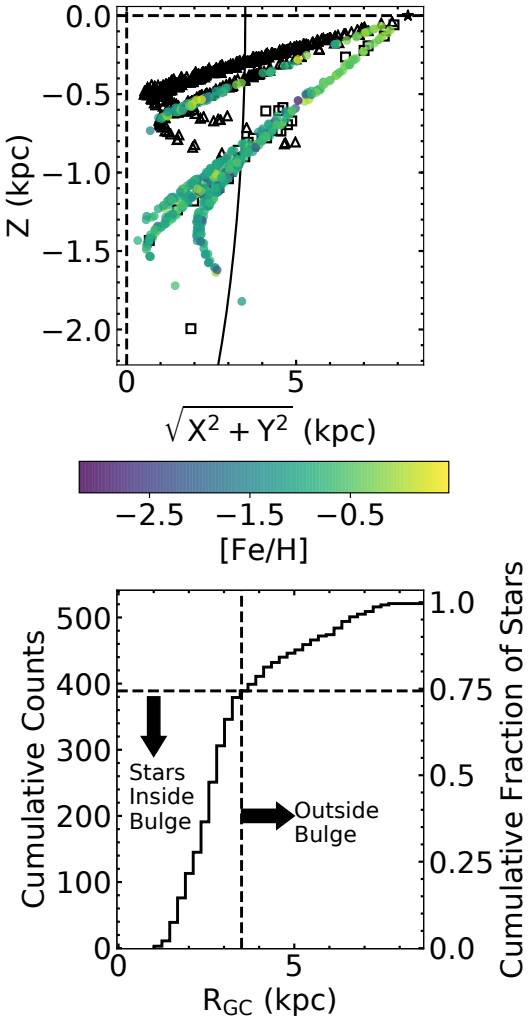

Figure 3.6: The top plot shows the positions of our observed stars with respect to the Galactic center (0,0) colored by metallicity. We also show the GIBS (Gonzalez et al., 2015) and EMBLA (Howes et al., 2016) samples in black open triangles and open squares, respectively. The Sun is shown as a black star at (8.3,0) kpc. We also show the outline of what we define as the bulge at a distance of 3.5 kpc from the Galactic center as a solid black line. We have some contamination in our sample from metal-rich disk stars along the line-of-sight towards the bulge. In the bottom plot we show the cumulative distribution of the distance from the Galactic center ($R_{GC} = \sqrt{X^2 + Y^2 + Z^2}$) where the vertical dashed line corresponds to a distance of 3.5 kpc, which 73% of the sample (381 stars) lies within.

Jones et al. (2018) we find the results are generally consistent. Only three stars have distances that are inconsistent with the Bailer-Jones et al. (2018) results. These stars all have negative parallaxes and distances of ∼13 kpc in the Bailer-Jones et al. (2018) catalog, which would put them all outside of the bulge. Only one of these stars has a shorter distance in our catalog and is determined to be currently within the bulge.

We then use the RA, DEC, and measured RV to convert the proper motions and distances into 3D Galactic positions and velocities. To do this, we sample normal distributions for the RA, DEC and RV that are centered on the measured values with widths equivalent to the measured errors. We create as many samples as the length of the MCMC chain. We then combine these samples with the MCMC chain to calculate the 3D Galactic positions and velocities with the covariances propagated through.

We show the Galactocentric distribution of the 523 stars in Figure 3.6. The top panel shows the cylindrical Galactocentric positions ($R = \sqrt{X^2 + Y^2}, Z$) colored by the metallicities. We also show literature bulge studies from the GIBS survey (Gonzalez et al., 2015) and the EMBLA survey (Howes et al., 2015) in black for comparison. We show the position of the Sun as a black star at (8.3,0) kpc (Reid et al., 2014). We also show the edge of what we consider the bulge as a black line, which corresponds to a distance of 3.5 kpc from the Galactic center and is consistent with what is typically used in the literature (e.g., Ness et al., 2013b; Arentsen et al., 2020a; Kunder et al., 2020). Our sample clearly has some contamination from disk stars that are along the

line-of-sight towards the bulge. These stars are typically more metal-rich than the stars that are within or close to within the bulge. This contamination is typical of bulge surveys, including the EMBLA (Howes et al., 2015) and GIBS (Gonzalez et al., 2015) surveys. In the bottom panels we show the cumulative distribution of the distance from the Galactic center for our sample. The vertical dashed line indicates a distance of 3.5 kpc. The dashed horizontal line corresponds to the number of stars within 3.5 kpc (381) on the left y-axis and the fraction of stars that are within 3.5 kpc (0.73) on the right y-axis. Therefore, 73% of our sample, or 381 stars, are currently within the bulge.

3.4.2 Orbital Properties

We aim to determine whether the metal-poor stars currently in the bulge are confined to or merely passing through the bulge. To this end, we calculate the orbits of all stars in the sample. We do this using the GALPY[8] package and the 2014 MW potential (Bovy, 2015). However, this potential is axisymmetric and does not contain a bar. Since all of our stars are near to the Galactic center it is essential that we add a bar to this potential. Therefore, we add a Dehnen bar potential (Dehnen, 2000) generalized to 3D following Monari et al. (2016):

[8]http://github.com/jobovy/galpy

$$\Phi(R,z,\phi) = A_f \cos(2(\phi - \phi_{\rm b} - \Omega_{\rm b} t)) \left(\frac{\rm R}{\rm r}\right)^2 \times \begin{cases} -(R_b/r)^3, & \text{if } r \geq R_b \\ (R_b/r)^3 - 2, & \text{if } r \leq R_b \end{cases} \tag{3.2}$$

where $r = \sqrt{R^2 + z^2}$ is the spherical radius, R_b is the bar radius, Ω_b is the rotation speed of the bar, ϕ_b is the bar angle and A_f is the bar strength. The bar strength is defined as α, where $\alpha = 3(A_f/v_0^2)(R_b/r_0)^3$, v_0 is the local circular speed and r_0 is the Sun's distance from the Galactic center. This potential is included in the GALPY package. We use measured MW parameters to intialize the bar potential. Specifically, we use ϕ_b= 27° (Wegg & Gerhard, 2013), α=0.01 (Monari et al., 2016), R_b=5 kpc (Wegg et al., 2015), and Ω_b=39 km/s kpc^{-1} (Portail et al., 2017)[9].

For each star we pick 1000 random points from the MCMC chain of positions and velocities. We then initialize 1000 different orbits at those points in order to propagate the errors and covariances through to the orbital properties. We integrate all of the orbits for 1 Gyr. We report the orbital properties (ecccentricity, apocenter, pericenter, z_{max}) as the median of those 1000 orbits and the asymmetric errors as 1σ. In addition, we report the probability that a star stays confined to the bulge (P(conf.)) as the number of orbits out of the 1000 that have apocenter < 3.5 kpc divided by 1000.

[9]We also performed the analysis using parameters for a shorter, faster bar. Specifically, we used ϕ_b= 25° (Dehnen, 2000), α=0.01 (Monari et al., 2016), R_b=3.5 kpc (Dehnen, 2000), and Ω_b=52.2 km/s kpc^{-1} (Dehnen, 2000). Using these parameters only decreases the number of stars that stay confined to the bulge by ∼5% and does not impact our conclusions.

3.5 Do Metal-Poor Stars in the Bulge Stay in the Bulge?

The first step toward determining the origins of the metal-poor bulge stars is to separate the confined bulge stars from the halo interlopers. In this section, we use the measured probabilities of being confined to the bulge, which are defined in Section 3.4.2, to determine the rate at which our sample is contaminated by halo stars.

In Figure 3.7, we show the reverse cumulative distribution of the probabilities that the stars are confined to the bulge. We color the line by the median apocenter of stars with that probability to demonstrate that P(conf.)$\approx$ 50% corresponds to a median apocenter of $\sim$3.5 kpc. The dashed lines correspond to the number of stars with P(conf.)$>$ 50% (223 stars or $\sim$42% of the sample) and P(conf.)$>$ 90% (54 stars or $\sim$10% of the sample). Based off the derived Galactic positions, we determined that 73% or 381 stars are currently within the bulge (see Section 3.4.1). Of these 381, only 223, or 59%, have P(conf.)$>$ 50%. Therefore, almost half of the stars in our sample are likely halo interlopers. However, it is possible that many of these stars that do not stay confined to the bulge could be metal-weak thick disk stars or bulge stars that have apocenters only slightly larger than 3.5 kpc. Although, most of the stars that do not stay confined have eccentricity $>$0.6 and apocenter $>$ 6 kpc, indicating that they are most likely halo stars.

We also find that the percentage of stars that stay confined to the bulge decreases with decreasing metallicity. In Figure 3.8, we show the fraction of stars that will stay in the bulge with various probabilities over the number of

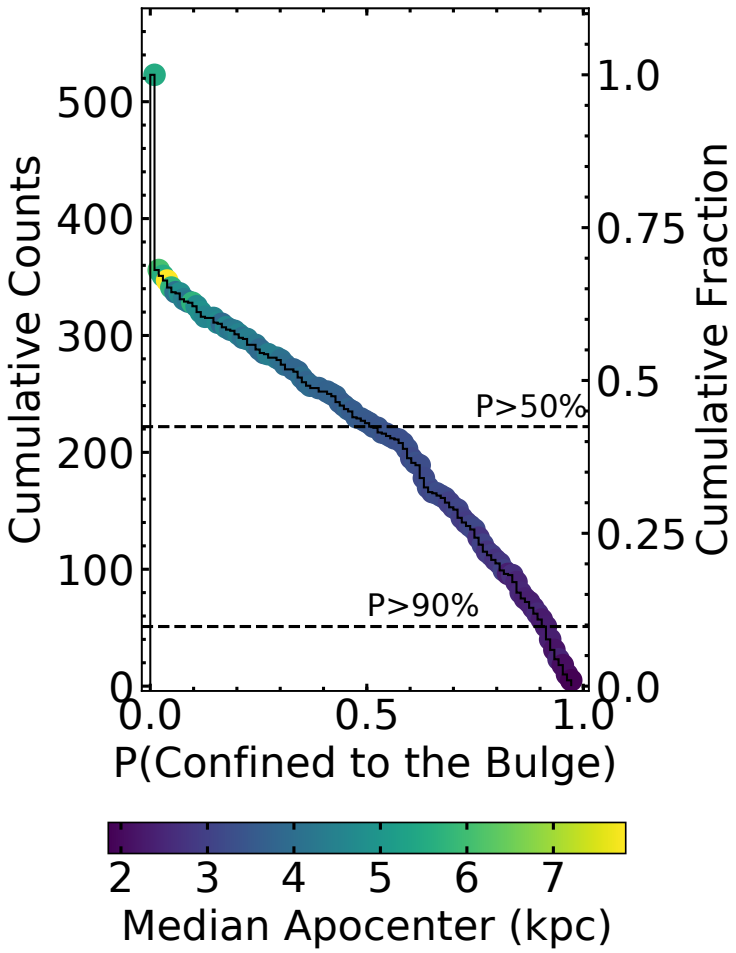

Figure 3.7: The distributions of probabilities that the stars stay confined to the bulge, which we define as within 3.5 kpc from the Galactic center. The points are colored by the median apocenter at that probability. The dashed lines correspond to the number of stars with probability $> 50\%$ and $>90\%$, which are $\sim 43\%$ and $\sim 10\%$ of the sample, respectively.

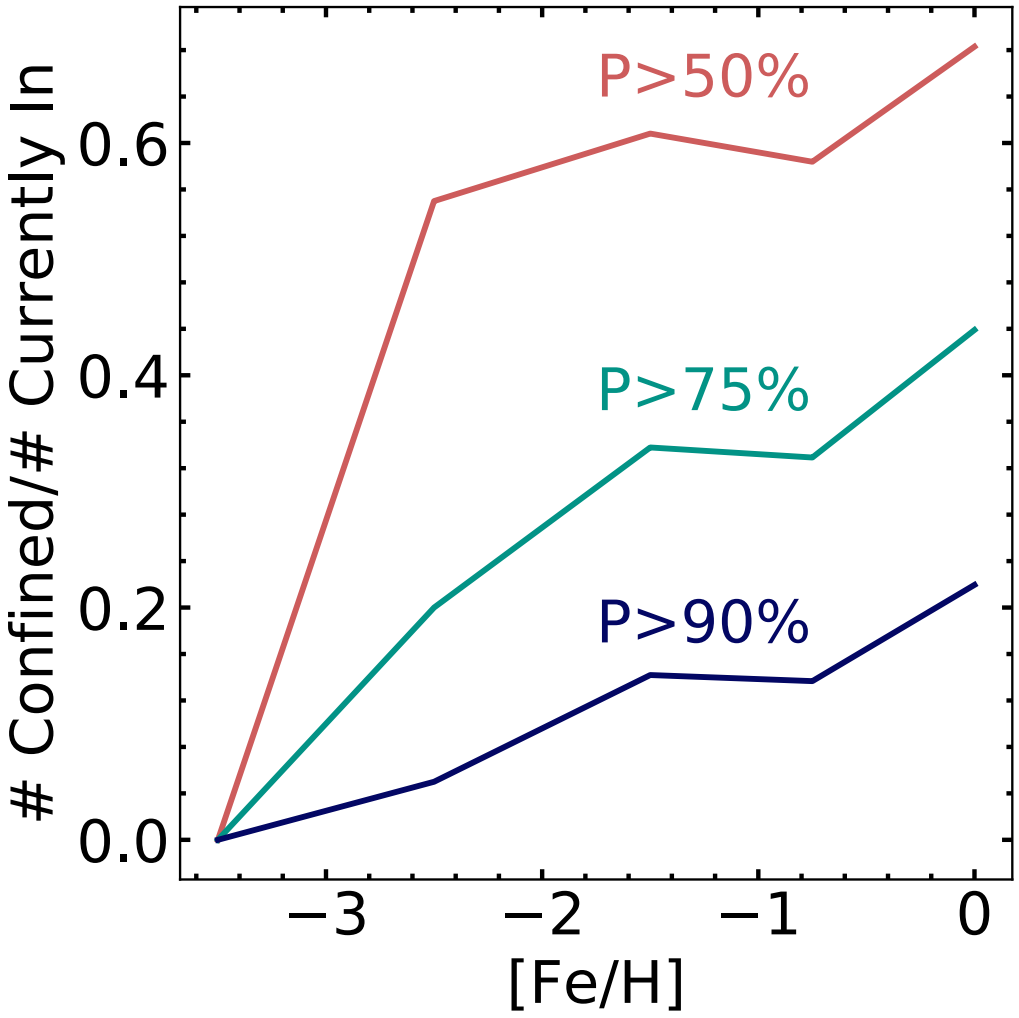

Figure 3.8: The fraction of stars that are currently in the bulge that have a >50% (red), >75% (green) and >90% (dark blue) probability of staying within 3.5 kpc of the Galactic center as a function of metallicity.

stars currently in the bulge as a function of metallicity. However, the number of stars in our sample also decreases with decreasing metallicity for [Fe/H] <-1 dex. For example, there is only 1 star with [Fe/H] < -3 dex in our sample that is currently within the bulge (Lucey et al., 2019). This star has a P(conf.) = 0%. There are 21 stars in our sample with -3 dex $\leq$ [Fe/H] < -2 dex that are currently in the bulge. Only 11 of these stars have P(conf.) > 50%. However, this drops to 4 stars when we restrict to stars with P(conf.) > 75%.

These results demonstrate the importance of performing orbit analysis to remove the contamination when studying metal-poor bulge stars, especially for stars with [Fe/H]< -2 dex. Previous and future studies of the metal-poor star in the Galactic bulge may have different selection functions, which may result in differing rates of contamination by halo interlopers. For example, Kunder et al. (2020) found that only 25% of their sample of RR Lyrae stars had apocenters> 3.5 kpc. However, we note that the kinematic results, specifically the Galactocentric line-of-sight velocity distributions as a function of Galactic longitude, for studies which did not target RR Lyrae stars (e.g., Ness et al., 2013b; Arentsen et al., 2020a) show results similar to ours when we do not remove the contamination. This may indicate similar rates of contamination with halo interlopers in these studies. Furthermore, the EMBLA survey estimates that roughly 50% of their 23 very metal-poor stars were confined to the bulge (Howes et al., 2015), which is consistent with our results.

3.6 Properties of Confined Metal-Poor Bulge Stars

Now that we can separate the halo interlopers from the confined metal-poor bulge stars, we have the opportunity to study this unique population. With our data we can provide new insights on the metal-poor tail of the bulge MDF and the kinematics of these stars, which will lead to new constraints on the origins of confined metal-poor bulge stars and on the formation history of the central region of our Galaxy.

3.6.1 Metallicity Distribution Function

The MDF can provide critical information about the history of this unique metal-poor population. However, our results are heavily influenced by the metallicity selection method described in Section 6.2. For example, the SkyMapper photometry, which is used for target selection, may be biased against selecting CEMP stars (Starkenburg et al., 2017b; Da Costa et al., 2019). If the majority of confined bulge stars with [Fe/H] <-2 dex are CEMP stars, it is possible that we would not have observed these stars. Despite this, the MDF as a function of confinement probability shows a clear trend. In Figure 3.9, we show the MDFs for three different cuts in the probability of confinement. In light blue, we show the stars with P(conf.) $< 50\%$, which are likely to be mostly halo stars and metal-weak thick disk contamination as we do not constrain the stars to be currently within 3.5 kpc of the Galactic center. In red, we show stars with P(conf.) $\geq 50\%$ and in dark blue we show stars with P(conf.) $> 90\%$. As we make the cut in probability of confinement more

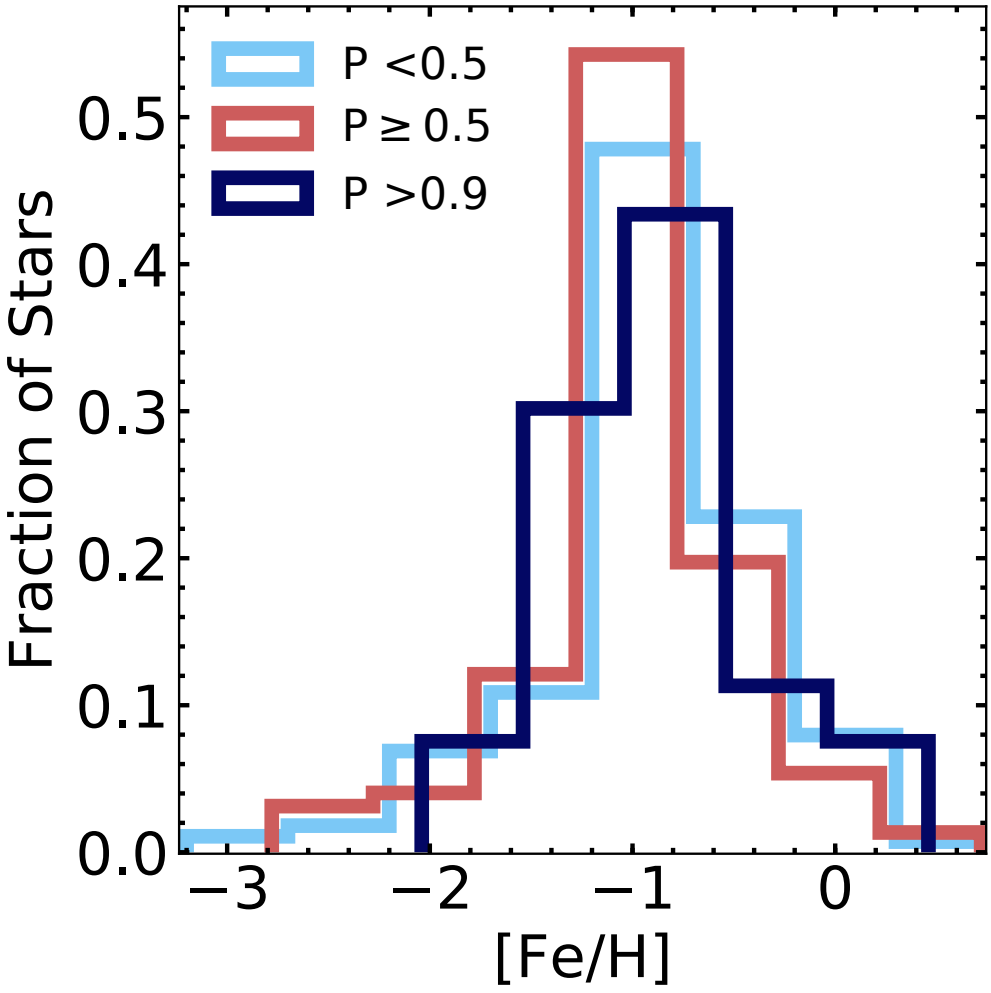

Figure 3.9: The metallicity distribution function of stars with different probabilities of staying confined to the bulge.

stringent, we see the most metal-poor tail of the distribution disappears. It is important to consider that we have a small number of stars at the most metal-poor end so it is difficult to draw strong conclusions from the disappearance of this tail. Nonetheless, it is interesting to note that the metal-weak thick disk metallicity distribution is thought not to go below [Fe/H]≈-1.8 dex (Beers et al., 2014; Carollo et al., 2019), which is consistent with the lowest metallicity observed for the population with P(conf.) $>$ 90% (-2.04 dex), indicating that these two populations may have similar origins. However, recent results by Sestito et al. (2020) argue that the metal-weak thick disk extends to [Fe/H] $<$-2.5 dex. It is difficult to further compare the MDF of our stars to the thick disk because of our complicated selection function from the photometric metallicity targeting.

3.6.2 Kinematics

The kinematics of our stars can also inform us about the origins of the metal-poor bulge population. One of the main open questions about this population is whether they participate in the B/P bulge structure or if they are more consistent with a classical bulge population. In this section, we aim to answer this question and gather new insights on the history of this population.

To do this, we compare our observed kinematics to what is expected from simulations. Specifically, we use the star-forming simulation presented in Cole et al. (2014) and Ness et al. (2014). In short, this simulation forms a disk galaxy through gas cooling and settling into a disk, which triggers continuous

star formation. A bar forms in the model after ∼3.2 Gyr and continues to grow. By 10 Gyr, a B/P bulge has formed. Since the bar in this model is only 3 kpc long, we multiply the spatial coordinates by 1.7 to match the MW, which has a bar measured to be 5 kpc long (Wegg et al., 2015). In addition, we multiply the velocities by 0.48, which is consistent with Ness et al. (2014) and Debattista et al. (2017), which also use this simulation. We also rotate the model to match the position of the bar with respect to the Sun, which is at an angle of 27° from the line-of-sight to the center of the Galaxy (Wegg & Gerhard, 2013). We choose to only use stars from the simulation with the same line-of-sight towards the Galactic center as our observations and that are within 3.5 kpc of the Galactic center in order to be consistent with our observations.

3.6.2.1 Line-of-Sight Velocities

Often in bulge literature, RVs are used over full 3-D motion because the proper motions and distances are poorly constrained or not measured at all. In this work, the measured RVs are considerably more precise than the 3D velocities, which depend on the distance estimate. Therefore, they can be used to provide a detailed view of bulge dynamics and an accurate comparison to the literature. However, to understand them in a Galactic context, we first need to convert them from a heliocentric rest frame to a Galactocentric one. We convert the radial velocities to Galactic Standard of Rest (v_{gsr}) assuming the local standard of rest velocity at the Sun to be 220 km/s (Kerr & Lynden-

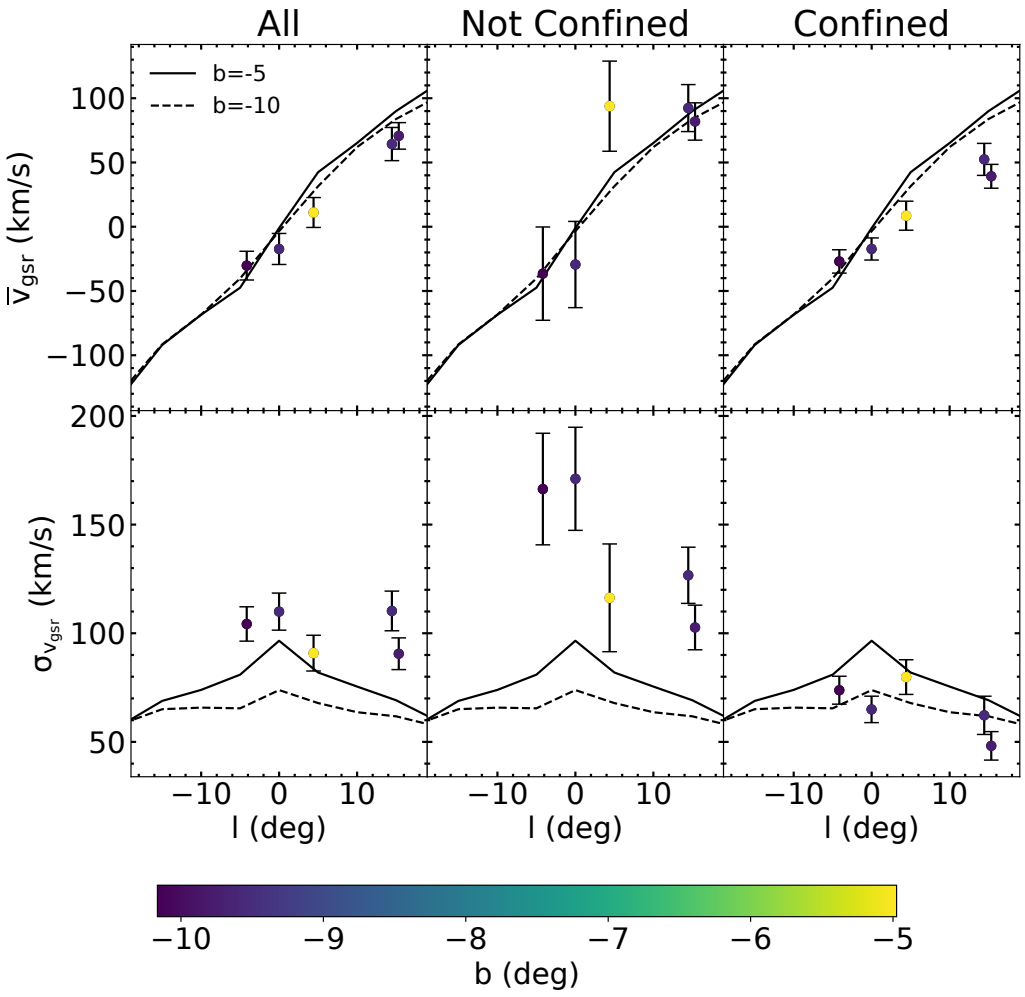

Figure 3.10: The mean and standard deviation of the Galactocentric line-of-sight velocities (v_{gsr}) as a function of Galactic longitude (l). The points are colored by the Galactic latitude (b). The error bars on the mean are $\sigma/\sqrt{N}$ where σ is the standard deviation and N is the number of stars. The error bars on the standard deviation are $\sigma/\sqrt{2N}$. In the left panel, we show results for all stars in our sample that are currently within 3.5 kpc of the galactic center. In the middle panel, we show stars with a probability of being confined to the bulge $< 50\%$ and in the right panel, we show only stars with a probability of being confined $\geq 50\%$. We also show results from the simulation of a B/P bulge presented in Cole et al. (2014) and Ness et al. (2014) (black solid and dashed lines). These lines are created only using stars that formed within the first Gyr of star formation.

Bell, 1986; Bovy et al., 2012), which is consistent with the Galactic potential used to calculate the orbits in Section 3.4.2 (Bovy, 2015). We also assume the Sun's peculiar velocity to be 17.1 km/s in the direction (l,b) = (58°, 22°) (Coşkunoğlu et al., 2011). Recent estimates of the Sun's peculiar velocity can differ by up to ∼3 km/s (Bland-Hawthorn & Gerhard, 2016). Therefore, adopting different values only has a small impact on our results and does not impact our conclusions. With these values, the Galactocentric line-of-sight velocity in terms of the heliocentric radial velocity (v_{hc}) is then:

$$\begin{aligned} v_{gsr} =& v_{hc} + 220[\sin(l)\cos(b)] + 17.1[\sin(b)\sin(22)+ \\ & \cos(b)\cos(22)\cos(l-58)] \end{aligned} \tag{3.3}$$

where v_{hc} is in km/s and angles (l,b) are in degrees.

We present the mean and standard deviation of the Galactocentric line-of-sight velocities (v_{gsr}) as a function of Galactic longitude (l) in Figure 3.10 where the points are colored by the Galactic latitude (b). In the left panel, we show all 523 stars. In the middle panel, we show only stars with a P(conf.) $< 50\%$ (halo interlopers) and in the right panel we show stars with a P(conf.) $\geq 50\%$. For comparison, we also show results from the simulation. We choose to use only stars that form within the first Gyr of the simulation as we expect these stars will be most similar to the metal-poor stars.

Stars that do stay confined have a different velocity distribution than the halo interlopers (unconfined stars). For example, the halo interlopers have a steeper slope with the Galactic longitude than the confined stars, which is indicative of faster rotation. This is especially interesting given that we expect

the opposite, i.e., that the bulge/bar rotates more rapidly than the halo. It is possible that the appearance of rotation in the population of stars that are not confined to the bulge is caused by thick disk stars and bulge stars in the sample which may reach out to distances > 3.5 kpc from the Galactic center. In other words, it is possible that 3.5 kpc is too stringent of a cut and that many stars which participate in the bulge/bar may have apocenters > 3.5 kpc (Portail et al., 2017). However, as noted in Section 3.5, the majority of stars that do not stay confined have eccentricity >0.6 and apocenter > 6 kpc indicating that they are likely halo stars. It is also possible that halo stars that come within 3.5 kpc of the Galactic center have significant prograde rotation. This is not unreasonable given that it has already been observed that halo stars within $\sim$10 kpc of the Galactic center can have prograde rotation up to 50 km/s (Carollo et al., 2007). Furthermore, the confined stars appear to be rotating slower than expectations from the simulation (see right panel of Figure 3.10). This has previously been observed among metal-poor bulge stars in Arentsen et al. (2020a). However, since they cannot distinguish between the halo interlopers and confined stars, it is difficult to determine if the slower rotation observed in Arentsen et al. (2020a) is a result of halo contamination or the confined bulge stars. Our results indicate that it is in fact the confined stars that rotate slower than expected given the simulations. The slower rotation among confined stars will be discussed further in Section 3.6.2.2, where we present the rotational velocity (v_ϕ) distribution of confined stars.

In addition, to the differences in rotation, the confined and not con-

fined stars show differences in velocity dispersions. Specifically, the stars that are not confined show much higher velocity dispersions than those which are confined. Our results for all of the stars (left panel of Figure 3.10) is consistent with previous work where metal-poor bulge stars have a line-of-sight velocity dispersion of $\sim$100 km/s regardless of Galactic longitude or latitude (Ness et al., 2013b; Kunder et al., 2016; Arentsen et al., 2020a). However, previous studies did not perform orbit analysis and therefore were unable to determine if this high dispersion was indicative of a classical bulge or merely caused by halo interlopers. In the Figure 3.10, we show that the velocity dispersion is significantly lower for the confined stars than for the not confined stars. The signature of a B/P bulge is a peak in the velocity dispersions at l=0° that decreases moving outwards from the Galactic Center. It also generally has lower velocity dispersion moving away from the Galactic plane to higher $|b|$. A classical bulge, on the other hand, would have a velocity dispersion that is independent of Galactic longitude or latitude and would be represented as a horizontal line in Figure 3.10. Therefore, our velocity dispersions for the confined stars are consistent with a B/P bulge and there is no need to invoke a classical bulge population.

3.6.2.2 3D Velocities

In addition to the line-of-sight velocities, the full 3D Galactocentric velocities can inform us of the structure and formation history of this population. Specifically, we look at the Galactocentric cylindrical velocities to study

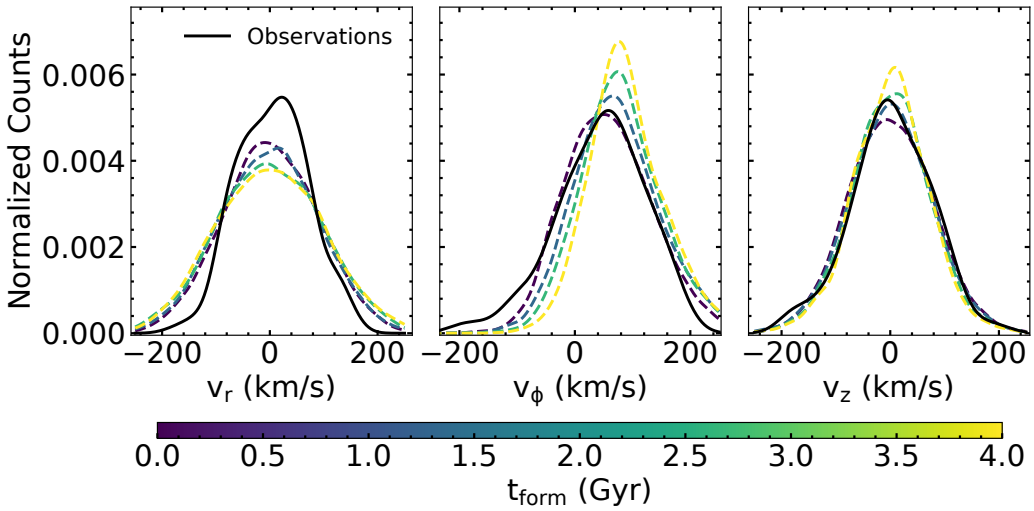

Figure 3.11: Distribution of the Galactocentric cylindrical velocities for stars with probability of confinement $\geq$50% (black) compared to populations with different formation times from the simulation (dashed lines) presented in Cole et al. (2014) and Ness et al. (2014). The distributions from the simulation are determined by using only stars within 3.5 kpc of the Galactic center and along the same line-of-sight as our observations. We only show stars that formed within the first 4 Gyr although the simulation forms stars for all 10 Gyr. Each line is created using 1 Gyr of star formation.

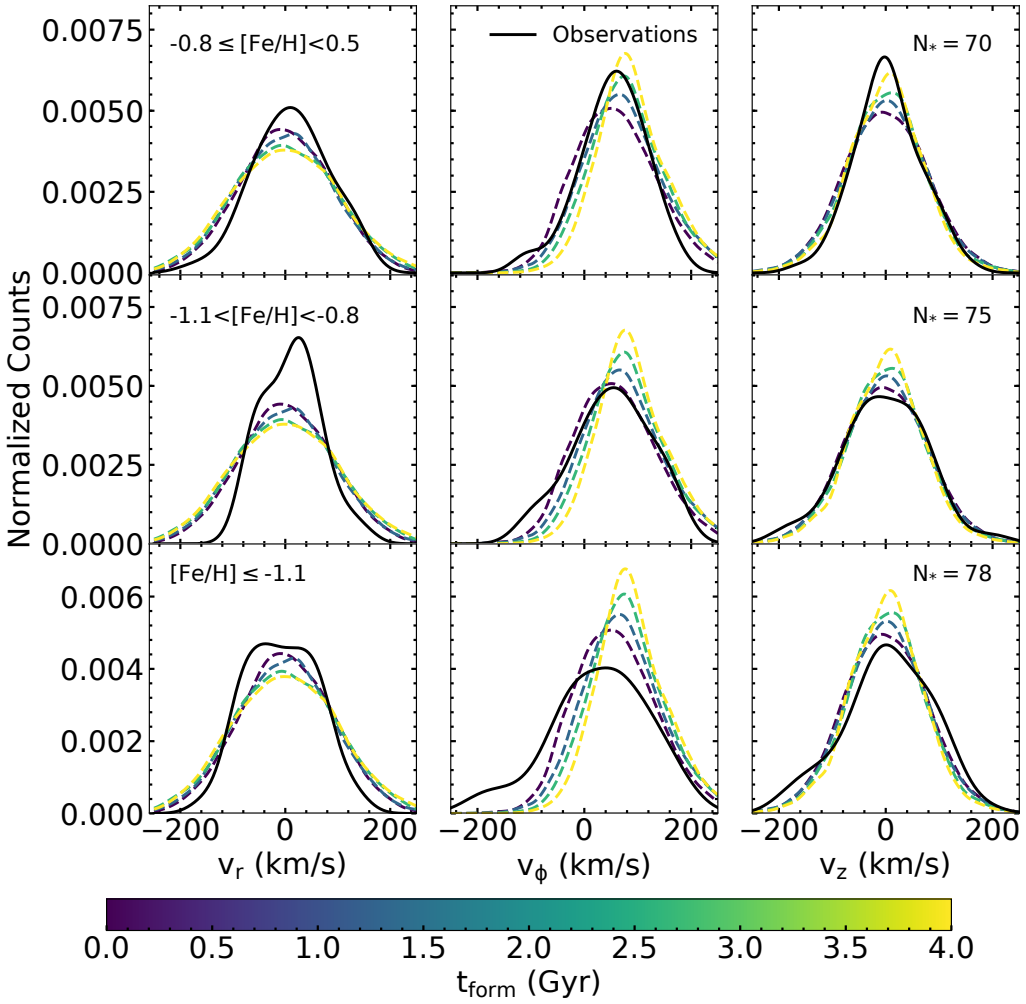

Figure 3.12: Distribution of the Galactocentric cylindrical velocities for stars with probability of confinement $\geq 50\%$ and varying metallicities (black) compared to populations with different formation times from the simulation (dashed lines) presented in Cole et al. (2014) and Ness et al. (2014). The simulation lines are the same as those shown in Figure 3.11. As we move to lower metallicities our observations better match the v_ϕ distributions for stars that formed earlier with the exception of a growing counter-rotating population.

the radial motion (v_r), rotation (v_ϕ), and vertical motion (v_z). In Figure 3.11, we show the distribution of these velocity components for our stars that have P(conf.) $\geq$ 50% (black line) along with distributions from the simulation. These distributions are determined by applying a kernel density estimator (KDE) to the observed and simulated distributions. The colored lines shown correspond to populations with different formation times from the simulation.

The differences in the simulated distributions for different formation ages shown in Figure 3.11 can be explained by kinematic fractionation. Kinematic fractionation, which refers to the separation of populations with different initial kinematics by a growing/forming bar, has been shown to result in older (hence more metal-poor) populations having distinct structure and kinematics that differ from younger (more metal-rich) populations (Debattista et al., 2017). One of the clear trends shown in Figure 3.11 is that the peak of the simulated v_ϕ distributions approaches zero for stars that formed at earlier times. Therefore, stars that formed earlier generally rotate slower than stars that form later.

As shown in Figure 3.11, our observed velocity distributions are mostly consistent with the simulation. However, our observed distribution in v_r is narrower than the simulated distributions. This is likely because we do not confirm that the stars stay confined to within 3.5 kpc of the Galactic center when we calculate the simulated distributions. Therefore, we presumably include more stars with larger $|v_r|$ causing the simulated distributions to be wider than our observed distribution which only includes stars with P(conf.)$\geq$50%. Ad-

ditionally, our observed v_ϕ distribution has a stronger tail of counter-rotating stars than any of the simulated distributions. Specifically, there is a clear over-abundance of fast retrograde rotating stars (v_ϕ <-100 km/s) in our observed distribution. This difference in the distribution likely causes the appearance of slower rotation observed in the right panel of Figure 3.10 by decreasing the mean line-of-sight velocity. The tails of the v_z distribution are also slightly asymmetrical and differ from the simulation. However, these differences are small and are likely due to stochastic noise in the observed distribution.

In Figure 3.12, we show the cylindrical Galactocentric velocity distributions for stars with P(conf.)$\geq$ 50% divided into three metallicity bins. Additionally, in each panel we show the same simulated distributions as Figure 3.11. The bins are designed to have similar numbers of stars with the most metal-rich bin having 70 stars, the next bin having 75 stars and the most metal-poor bin having 78 stars. As we move to lower metallicities, the peak of the observed v_ϕ distribution moves closer to zero. The observed v_ϕ distribution for the most metal-rich stars (-0.8 dex $\leq$ [Fe/H] $<$ 0.5 dex) is most consistent with the v_ϕ distribution of stars that formed between 2-3 Gyrs after the start of the simulation. For stars with -1.1 dex $\leq$ [Fe/H] <-0.8 dex, the observed v_ϕ distribution best matches the simulated distribution for stars that formed between the first 1-2 Gyrs of the simulation. Lastly, the most metal-poor stars ([Fe/H]$\leq$-1.1 dex) have a v_ϕ distribution similar to the stars that formed within the first Gyr of the simulation. Therefore, our results are consistent with kinematic fractionation if we assume the more metal-poor stars are older.

We also see a strong counter-rotating tail that is increasingly prominent at lower metallicities that is not in agreement with the simulation distributions. Counter-rotating stars have been observed in the bulge in significant numbers (Queiroz et al., 2020). Although, simulations do predict the presence of some counter-rotating stars in a B/P bulge (see middle panel of Figures 3.11 and 3.12). Our observations, however, specifically show an overabundance of stars with v_ϕ<-100 km/s and [Fe/H]≤-1.1 dex, which does warrant further investigation. It is possible that these stars are contamination by halo interlopers, especially given that we have found that the likelihood a star stays confined to the bulge declines with decreasing metallicity (see Section 3.5 and 3.6.1). On the other hand, if these stars are bonafide confined bulge stars, it is possible that this is an accreted population. However, they could also be the result of secular evolution, but are not produced in the simulation because of missing physics. For example, the simulation does not include clump formation, which can result in counter-rotating stars (Amarante et al., 2020). In the next installment of this survey we will present the elemental abundances for these stars, which will provide further insights into the origins of these interesting counter-rotating stars.

Furthermore, the v_r and v_z distributions also deviate more strongly from the simulation distributions with decreasing metallicity (see Figure 3.12). There are a number of factors that may contribute to these deviations. First, as previously discussed, this may be a result of increasing contamination with halo interlopers with decreasing metallicity which is consistent with our results

that the frequency of halo interlopers increases with decreasing metallicity (see Figure 3.8). These deviations are also consistent with a possible accreted system that stays within 3.5 kpc of the Galactic center (e.g., Horta et al., 2020). However, it is also possible that these distributions contain only stars that participate in the B/P bulge and that these deviations are caused by a combination of stochastic noise and varying contributions from different lines-of-sight. Specifically, consistent with a radial and vertical metallicity gradient (Zoccali et al., 2008; Gonzalez et al., 2011; Johnson et al., 2011, 2013a), the fraction of stars observed at higher $(|l|, |b|)$ becomes larger with decreasing metallicity. On the other hand, the simulated distributions have the highest counts of stars at $(|l|, |b|)$ closer to zero. Therefore, the spatial distribution of the observed sample becomes less similar to the spatial distribution of the simulated sample with decreasing metallicity, which can also cause deviations in velocities, especially in v_r. In future work, we will add chemistry information for these stars which will help us distinguish between these possible scenarios.

3.7 Discussion and Conclusions

Many state-of-the-art simulations now indicate that the metal-poor stars in the Galactic bulge are likely to be some of the oldest stars in the Galaxy (Salvadori et al., 2010; Tumlinson, 2010; Starkenburg et al., 2017a; El-Badry et al., 2018b). However, in order to determine if these stars are truly ancient, we must understand their origins. For example, it is currently unknown how many, if any, of these stars are confined to the Galactic bulge

or are just halo interlopers passing through the bulge. If these stars do stay confined to the bulge, they could participate in the B/P bulge structure or be a classical bulge population. On the other hand, if they are halo interlopers, they could be a unique accreted population (e.g., Horta et al., 2020) or part of the in-situ halo population. The chemodynamical properties of these stars can provide crucial insight into distinguishing between these possible origins.

Previous work on the metal-poor bulge has mostly been consistent with a classical bulge population. Studies of the chemical make-up of these stars have indicated that they are distinct from halo stars. Specifically, it has been shown that they have lower dispersion and higher Ca abundances than halo stars (Duong et al., 2019a; Lucey et al., 2019) along with differing rates of CEMP stars (Howes et al., 2015, 2016; Koch et al., 2016) and neutron-capture enhanced stars (Koch et al., 2019; Lucey et al., 2019; Duong et al., 2019a). Dynamics of metal-poor bulge stars, specifically the line-of-sight velocities, have indicated that these stars are more consistent with a classical bulge compared to a B/P bulge (Kunder et al., 2016). It has also been shown that the metal-poor stars in the bulge have a higher velocity dispersion than the metal-rich stars, which is inconsistent with a B/P bulge (Ness et al., 2013b; Arentsen et al., 2020a). These studies also determined that the metal-poor bulge stars rotate slower than the metal-rich stars, which may indicate different origins. However, using N-body simulations, Gómez et al. (2018) demonstrate that a classical bulge population would show even slower rotation than what has been observed among metal-poor bulge stars and that the observations can be

explained by a thick disk component. Nevertheless, it is unclear how many, if any of these stars in previous studies are confined bulge stars rather than halo interlopers which are just passing through the bulge.

There have been a few studies which have performed orbital analysis on metal-poor bulge stars to determine if they stay confined to the bulge. The EMBLA survey found that $\sim$50% of their sample of very metal-poor stars ([Fe/H]$<$ -2 dex) stay confined to the bulge (Howes et al., 2015). However, only 2 out of the 10 stars that they performed orbital analysis for have apocenters $<$ 3.5 kpc, which we define as the edge of the bulge in this work. Recently, Reggiani et al. (2020) determined that 2 out of the 3 very metal-poor inner bulge stars that they studied have apocenters $<$3.5 kpc. Finally, only 25% of the 1389 RR Lyrae stars studied in Kunder et al. (2020) do not stay within 3.5 kpc of the Galactic center. Therefore, the rate at which metal-poor bulge stars stay confined to the bulge varies from 20-75% depending on selection function.

In this work, we separate the the halo interlopers from the confined metal-poor bulge stars with a probabilistic kinematic method. Using spectra of 523 stars from the VLT/GIRAFFE and VLT/UVES spectrographs along with information *Gaia* DR2 data, we determine the 3D Galactic positions and velocities utilizing a Markov Chain Monte Carlo (MCMC) simulation and Bayesian inference with a Galactic model prior (Rybizki et al., 2018). We then measure the orbital properties and associated errors along with the probability that the star stays confined to the bulge. We also develop a method to derive

metallicities from the CaT, which achieves similar precision to previous work (Battaglia et al., 2008; Carrera et al., 2013) without the need for an estimate of the star's luminosity. We use this method to determine metallicities for the GIRAFFE spectra and also use metallicities determined in Lucey et al. (2019) for the UVES spectra.

Given these data we can conclude:

1. Only ∼59% of the stars in our sample that are currently residing in the bulge have P(conf.)> 50%. This value drops to ∼14 % if we only consider stars whose orbits are confined to the bulge with P(conf.) > 90 %. This indicates that all future and previous studies on the metal-poor bulge that do not perform orbit analysis are likely contaminated by halo stars.

2. The rate of contamination with halo interlopers increases with decreasing metallicity. Therefore, it is especially important to perform orbit analysis to separate the halo interlopers from the confined stars when studying stars with [Fe/H] < -2 dex.

3. By removing the halo interlopers we are able to study the properties of the confined metal-poor bulge stars. We find that the MDF for stars with P(conf.) >90% ends at [Fe/H]≈-2 dex. This is consistent with the MDF of the metal-weak thick disk (Beers et al., 2014; Carollo et al., 2019).

4. We study the kinematics of confined metal-poor bulge stars and find they are consistent with a B/P bulge and kinematic fractionation (Debattista

et al., 2017). This is different from previous results, which appeared to be more consistent with a classical bulge because they were unable to remove the halo interlopers (Ness et al., 2013b; Kunder et al., 2016; Arentsen et al., 2020a).

In the next installment of the COMBS survey, we plan to perform chemical abundance analysis for all 550 GIRAFFE spectra in order to gain further insight on the origins of these stars. For example, we will explore chemical signatures of an accreted population among the stars that do not stay confined to the bulge and test for similarity with the metal-weak thick disk for the stars that do stay confined. We will also search for signatures of globular cluster origins for these stars (e.g., Schiavon et al., 2017). Combining the dynamical results from this work with chemistry will give us a powerful data set for searching for the oldest stars and studying the origin of the metal-poor bulge population.

Chapter 4

The COMBS Survey - III. The Chemodynamical Origins of Metal-Poor Bulge Stars

Abstract: The characteristics of the stellar populations in the Galactic Bulge inform and constrain the Milky Way's formation and evolution. The metal-poor population is particularly important in light of cosmological simulations, which predict that some of the oldest stars in the Galaxy now reside in its center. The metal-poor bulge appears to consist of multiple stellar populations that require dynamical analyses to disentangle. In this work, we undertake a detailed chemodynamical study of the metal-poor stars in the inner Galaxy. Using R$\sim$ 20,000 VLT/GIRAFFE spectra of 319 metal-poor (-2.55 dex$\leq$[Fe/H]$\leq$0.83 dex, with $\overline{\text{[Fe/H]}}$=-0.84 dex) stars, we perform stellar parameter analysis and report 12 elemental abundances (C, Na, Mg, Al, Si, Ca, Sc, Ti, Cr, Mn, Zn, Ba, and Ce) with precisions of $\approx$0.10 dex. Based

[1] This chapter is based on Lucey M., Hawkins K., Ness M., Nelson T., Debattista V.P., Luna A., Bensby T., Freeman K.C., Kobayashi C., 2022, MNRAS, 509, 122. The author of this document, Madeline Reinke Lucey, completed most of the analysis and wrote the publication. M. Ness led the proposal to obtain the observations necessary to achieve this work. K. Hawkins supervised my work on this project and T. Nelson assisted in part of the analysis.

on kinematic and spatial properties, we categorise the stars into four groups, associated with the following Galactic structures: the inner bulge, the outer bulge, the halo, and the disk. We find evidence that the inner and outer bulge population is more chemically complex (i.e., higher chemical dimensionality and less correlated abundances) than the halo population. This result suggests that the older bulge population was enriched by a larger diversity of nucleosynthetic events. We also find one inner bulge star with a [Ca/Mg] ratio consistent with theoretical pair-instability supernova yields and two stars that have chemistry consistent with globular cluster stars.

4.1 Introduction

The goal of Galactic archaeology is to understand the Milky Way's (MW) formation and evolution through the chemodynamical properties of its stars. Using observations (Ortolani et al., 1995; Kuijken & Rich, 2002; Zoccali et al., 2003; Clarkson et al., 2011; Brown et al., 2010; Valenti et al., 2013; Calamida et al., 2014; Howes et al., 2014) and simulations (Tumlinson, 2010; Kobayashi & Nakasato, 2011; Starkenburg et al., 2017a; El-Badry et al., 2018b), the bulge of the MW has been shown to contain many of the oldest stars in our Galaxy. Studies of the chemodynamics of these old stars can reveal new insights into the formation and early chemical evolution of the MW.

The bulge is a complex Galactic component, with many overlapping stellar populations. Spectroscopic studies of the stars in the bulge have revealed a metallicity distribution function (MDF) with multiple components.

Specifically, the Abundances and Radial velocity Galactic Origins Survey (ARGOS; Freeman et al., 2013) found that the MDF of the bulge has five components (Ness et al., 2013a). The two most metal-rich components, which are associated with the bulge, peak at [Fe/H] = +0.12 dex and -0.25 dex. The other three components, which peak at [Fe/H] = -0.70 dex, -1.18 dex and -1.70 dex, they associate with the thin disk, thick disk and halo components of the MW, respectively. However, it is important to note that the metal-rich components dominate with only 5% of bulge stars having [Fe/H] < -1 dex (Ness & Freeman, 2016). Although many studies have found similar results (e.g., Zoccali et al., 2008; Johnson et al., 2013a; Rojas-Arriagada et al., 2014b; Zoccali et al., 2017; Rojas-Arriagada et al., 2017; Duong et al., 2019a), Johnson et al. (2020) argue that the multi-modal MDF is only valid for the outer bulge and that inside a Galactic latitude of $(b) \sim 6^{\circ}$ the MDF is consistent with a closed box model (a single peak with a long metal-poor tail). However, Bensby et al. (2013, 2017) found strikingly similar results to Ness et al. (2013a) using bulge micro-lensed dwarf stars within $-6^{\circ}<b<-2^{\circ}$.

The discovery of metallicity-dependent structure and kinematics in the bulge provides further evidence for multiple stellar populations (Ness et al., 2013a,b). Today, it is generally accepted that the majority of the mass in the bulge participates in a boxy/peanut-shaped (B/P) bulge (Howard et al., 2009; Shen et al., 2010; Ness et al., 2013b; Debattista et al., 2017). A B/P bulge is a rotation-supported structure, which is the result of secular disk and bar evolution (Combes & Sanders, 1981; Combes et al., 1990; Raha et al.,

1991; Merritt & Sellwood, 1994; Quillen, 2002; Bureau & Athanassoula, 2005; Debattista et al., 2006; Quillen et al., 2014; Sellwood & Gerhard, 2020). However, it is also suggested that the MW may host a less-massive metal-poor classical bulge component (Babusiaux et al., 2010; Hill et al., 2011; Zoccali et al., 2014), which is a spheroidal, pressure-supported structure formed by hierarchical accretion (Kauffmann et al., 1993; Kobayashi & Nakasato, 2011; Guedes et al., 2013). Evidence for a metal-poor classical bulge has been found in studies of the kinematics of bulge stars as a function of metallicity. Specifically, metal-poor stars in the bulge rotate slower and have a higher velocity dispersion than the metal-rich stars (Ness et al., 2013b; Kunder et al., 2016; Arentsen et al., 2020a). However, Debattista et al. (2017) demonstrated that these observations may be the result of an overlapping halo population rather than a classical bulge. In fact, Kunder et al. (2020) found that 25% of the RR Lyrae stars currently in the bulge are actually halo interlopers. Similarly, Lucey et al. (2021) found that about 50% of their sample of metal-poor giants are halo interlopers and that the fraction of interlopers increases with decreasing metallicity. When they removed the halo interlopers from the sample, Lucey et al. (2021) found that the velocity dispersion decreased and there was no evidence for a classical bulge component in the kinematics.

With the advent of metallicity-sensitive photometric surveys such as the Skymapper (Casagrande et al., 2019) and Pristine (Starkenburg et al., 2017b) surveys, there is great potential to target and study the metal-poor stars in the Galactic bulge. These metal-poor stars are especially exciting because previous

work on old stars have focused on the Galactic halo, where the majority of stars are metal-poor (e.g., Frebel et al., 2006; Norris et al., 2007; Christlieb et al., 2008; Keller et al., 2014). Simulations now indicate that targeting metal-poor stars in the bulge is most conducive to the discovery of ancient stars. For example, simulations predict that if Population III stars exist in our Galaxy, they are most likely to be found in the bulge (White & Springel, 2000; Brook et al., 2007; Diemand et al., 2008). Furthermore, simulations predict that stars of a given metallicity are more likely to be older if they are found closer to the Galactic center (Salvadori et al., 2010; Tumlinson, 2010; Kobayashi & Nakasato, 2011). Specifically, metal-poor bulge stars are ancient in that they formed before $z > 5$ and are older than 12 Gyr (Kobayashi & Nakasato, 2011).

The chemistry of ancient stars is of special interest, given that they are thought to be primarily enriched by Population III stars. Therefore, their chemistry can provide insight into the properties of Population III stars and the early universe in which they formed. Several studies have found that a significant fraction of Population III stars would explode as pair-instability supernovae (PISNe) given that simulations of metal-free star formation yield a top-heavy initial mass function (IMF; Tumlinson, 2006; Heger & Woosley, 2010; Bromm, 2013). Results of simulated yields from PISNe predict that a star which is 90% enriched by a PISNe would have [Fe/H] ≈ -2.5 dex (Karlsson et al., 2008) and would contain barely any elements heavier than Fe (Karlsson et al., 2008; Kobayashi et al., 2011b; Takahashi et al., 2018). Recently, Takahashi et al. (2018) found that the two most discriminatory abun-

dance ratios that indicate enrichment from PISNe are [Na/Mg] ≈ -1.5 dex and [Ca/Mg]$\approx$0.5-1.3 dex. Excluding PISNe (i.e., if the IMF is truncated at $< 140 M_{\odot}$), ancient stars are expected to have higher levels of α-element enhancement than typical MW stars due to the top-heavy IMF of Population III stars and the mass-dependent yields of Type II supernovae (Tumlinson, 2010; Heger & Woosley, 2010; Bromm, 2013). Another important chemical signature of ancient stars is lower copper (Cu), manganese (Mn), sodium (Na), and aluminum (Al) abundances with respect to typical MW stars given the metallicity dependence of these yields in Type II supernovae (Kobayashi & Nakasato, 2011).

Recently, there have been many spectroscopic surveys targeting the metal-poor stars in the bulge (e.g., Howes et al., 2014, 2015, 2016; Duong et al., 2019a,b; Lucey et al., 2019; Arentsen et al., 2020b). The first installment of the Chemical Origins of Metal-poor Bulge Stars (hereafter COMBS I) studied the detailed chemistry of 26 metal-poor bulge stars (Lucey et al., 2019). One of the major results from this work was the discovery of higher levels of calcium enhancement in the bulge compared to Galactic halo stars of similar metallicity. Furthermore, COMBS I found lower scatter in many elemental abundances for very metal-poor bulge stars compared to halo stars. The HERMES Bulge Survey (HERBS; Duong et al., 2019a) and Fulbright et al. (2007) found similar results with respect to higher levels of Ca enhancement and lower scatter for their sample of metal-poor stars. Further differences between metal-poor bulge stars and halo stars include the rate of carbon (C)

and neutron process enhancements. C-Enhanced Metal-Poor (CEMP) stars occur at a rate of 15-20% among halo stars with [Fe/H]<-2 dex (Yong et al., 2013). However, in the bulge, the rate of CEMP stars is estimated at ∼6% for the same metallicity range (Arentsen et al., 2021). Furthermore, neutron-capture element-enhanced stars are rarely observed in bulge spectroscopic surveys (Johnson et al., 2012; Koch et al., 2019; Lucey et al., 2019; Duong et al., 2019b).

It is important to note, however, that ∼25-50% of metal-poor stars in the bulge are actually halo interlopers (Kunder et al., 2020; Lucey et al., 2021). Therefore, it is unclear if these chemistry results simply apply to the Galactic halo in the inner Galaxy, to the Galactic bulge, or both. Consequently, dynamical analysis is essential to study these populations separately. Given results from simulations (Tumlinson, 2010), metal-poor stars on tightly bound orbits are expected to have formed as early as $z \sim 20$ while stars on loosely bound orbits only form as early as $z \sim$ 10-13. This is because stars on loosely bound orbits, which are accreted more recently, originate from small dark matter halos which form later than the most massive main progenitors (Tumlinson, 2010). This is consistent with recent simulation results demonstrating that the majority of stars within 2 kpc of the Galactic center formed in the most massive main progenitor of the MW (Santistevan et al., 2020b). Therefore, we expect stars confined to the inner bulge region are more ancient than loosely bound halo stars. However, it is essential to combine chemical and dynamical information to test this prediction and compare these populations in detail.

In this work, we aim to determine the origins of the metal-poor stars in the Galactic bulge through chemodynamial analysis. Specifically, we will test predictions from simulations that the metal-poor bulge stars are ancient and search for signatures of PISNe. To accomplish this, we present the stellar parameters and elemental abundances for a sample of 319 stars selected to be metal-poor bulge stars using SkyMapper photometry. We combine this analysis with dynamical results from the second installment of the COMBS survey (Lucey et al., 2021, hereafter COMBS II) for a full chemodynamical picture. In Section 6.2 we present the VLT/GIRAFFE observations and data reduction method. The stellar parameter and elemental abundance analysis are described in Sections 4.3 and 4.4, respectively. We perform a comparison between our analysis, the ARGOS survey and the HERBS survey in Section 4.5. We present our MDF and elemental abundance results in Sections 4.6 and 4.7. We separate our population into four dynamical groups and compare their chemistry in Section 4.8. We discuss chemical signatures of pair-instability supernovae in Section 4.9 and possible globular cluster origins for our stars in Section 4.10. Last, we present our final conclusions in Section 7.1.

4.2 Data

Given the high levels of extinction and primarily metal-rich population, obtaining large spectroscopic samples of metal-poor stars in the Galactic bulge has historically been difficult. With the advent of metallicity-sensitive photometric surveys, like the SkyMapper (Wolf et al., 2018) and Pristine (Starken-

burg et al., 2017b) surveys, it is now possible to target and observe these rare stars in large numbers. In this work, we use SkyMapper photometry and ARGOS spectra (Freeman et al., 2013) to select metal-poor giants for spectroscopic follow-up. For further information on the target selection, we refer the reader to Section 2 of COMBS I.

The observations presented in this work are from the FLAMES spectrograph (Pasquini et al., 2002) on the European Southern Observatory's (ESO) Very Large Telescope (VLT). The FLAMES instrument is fiber-fed with fibers going to both the UVES and GIRAFFE spectrographs. Therefore, observations with both spectrographs can be simultaneously obtained. For the COMBS survey, we observed 555 stars with the GIRAFFE spectrograph along with 40 stars with the UVES spectrograph. For the UVES spectra, we used the RED580 setup which has a resolution (R=$\lambda/\Delta\lambda \approx$ 47,000) and wavelength coverage 4726-6835 Å. The stellar parameters and elemental abundances of the UVES spectra have already been published in COMBS I. In this work, we present the stellar parameter and chemical abundance analysis of the GIRAFFE spectra.

4.2.1 Medium Resolution GIRAFFE Spectra

For the GIRAFFE spectra, we use the HR06 and HR21 setups. The HR06 setup has resolution R≈24,300 and wavelength coverage 4538-4759 Å, while the HR21 setup has resolution R≈18,000 and wavelength coverage 8484-9001 Å. The HR21 spectra contain the Calcium II near-infrared triplet (CaT),

which is useful for determining accurate radial velocities. The HR06 spectra contain many metal lines including iron (Fe) lines for constraining the metallicity and even a barium (Ba) line (4554 Å) in order to measure the s-process abundance. It also contains a number of C_2 Swan band features with band heads at approximately 4715 Å, 4722 Å, 4737 Å, and 4745 Å. Therefore, we can also determine if a star is a C-enhanced metal-poor (CEMP) star with or without s-process enhancement (CEMP-s or CEMP-no).

As these spectra were used to perform kinematic analysis in COMBS II, the full description of the reduction process can be found in Section 2.2 of that paper. In short, we use the EsoReflex[2] workflow to perform the bias and flat-field subtraction, along with fiber-to-fiber corrections, cosmic ray cleaning, wavelength calibration, and extraction. We then use IRAF to perform sky subtraction. Last, we use iSpec (Blanco-Cuaresma et al., 2014) to radial velocity (RV) correct, coadd and normalize the spectra. During the radial velocity determination, we find two possible spectroscopic binary stars (labeled as 6406.0 and 6400.2 in the ESO Phase 3 Data Products archive[3]) which both have two significant peaks (peak probability > 0.5) in the cross-correlation function. As unresolved spectroscopic binaries can lead to systematic biases in stellar parameters (e.g. El-Badry et al., 2018a), we do not perform stellar parameter analysis on these stars.

We estimate the signal-to-noise ratio (SNR) using the flux uncertainty

[2] `https://www.eso.org/sci/software/esoreflex/`
[3] `http://archive.eso.org/wdb/wdb/adp/phase3_spectral/form`

estimates from the EsoReflex pipeline which are propagated through the reduction process. We do not use any individual spectra with SNR < 10 pixel^{-1}. Out of 555, there are 545 stars with HR21 spectra with SNR > 10 pixel^{-1} and only 389 stars with both HR06 and HR21 spectra having SNR > 10 pixel^{-1}. It is expected that the HR06 spectra have lower SNR on average compared to the HR21 spectra since they are bluer and therefore more impacted by the high levels of extinction towards the Galactic center. In this work, we analyze only stars that have both HR06 and HR21 spectra for consistency. Therefore, after removing the two possible binary stars, there are a total of 387 stars for which we perform stellar parameter analysis.

4.3 Stellar Parameter Analysis

Given the wavelength coverage and resolution of our spectra, there are not enough clean Fe I and Fe II lines to perform the standard Fe-excitation-ionization balance technique to determine the stellar parameters. Therefore, in this work we use a full-spectrum χ^2 fitting technique to determine the effective temperature ($T_{\rm eff}$), surface gravity ($\log g$), metallicity ([M/H]), and rotational velocity ($V \sin i$).

The model spectra, which we use to compare to the observed spectra, are synthesized using Spectroscopy Made Easy (SME) v574 (Valenti & Piskunov, 1996; Piskunov & Valenti, 2017). To synthesize spectra, we utilize the 1D, local thermodynamic equilibrium (LTE) MARCS model atmosphere grid (Gustafsson et al., 2008) and the fifth version of the Gaia-ESO atomic

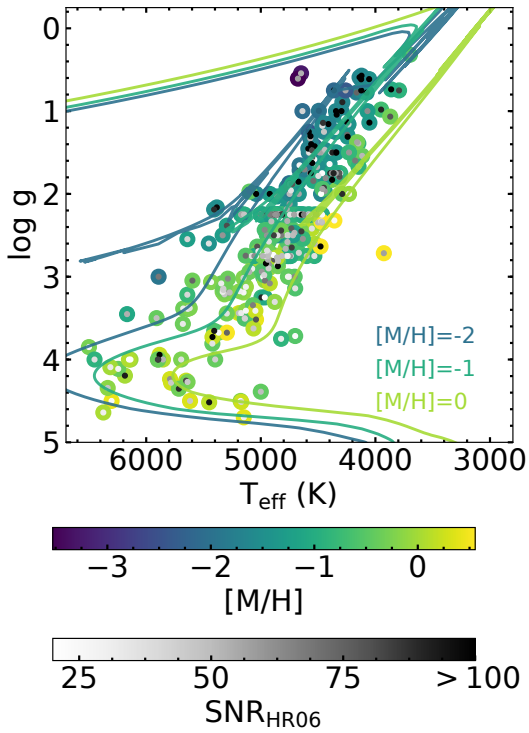

Figure 4.1: Kiel diagram for our sample of 319 stars for which we report stellar parameters and elemental abundances. The points are colored by SNR in the center and metallicity in the outer ring. We also plot 10 Gyr MIST isochrones with [M/H]=0, -1 and -2 dex in green, light blue and dark blue lines, respectively. These lines match the metallicity color scale. Our data are well represented by the models, with the exception of outliers which typically have low SNR.

line list which includes hyperfine structure (Heiter et al., 2020). In addition, we use solar abundances from Grevesse et al. (2007). We incorporate non-LTE (NLTE) line formation for a number of elements using grids of departure coefficients. We use all grids available with SME v574 which includes lithium (Li; Lind et al., 2009), oxygen (O; Amarsi et al., 2016), Na (Lind et al., 2011), magnesium (Mg; Osorio et al., 2015), Al (Nordlander & Lind, 2017), silicon (Si; Amarsi & Asplund, 2017), calcium (Ca; Mashonkina et al., 2008), titanium (Ti; Sitnova et al., 2020), Fe (Amarsi et al., 2016) and Ba (Mashonkina et al., 2008).

As we targeted stars in the bulge, which is over 5 kpc away from the Sun, we expect most of our stars to be giants with log $g < 3$ dex given that only giants would be sufficiently luminous to be observed at the bulge. However, the results from COMBS II indicate that our target selection has been contaminated by a number of nearby disk stars. Therefore, we require a synthetic grid with a wide range of possible parameters, including dwarf, giant, metal-rich, and metal-poor stars. Our grid covers the following range:

- 2500 K $\leq$ T_{eff} $\leq$ 6500 K, steps = 250 K
- -0.5 dex $\leq$ log $g \leq$ 5 dex, steps = 0.25 dex
- -5 dex $\leq$ [M/H] $\leq$ 0.75 dex, steps = 0.25 dex

We scale the microturbulence (v_{micro}) with T_{eff} using the relationship cali-

brated from the Gaia-ESO survey (Smiljanic et al., 2014):

$$\begin{aligned} v_{micro} =& 1.1 + 1.0 \times 10^{-4} \times (T_{eff} - 5500) \\ &+ 4.0 \times 10^{-7} \times (T_{eff} - 5500)^2 \end{aligned} \tag{4.1}$$

We also scale the global [α/Fe] with [M/H] as follows:

$$[\alpha/Fe] = \begin{cases} 0, & \text{if } [M/H] \geq 0 \\ -0.4 \times [M/H], & \text{if } -1 \leq [M/H] \leq 0 \\ 0.4, & \text{if } [M/H] < -1, \end{cases} \tag{4.2}$$

in order to match the model atmospheres as well as empirical MW chemical evolution.

Following Carroll (1933a,b), we add a convolution term to account for rotational (V sin i) and instrumental broadening. We allow this term to vary between 0 km s^{-1} $\leq$ V sin i $\leq$ 30 km s^{-1}. However, since we have two unique parts of our spectra (HR06 and HR21) which have different wavelength resolutions (R$\approx$24,300 and R$\approx$18,000, respectively) the convolution term must be different for each part. Therefore, we multiply the convolution term by 1.35 (the ratio of the resolutions) before applying it to the HR21 spectra. We attempt to fit the convolution terms for the HR21 and HR06 spectra separately, but the degeneracy between the effect of log g and convolution on the CaT is too strong. Therefore, we must use what we know about the convolution from the HR06 spectra to constrain the HR21 convolution. To interpolate between grid points, we use a piece wise linear interpolator.

In order to avoid getting stuck in a local minimum when performing the χ^2 fit, we ensure that we start with an accurate guess for the stellar

parameters. We do this by performing a quick cross-correlation with a grid of model spectra that is similar, but smaller than our grid for the χ^2 fit. This smaller grid covers the following range:

- 3500 K $\leq$ $T_{eff} \leq$ 6500 K, steps= 250 K
- 0.5 dex $\leq$ log $g \leq$ 4 dex, steps=0.5 dex
- -5 dex $\leq$ [M/H] $\leq$ 0.5 dex, steps=0.5 dex

There are many observational and modeling effects that may cause our model spectra to differ from the observed spectra in ways that can negatively impact the fit. For example, the cores of strong lines, like the CaT, are known to be strongly impacted by NLTE, even when using departure coefficients for population levels. Therefore, we mask pixels that are not well-matched by the model spectra in order to minimize their impact on the spectral fitting. To do this, we compare our model spectra to *Gaia* Benchmark stars (GBS; Blanco-Cuaresma et al., 2014). As these stars are observed in the Gaia-ESO survey (Gilmore et al., 2012), they have GIRAFFE HR21 spectra. However, they do not have HR06 spectra. Instead, we download reduced HARPS spectra (Mayor et al., 2003) from the ESO archive[4] and degrade the resolution and wavelength coverage to match that of HR06 spectra. We then compare the observed spectra to synthesized spectra of the corresponding parameters derived in Jofré et al. (2014); Heiter et al. (2015). We mask any pixels that differ from the

[4] `https://archive.eso.org/scienceportal/`

observed spectra by > 0.1 in normalized flux. As the ability of the synthesis to accurately reproduce each pixel of the observed spectra is a function of the stellar parameters, we make the masks using four different benchmark stars depending on the stellar parameters. Specifically, we use the initial guess parameters to chose between four different spectra: (1) for metal-poor giants (log g <2.5 dex and [M/H] $\leq$ -1.5 dex) we use HD 122563, (2) for metal-rich giants (log g < 2.5 dex and [M/H] > -1.5 dex) we use Arcturus, (3) for metal-poor sub-giants/dwarfs (log $g \geq$ 2.5 and [M/H] $\leq$ -1.5 dex) we use HD 140283, and (4) for metal-rich sub-giants/dwarfs (log $g\geq$ 2.5 dex and [M/H] > -1.5 dex) we use ϵ For.

In addition to the masking, we also use the difference between the observed benchmark spectra and the corresponding model spectra as an uncertainty term in our fit (σ_{synth}). Therefore, we essentially underweight pixels in the χ^2 fit that are not well reproduced by the model spectra. We add this term in quadrature with the flux uncertainties. We then use this combined uncertainty in the χ^2 fit.

Thus, the χ^2 equation which we minimize is:

$$\chi^2 = \sum \frac{(observed - model)^2}{(\sigma_{flux}^2 + \sigma_{synth}^2)} \tag{4.3}$$

where *observed* is the observed flux, *model* is the synthesis flux, σ_{flux} is the flux uncertainties and σ_{synth} is the synthesis uncertainty as described above. We use the Nelder-Mead algorithm to find the global minimum.

Of the 387 stars for which we attempt stellar parameter analysis, we

find a number of stars that we are unable to fit. Upon visual inspection, it is clear that one of these stars (899.0) is a CEMP-s star from the overwhelming C_2 Swan band features and strong Ba line absorption at 4554 Å. However, we do not report results for this star in this work, as it requires separate analysis and will be thoroughly studied in a future installment of the COMBS survey. We also find 2 stars (1386.0 and 1659.0) that may show C enhancement and are unable to be fit by our pipeline. Although we will attempt to analyze them in future work with 899.0, these stars are not obviously CEMP stars. In addition, we find 7 stars that continually give solutions at the edge of our grid, with T_{eff}=6500 K. We exclude these stars given that solutions at the edge of the grid are not trustworthy.

Upon visual inspection, we choose to only perform elemental abundance analysis for spectra with SNR $>$ 20 pixel^{-1}. Of the 377 stars with SNR $>$ 10 pixel^{-1} for which we have stellar parameter solutions, 344 have SNR $>$ 20 pixel^{-1}. Furthermore, 319 of these stars have a match in *Gaia* DR2 within 1 arcsecond and a *Gaia* DR2 renormalized unit weight error (ruwe) $<$1.4 (Lindegren, 2018). Therefore, only these 319 stars have measured dynamics from COMBS II. For the rest of this work, we focus on these 319 stars since combining the dynamical analysis with the measured chemistry is essential to the goal of this work.

We present a Kiel diagram of these 319 stars in Figure 4.1. The center of the points is colored by the SNR of the HR06 spectra. We also create rings around the points that are colored by the metallicity. Along with our

data, we also show 10 Gyr MIST isochrones with various metallicities (Dotter, 2016; Choi et al., 2016; Paxton et al., 2011, 2013, 2015). Our data are well represented by these models, which is consistent with MW bulge age estimates (Zoccali et al., 2003).

4.3.1 Stellar Parameter Uncertainties

In order to accurately evaluate the uncertainties on the stellar parameters, we must take into account the internal uncertainties, caused by noise in the data and biases in the fitting procedure, as well as the external uncertainties, caused by imperfections in the model spectra. To account for the internal uncertainties, we aim to evaluate the precision of our fitting procedure as a function of SNR. To do this, we run our fitting procedure on synthetic spectra with known stellar parameters and various SNRs. To create these spectra, we use the same synthesis method as was used to create the model spectra grid and we randomly select 100 sets of parameters where 3500 K $\leq$ T_{eff} $\leq$ 5500 K, 0.5 dex $\leq$ log g $\leq$ 4 dex and -5 dex $\leq$ [M/H] $\leq$ 0.5 dex. After synthesizing these 100 spectra with random parameters, we add synthetic Gaussian noise according to the desired SNR. As we aim to evaluate the precision of our method across the entire SNR range of our observed sample, we add noise in order to create spectra with 10 pixel^{-1} $\leq$ SNR $\leq$ 250 pixel^{-1} in steps of 10 pixel^{-1}. We do this for each of our 100 synthetic spectra with random parameters, resulting in a total of 2,500 spectra with varying parameters and SNRs with which we can evaluate our precision.

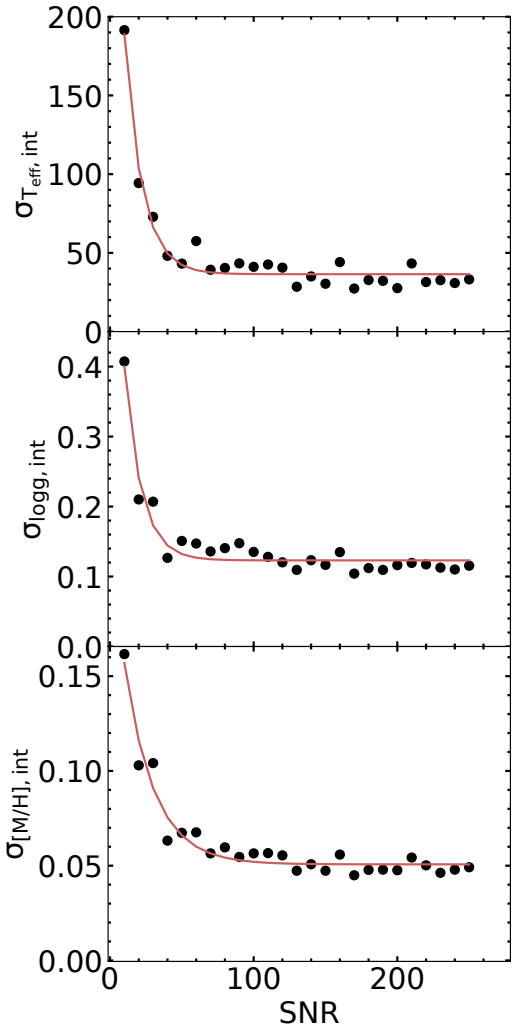

Figure 4.2: The estimates of the internal uncertainty for $T_{\rm eff}$, log g, and [M/H] as a function of SNR. The black points represent the standard deviations of the differences between the derived and synthesized parameters for 100 random synthetic spectra as a function of the SNR. The red lines are the best fit exponentially decreasing functions which are then used to determine the internal uncertainty estimates for our observed data.

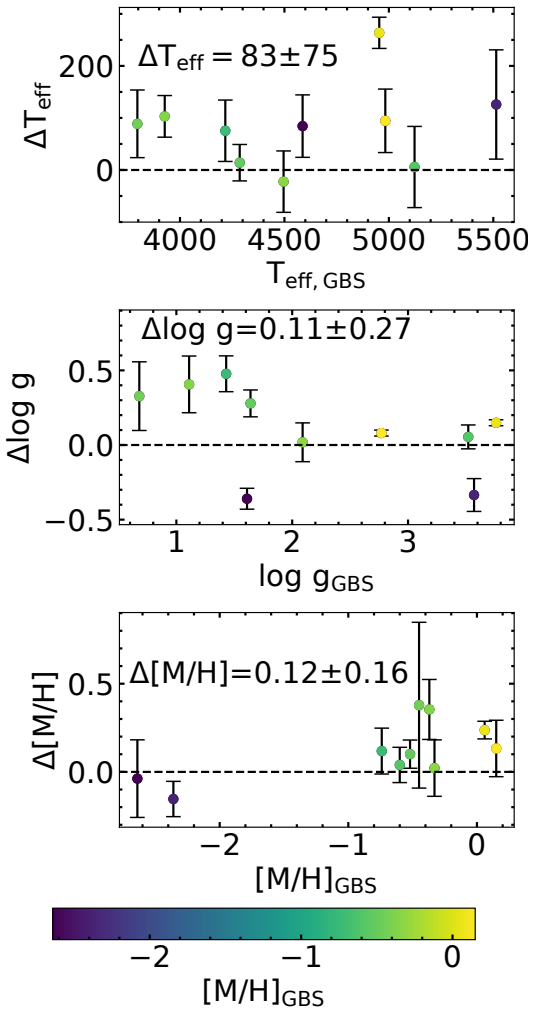

Figure 4.3: The differences between our derived values and the reference values from Heiter et al. (2015) and Jofré et al. (2014) for 10 *Gaia* Benchmark stars (GBS). The differences are (this work – GBS). The points are colored by the reference metallicity. The error bars shown are for the reference values. We also provided the mean and standard deviation of the differences for each parameter in the black text. The standard deviation of the differences is used as our external uncertainty estimate for the given parameter.

We put each of the 2,500 synthetic spectra through our parameter analysis pipeline and compare the derived parameters to the true values. For every 100 spectra with the same SNR, we take the standard deviation of the differences between the derived and true values. We use this value as our estimate for the internal precision at that SNR. Therefore, we have internal precision estimates for 25 different SNR values.

We show the calculated internal precision for a range of SNRs in Figure 4.2. We fit exponentially decreasing functions to estimate the precision, or internal uncertainty, as a function of SNR. We find the internal uncertainties are best described as:

$$\sigma_{T_{eff},int} = 345 \text{ K } e^{-0.082 \times SNR} + 36 \text{ K} \tag{4.4}$$

$$\sigma_{logg,int} = 0.653 e^{-0.086 \times SNR} + 0.123 \tag{4.5}$$

$$\sigma_{[M/H],int} = 0.173 e^{-0.049 \times SNR} + 0.051 \tag{4.6}$$

Therefore, we can use these equations to evaluate the $T_{\rm eff}$, log g and [M/H] internal uncertainties for each of our stars. Specifically, we calculate the internal uncertainties using the SNR estimates for the HR06 spectra which are always lower than the SNR estimates for the HR21 spectra. Given that the SNR was the same for both HR06 and HR21 in our synthetic analysis, we may be slightly overestimating our uncertainties since the HR21 spectra will have higher SNR in our observations.

To evaluate the external uncertainties, we use a sample of 10 *Gaia* Benchmark giant and subgiant stars. These stars are common calibration

stars that are frequently used to evaluate the accuracy and precision of stellar parameter pipelines (e.g., Smiljanic et al., 2014; Buder et al., 2018; Duong et al., 2019a). They are especially useful to compare to spectroscopically-derived parameters since their reference T_{eff} and log g values are determined independently from their spectra. Specifically, the bolometric flux and angular diameter are used to determine the T_{eff}. The log g is then determined using the angular diameter and mass estimate.

In Figure 4.3, we show the comparison of our results to the reference values for 10 GBS. We color each point by metallicity in order to track the impact of metallicity on the T_{eff} and log g determination. The differences on the y-axis are (this work – GBS). For T_{eff}, we find a mean bias of 83 K with a standard deviation of 75 K. For log g, we find a bias of 0.11 dex with a standard deviation of 0.27 dex. Lastly, for [M/H], we find a bias of 0.12 dex with a standard deviation of 0.16 dex. However, it is important to note that we are comparing our global metallicity value to their metallicity derived from only Fe lines, which may introduce some bias as a function of [M/H]. Overall, these results are comparable to the HERBS survey which has a similar sample and analysis method as this work (see Figure A1 in Duong et al., 2019a).

We use the derived standard deviations of the differences for T_{eff}, log g, and [M/H] as our external uncertainty estimates. Our overall uncertainty estimate is calculated by adding the internal and external uncertainty estimates in quadrature. The external uncertainty is larger than the internal uncertainty for T_{eff}, log g and [M/H] at high SNR (SNR $\gtrsim$ 100 pixel^{-1}). Therefore, the

external uncertainty dominates our stellar parameter uncertainties for stars with SNR $\gtrsim$ 100 pixel^{-1} and the internal uncertainty only becomes important at SNR $\lesssim$ 50 pixel^{-1}.

4.4 Elemental Abundance Analysis

Once the stellar parameters are determined, we perform a line-by-line χ^2 fit to determine the individual elemental abundances. For each line, we compute synthetic spectra using the same method as in the stellar parameter analysis, including all of the same NLTE departure coefficient grids. Specifically, we compute five different spectra with [X/Fe] = (-0.6, -0.3, 0.0, 0.3, 0.6) dex. If the derived solution is [X/Fe]=0.6 dex or -0.6 dex, we repeat the analysis but add or subtract 1 dex from the synthesized [X/H] values. We use the derivatives of the spectrum with respect to the elemental abundance to determine the pixel selection. Explicitly, going out from the line core, we include all pixels until the derivative changes sign or becomes < 0.01 dex^{-1}. However, we also force the minimum line window to be 0.2 Å wide and the maximum line window to be 10 Å wide. This method is similar to what is applied in other spectroscopic codes (e.g. the BACCHUS code; Masseron et al., 2016; Hawkins et al., 2015).

As the strength of absorption features is strongly dependent on the metallicity, we find that it is necessary to use a metallicity-dependent line selection to avoid weak, blended, or saturated lines across our entire metallicity range. Specifically, we have a very metal-poor ([M/H]$\leq$-2.0 dex), metal-poor (-

2.0 dex < [M/H] ≤ -0.5 dex) and metal-rich ([M/H] > -0.5 dex) line selection. However, we include many of the same lines between the selections to ensure continuity.

Although we report the abundance derived from each individual line, we use the mean of the lines as our final [X/H] value. We report elemental abundances for C, Na, Mg, Al, Si, Ca, Ti, chromium (Cr), Mn, Fe, zinc (Zn), Ba, and cerium (Ce). Of those, the only elements for which we do *not* use NLTE departure coefficient grids are C, Cr, Mn, Zn, and Ce. We note that the NLTE effects of Cr and Mn are important when we constrain the enrichment source from the abundance pattern, in particular for low-α stars (Kobayashi et al., 2014).

For each atomic line, we determine an associated uncertainty for the derived abundance based on the χ^2 fit. The uncertainty is the distance in abundance space from the minimum χ^2 to where the reduced χ^2 equals the minimum χ^2 plus one (e.g., FERRE[5] code; Allende Prieto, 2004; Allende Prieto et al., 2006, 2008a, 2009). After visual inspection of 50 stars with varying SNR, we find that an individual line abundance uncertainty $\gtrsim$ 0.25 dex tends to indicate an untrustworthy fit and requires further visual inspection to determine if the line fit should be discarded. We also inspect stars whose line-by-line scatter in the abundance is $\gtrsim$ 0.25 dex. For our final abundance uncertainties, we propagate the individual line-by-line abundance uncertain-

[5]Available from `http://hebe.as.utexas.edu/ferre`

ties through the mean. The result is the individual line-by-line uncertainties added in quadrature and then divided by the number of lines used.

4.5 Comparison with ARGOS and HERBS Surveys

In order to test the accuracy and precision of our stellar parameters, we compare them to other large Galactic bulge surveys. Specifically, we compare to the ARGOS survey which uses R$\sim$11,000 spectra of $\sim$28,000 stars (Freeman et al., 2013). This survey measured the RV, $T_{\rm eff}$, log g, [Fe/H], and [α/Fe] ratio of their program stars. Our work has 26 stars in common with the ARGOS survey. In addition, we also compare to the HERBS survey which uses R$\sim$28,000 spectra of 832 stars (Duong et al., 2019a,b). However, we only observed 3 stars in common with the HERBS survey, which is not enough for a thorough comparison. Fortunately, the HERBS survey performs a detailed comparison with the ARGOS survey. Therefore, we can compare to the HERBS survey through a comparison with the ARGOS survey.

In Figure 4.4, we show the comparison between our derived stellar parameters and the values from the ARGOS survey. The differences shown are (this work – ARGOS). The points are colored by the ARGOS-derived metallicity. The error bars are the uncertainties on our derived parameters. In the bottom panel, we compare the ARGOS metallicity to our [Fe/H] value derived from Fe lines, rather than the global [M/H] derived during the stellar parameter analysis. However, we have also performed the comparison using the global [M/H] and found the results to be similar to [Fe/H]. We find that

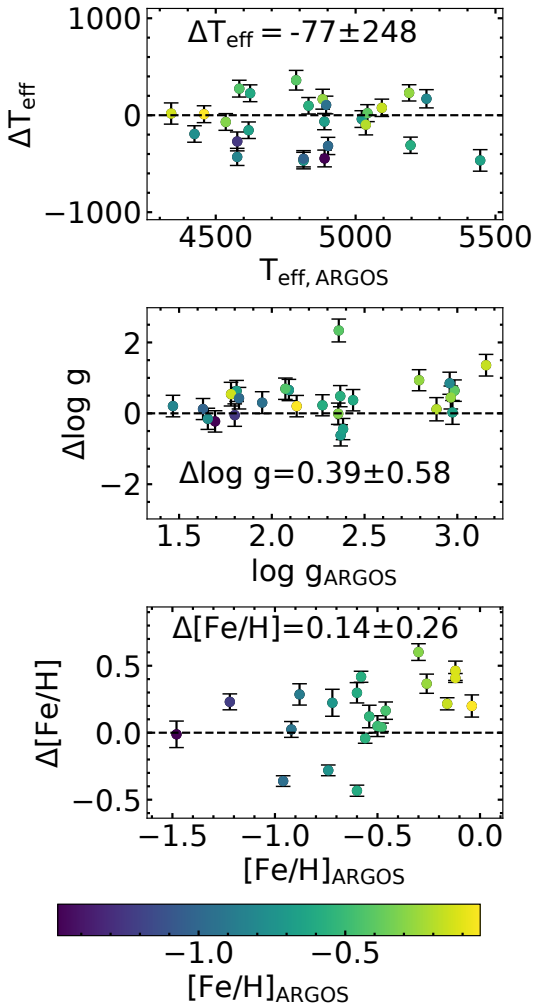

Figure 4.4: Comparison of the derived stellar parameters compared to results from the ARGOS survey (Freeman et al., 2013) for 26 stars in common. The differences shown are (this work - ARGOS). The points are colored by the [Fe/H] from the ARGOS survey to ensure there are no trends in accuracy and precision of the stellar parameters with [Fe/H]. The error bars are the uncertainties for our derived parameters. The text gives the mean and standard deviations of the differences for each stellar parameter.

the mean difference in T_{eff} is -77 K with a standard deviation of 248 K. The mean difference in log g is 0.39 dex with a standard deviation of 0.58 dex, while the mean difference in [Fe/H] is 0.14 dex with a standard deviation of 0.26 dex.

When comparing to the ARGOS survey, the HERBS survey reports the median, 1σ and standard deviation (after excluding 3σ outliers) of the differences between derived stellar parameters (Duong et al., 2019a). They find a median difference in T_{eff} of -64 K, which is consistent with our value of -77 K. However our 1σ value (246 K), which is also very similar to our standard deviation before (248 K) and after excluding 3σ outliers (248 K), is significantly larger than the value reported by the HERBS survey (117 K). We expect that this difference is largely due to the different metallicity distribution of our sample. As the ARGOS survey derives the T_{eff} using the photometric colors, it is reasonable to assume that their T_{eff} precision would be metallicity-dependent, given that metallicity also impacts the photometric colors. Specifically, it is possible that the ARGOS survey may have worse T_{eff} precision for metal-poor stars. In fact, Freeman et al. (2013) notes that using different empirical T_{eff} - colour calibrations lead to differences in T_{eff} estimates up to 200 K for metal-poor stars (Bessell et al., 1998; Alonso et al., 1999). Given that our survey is significantly more metal-poor than the HERBS survey, we would therefore expect the ARGOS precision to be worse for our sample than the HERBS sample. Furthermore, we note that for the 3 stars we have in common with the HERBS survey we find the standard deviation for

the differences in T_{eff} between our values and the HERBS values is 168 K. In addition, it is interesting to note that when comparing APOGEE DR16 stellar parameters (Ahumada et al., 2020) to ARGOS, Wylie et al. (2021) find the differences in T_{eff} have a standard deviation of 321 K, which is significantly larger than our value of 248 K.

For log g, we find that our results are very consistent with the HERBS survey. Specifically, our median difference is 0.39 dex while the HERBS survey reports a median difference of 0.29 dex. The 1σ difference for our work is 0.30 dex while the HERBS survey finds a 1σ of 0.29 dex. Last, the standard deviation we find after removing 3σ outliers is 0.34 dex, while the HERBS survey reports 0.38 dex. These results indicate that our stellar parameter analysis is consistent with the results from the HERBS survey.

Last, for [Fe/H], we find a median difference of 0.20 dex between our [Fe/H] and the values from ARGOS, while the HERBS survey reports a value of 0.04 dex. From Figure 4.4, it is clear that our large bias is mostly due to our [Fe/H] being significantly larger than the ARGOS values for stars with [Fe/H] $>$ -0.5 dex in ARGOS. We note that the median offset between our [Fe/H] results and the HERBS survey for the 3 stars in common is 0.03 dex. It is also important to note that these 3 stars have -0.7 dex $<$[Fe/H]$_{\rm HERBS}$ $<$-0.3 dex, which is the same range where we are most inconsistent with ARGOS. We find that our spread in [Fe/H] differences with ARGOS is similar to the differences reported in the HERBS survey. Specifically, we find a 1σ of 0.17 dex while HERBS reports a 1σ of 0.14 dex. After removing 3σ outliers, we

find a standard deviation of 0.17 dex. While using the same method, HERBS finds a standard deviation of 0.16 dex. Therefore, we find our stellar parameter results to be generally consistent with the HERBS survey.

4.6 Metallicity Distribution Function

The MDF of the Galactic bulge is well-studied through photometric and spectroscopic surveys and is primarily composed of a metal-rich population with [Fe/H] > -1 dex (Zoccali et al., 2008; Ness et al., 2013a; Johnson et al., 2013a; Zoccali et al., 2017; Bensby et al., 2013; Rojas-Arriagada et al., 2014b; Bensby et al., 2017; Rojas-Arriagada et al., 2017; García Pérez et al., 2018; Duong et al., 2019a; Rojas-Arriagada et al., 2020; Johnson et al., 2020). In this work, we have used SkyMapper photometry to target the metal-poor tail of the Galactic bulge MDF. Therefore, we expect our sample to have an MDF that is on the metal-poor end with [Fe/H] < -1 dex.

In COMBS II, metallicity estimates were determined from the CaT using the same spectra presented in this work. In Figure 4.5, we show a comparison between the results presented in COMBS II and the [M/H] results determined in the stellar parameter analysis of this work. For this figure, we only show results for stars with $\log g \leq 3$ dex as our CaT method was designed to be applied to giant stars similar to previous work on metallicity estimates from the CaT (Armandroff & Zinn, 1988; Olszewski et al., 1991; Armandroff & Da Costa, 1991; Cole et al., 2004; Battaglia et al., 2008; Starkenburg et al., 2010; Li et al., 2017). The error bars shown are those derived for the [M/H]

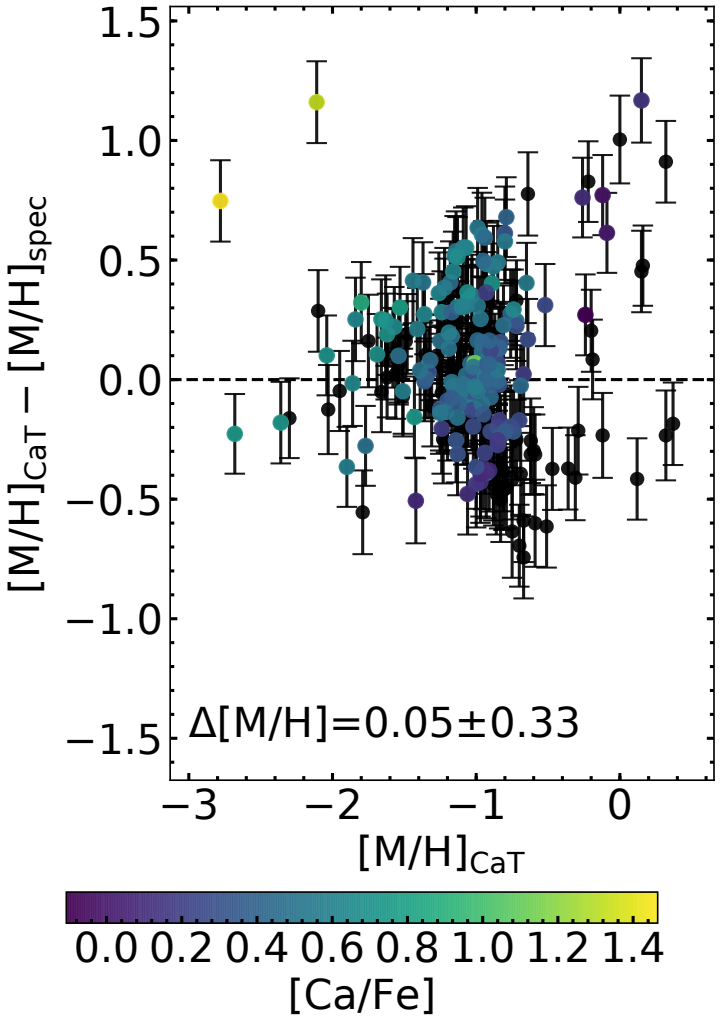

Figure 4.5: Comparison between metallicity estimates from the CaT presented in COMBS II to the [M/H] results presented in this work. The points are colored by the [Ca/Fe] abundance when available. The error bars shown are the uncertainty estimates on [M/H] from this work. The black text shows the bias, or mean difference, (0.05 dex) and the standard deviation of the differences (0.33 dex).

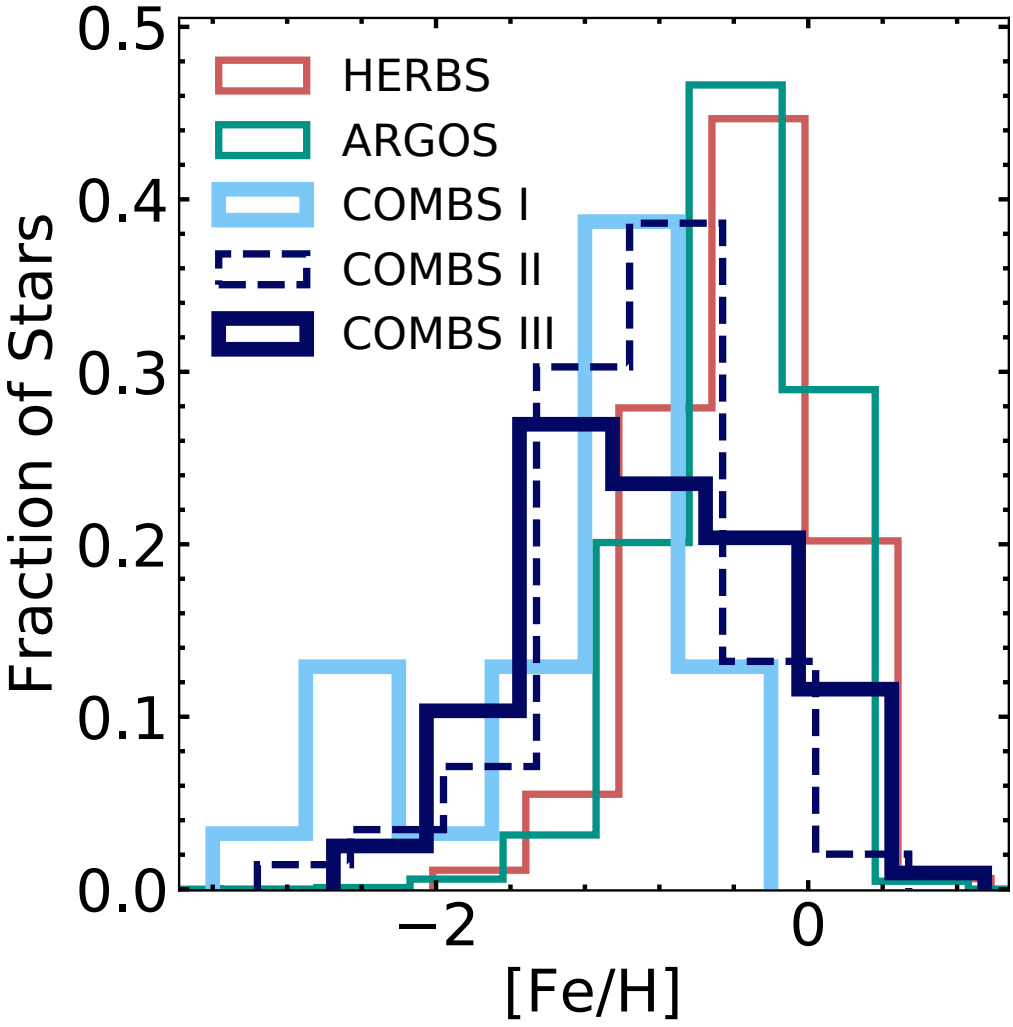

Figure 4.6: The metallicity distribution function (MDF) for our results (dark blue solid line), compared to results from COMBS II (dark blue dashed line), COMBS I (light blue solid line), ARGOS (green solid line; Freeman et al., 2013; Ness et al., 2013a), and HERBS (red solid line; Duong et al., 2019a). Our MDF is more metal-poor than surveys that did not target metal-poor stars (ARGOS and Bensby et al., 2017). Therefore, our selection of metal-poor stars with SkyMapper photometry was successful.

value in this work. We color the points by the [Ca/Fe] abundance. The metallicity estimates from COMBS II are generally consistent with the [M/H] results from this work, with only a 0.05 dex bias. the standard deviation of the differences is 0.33 dex which is only slightly larger than the uncertainty on the metallicity estimates from the CaT (0.22 dex) added in quadrature with the mean [M/H] uncertainty in this work (0.17 dex).

We present the MDF of our sample in Figure 4.6 using the derived [Fe/H] abundances (dark blue solid line). We also show the results from COMBS II (dark blue dashed line), COMBS I (light blue solid line), the ARGOS survey (green solid line; Freeman et al., 2013; Ness et al., 2013a) and the HERBS survey (red solid line; Duong et al., 2019a). Our MDF peaks at [Fe/H] $\approx$ -1 dex, while the results for the surveys which did not target metal-poor stars (ARGOS and HERBS) peak at [Fe/H] $\gtrsim$ -0.5 dex. Therefore, our use of SkyMapper photometry to select metal-poor stars was successful. However, we have relatively fewer stars with [Fe/H] <-2 dex compared to COMBS I. This is expected, given that the most promising metal-poor targets were prioritized for the high-resolution UVES spectra which were presented in COMBS I. Compared to COMBS II, we see a stronger metal-rich tail which broadens the MDF. This was likely missed in COMBS II because the [Ca/Fe] ratio decreases at [Fe/H] > -1 dex. This causes a smaller increase in [Ca/H] for a given increase in [Fe/H]. Therefore, [Fe/H] values estimated from Ca lines would be underestimated in this [Fe/H] range.

4.7 Elemental Abundance Results

The chemical abundances of stars provide unique insight into the formation and evolution of stellar populations. However, in order to interpret the abundances, we need to contextualize our results in terms of other stellar populations and nucleosynthetic pathways. In this section, we present our abundance results and discuss the formation mechanisms for each element. We also compare our results with other MW populations and literature samples.

4.7.1 C

C is primarily produced in massive stars ($> 10M_{\odot}$) and low-mass asymptotic giant branch (AGB) stars. The [C/Fe] yield is especially increased in low-mass stars where the Fe yield is essentially zero (Kobayashi et al., 2011a). In addition, high levels of C-enhancement ([C/Fe] >1 dex) among metal-poor stars is thought to come from Population III supernovae, specifically faint supernovae (e.g., Nomoto et al., 2013).

In this work, we measure elemental C abundances from the atomic line at 8727 Å. However, in stars with [Fe/H] <-2 dex, we find that this line is too weak to measure an accurate abundance from. Furthermore, as stars move up the red giant branch (RGB), they experience the second dredge-up which depletes the photospheric C abundance. To account for this depletion, we apply a correction factor to our derived C abundances. These correction factors come from Placco et al. (2014) and are a function of the log g, [Fe/H] and uncorrected [C/Fe] ratio. We show the corrected abundances in Figure

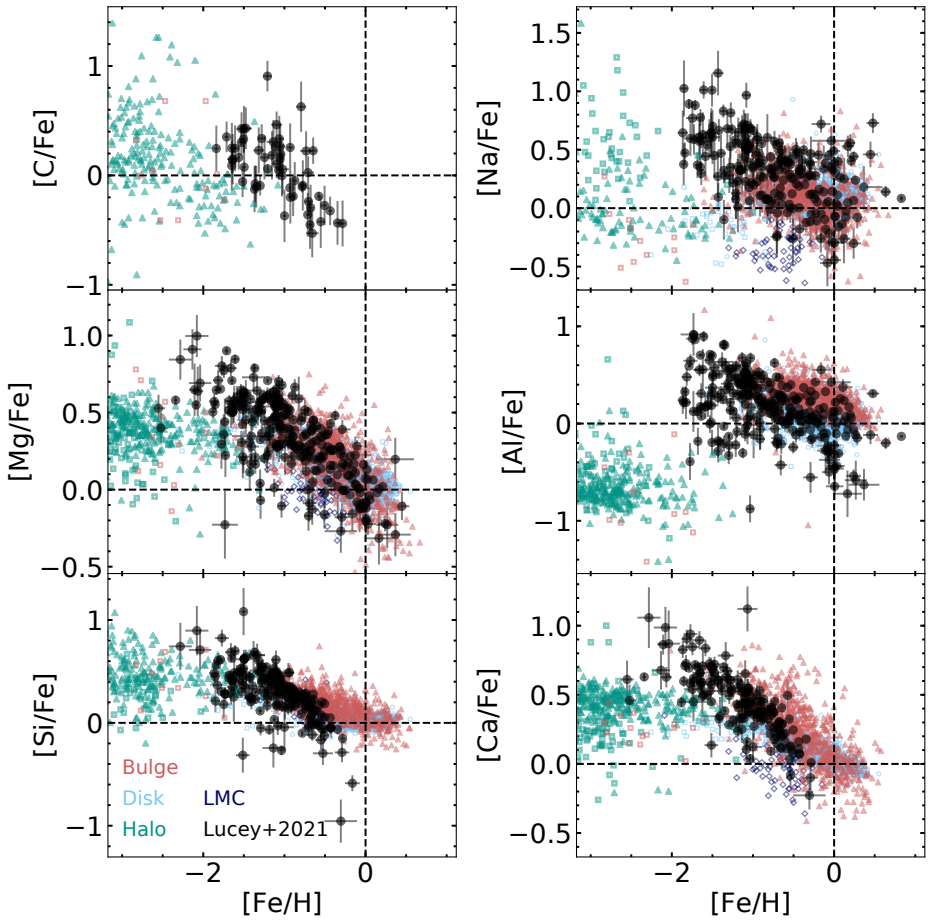

Figure 4.7: Light and α-element abundances for all of the stars in our sample (black circles) compared to other Milky Way samples from the literature. Specifically, we show other Milky Way bulge samples in red, including results from the HERBS survey (red open triangles; Duong et al., 2019a,b) and results from the EMBLA survey (red open squares; Howes et al., 2016). Also shown are abundances for the halo (green), the Large Magellanic Cloud (LMC; dark blue), and the disk (light blue). The halo abundances are from Roederer et al. (2014, green triangles) and Yong et al. (2013, green open squares). The LMC abundances are from Van der Swaelmen et al. (2013, dark blue open diamonds). The disk abundances are from Bensby et al. (2014, light blue open squares), Adibekyan et al. (2012, light blue open circles), and Battistini & Bensby (2015, light blue open diamonds).

4.7. We note that the shown literature abundances from Roederer et al. (2014) and Howes et al. (2016) have not been corrected.

At [Fe/H] $\gtrsim$ -1 dex, the [C/Fe] ratio decreases with increasing [Fe/H]. This is consistent with chemical evolution models and the onset of Type Ia Supernovae (SNe Ia) which overproduce Fe with respect to C. At [Fe/H] $\lesssim$ -1 dex, generally [C/Fe] >0 dex. In order to reach this level of C enhancement, it is likely that inhomogenous mixing needs to be taken into account which allows AGB stars to contribute C yields at [Fe/H] $\lesssim$ -1.5 dex (Kobayashi et al., 2014; Vincenzo & Kobayashi, 2018).

4.7.2 α-elements

The α-elements are generally divided into two categories based on their formation site. Specifically, the hydrostatic α-elements (Mg) primarily form in the hydrostatic burning phase of massive stars, while the explosive α-elements (Ca and Si) are primarily produced through explosive nucleosynthesis of core-collapse, or Type II, supernovae (SNe II; Woosley & Weaver, 1995; Woosley et al., 2002). Specifically, Mg is produced from C and neon (Ne) burning, while Si and Ca are primarily synthesized from explosive O burning. Thus the yields of explosive α-elements depend on the explosion energy (Kobayashi et al., 2006). Although they have different formation sites, the hydrostatic and explosive elements tend to trace each other as they are usually mixed during supernova explosions and dispersed into the interstellar medium (ISM). At low metallicities, before the onset of SNe Ia, the α-element abundances are

generally indicative of the initial mass function (IMF) of the enriching stellar population, given that their yields in SNe II are mass-dependent. On the other hand, SNe Ia overproduce Fe with respect to the α-elements and cause the [α/Fe] ratio to decrease. Therefore, the [Fe/H] value at which the [α/Fe] ratio begins to decrease specifies the amount of Fe built up by SNe II before the onset of SNe Ia. Furthermore, the behavior of the [α/Fe] ratio as a function of [Fe/H] is indicative of the star formation timescale, where a short star formation timescale leads to a large build-up of Fe in the ISM before the onset of SNe Ia.

4.7.2.1 Mg

Mg abundances at [Fe/H] $\gtrsim$ -1 dex are slightly higher in the bulge than in the disk (McWilliam & Rich, 1994; Rich & McWilliam, 2000; McWilliam & Rich, 2004; Fulbright et al., 2007; Johnson et al., 2014; Gonzalez et al., 2015; Bensby et al., 2017; Duong et al., 2019a). This is consistent with a shorter star formation timescale causing a larger build-up of Fe and Mg from SNe II before the contribution from SNe Ia begins. As shown in Figure 4.7, our results are consistent with the literature at [Fe/H] $\geq$ -1 dex.

At [Fe/H] $\lesssim$ -1 dex, our abundance measurements generally continue to show high levels of Mg enhancement. Specifically, when compared to the EMBLA survey (Howes et al., 2015), our Mg abundances are generally higher. Furthermore, the Mg abundances reported by the EMBLA survey appear to be more consistent with a Galactic halo population, while our Mg abundances

are higher than results from the halo (Roederer et al., 2014; Yong et al., 2013). However, it is difficult to draw strong conclusions here because there may be systematic offsets between surveys that impact the comparative results.

4.7.2.2 Ca and Si

Measurements of Ca and Si abundances in the bulge at [Fe/H] $\gtrsim$ -1 dex are generally higher than what is found in the disk (McWilliam & Rich, 1994; Rich & McWilliam, 2000; McWilliam & Rich, 2004; Fulbright et al., 2007; Johnson et al., 2014; Bensby et al., 2017; Duong et al., 2019a). However, our abundances at [Fe/H] $\gtrsim$ -1 dex are slightly lower than literature values for the bulge. This is likely a systematic effect possible from our photometric targeting method, or offsets between surveys resulting from differences in analysis methods.

We measure high levels of Ca and Si enhancement at [Fe/H] $\lesssim$ -1 dex. Similar to Mg, we find that our Ca and Si abundances are generally higher than what has been observed in the bulge by the EMBLA survey (Howes et al., 2015) and in the halo (Yong et al., 2013; Roederer et al., 2014). Our Ca abundances are especially high. This is interesting given that many Population III stars are thought to explode as PISNe which are theorized to have high Ca yields with [Ca/Fe] as high as 2 dex. However, high [Ca/Fe] itself does not suggest PISNe since faint SNe give high [(Mg,Si,Ca)/Fe] as well. We discuss further signatures of PISNe, including the discriminatory [Ca/Mg] ratio, in Section 4.9.

4.7.3 Odd-Z elements

The odd-Z elements are light elements that have an odd atomic number and therefore could not be produced by successive addition of α particles. In this work, we measure Na and Al. The yields of Na and Al from SNe II are metallicity-dependent, with higher yields from more metal-rich stars (Kobayashi et al., 2006). This leads to an increase in the [(Na,Al)/Fe] ratio with increasing [Fe/H]. However, Fe is overproduced relative to Na and Al in SNe Ia which causes the [(Na,Al)/Fe] ratio to decrease as these types of explosions become relevant.

4.7.3.1 Na

At [Fe/H] $\gtrsim$ -1 dex, the bulge and disk show similar trends in [Na/Fe] (Bensby et al., 2017; Duong et al., 2019b). Consistent with our observations, the [Na/Fe] ratio decreases with metallicity indicating contributions from SNe Ia, similar to the behaviour of α elements. At [Fe/H] $\lesssim$ -1 dex, we generally measure [Na/Fe] >0 dex, while the results from the EMBLA survey generally have [Na/Fe] <0 dex (Howes et al., 2015). The results from Yong et al. (2013) in the halo show high levels of [Na/Fe]. However, when they take NLTE into account, their results approach [Na/Fe] $\approx$ 0 dex, similar to Roederer et al. (2014). Our results already take NLTE into account and use the same NLTE corrections as Roederer et al. (2014) and Howes et al. (2015). Therefore, it is unlikely that our higher [Na/Fe] abundances, with respect to halo observations, are merely a NLTE effect. However, it is possible that differences in analysis

methods (e.g., line lists, model atmospheres, etc.) causes systematic offsets between ours and other survey's abundances.

Assuming systematic offsets do not entirely account for the higher [Na/Fe] ratio we measure in the bulge compared to the Galactic halo population, we can infer some of the differences in their chemical evolution histories. Given the metallicity dependence of Na yields from SNe II, where more metal-rich stars have higher yields, our stars must have been enriched by a more metal-rich population than stars of similar metallicity in the Galactic halo. Therefore, our results indicate a short star formation timescale, and rapid enrichment consistent with chemical evolution models for the bulge (e.g., Kobayashi & Nakasato, 2011). However, it is important to note that the Na lines used (4668.6 Å and 4751.8 Å) are too weak to measure low Na abundances for metal-poor stars. Therefore, it is possible that our lack of stars with [Na/Fe] <0 dex at low metallicity is a measurement effect.

4.7.3.2 Al

Al abundances in the bulge are typically higher than in the disk at [Fe/H]$\gtrsim$-1 dex (Bensby et al., 2017; Duong et al., 2019b). However, our [Al/Fe] abundances are generally consistent with the disk at [Fe/H] $\gtrsim$ -1 dex, although they show large scatter. At [Fe/H] $\lesssim$ -1 dex, our reported [Al/Fe] abundances continue to show a large scatter. However, they are generally higher than abundances from the EMBLA survey (Howes et al., 2015) and the Galactic halo (Roederer et al., 2014; Yong et al., 2013). Unlike our abundances, Howes

et al. (2015); Yong et al. (2013); Roederer et al. (2014) do not perform NLTE line corrections, which may account for some of the offset at low metallicity. Similar to the Na abundances, the Al abundances are consistent with a short star formation timescale and rapid chemical evolution.

The high scatter in the Al abundances may indicate inhomogeneous mixing or multiple populations. We note that the standard deviation of our [Al/Fe] abundances is $\sim$0.51 dex while the mean uncertainty is $\sim$ 0.07 dex. Therefore, it is unlikely that the observed scatter is merely due to uncertainties in the abundances. Interestingly, large Al enhancement is a signature of second-generation globular cluster stars. This signature has been identified in a couple of stars in this work and will be further discussed in Section 4.10.

4.7.4 Fe-peak elements

The Fe-peak elements, although formed in a variety of ways, generally trace the Fe abundance with only small variations (Iwamoto et al., 1999; Kobayashi et al., 2006; Nomoto et al., 2013). However, these slight variations can be extremely informative for supernova physics and chemical evolution models (Kobayashi & Nakasato, 2011). Of the Fe-peak elements, we measure Ti, Cr, Mn, and Zn. We show these results in Figure 4.8 compared to other MW populations from the literature.

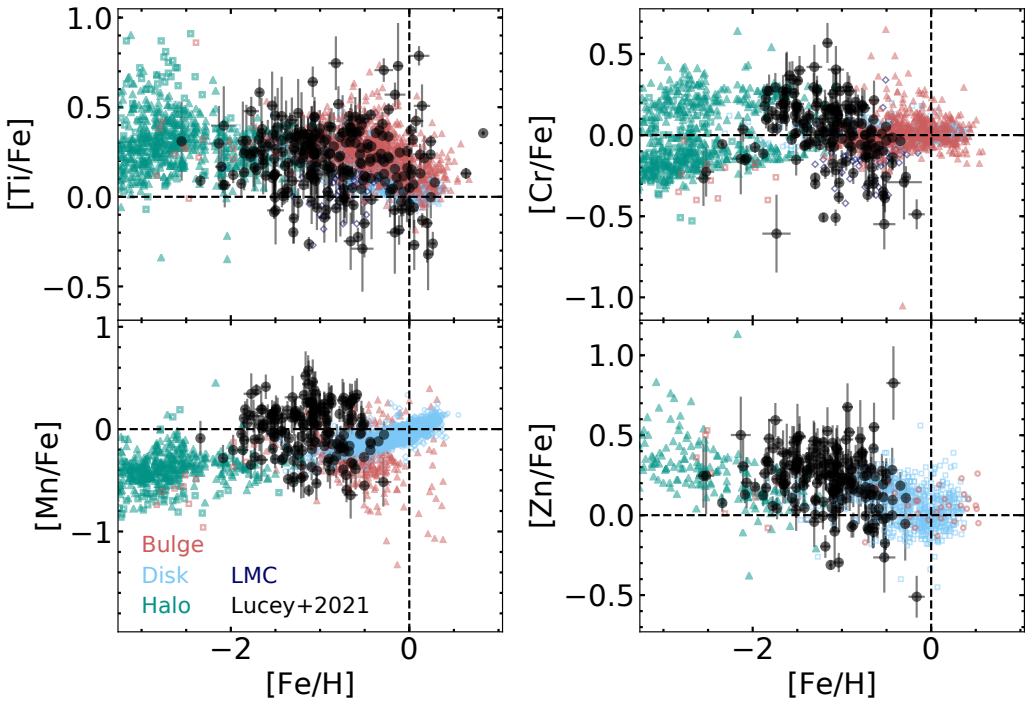

Figure 4.8: Abundance ratios as a function of metallicity for the Fe-peak elements (Ti, Cr, Mn, and Zn). Symbols are the same as in Figure 4.7. However, we also include Zn abundances from Bensby et al. (2017, red open circles).

4.7.4.1 Ti

Frequently considered an α-element, Ti is similarly overproduced in SNe II and underproduced in SNe Ia with respect to Fe. Therefore, it is expected to behave similarly to the α-elements. In the bulge, the [Ti/Fe] ratio is generally higher than the disk at [Fe/H] $\gtrsim$ -1 dex (Bensby et al., 2017; Duong et al., 2019a). Our abundances, however, show a large scatter even at high metallicity, with some stars matching the low Ti abundances observed in the Large Magellanic Cloud (LMC; Van der Swaelmen et al., 2013). This is difficult to draw strong conclusions from given that our analysis uses NLTE while the other bulge surveys do not (Bensby et al., 2017; Duong et al., 2019a). Nonetheless, this result suggests that our sample is a mixed stellar population with a variety of origins.

4.7.4.2 Cr

Cr abundances in the bulge and disk closely follow the Fe abundance (Bensby et al., 2014, 2017; Duong et al., 2019b). This is mostly true for our sample at [Fe/H] $\gtrsim$ -1 dex, although we observe large scatter and an over-abundance of stars with [Cr/Fe] <0 dex. Interestingly, we observe a number of stars with [Cr/Fe] abundance ratios similar to the LMC (Van der Swaelmen et al., 2013). At [Fe/H] $\lesssim$ -1 dex, the [Cr/Fe] ratio decreases with decreasing metallicity similar to results from the EMBLA survey (Howes et al., 2015). It is interesting to note that low [Cr/Fe] is inconsistent with chemical enrichment from PISNe.

4.7.4.3 Mn

Mn has a metallicity-dependent yield in SNe II. In general, it is thought to be underproduced with respect to Fe in SNe II and overproduced in SNe Ia. Therefore, at [Fe/H] $\gtrsim$ -1 dex in the MW [Mn/Fe] increases. This trend is observed in the disk, as shown in Figure 4.8. However, this is not observed in our sample or the sample from the HERBS survey (Duong et al., 2019b). Both of these bulge samples show high scatter that is generally centered at [Mn/Fe] $\approx$ 0 dex, although the number of stars with [Mn/Fe] $<$ 0 dex increases with increasing [Fe/H]. This result is interesting and likely indicates inhomogeneous mixing of the ISM or that the bulge is made up of multiple stellar populations with different chemical evolution histories. Of the samples shown in Figure 4.8, the only work to perform NLTE line corrections is Battistini & Bensby (2015), shown in light blue open diamonds.

4.7.4.4 Zn

Zn is produced in core-collapse supernovae with high explosion energy (i.e., hypernovae) and its yields depend strongly on supernova physics. At [Fe/H] $\gtrsim$ -1 dex the [Zn/Fe] ratio decreases with increasing metallicity in our sample as well as literature samples for the disk and bulge (Bensby et al., 2014, 2017). This is consistent with yields from SNe Ia. At [Fe/H] $\lesssim$ -1 dex, our observed [Zn/Fe] ratios are consistent with the EMBLA survey (Howes et al., 2015) and the Galactic halo (Roederer et al., 2014). This is also consistent with Galactic chemical evolution models where the large spread in [Zn/Fe] is a result

of the metallicity and mass-dependent yields from hypernovae (Kobayashi & Nakasato, 2011; Kobayashi et al., 2020).

4.7.5 Neutron-Capture Elements

Neutron-capture elements are produced through the successive capture of neutrons either through a rapid (r) process or a slow (s) process. In this work, we measure Ba and Ce abundances which are thought to be primarily produced through s-processes, specifically in AGB stars. However, they can both be produced in r-process sites as well (Kobayashi et al., 2020). We show the results for these elements in Figure 4.9.

4.7.5.1 Ba

Generally, stars in the MW with [Fe/H] $\gtrsim$ -1 dex, show [Ba/Fe] ratios that are roughly solar (Bensby et al., 2014, 2017). In the Galactic halo for stars with [Fe/H] $\lesssim$ -1 dex a large scatter in [Ba/Fe] is observed (Yong et al., 2013; Roederer et al., 2014). Nonetheless, the general trend in the halo is [Ba/Fe] decreasing with decreasing metallicity. However, r-process events, like electron-capture (EC) supernovae (Truran, 1981; Cowan et al., 1991), magneto-rotationally driven (MRD) supernovae (Winteler et al., 2012; Nishimura et al., 2015), or neutron star mergers (Rosswog et al., 1999), for example, can enhance the [Ba/Fe] ratio to values $>$ 1 dex (Cescutti & Chiappini, 2014).

The EMBLA survey found that most of their metal-poor bulge stars

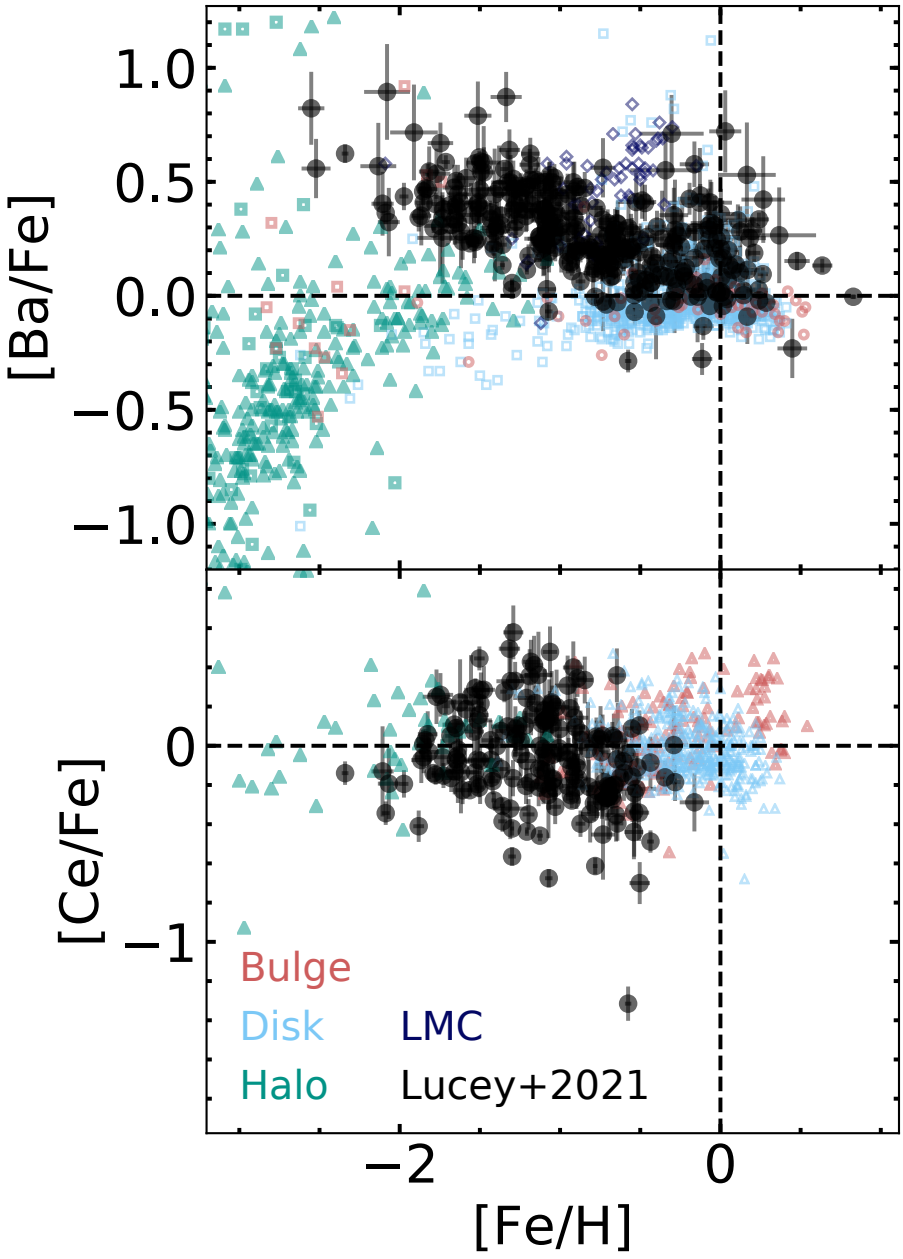

Figure 4.9: Abundance ratios as a function of metallicity for the neutron-capture elements Ba and Ce. Symbols are the same as in Figure 4.7 and 4.8, with the addition of Ce abundances from Battistini & Bensby (2016) in red triangles.

show a decreasing trend of [Ba/Fe] with decreasing metallicity, and therefore did not find evidence for an r-process event (Howes et al., 2015). However, our sample shows the opposite trend with the [Ba/Fe] ratio increasing at lower metallicities. We note that our survey performs NLTE abundance corrections for Ba while the EMBLA survey does not (Howes et al., 2016). In order to have [Ba/Fe] > 0 and increasing at lower metallicities, it is likely that an r-process event enriched the gas from which these stars formed.

Given the predictions from cosmological simulations that the metal-poor stars in the bulge are ancient (Tumlinson, 2010; Kobayashi & Nakasato, 2011; Starkenburg et al., 2017a; El-Badry et al., 2018b), the r-process event which enriched these stars must have occurred on a short timescale. As neutron star mergers are thought to occur on timescales $\gtrsim$ 4 Gyr, it is unlikely that our sample received its r-process material from one of these events. MRD SNe have the shortest timescale, with 1-10% of stars with 10 $M_\odot \leq M \leq$ 80 $M_\odot$ exploding as MRD SNe (Woosley & Heger, 2006; Winteler et al., 2012; Cescutti & Chiappini, 2014). EC SNe, on the other hand, are thought to occur for all stars with 8 $M_\odot \leq M \leq$ 10 $M_\odot$ (Cescutti et al., 2013). Cescutti et al. (2018) demonstrated that the MRD SNe scenario occurs on a fast enough timescale to enhance [Ba/Fe] ratios in metal-poor bulge stars, while the EC SNe scenario does not.

4.7.5.2 Ce

In the MW, at all metallicities, Ce tracks the Fe abundance, with the [Ce/Fe]$\approx$ 0 dex (Battistini & Bensby, 2016; Roederer et al., 2014; Duong et al., 2019b). However, at low metallicities in the Galactic halo, there is large scatter in the [Ce/Fe] ratio, similar to [Ba/Fe]. Unlike [Ba/Fe], our stars do not show r-process enhancement in the [Ce/Fe] ratio. Given that the r-/s- process ratio for Ba and Ce are very similar (Simmerer et al., 2004), it is expected that they would be equally enhanced in r-process events and display similar trends with [Fe/H]. However, unlike Ba, we do not perform NLTE abundance corrections for Ce. Therefore, it is possible that NLTE effects may be obscuring a trend in [Ce/Fe] with [Fe/H]. Future work to measure further NLTE neutron-capture abundances is essential for constraining the chemical enrichment history of the metal-poor bulge.

4.8 Dynamically Separating the Mixed Stellar Populations

Results from COMBS II demonstrate that metal-poor bulge stars ([Fe/H] $<$ -1 dex) are comprised of multiple stellar populations that can be separated dynamically. Specifically, COMBS II separated these stars into a population that stays confined to within 3.5 kpc of the Galactic center throughout their orbits and those that do not. In this work, we go one step further and divide the unconfined population into multiple dynamically defined groups.

Table 4.1: Properties of the Dynamical Groups.

Associated Structure	P(conf.)	r_{apo} (kpc)	z_{max} (kpc)	Number of Stars
Inner Bulge	>0.5			136
Outer Bulge	≤0.5	≤5	≤ 2.5	84
Halo	≤0.5		>2.5	32
Disk	≤0.5	>5	≤ 2.5	67

4.8.1 Selection Method

In total, we separate our observed stars into four groups. The groups are defined using the probability of confinement (P(conf.); see Section 4.2 in COMBS II for more details on how this is determined), the apocenter (r_{apo}), and the maximum distance from the Galactic plane that the stars reach during their orbit (z_{max}). The orbital properties are calculated in COMBS II using GALPY (Bovy, 2015). Specifically, we use a Dehnen bar potential (Dehnen, 2000) generalized to 3D (Monari et al., 2016) with parameters designed to match the long, slow bar model put forth by Portail et al. (2017). The selection of the dynamical groups is described in Table 5.2.

We label the groups based on the Galactic structures to which the majority of the stars belong. However, as with most methods of tagging stars to Galactic structures, there is likely contamination since the structures overlap spatially and kinematically (Carrillo et al., 2020). Our inner bulge population is based on an apocenter cut of <3.5 kpc. However, it is now thought that the bar likely extends out to 5 kpc (Wegg et al., 2015). Therefore, we also define an outer bulge population which is likely part of the bulge but does

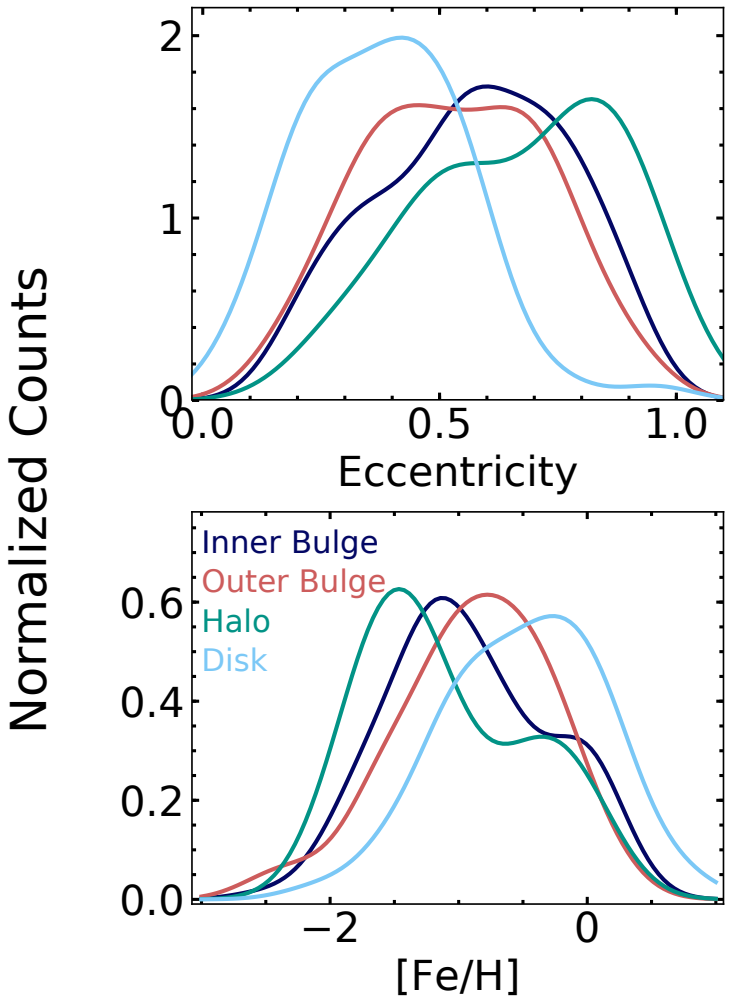

Figure 4.10: Properties of the populations we associate with various Galactic structures. In the top plot, we show the eccentricity distributions, while the bottom plot shows the metallicity distribution functions. The inner (136 stars; dark blue) and outer bulge (84 stars; red) have eccentricity distributions consistent with expectations for the Milky Way's bulge. The halo population (32 stars; green) is consistent with highly eccentric halo stars that pass through the Galactic center region. The disk population (67 stars; light blue) has an eccentricity distribution consistent with the Milky Way disk. The metallicity distribution functions are consistent with expectations given our photometric selection method. Namely, the halo is the most metal-poor component and the disk is the most metal-rich.

not stay confined to within 3.5 kpc of the Galactic center. To separate the outer bulge and halo population we use a z_{max} cut of 2.5 kpc. This cut is based on the z_{max} distribution of the inner bulge stars. Given the X-shape of the MW bulge, it is possible that the outer bulge is more flared and reaches larger heights above and below the Galactic plane than in the inner regions. This would cause contamination of the halo population by stars belonging to the bulge. However, after visual inspection of many of the orbits of stars in the halo group, the overwhelming majority have Galactic halo-like orbits and clearly do not belong to the bulge. To separate the outer bulge from the disk population, we use an r_{apo} cut of 5 kpc based on the proposed length of the bar from Wegg et al. (2015). It is important to note that there is certainly a disk population within 5 kpc of the Galactic center which is included in our outer bulge population. However, we are most concerned with simply removing the solar vicinity disk contamination from our sample, rather than selecting bar/bulge stars. Primarily, we aim to compare the metal-poor stars in the inner-most region of the Galaxy to the metal-poor stars in the surrounding regions. Therefore, we mostly focus on the inner bulge, outer bulge and halo populations for the rest of this work.

In Figure 4.10, we show the properties of our four groups to confirm that they match expectations for the associated structures. For each group we apply a Gaussian kernel density estimator (KDE) to the eccentricity and metallicity distributions. The eccentricity distributions of the inner and outer bulge populations are very similar, consistent with the stars being different

parts of the same structure. Furthermore, our halo population has highly eccentric orbits with a median eccentricity of $\sim$0.67. Lastly, the disk is the least eccentric population, which also matches expectations.

We show the MDFs of the dynamically defined groups in the bottom panel of Figure 4.10. These distributions are determined using KDEs. It is important to note that we do not expect these MDFs to represent the associated structures, given our photometric selection method. Nonetheless, our results generally match expectations for the given structures and selection method. Specifically, we see that our target selection was generally successful and our inner bulge population peaks at [Fe/H]$\approx$-1 dex. However, there is some contamination by metal-rich bulge stars, as the inner bulge distribution also contains a metal-rich peak at [Fe/H]$\approx$0 dex. The outer bulge distribution is very similar to the inner bulge distribution, although the peak's metallicity is slightly higher. In addition, the outer bulge distribution does not have a second metal-rich peak. Although, this is likely a selection effect.

The halo population has the most metal-poor peak, consistent with results from COMBS II, which found that the fraction of halo interlopers increases with decreasing metallicity. However, it is interesting to note the second metal-rich peak. We confirm these stars have high eccentricity ($e>\sim$0.5) and their orbits match expectations for halo stars. However, more precise positional and kinematic data is required to confirm the existence of this metal-rich halo population in the inner Galaxy. The most metal-rich population in our sample is the disk, but it has a large metal-poor tail. This is expected for the

disk population, as it is known to have a metal-weak component (Beers et al., 2014; Carollo et al., 2019).

4.8.2 Distinct Chemical Distributions of Dynamically-Defined Groups

In addition to dynamical and metallicity differences, the halo, outer bulge, and inner bulge all show differences in their abundance trends. In Figure 4.11, we show the abundance trends for the halo, outer bulge, and inner bulge populations as a function of metallicity for a number of key elements. Specifically, we show the α-elements (Mg, Si, and Ca), one odd-Z element (Na), one Fe-peak element (Mn), and one neutron-capture element (Ba). For each population, the lines shown are the median values, and the error bars correspond to the asymmetric 1σ spread. We also show the uncertainty on the median as $\sigma/(N-1)^{0.5}$ where N is the number of stars.

The comparison of α-element trends between the halo, outer bulge, and inner bulge populations shows a consistent story. At low metallicities ([Fe/H] $\lesssim$ -1 dex), the three populations show similar plateau values. However, the outer bulge consistently has the highest median, followed by the halo and then the inner bulge population. It is interesting to note that the difference between the median α-abundance trends at the lowest [Fe/H] is smallest for Mg ($\sim$0.1 dex) which is a hydrostatic α-element, while the explosive α-elements, Si and Ca, have larger differences ($\sim$0.2-0.3 dex). At this metallicity, the inner bulge population's median [α/Fe] is lower than the halo and outer bulge values because of a few stars with especially low [α/Fe] ratios. It is important

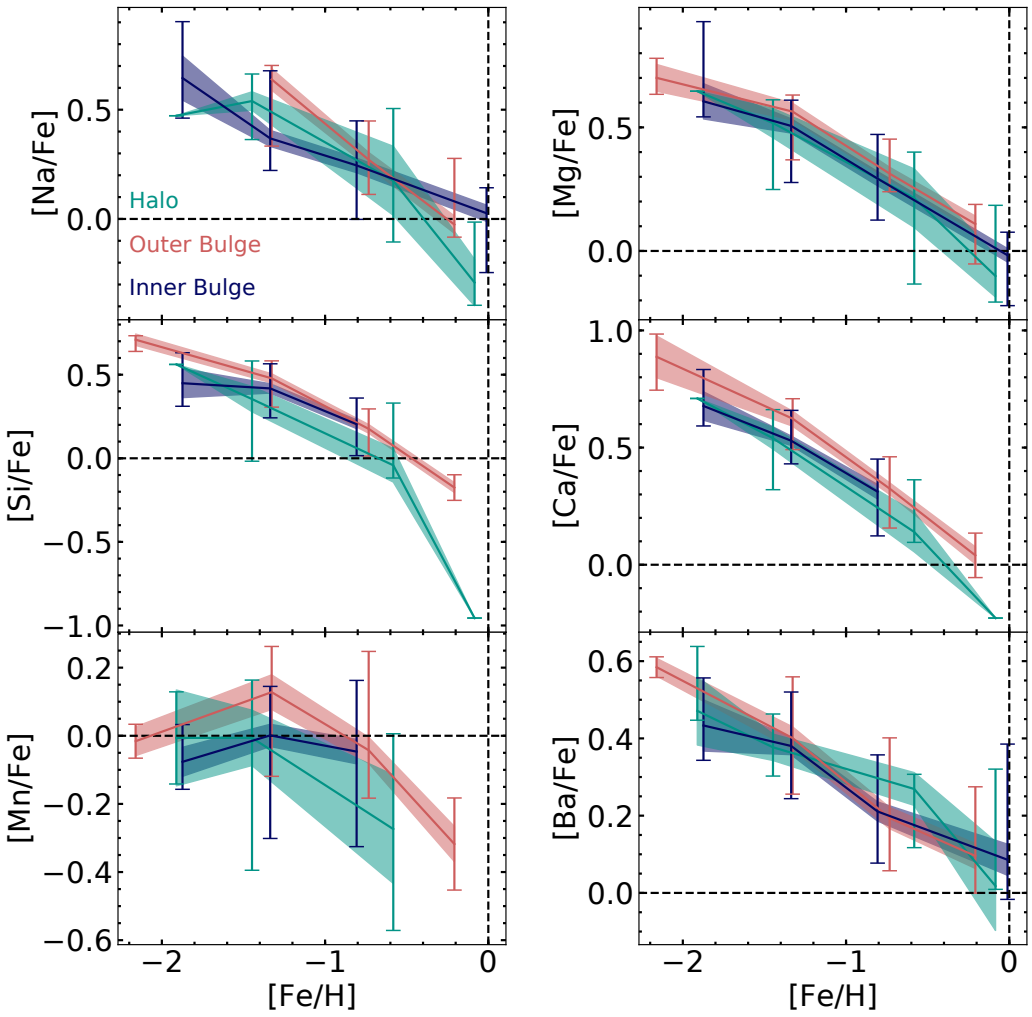

Figure 4.11: The distributions of a number of key elements as a function of metallicity for the halo (red), outer bulge (green) and inner bulge (dark blue) samples. Specifically, we show the α-elements (Mg, Si and Ca), along with one odd-Z (Na), Fe-peak (Mn) and neutron-capture element (Ba). The lines shown are the median values of the distributions and the error bars correspond to the scatter. We also show the uncertainty on the medians as the shaded regions.

to note the inner bulge population contains stars with [α/Fe] values as high as the most α-enhanced outer bulge stars, while the halo population does not.

The halo population's [α/Fe] ratio decreases sharply, with the halo becoming the least α-enhanced population at -2 dex $\lesssim$ [Fe/H] $\lesssim$ -1 dex. This change might be due to the onset of contributions from SNe Ia. However, the decreasing trend of [Mn/Fe] cannot be explained by SN Ia enrichment. This trend continues to higher metallicities, with the halo population generally having lower [α/Fe] values, indicating a longer star formation duration. On the other hand, the outer and inner bulge populations have very similar [α/Fe] distributions at high metallicities indicating similar star formation histories.

To test the statistical significance of the differences in the distributions, we perform 2D Kolmogorov-Smirnov tests (Peacock, 1983; Fasano & Franceschini, 1987). We perform the test 1000 times sampling the abundances from a Gaussian distribution centered on their measured value with a width corresponding to the uncertainty. We then report the mean p-value of those 1000 test as our final confidence level. The [Ca/Fe] and [Mg/Fe] distributions as a function of [Fe/H] for the outer bulge are different from the halo distributions to a >90% confidence level. However, the inner bulge and halo distributions are not significantly different in [Ca/Fe] or [Mg/Fe], as they both have large scatter. On the other hand, the differences between [Si/Fe] as a function of [Fe/H] distributions for the halo compared to both the inner and outer bulge populations are statistically significant to $>$ 90% confidence. The inner and outer bulge distributions are not significantly different for any α-elements.

The only elements for which the differences between the outer and inner bulge populations are statistically significant is Mn and Na, which both have metallicity-dependent yields in SNe II. At low metallicities ([Fe/H] $\lesssim$ -1 dex), the inner bulge population has lower values in [Mn/Fe] and [Na/Fe] than the outer bulge population. Therefore, the inner bulge stars were generally enriched by a more metal-poor population than the outer bulge stars. This is consistent with results from simulations indicating that more tightly bound stars are older than less tightly bound stars of similar metallicity (Tumlinson, 2010; El-Badry et al., 2018b).

The difference between [Mn/Fe] and [Na/Fe] as a function of [Fe/H] distributions for the inner bulge and halo populations is not statistically significant. The [Mn/Fe] and [Na/Fe] distributions for the halo population have large scatter with generally lower values than the outer and inner bulge populations. For [Mn/Fe], the halo population starts to decrease at [Fe/H] $\sim$-1.5 dex, consistent with the onset of SNe Ia and a longer star formation timescale than the inner and outer bulge populations. The difference between [Mn/Fe] and [Na/Fe] as a function of [Fe/H] distributions for the halo compared to the outer bulge population is statistically significant to the >90% level.

The [Ba/Fe] distributions of the three groups are surprisingly similar to the [α/Fe] distributions at low metallicity. Specifically, we see the same trend in that the three populations all have similar values at the lowest metallicities, but the outer bulge population has the highest level of enhancement, followed by the halo population and then the inner bulge population. This may indi-

Table 4.2: Chemical Complexity of the Dynamical Groups.

Associated Structure	Mean Absolute Correlation Strength	Variance Explained by 4 Components	Relative Chemical Complexity
Inner Bulge	0.36±0.12	96.6±0.4%	Highest
Outer Bulge	0.55±0.25	95.0±1.0%	
Halo	0.59±0.30	98.6±0.5%	Lowest

We define stellar populations that have higher chemical dimensionality and less correlated abundances as being more *chemical complex* than populations with lower dimensionality and more highly correlated abundances.

cate that the origin of Ba in the low metallicity stars of these populations is similar to the origin of the α-elements. However, the similarity to the [α/Fe] distribution ceases at higher metallicities where the [Ba/Fe] ratio for the halo is not significantly lower than for the inner and outer bulge populations. In general, the distribution in [Ba/Fe] is much more scattered in the inner and outer bulge populations than in the halo. The differences between the halo distribution of [Ba/Fe] as a function of [Fe/H] and the outer bulge distribution are statistically significant to the >90% confidence level. On the other hand, the outer and inner bulge populations show strikingly similar distributions in [Ba/Fe] as a function of [Fe/H]. This is similar to the Ca, and Mg abundances, providing further evidence that the halo population has a significantly different chemical evolution history than the outer bulge population.

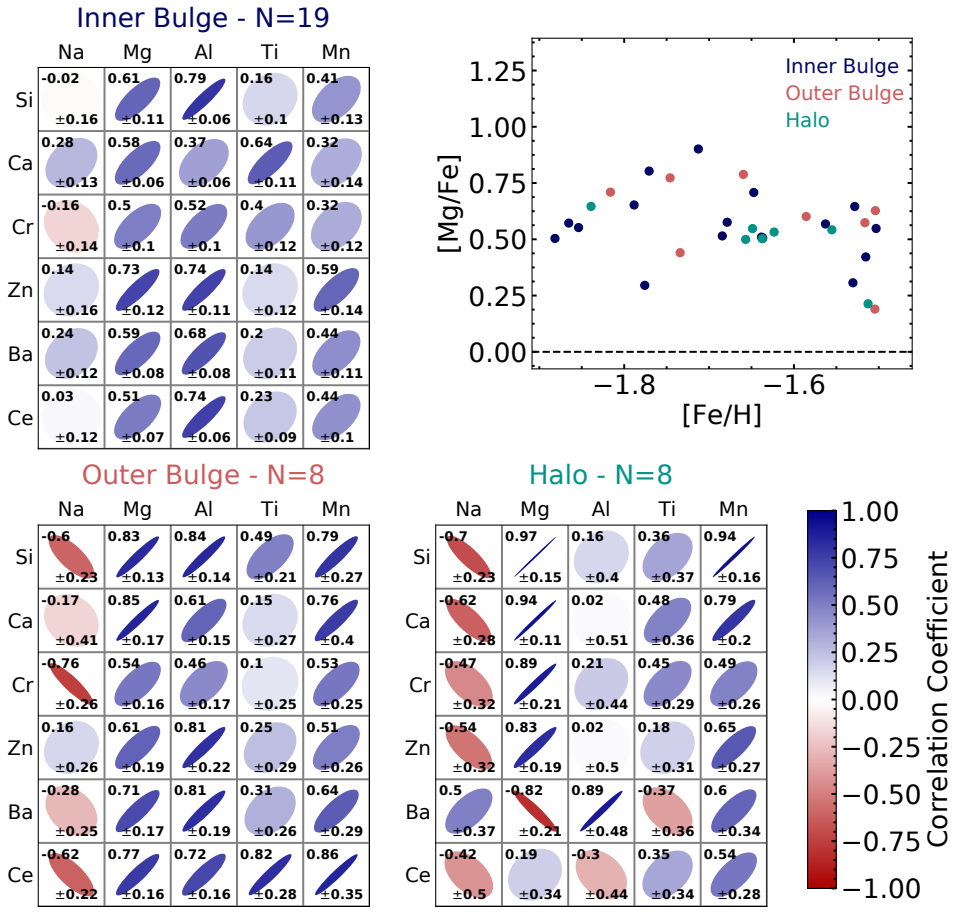

Figure 4.12: The Pearson correlation coefficients between a number of key elements for the halo (bottom right), outer bulge (bottom left) and inner bulge (top left) populations. Specifically we compare (Na, Mg, Al, Ti and Mn) to (Si, Ca, Cr, Zn, Ba and Ce). The correlations are calculated using [X/Fe] for stars with -2 dex $\lesssim$ [Fe/H] $\lesssim$ -1.5 dex and SNR$>$ 40 pixel^{-1}. The top right plot shows the [Mg/Fe] abundances as a function of [Fe/H] for inner bulge (dark blue), outer bulge (green) and halo (red) stars, for reference. To aid in the visualization, we show an oval for each correlation coefficient whose ellipticity, rotation, and color corresponds to the strength and direction of the correlation. We also print the correlation coefficient value in the top left of each correlation box and the corresponding uncertainty on the correlation coefficient in the bottom right. We include the number of stars used in calculating the correlations for the different groups in the title above each correlation plot.

4.8.3 Chemical Complexity of Inner and Outer Bulge Compared to Halo Population

In addition to the individual elemental distributions, we also study the correlation between elements and the chemical dimensionality of the inner bulge, outer bulge and halo populations. Through this analysis, we shed light on the diversity of nucleosynthetic events that enriched each population.

In Figure 4.12, we show the Pearson correlation coefficients for pairs of a number of key elements in the inner bulge, outer bulge, and halo populations. Specifically, we calculate the correlation coefficient for the [X/Fe] values, comparing (Na, Mg, Al, Ti, and Mn) to (Si, Ca, Cr, Zn, Ba, and Ce). The correlation coefficients are calculated using stars with SNR$>$ 40 pixel^{-1} and -2 dex $<$[Fe/H] $<$ -1.5 dex, in order to isolate yields from core-collapse supernovae and limit the impact of metallicity on the correlations. In the top left, we show the results for the inner bulge population which uses 19 stars, while the outer bulge is shown in the bottom left, using 8 stars. We also show results for the halo population on the bottom right, using 8 stars. The top right plot shows [Mg/Fe] as a function of [Fe/H] for the stars used in the correlation plots, as a reference. This figure demonstrates that the stars used for the halo (red), outer bulge (green), and inner bulge (dark blue) populations span similar metallicity ranges. In the three correlation plots, each small box contains an ellipse whose eccentricity and color corresponds to the strength of the correlation. In addition, we print the correlation coefficient in the top right corner, with the corresponding uncertainty on the coefficient in

the bottom right corner.

The uncertainties are calculated using a bootstrap method in order to propagate the impact of the abundance uncertainties and the limited number of stars. To account for the abundance uncertainties, we recalculate the correlation coefficient 1000 times with new abundance values each time. These values are randomly selected from Gaussian distributions that are centered on the measured abundance value with a width equivalent to the uncertainty. We then define the correlation coefficient's uncertainty due to abundance uncertainties as the median of the differences between the original correlations and the recalculated values. Similarly, to account for the limited number of stars, we recalculate the coefficients N times dropping out 1 star from the sample each time. Again, we use the median of the differences between the original correlations and the recalculated values as the uncertainty due to the limited number of stars. We then add the uncertainties due to the number of stars and the uncertainties due to the abundance uncertainties in quadrature for our total uncertainty values. We note that the uncertainties due to the abundance uncertainties are dominant with the uncertainties due to the number of stars being on the order of $\sim$0-0.01.

Overall, the inner bulge population shows the weakest correlations, followed by the outer bulge population and then the halo. As they are all α-elements, it is expected for Mg, Si, and Ca to be tightly correlated. This is observed in the halo population, but the correlations are weaker in the outer and inner bulge populations. This is especially interesting given that PISNe

yields have [Ca/Mg] and [Si/Mg] abundance ratios that are mass-dependent. Therefore, yields from PISNe of varying masses would cause the correlation between Mg, Si, and Ca to weaken and become noisier as seen in the inner and outer bulge populations.

Furthermore, the correlation of Ca and Si with Mn in the halo is strikingly strong. This is surprising given that Mn is thought to have metallicity-dependent yields in SNe II while Si and Ca do not. This may indicate that the halo stars were enriched by a population with a narrow metallicity range. This correlation becomes sequentially weaker as we move to more tightly bound stars in the outer and inner bulge populations. In general, the inner bulge population only shows weak correlations with Mn. In addition, the negative correlation of Na with Si, Ca, and Zn are significant in the halo, but almost completely disappear in the outer bulge population and are non-existent in the inner bulge population. Similar results are found for the positive Na to Ba correlation.

Excluding Al, which is discussed later, the mean of the absolute correlations of the abundance pairs shown in Figure 4.12 is 0.59 ± 0.30 for the halo population, while the means for the outer and inner bulge populations are 0.55 ± 0.25 and 0.36 ± 0.12, respectively. The uncertainties on the mean are determined by recalculating the mean using the correlation strengths with the individual correlation uncertainties added/subtracted. Therefore, we find evidence that the elemental abundances in the halo population are generally more correlated than in similar metallicity stars in the inner bulge populations.

This result may indicate a less diverse chemical enrichment history in the halo population as compared to the inner bulge.

Furthermore, the abundance pairs which do not follow the above trend can provide interesting insight into the possible differences between the chemical enrichment histories of these populations. For example, the Al abundances show the opposite trend in that the inner and outer bulge populations have strong correlations while the Al abundances for the halo population are generally not correlated with any elements, except for Ba . This is especially difficult to interpret given that Na and Al are thought to be produced in similar ways, but the inner bulge population does not show strong correlations for Na with any elements. This result solicits further investigation into possible nucleosynthetic sites, beyond SNe II, for Al in the inner bulge population.

Another striking difference between the outer bulge, inner bulge, and halo populations is the strength of the positive Mg, Ba, and Ce correlations in the outer and inner bulge populations, while the halo population shows negative or weak correlations. This is further evidence for the similar origin of Ba and α-elements at low metallicities in the inner and outer bulge populations. Specifically, this result further supports MRD SNe as the origin for Ba in these ancient stars (Kobayashi et al., 2020). MRD SNe produce high levels of Ba and Ce as well as α-elements (Yong et al., 2013). However, further work analyzing and comparing MRD SNe theoretical yields to the observed abundances are required.

Ti is another interesting case that does not match the general trend of

strong correlations in the halo and weak correlations in the inner bulge population. Specifically, Ti generally does not have significantly strong correlations with any element except for with Ca in the inner bulge population. We note that the outer bulge shows a somewhat strong correlation between Ti and Ce, however, the uncertainty is large at 0.28. It is possible that the Ca and Ti correlation in the inner bulge population is insignificant, but it may also indicate an interesting origin for some of the Ca in this population.

In addition to the correlation analysis, we perform a chemical dimensionality analysis to further explore the differences in the inner bulge, outer bulge and halo populations. Specifically, we perform Principal Component Analysis (PCA) on the elemental abundances for each population. Essentially, PCA sequentially finds orthogonal components which explain the most variance in the given data. For the analysis, we include all stars in each population with SNR$>$ 40 pixel^{-1}, [Fe/H]$<$-1 dex, and a complete set of elemental abundances for Na, Mg, Al, Si, Ca, Ti, Cr, Mn, Zn, Ba and Ce. Similar to the correlation analysis, we choose to only focus on metal-poor stars ([Fe/H] $<$-1 dex) in this analysis to limit the impact of SNe Type Ia. However, since the PCA analysis requires a complete set of abundances, we are left with only 7 stars from the halo population, 11 stars from the outer bulge population and 20 stars from the inner bulge population, even though the metallicity range used is larger than for the correlation analysis. To account for the uncertainties in the abundances, we perform the PCA analysis 1000 times with new abundances sampled from a normal distribution centered on the measured

abundance with a width corresponding to the abundance uncertainty.

To explore the comparative dimensionality of the elemental abundances, we investigate the percentage of variance explained by each component derived from the PCA. Consistently, we find that for the same number of components, a higher percentage of the variance in the halo population is explained compared to the inner and outer bulge populations. For example, 92.2±1.7% of the variance is explained by 2 components in the halo population while only 85.7±2.6% and 91.3±1.0% is exaplined in the outer and inner bulge populations, respectively. Furthermore, when using 4 components, 98.6±0.5% of the variance in the halo is explained, while only 95.0±1.0% and 96.6±0.4% of the variance is explained in the outer and inner bulge populations, respectively. Therefore, we find evidence that the halo population has lower chemical dimensionality than the inner and outer bulge populations.

To describe the combination of our correlation and dimensionality analysis, we define a new term: *chemical complexity*. In total, we find that the elemental abundances in the halo population are highly correlated with a mean correlation of 0.59±0.30, while the mean for the outer and inner bulge populations are 0.55±0.25 and 0.36±0.12, respectively. Furthermore, we found that the halo population has lower chemical dimensionality than the inner and outer bulge populations. Specifically, when using 4 components, only 96.6±0.4% and 95.0±1.0% of the variance in the elemental abundances is explained for the inner and outer bulge populations while the same is true for 98.6±0.5% of the elemental abundance variance in the halo population. *Therefore,*

we describe the highly-correlated, lower dimensional halo population as less chemically complex compared to the inner and outer bulge populations whose elemental abundances are less correlated and have higher dimensionality. This measure of relative chemical complexity is indicative of the diversity of chemical enrichment events. Therefore, we suggest that the inner and outer bulge populations have a higher diversity of enrichment events compared to the halo population. However, it is important to note that these results may also be impacted by the rate of mixing in the ISM at the different formation times. Specifically, higher chemical complexity could also indicate a less well-mixed ISM.

In total, we discover a number of key results from our comparison between the abundances of the inner bulge, outer bulge, and halo populations. First, we find that the inner and outer bulge populations have shorter star formation timescales and more rapid chemical evolution than the halo population. In addition, our results solicit further investigation into the nucleosynthetic origins of Ba and Al in metal-poor inner bulge stars. Furthermore, we find that the abundances are consistent with the inner bulge being the oldest population, compared to the outer bulge and halo populations. We also find that at low-metallicity, the inner bulge is the most chemically complex population, followed by the outer bulge and then halo population. Combined, these results suggest that older bulge populations are more chemically complex. This may be due to a combination of diversity of chemical enrichment events (e.g., PISNe, EC SNe, MRD SNe, and other SNe predictions for Popu-

lation III stars), as well as inhomogeneous mixing of the ISM.

4.9 Pair-Instability supernovae signatures

PISNe are highly energetic thermonuclear explosions that occur after the hydrodynamical collapse caused by electron-positron pair production in massive (> 25 $M_{\odot}$) CO cores (Barkat et al., 1967; Rakavy et al., 1967). It is predicted that $\sim$25% of the first stars would explode as PISNe (Hirano et al., 2015). Therefore, it is expected that $\sim 1/400$ stars with [Ca/H] $<$ -2 dex would be enriched by a PISN (Takahashi et al., 2018). However, chemical signatures of PISNe in studies of metal-poor stars have been elusive. A number of candidates have been put forward, but none perfectly match the predicted abundance trends from simulations (Takahashi et al., 2018). Whether the lack of PISNe chemical signature detections is an observational effect or the result of incorrect simulated rates and yields is yet to be determined.

In Figure 4.13, we plot our sample's abundances with respect to the predicted PISNe abundance trends from Takahashi et al. (2018). Specifically, we plot abundance ratios that are thought to be especially discriminatory in PISNe yields: [Al/Mg] and [Ca/Mg]. The range of predicted PISNe abundance yield ratios is shown in the blue-shaded regions. The measured abundances of our sample are shown in points colored by their metallicity, with corresponding uncertainties as black error bars. We discover two stars that have [Ca/Mg] ratios consistent with predictions for PISNe yields. However, neither of these stars has a consistent [Al/Mg] ratio. Out of the two stars (544.1 and 2021.0)

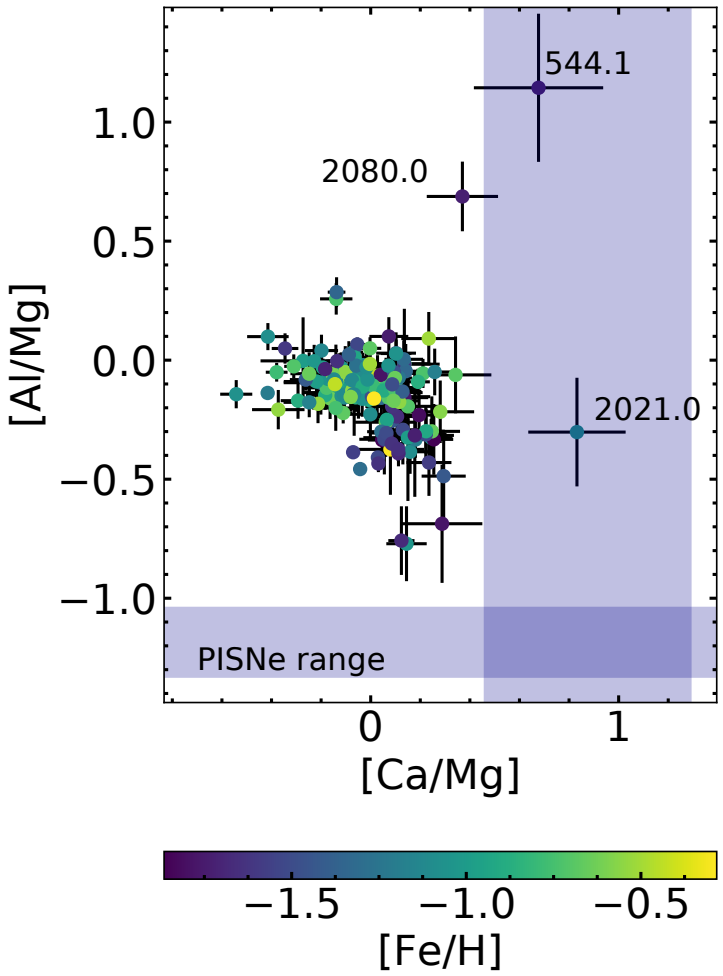

Figure 4.13: The [Al/Mg] ratios as a function of [Ca/Mg] for our sample stars, colored by [Fe/H]. We shade the regions corresponding to simulated PISNe yields (Takahashi et al., 2018). We have two stars (544.1 and 2021.0) with [Ca/Mg] ratios consistent with PISNe predictions, but their [Al/Mg] ratios are significantly higher than predictions.

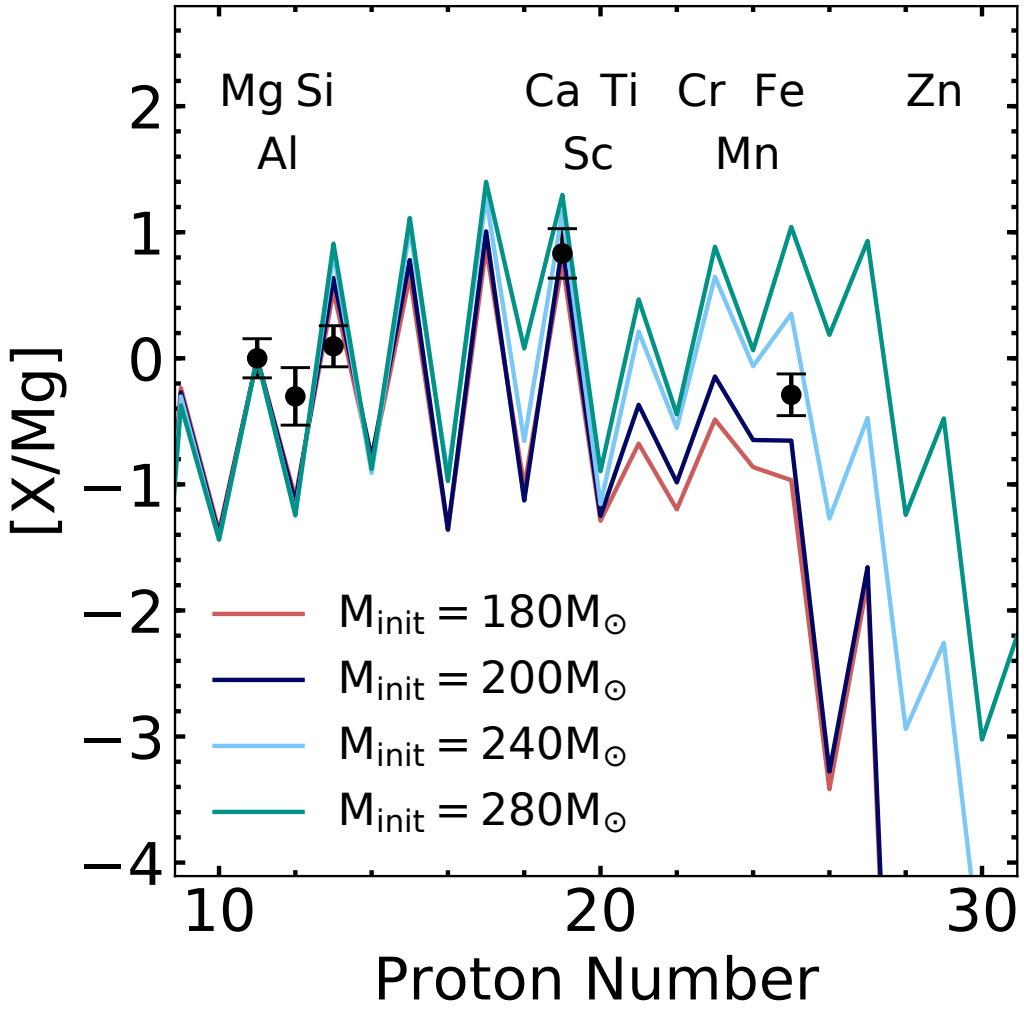

Figure 4.14: The [X/Mg] ratios for star 2021.0 compared to non-rotating model PISNe yields of various initial masses from Takahashi et al. (2018). We are only able to measure Mg, Al, Si, Ca, and Fe for this star as it has SNR=21 pixel^{-1}. The [Ca/Mg] and [Fe/Mg] ratios match PISNe signatures, but the [Al/Mg] and [Si/Mg] ratios do not.

with high enough [Ca/Mg] ratios, we focus on 2021.0 which has an [Al/Mg] ratio closest to PISNe yield predictions.

Star 2021.0 has [Fe/H]=-1.07 dex and [Ca/H] = 0.05 dex. We show all measured abundances for this star in Figure 4.14. Specifically, we show [Mg/Mg], [Al/Mg], [Si/Mg], [Ca/Mg] and [Fe/Mg]. We also attempted to measure the other elements presented in this work, but the HR06 spectrum has only SNR=21 pixel^{-1}, making many of the elements difficult to measure reliably. In Figure 4.14, we also plot predicted PISNe yields for non-rotating models with various initial masses from Takahashi et al. (2018). Our [Ca/Mg] and [Fe/Mg] ratios match predictions for PISNe, but our [Al/Mg] and [Si/(Mg,Ca,Fe)] ratios do not. In fact, our measured [Si/(Mg,Fe)] ratio is rather consistent with normal core-collapse supernovae. Furthermore, the metallicity of 2021.0 is higher than expectations for a Population II star which was enriched solely by a single PISNe (Karlsson et al., 2008). Therefore, it is possible that this star was enriched by a PISNe along with an SNe II. However, further observations are needed to measure more elemental abundances in this star to confirm the PISNe signature. It is also important to note that that star 2021.0 is part of the inner bulge population with a P(conf.)=0.93. Furthermore, star 2021.0 is tightly bound with a pericenter of 0.49 kpc, r_{apo}= 2.31 kpc and z_{max}=1.15 kpc. Therefore, it is likely that this star formed in the first few Gyrs of star formation in the Universe. However, asteroseismology is required to further constrain its age.

4.10 Globular Cluster Origin

Recent work suggests that the metal-poor bulge may be at least partially built up by dissipated globular clusters (Kruijssen, 2015; Shapiro et al., 2010; Bournaud, 2016). To date, a significant number of stars in the bulge with chemistry consistent with globular clusters have been detected (Schiavon et al., 2017; Fernández-Trincado et al., 2017; Lucey et al., 2019). Specifically, the chemical signatures encountered include nitrogen enhancement and the Al-Mg and Na-O anti-correlations which are signatures of second-generation globular cluster stars (Gratton et al., 2004). However, the rate at which these stars occur among metal-poor bulge stars and whether they are confined stars as opposed to interloping halo stars is yet to be determined.

In this work, we find two stars (544.1 and 2080.0) that have enhanced Al with respect to their Mg abundances. In Figure 4.15, we show the [Al/Fe] abundances as a function [Mg/Fe] for our sample. The confined bulge population is shown as black points while the unconfined stars are shown as black crosses. We also show a number of surveys from the literature for comparison. Specifically, we show halo samples from Roederer et al. (2014, green open triangles) and Yong et al. (2013, green open squares), along with a disk sample from Bensby et al. (2014, light blue open squares). In addition, we show abundances from the globular clusters NGC 4833 (red open circles), NGC 7089 (red open triangles), and NGC 2808 (red open diamonds) from Pancino et al. (2017), along with NGC 6121 (red open squares) from Marino et al. (2008). The stars 544.1 and 2080.0 match trends seen in globular clusters and have much higher

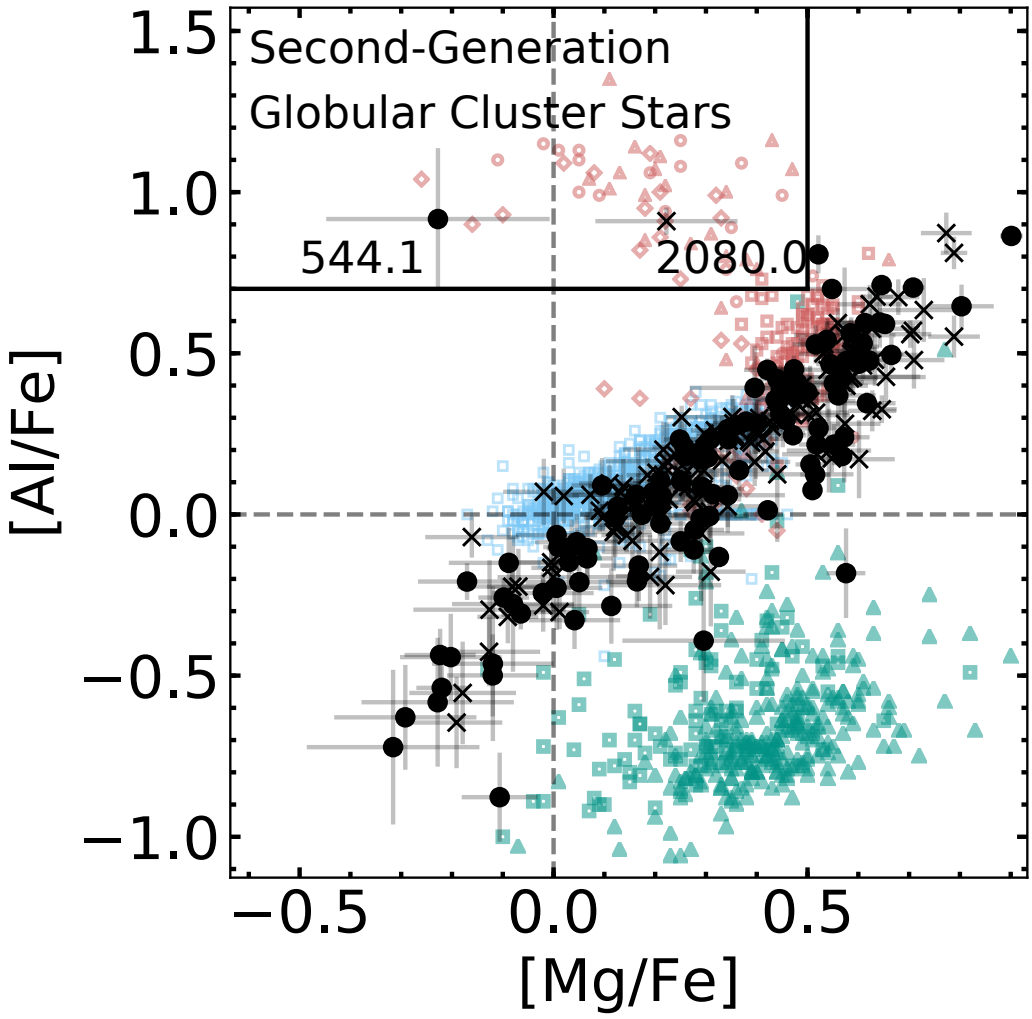

Figure 4.15: The [Al/Fe] abundance ratios as a function of [Mg/Fe] for our sample. We show confined bulge stars (P(conf.)>0.5) as black points and unconfined (P(conf.)≤0.5) stars as black crosses. We also show halo (Roederer et al., 2014; Yong et al., 2013, green open triangles and squares, respectively), disk (Bensby et al., 2014, light blue open squares), and globular cluster literature samples for comparison. Specifically, we show NGC 4833 (red open circles), NGC 7089 (red open triangles), and NGC 2808 (red open diamonds) from Pancino et al. (2017), along with NGC 6121 (red open squares) from Marino et al. (2008). We have two stars (544.1 and 2080.0) that have chemistry consistent with second-generation globular cluster stars.

[Al/Fe] ratios compared to other stars in our sample with similar [Mg/Fe]. Star 2080.0 is unconfined and belongs to the disk dynamical group. However, its orbit is unusual for a disk star, with a pericenter of 0.19 kpc, r_{apo}=8.6 kpc and z_{max}=0.90 kpc. On the other hand, star 544.1 is on a typical inner bulge orbit with a pericenter of 0.77 kpc, r_{apo}=2.79 kpc and z_{max}=1.95 kpc. It is especially interesting to note that 544.1 specifically matches abundance trends from NGC 2808, one of the MW's most massive globular clusters, that is theorized to be part of the Gaia-Enceladus system (Myeong et al., 2018).

Schiavon et al. (2017) and Horta et al. (2021) estimate that ∼25% of the stellar mass in the inner 2 kpc of the Galaxy are disrupted globular cluster stars, assuming nitrogen-rich stars are second-generation globular cluster stars. Given these results, it is expected that more than 2 out of our 241 stars with Al and Mg measurements would be second-generation globular cluster stars and would therefore show the Al-Mg anti-correlation. However, it is unclear whether all second-generation globular cluster stars can be detected using the Al-Mg anti-correlation. To perform an apples-to-apples comparison, further observations are required to determine the fraction of N-rich stars in our sample. Another possible explanation for the apparent lack of second-generation globular cluster stars in our sample could be the result of SkyMapper photometry for target selection. It is known that photometric selection of metal-poor stars using SkyMapper can be biased against selecting C-enhanced stars (Da Costa et al., 2019). As nitrogen-rich stars can frequently be C-rich (Horta et al., 2020), we may be biased against selecting nitrogen-rich stars and there-

fore second-generation globular cluster stars as well. Last, our results could be discrepant with estimates from Schiavon et al. (2017) and Horta et al. (2021) due to their assumption that all N-rich stars are disrupted globular cluster stars which would lead to an overestimate of the contribution of dissipated globular clusters to the stellar mass. Other origins for N-rich stars have been suggested (e.g., Bekki, 2019), which could explain the high fraction of N-rich stars in the inner Galaxy.

4.11 Summary and Conclusions

The Galactic bulge is a complex structure with overlapping stellar populations which can provide crucial information about the formation and evolution of the MW. The metal-poor population in the bulge is of special interest given that cosmological simulations predict they are some of the oldest stars in the Galaxy (Salvadori et al., 2010; Tumlinson, 2010; Kobayashi & Nakasato, 2011; Starkenburg et al., 2017a; El-Badry et al., 2018b). However, this population has historically been difficult to study given that it compromises only $\sim$5% of bulge stars. Now, with the recent advent of metallicity-sensitive photometric surveys (Starkenburg et al., 2017b; Wolf et al., 2018; Casagrande et al., 2019), we can target metal-poor stars in the Galactic bulge and study them in large numbers (Arentsen et al., 2020b). Recent work has determined that many metal-poor stars found in the bulge are actually halo interloping stars (Kunder et al., 2020; Lucey et al., 2021). Therefore, it is necessary to combine dynamical and chemical information to disentangle the metal-poor

bulge population and study its origins in detail.

In this work, we successfully target metal-poor stars in the Galactic bulge using Skymapper photometry and observe 555 stars with the VLT/GIRAFFE spectrograph. We report stellar parameters and abundances for 319 which have SNR > 20 pixel^{-1} and astrometry from *Gaia* DR2. The stellar parameters and abundances are determined using a χ^2 fit to model spectra synthesized using SME with NLTE departure coefficients for Li, O, Na, Mg, Al, Si, Ca, Ti, Fe, and Ba (Valenti & Piskunov, 1996; Piskunov & Valenti, 2017). We compare our stellar parameters to results for *Gaia* Benchmark stars (Heiter et al., 2015; Jofré et al., 2014; Hawkins et al., 2016), the ARGOS survey (Freeman et al., 2013), and the HERBS survey (Duong et al., 2019a) and find they are generally consistent. We report elemental abundances for C, Na, Mg, Al, Si, Ca, Ti, Cr, Mn, Fe, Zn, Ba, and Ce. Using results from Lucey et al. (2021), which defines confined bulge stars as those with apocenters <3.5 kpc, we divide our sample into 5 groups based on their dynamics. We associate these groups with different Galactic structures. Specifically, we label them as the inner bulge population, the outer bulge, the halo, and the thick and thin disks.

Given these data we find evidence that:

1. The halo stars which pass through the inner Galaxy have relatively low chemical complexity compared to the inner and outer bulge populations. Specifically the elemental abundances are highly correlated (mean correlation coefficient of 0.57) and have lower dimensionality (98.0% of vari-

ance explained by 4 components) than the inner and outer bulge populations. This may indicate that these halo stars formed in-situ in the disk and were heated to halo kinematics by a merger event (e.g., Di Matteo et al., 2019). However, it is also possible these stars formed ex-situ in a single chemically simple progenitor or in many progenitors but the universe, in general, was less chemically complex. The abundances for this halo population are consistent with a longer star formation timescale when compared to the outer and inner bulge population.

2. The outer bulge population is very similar to the inner bulge population, although more chemically correlated (mean correlation coefficient of 0.53). The outer bulge is significantly distinct from the inner bulge stars in only its Na and Mn abundances, which both have metallicity-dependent yields in SNe II. Given that Na and Mn yields are higher in more metal-rich stars, it is likely the outer bulge stars were enriched by a more metal-rich population than the inner stars. This result is consistent with predictions from cosmological simulations that the outer bulge is younger than the inner bulge population (Tumlinson, 2010).

3. The confined (or inner) bulge population is more chemically complex (mean correlation coefficient of 0.38 and 96.6% of the variance explained by 4 components) than the unconfined stars in the bulge. Additionally, results from simulations predict that confined, or tightly bound stars are generally older than unconfined, loosely bound stars (Tumlinson, 2010). Combined, these results indicate that older populations in

the inner Galaxy are generally more chemically complex than younger populations of similar metallicity. Furthermore, this suggests that the universe is more chemically complex early on indicating either more diversity in chemical enrichment events or inhomogeneous mixing in the ISM.

4. We also find evidence that the Ba in low-metallicity ([Fe/H]$\lesssim$-1 dex) outer and inner bulge populations have similar origins to the α-elements. Specifically, we find the Ba and α-element abundances are positively correlated in these populations, but negatively correlated in the halo population.

5. In our inner bulge population, we find one star that may show a signature of PISNe. Explicitly, this star has [Fe/H]=-1.07 dex and [Ca/Mg]=0.83 dex, but its [Al/Mg] ratio (-0.30 dex) is higher and its [Si/(Mg,Ca,Fe)] ratio is lower than expected for PISNe yields. Further observations are needed to measure more chemical abundances for this star and compare them to model PISNe yields.

6. We detect 2 stars whose chemistry is consistent with second-generation globular cluster stars in that they show the signature Mg-Al anti-correlation. One of these stars belongs to the inner bulge population while the other belongs to the outer bulge population. It is especially interesting that one star has a [Al/Mg] ratio that is similar to what is observed for NGC 2808 which is theorized to be the core of the Gaia-Enceladus system (Myeong

et al., 2018).

In total, this work demonstrates the power and necessity of combining chemistry with dynamics to disentangle and separately study the metal-poor stellar populations in the bulge region. In future work, we hope to achieve more precise dynamical parameters with improved astrometry from further *Gaia* data releases and the use of spectro-photometric distances. In addition, our work signifies the need for more measurements of neutron-capture elements in metal-poor bulge stars. However, further work on nucleosynthetic yields of Ba from Population II and III stars is needed to understand the correlation between Ba and α-elements observed in this work. Furthermore, more precise photometry in the bulge is required to continue to target the most metal-poor bulge stars in large numbers with lower contamination rates from metal-rich stars.

Chapter 5

Dynamically constraining the length of the Milky Way bar

Abstract: We present a novel method for constraining the length of the Galactic bar using 6D phase space information to directly integrate orbits. We define a pseudo-length for the Galactic bar, named $R_{\rm Freq}$, based on the maximal extent of trapped bar orbits. We find the $R_{\rm Freq}$ measured from orbits is consistent with the $R_{\rm Freq}$ of the assumed potential only when the length of the bar and pattern speed of said potential is similar to the model from which the initial phase-space coordinates of the orbits are derived. Therefore, one can measure the model's or the Milky Way's bar length from 6D phase-space coordinates by determining which assumed potential leads to a self-consistent measured $R_{\rm Freq}$. When we apply this method to ≈210,000 stars in APOGEE DR17 and *Gaia* eDR3 data, we find a consistent result only for potential models with a dynamical bar length of ≈3.5 kpc. We find the Milky Way's

[1] This chapter is based on Lucey M., Pearson S., Hunt J.A.S., Hawkins K., Ness M., Petersen M.S., Price-Whelan A.M., Weinberg M.D., 2023, MNRAS, 520, 4479. The author of this document, Madeline Reinke Lucey, completed all of the analysis and wrote the publication. The project was developed in collaboration with and supervised by S. Pearson and J.A.S. Hunt, who also helped complete the analysis.

trapped bar orbits extend out to only ≈3.5 kpc, but there is also an overdensity of stars at the end of the bar out to 4.8 kpc which could be related to an attached spiral arm. We also find that the measured orbital structure of the bar is strongly dependent on the properties of the assumed potential.

5.1 Introduction

Stellar bars are non-axisymmetric, elongated structures in the inner parts of disk galaxies. More than 30% of massive disk galaxies ($M_* > 10^{10}$ $M_\odot$) in the local Universe host strong stellar bars (Sellwood & Wilkinson, 1993; Masters et al., 2011; Gavazzi et al., 2015). Although many open questions remain concerning how stellar bars form and evolve, it is clear that they play pivotal roles in the secular evolution of disk galaxies (Debattista et al., 2004; Athanassoula, 2005).

The Milky Way hosts a stellar bar at its center, which was originally discovered from near-infrared emission (Blitz & Spergel, 1991; Weiland et al., 1994) and gas kinematics (Binney et al., 1991; Peters, 1975). Stellar kinematics demonstrate that most of the mass in the inner Galaxy participates in the bar structure (Howard et al., 2009; Shen et al., 2010; Ness et al., 2013b; Debattista et al., 2017). Currently, it is under debate whether a small pressure-supported component distinct from the disk or halo (e.g., a classical bulge) overlaps with the bar (Kunder et al., 2020; Arentsen et al., 2020a; Lucey et al., 2021). It has also been discovered that the center of the MW has an X-shaped structure (Nataf et al., 2010; McWilliam & Zoccali, 2010; Ness et al., 2012; Wegg &

Gerhard, 2013; Ness & Lang, 2016), which is characteristic of a boxy/peanut-shaped (B/P) bulge and consistent with simulations and observations of barred galaxies (Combes et al., 1990; Athanassoula, 2005; Martinez-Valpuesta et al., 2006; Bureau et al., 2006; Laurikainen et al., 2014).

The discovery of the MW's stellar bar provides the unique opportunity to study a bar in exquisite detail using resolved stars. However, the high levels of variable extinction have historically made the MW's bar difficult to observe (Nataf et al., 2013). Parameterizing the MW bar's mass, length and pattern speed is essential for many studies of MW dynamics. The bar greatly influences the perturbative kinematics of the Galactic disk, including in the Solar neighborhood (Dehnen, 2000; Minchev & Famaey, 2010; Antoja et al., 2018; Hunt & Bovy, 2018; Fujii et al., 2019). The Galactic bar can also impact the structure of stellar streams in the halo and the ability to interpret dark matter substructure signatures in the streams (Price-Whelan et al., 2016b; Hattori et al., 2016; Pearson et al., 2017; Erkal et al., 2017; Banik & Bovy, 2019; Bonaca et al., 2020).

There have been a number of efforts to map the three dimensional structure of the bulge/bar region of the Galaxy, primarily using star counts (Saito et al., 2011; Wegg & Gerhard, 2013). However, the existence of a long ($\approx$4 kpc) bar, discovered initially by Hammersley et al. (1994), has led to controversy on whether it is a separate structure from the B/P bulge (Hammersley et al., 2000; López-Corredoira et al., 2007; Cabrera-Lavers et al., 2007, 2008; Martinez-Valpuesta & Gerhard, 2011). Using the 3D number density of red

clump giants from VVV, UKIDSS, GLIMPSE, and 2MASS data, Wegg et al. (2015) demonstrated that the long bar is the extension of the B/P bulge and they are in fact one unified structure. Furthermore, Wegg et al. (2015) found that the bar has a half length of 5 kpc and is at an angle of (28-33)° from the Sun-Galactic center line. However, it is possible that spiral arms connected to the bar may cause it to appear 1-1.5 kpc longer in the number density counts than when the spiral arms are not connected (Gonzalez & Gadotti, 2016; Hilmi et al., 2020). To account for this effect, it is critical to further constrain the length of the bar using a dynamical method which can distinguish between trapped bar stars and those whose major-axes do not participate in solid body rotation.

The pattern speed of the bar, however, is better constrained with recent estimates from multiple methods clustering around 40 km $s^{-1}$$kpc^{-1}$ (e.g., Wang et al., 2013; Binney, 2020). Adding kinematic data from the ARGOS survey (Freeman et al., 2013; Ness et al., 2013a) to the work of Wegg et al. (2015), Portail et al. (2017) found a pattern speed of 39.0 ± 3.5 km $s^{-1}$$kpc^{-1}$ using the Made-to-Measure method. Sanders et al. (2019) measured a pattern speed of 41 ± 3 km $s^{-1}$$kpc^{-1}$ using a direct method derived from the continuity equation (Tremaine & Weinberg, 1984). In addition, they used proper motion data of stars within 2 kpc of the Galactic center from *Gaia* DR2 and VVV surveys. Using a similar method, Bovy et al. (2019) and Leung et al. (2022) created kinematic maps of Apache Point Observatory Galactic Evolution Experiment (APOGEE; Majewski et al., 2017) and *Gaia* DR2 data (Gaia Collaboration

et al., 2016a, 2018a) to measure a pattern speed of 41 $\pm$ 3 $s^{-1}kpc^{-1}$ out to a distance of 5 kpc from the Galactic center. However, there are also bar pattern speed estimates as high as 60 km $s^{-1}kpc^{-1}$ (e.g., Wang et al., 2012), leaving room for some debate.

In this paper, we take advantage of the 6D phase-space measurements at the center of our Galaxy to directly integrate the orbits of stars located in the Milky Way's bar. Specifically, we develop a novel method for constraining the MW's bar length and pattern speed. To verify our method, we use N-body simulations and compare the maximal extent of stars in the bar measured from the orbits to that of the potential model used to calculate the orbits. We find that these lengths are only consistent when the initial positions and velocities of the star particles come from a distribution similar to the potential in which the orbits are integrated. We test $\approx$60 different MW bar potential models, by integrating APOGEE/*Gaia* data within these potentials and determining whether the retrieved maximal extent is consistent with the given potential model. In Section 5.2, we describe the simulations we use to validate our method while in Section 6.2 we describe the observations used to constrain the MW's bar. We describe the method and verify its precision and accuracy in Section 5.4. Next, we apply our method to the MW data in Section 5.5 and discuss the different methods for measuring bar lengths in Section 5.6. Last, we present our conclusions in Section 7.1.

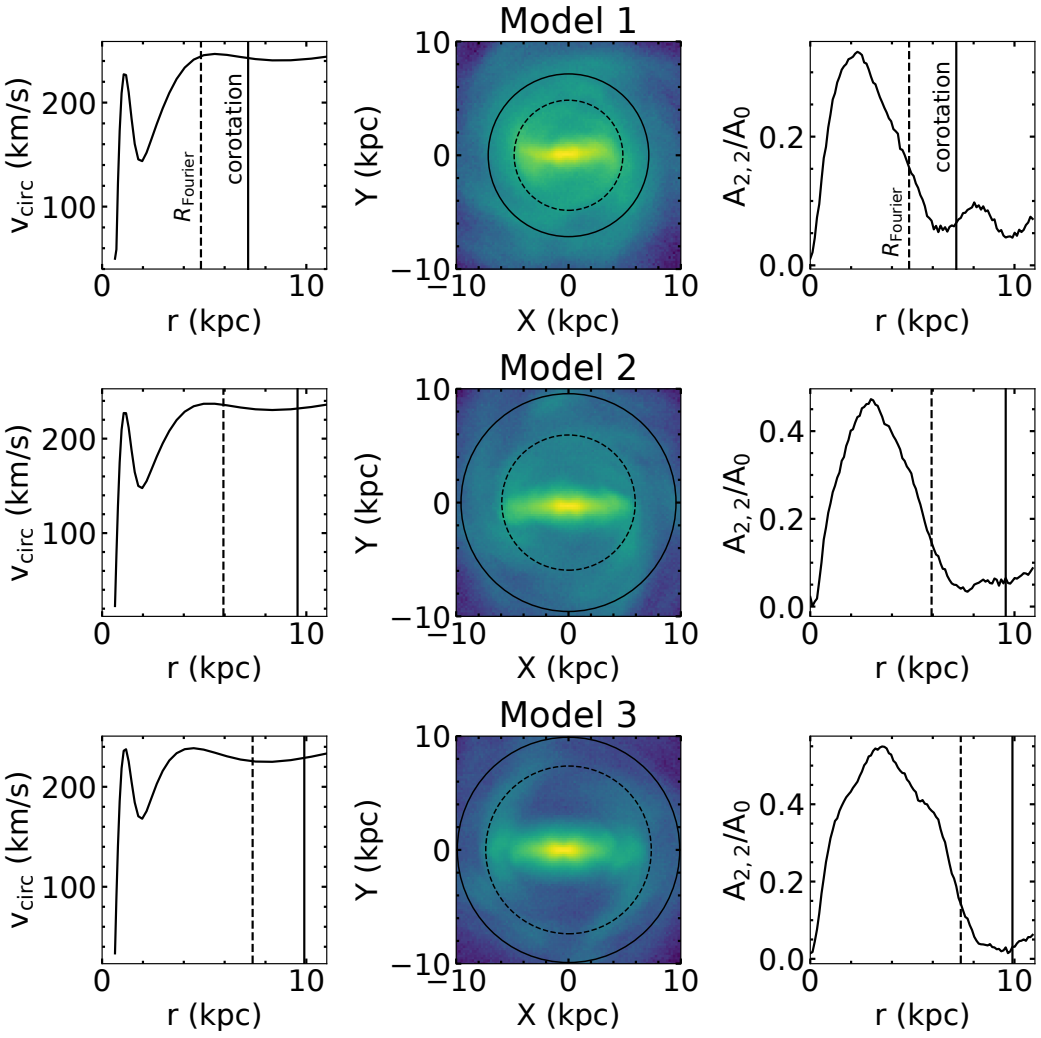

Figure 5.1: Properties of the three primary N-body snapshots that we utilize to validate our method. The leftmost column shows the circular velocity curves for each of the three models. In the rightmost column, we show the $A_{2,2}/A_0$ ratio (Equation 5.3) as a function of galactic radius. We define the bar length ($R_{\rm Fourier}$) as the radius at which $A_{2,2}/A_0$=0.15. In each plot, the bar length is shown as the black dashed line. We also show the corotation radius, defined as the radius where $\Omega_{\rm b} = v_{circ}(r)/r$, as a black solid line. In the center column, we show face-on images of each model with circles marking $R_{\rm Fourier}$ (black dashed) and corotaion radii (black solid). $R_{\rm Fourier}$ visually matches the drop in number density.

5.2 Simulations

We make use of two Milky Way-like N-body simulations from the literature. The primary simulation we use (hereafter Galaxy A) is a reproduction of the MWP14-3 model from Bennett et al. (2021). We also make use of another Milky Way-like simulation (hereafter Galaxy B) from Tepper-Garcia et al. (2021) to further validate our method and compare to Milky Way observational data. Specifically, we extract potentials from the mass distributions of 29 unique snapshots of each simulation. From Galaxy A we also extract three sets of 10,000 random initial positions and velocities of disk star particles from three different snapshots to use as initial phase-space coordinates for orbits. We call these snapshots Model 1, Model 2, and Model 3. Since we know the true underlying mass distribution for these initial phase-space coordinates, we can use them to test our method.

Face-on images of the three snapshots used to extract initial positions and velocities are shown in the middle column of Figure 5.1. Model 1, 2, and 3 correspond to the snapshots that are 2.94, 3.92, and 4.90 Gyr into the simulation's evolution, respectively. Over this time, the galactic bar grows and slows. Similar to previous work (e.g., Athanassoula & Misiriotis, 2002; Zana et al., 2018; Rosas-Guevara et al., 2020, 2021), we use the $m = 2$ mode of the Fourier decomposition of the face-on stellar surface density to estimate the length of the bar in number density in order to compare to our dynamical

estimate. We determine the Fourier components:

$$A_m(r) = \frac{1}{\pi}\int_0^{2\pi} \Sigma(r,\theta) cos(m\theta)\, d\theta, \qquad m = 0, 1, 2, ... \tag{5.1}$$

and

$$B_m(r) = \frac{1}{\pi}\int_0^{2\pi} \Sigma(r,\theta) sin(m\theta)\, d\theta, \qquad m = 1, 2, ... \tag{5.2}$$

where $\Sigma(r,\theta)$ is the stellar surface density. We then define

$$A_{2,2}/A_0 = \sqrt{A_2^2 + B_2^2}/A_0 \tag{5.3}$$

and calculate it as a function of r using equal width annuli of Δr= 0.10 kpc. Similar to Rosas-Guevara et al. (2021), we use the radius at which $A_{2,2}/A_0$=0.15 as our estimate for the bar length, which is shown as the black dashed in all panels of Figure 5.1. In this work, we denote bar lengths measurements derived using this method as $R_{\rm Fourier}$. The choice of value to use for $A_{2,2}/A_0$ can vary (e.g., Athanassoula & Misiriotis, 2002). Arbitrarily, we could also use the radius at which $A_{2,2}/A_0 = 0.20$ which would shorten the bar length estimate. For further discussion on the various methods for measuring bar lengths see section 5.6.

We calculate the bar's pattern speed, $\Omega_{\rm b}$, by measuring the change in the $m = 2$ phase angle ($\phi_2 = \frac{1}{2}\tan^{-1}(\rm B_2/A_2)$) between simulation outputs which are 9.79 Myr apart. Here we calculate $\rm B_2$ and $\rm A_2$ between radii of 1 to 5 kpc. In the leftmost column of Figure 5.1, we plot the circular velocity curve for each of the snapshots. We also plot the corotation radius, where $\Omega_{\rm b} = v_{\rm circ}(r)/r$, as a black solid vertical line. Consistent with expectations,

$R_{\rm Fourier}$ is shorter than the corotation radius (Contopoulos, 1980). Specifically, we find that $R_{\rm Fourier}$ is 74%, 68%, and 82% of the corotation radius for Models 1, 2, and 3, respectively, making the bar in Model 1 and 3 dynamically fast, while Model 2's bar is dynamically slow (Debattista & Sellwood, 2000).

In addition to these three models, we also use another 26 (29 in total) snapshots from Galaxy A, to create a variety of gravitational potentials with different bar lengths. These potentials are each 97.9 Myr apart, starting after bar formation, while Models 1, 2, and 3 are 979 Myr apart. We name each snapshot from which we extract a potential based on the number of years (in units of 97.9 Myr) the simulation has evolved past Models 1, 2, or 3. For example, Model 1.2 corresponds to 195.8 Myr (2×97.9 Myr) after Model 1. We use these as test potentials to determine how bar orbits are impacted by potentials with different bar strengths and lengths. Furthermore, we also integrate the APOGEE/*Gaia* data in these potentials in order to determine which potential best fits the data.

The initial conditions for the Galaxy A simulation are derived from the `GALPY` potential `MWPotential2014` (Bovy, 2015) and set up with the `GALIC` package (Yurin & Springel, 2014). However, Bennett & Bovy (2021) found that the halo mass of `GALPY`'s `MWPotential2014` needs to be increased in order to produce realistic asymmetries (e.g., spiral arms and a stellar bar) in simulations. Therefore, Galaxy A (MWP14-3) has a virial halo mass of $M_h = 1.4 \times 10^{12} M_\odot$ which is twice as heavy as the halo in `GALPY`'s `MWPotential2014`. It also has a disk scale height of 0.28 kpc and disk scale length of 3.0 kpc. In

total there are ≈9.3 million particles with 3,337,406 particles in dark matter halo, 5,000,000 particles in the disk and 996,403 particles in the bulge. The dark matter particles have masses of $3.48 \times 10^5 M_\odot$. While the disk and bulge star particles have masses of $4.50 \times 10^3 M_\odot$ and $1.34 \times 10^4 M_\odot$, respectively. In total, this simulation is evolved for ≈4.99 Gyr.

Although it is also set up to mirror the Milky Way, Galaxy B has significantly different initial conditions than Galaxy A. For a complete description of Galaxy B, we refer the reader to Tepper-Garcia et al. (2021). In short, Galaxy B is set up using the Action-based GAlaxy Modelling Architecture software package (`AGAMA`; Vasiliev, 2019). Compared to Galaxy A, Galaxy B has a lighter virial halo mass of $M_h = 1.18 \times 10^{12} M_\odot$. Furthermore, the disk of Galaxy B has a shorter scale height (0.3 kpc) and length (2.6 kpc) compared to Galaxy A as well as a large velocity dispersion ratio ($\sigma_R/\sigma_z = 2$).

Galaxy A and B are both simulated for about 5 Gyr and each have their bars fully formed between 2 and 2.5 Gyr. However, the bar in Galaxy A significantly grows and slows over the simulation whereas the bar in Galaxy B stays rather stable (see x-axis of Figure 5.4). Using an iso-density contour, Tepper-Garcia et al. (2021) measure a bar length of ≈4.5 kpc, and pattern speed of ≈40 km/s/kpc.

As for Galaxy A, we use a total of 29 snapshots from Galaxy B to create gravitational potentials. Similar to Galaxy A, these potentials are 95 Myr apart, starting after bar formation. However, as the bar is more stable in this simulation, these potentials have a much smaller range in bar lengths.

Importantly, these potentials allow us to ensure that our method works across different simulations and is not dependent on properties of the simulated galaxies' potentials other than the bar length and pattern speed. Given that the properties of bars are thought to be heavily impacted by dark matter halos (e.g., Petersen et al., 2019b; Debattista & Sellwood, 2000; Fragkoudi et al., 2021; Chiba & Schönrich, 2021; Collier & Madigan, 2021), it is especially important that we use two models that have different dark matter halo masses and profiles.

For each of the 58 snapshots (29 each from Galaxies A and B), we first use the mass distribution to extract the corresponding gravitational potential using the AGAMA package (Vasiliev, 2019). Specifically, we use a multipole expansion to represent the spherical bulge and dark matter halo components. For the disk, we use the `CylSpine` potential representation which uses azimuthal Fourier harmonics.

5.3 Data

5.3.1 APOGEE DR17 and Gaia eDR3

In order to constrain the Milky Way's galactic bar, we utilize one of the largest sets of 6D positional and kinematic data available. Specifically, we use a combination of *Gaia* eDR3 data (Gaia Collaboration et al., 2021b) with APOGEE DR17 (Abdurro'uf et al., 2021). APOGEE is a near-infrared (1.5-1.7 μm), high-resolution (R=$\lambda/\Delta\lambda \approx$ 22,500) large spectroscopic survey (Nidever et al., 2015; Wilson et al., 2019; Zasowski et al., 2017). APOGEE DR17

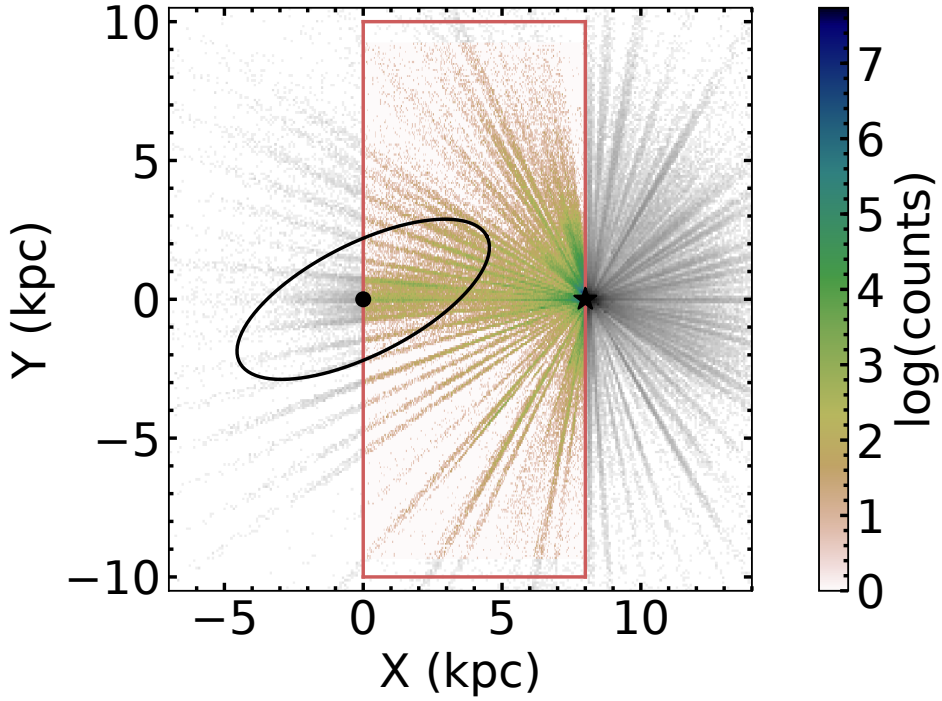

Figure 5.2: Galactic distribution of the astroNN catalog using APOGEE DR17 and *Gaia* eDR3 (Leung & Bovy, 2019). The Sun is located at (8.3,0,0) kpc with the Galactic center at (0,0,0) kpc. For this work, we use stars with 0 kpc $<$ X $<$ 8.3 kpc and |Y|$<$10 kpc (shown as a red box) in order to loosely target the Galactic bar. For reference we show the proposed bar model of Wegg et al. (2015) as an ellipse with a semi-major axis of 5 kpc and axis ratio of 0.4 rotated 27° from the Sun-Galactic center line.

contains over 657,000 stars observed using the APO 2.5m telescope (Gunn et al., 2006) and the 2.5m telescope at Las Campanas Observatory (LCO) (Bowen & Vaughan, 1973). In this work, we use the line-of-sight velocities from the ASPCAP pipeline (García Pérez et al., 2016; Smith et al., 2021), along with the spectrophotometric distance estimates from the astroNN catalog (Leung & Bovy, 2019) and proper motions from *Gaia* eDR3 (Gaia Collaboration et al., 2021b). Combining this data gives us typical phase-space uncertainties on the order of 5% for all components. We also repeat our analysis with distances from the StarHorse catalog (Queiroz et al., 2020) to ensure that our results are not impacted by a possible distance bias.

In Figure 5.2, we show the Galactic distribution of the astroNN catalog that we use in our analysis. For reference, we also show the proposed bar model of Wegg et al. (2015) as an ellipse with a semi-major axis of 5 kpc and axis ratio of 0.4, rotated 27° from the Sun-Galactic center line. As demarcated by the red box, we choose stars in between the Sun and the Galactic center, with 0 kpc$<$ X$<$ 8.3 kpc and |Y|$<$10 kpc, in order to loosely target the Galactic bar. We choose not to use stars with X $<$ 0 kpc due to the large distance uncertainties. This selection gives us a sample of 215,869 stars for which we have 6D spectrophotometric phase-space information for use in our analysis. We also redo our analysis only with stars that were targeted as part of APOGEE's main science program for the bulge which is based on a simple color cut criterion. This test allows us to ensure that selection function effects do not dominate our results.

5.4 Using Orbit Integration to Constrain the Length of Bars

There are a number of methods used to estimate the length of a Galactic bars. In Table 5.2, we outline each measurement of bar length discussed in this work. In this section, we describe in detail the method that we develop for measuring the length of bars from orbit integration of 6D phase-space observations.

First, to separate trapped bar stars from regular disk stars, we perform fundamental frequency analysis in the rotating bar-frame where regular disk orbits will be symmetric in x and y (i.e., $\Omega_x = \Omega_y$) while bar orbits may not. Next, we define a quantity based on the apocenter distribution of orbits in the bar which we call $R_{\rm Freq}$, for short. Specifically, $R_{\rm Freq}$ is defined as the 99.5th percentile of the apocenter distribution of bar stars selected from frequency analysis. We perform a number of experiments to test how each input of the orbit simulations (gravitational potential, initial phase-space coordinates of particles, and pattern speed) impact the inferred $R_{\rm Freq}$. We find that only when the assumed potential has a similar bar length and pattern speed to the model from which initial 6D positions and velocities are extracted then the inferred $R_{\rm Freq}$ is equal to the assumed potential's $R_{\rm Freq}$. In other words, to achieve a self-consistent $R_{\rm Freq}$ in that the inferred value matches that of the gravitational potential used to calculate it, the assumed gravitational potential must have a bar length similar to that of the initial phase-space coordinates. We apply this method, first, to simulations in order to confirm the accuracy

Table 5.1: Different Measurements of Bar Length Used in This Work

Term	Description
R_{Fourier}	Estimate of the bar length calculated from the Fourier analysis of number density counts. Specifically, the radius at which $A_{2,2}/A_0$=0.15. See Section 5.2 for further information.
Potential's R_{Freq}	The bar length of the potential estimated by integrating 10,000 particles from the potential model in the potential rotating at the true bar pattern speed. The bar length is then the 99.5th percentile of the apocenter distribution of bar stars selected from orbital frequency analysis. See Section 5.4.1 for more information.
Inferred R_{Freq}	The 99.5th percentile of the apocenter distribution of bar stars selected from orbital frequency analysis. The orbits may be calculated with any combination of initial phase-space coordinates, potential model and pattern speed. See Section 5.4.1 for more information.
R_{x_1}	Estimate of the bar length based on the maximal extent of orbits classified as x_1. See Section 5.6 for more information.

and precision of the results. Next, we apply the method to the *Gaia* and APOGEE data set in order to constrain the length of the Milky Way's bar.

5.4.1 Defining R_{Freq}

In this work, we perform experiments to determine how the inferred R_{Freq} differs when changing the various inputs into orbit simulations. Specifically, as we are interested in applying this method to Milky Way data, we test how R_{Freq} changes for a given set of initial phase-space coordinates under various assumptions about the gravitational potential. For each experiment,

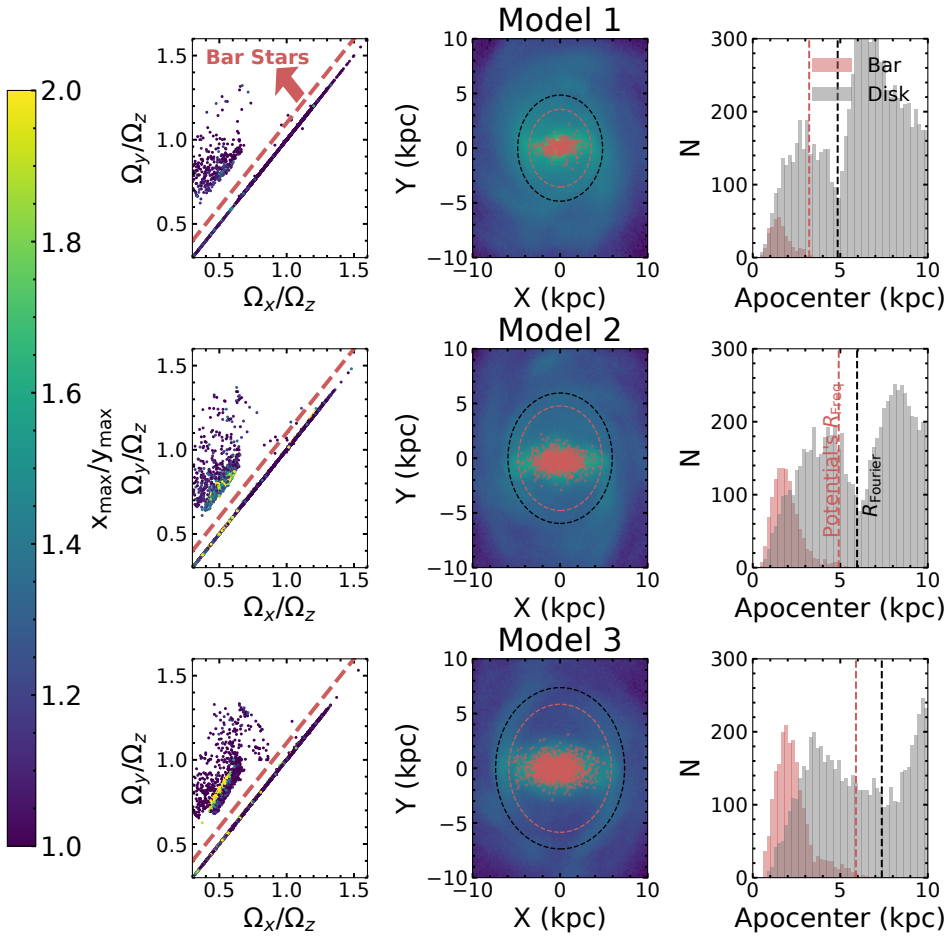

Figure 5.3: The selection and distribution of bar stars for three bar models. The first column shows the orbital frequency map for 10,000 disk stars randomly selected from the N-body models colored by the ratio of x_{max}/y_{max} where x is along the bar's major axis and y is along the minor axis. We show a red dashed line corresponding to $\Omega_y/\Omega_z=\Omega_x/\Omega_z+0.1$, as we select stars above this line as stars in the bar. The central column shows the spatial distribution of our selected bar stars (red points) compared to the rest of the stars in the models. The last column shows the apocenter distribution from the orbits integrated in the corresponding model potential for 1 Gyr. The selected bar stars are shown in red and the rest of the 10,000 stars are shown in grey. The red dashed line correspond to the 99.5th percentile of the bar stars' apocenter distribution which we define as the potential's $R_{\rm Freq}$.

we integrate 10,000 particles in a rotating potential for a total of 1 Gyr in timesteps of 1 Myr. We have also tried integrating the orbits for longer periods of time but do not see significant changes in our results. Although a typical bar's structure would likely evolve over 1 Gyr, assuming a stable bar for orbit integration is reasonable in our case where we are simply interested in measuring the present day bar length.

In order to calculate the inferred $R_{\rm Freq}$, we first must define bar orbits. To accomplish this, we use orbital frequency analysis. Regular orbits in triaxial potentials have three fundamental frequencies ($\mathbf{\Omega} \equiv \{\Omega_x, \Omega_y, \Omega_z\}$) which describe the periodic motion. As first demonstrated by Binney & Spergel (1982), Fourier transforms can be used to recover the fundamental frequencies. Specifically, the Fourier transform gives the spectrum of orbital oscillations in the chosen coordinate system, where dominant lines tend to correspond to the fundamental frequencies, though is not always the case. Referred to as "Numerical Analysis of Fundamental Frequencies" (NAFF), this method has been further developed and applied to galactic dynamics (e.g., Laskar, 1993; Valluri & Merritt, 1998; Valluri, 1999; Valluri et al., 2010; Price-Whelan et al., 2016a; Yavetz et al., 2021; Koppelman et al., 2021). In this work, we use the SUPERFREQ code (Price-Whelan, 2015a,b) to calculate the fundamental frequencies for each of our 10,000 stars. Specifically, we find the Cartesian fundamental frequencies ($\Omega_x, \Omega_y, \Omega_z$) in the rotating frame where the bar is stationary, which have been shown to better classify bar stars than frequencies in cylindrical coordinates (Valluri et al., 2016). Consistent with Valluri et al. (2016),

x corresponds to the direction along the bar's major axis, y is along the bar's minor axis and z is the direction out of the plane.

Disk stars on regular orbits lie along the $\Omega_x/\Omega_y = 1$ resonance line. As shown in Figure 5.3 and in Valluri et al. (2016), bar stars tend to lie above this line with $\Omega_x/\Omega_z > 0.3$. We select stars within this region as our sample of bar stars. Specifically, we use stars above the red dashed line where $\Omega_y/\Omega_z > \Omega_x/\Omega_z + 0.1$. Although this selection will certainly miss some of the bar stars, there is no contamination of the sample by disk stars. For our work, low contamination is prioritized over completeness. In Section 5.6, we present a more robust method for selecting bar stars. However, this method is significantly more computationally expensive. The frequency estimates provide a fast selection of bar stars which is required given that we wish to perform the bar length calculation for a large variety of initial phase-space conditions and potentials. For this part of the analysis, we primarily wish to perform an apples-to-apples comparison between the potential's $R_{\rm Freq}$ and the inferred $R_{\rm Freq}$to check for self-consistency. It is possible that the bar orbit family with the largest physical extent may vary for different bars. Therefore, missing a given family of lower-order bar orbits could potentially have disparate effects and cause an anomalously self-consistent result. However, we do not see evidence of this in our tests with simulations (see Section 5.4.2). In future work, we plan to build a faster method for classifying bar stars which will allow for a more robust analysis of the maximal extent of bar orbit families.

Now that we have isolated bar orbits, we can estimate the length of

the bar based on the maximal extent of these orbits. In this work we use the 99.5th percentile instead of the maximum of the apocenter distribution in order to minimize the effect of outliers.

In each experiment, we compare the inferred $R_{\rm Freq}$ to the bar length of the potential used to calculate it. In this way, we are checking for self-consistency and testing whether the bar length of the potential is consistent with the $R_{\rm Freq}$ inferred with it. As we wish to perform an apples-to-apples comparison, we measure the bar length of the potential using the same method as $R_{\rm Freq}$. To calculate the potential's $R_{\rm Freq}$, we use initial phase-space coordinates of particles extracted from the given potential model. Furthermore, we rotate the potential with the correct pattern speed, corresponding to the potential's N-body snapshot, measured from Fourier analysis (see Section 5.2). In this way, we are simulating the orbits as close as possible to the N-body snapshot on which the potential is based. Therefore, the potential's $R_{\rm Freq}$ is meant to be the ground truth $R_{\rm Freq}$ for the given potential.

In Figure 5.3, we demonstrate our method for defining stars in the bar and the potential's $R_{\rm Freq}$. Specifically, we show results for dynamically measuring the potential's $R_{\rm Freq}$ that correspond to Models 1, 2, and 3 (see Figure 5.1). The leftmost column shows orbital frequency maps for Models 1, 2, and 3, respectively. To create the frequency maps, we plot the ratio Ω_x/Ω_z on the x-axis and Ω_y/Ω_z on the y-axis. We color the points by the ratio of the maximum x-position (x_{max}) to the maximum y-position (y_{max}) for each star.

In the middle column of Figure 5.3 we show face-on images of the N-

body models with the bar stars selected from the orbital frequency maps (left panels) as red points. As expected, the selected bar stars all fall within the bar region. In the rightmost column of Figure 5.3, we plot the apocenter distribution of the orbits of these same stars (red) compared to the remaining disk stars (grey). We plot the potential's $R_{\rm Freq}$ as a red vertical dashed line. For Models 1, 2, and 3, we measure a potential $R_{\rm Freq}$ of 3.22 kpc, 4.89 kpc, and 5.88 kpc, respectively. We compare this to the $R_{\rm Fourier}$, which is shown as a black vertical dashed line. As shown, the potential's $R_{\rm Freq}$is consistently smaller than $R_{\rm Fourier}$. In fact, the potential's $R_{\rm Freq}$ is between 73% and 80% of $R_{\rm Fourier}$ for Models 1, 2, and 3. However, it is important to note that $R_{\rm Fourier}$ is known to overestimate the length of bars especially in the case of attached spiral arms (Hilmi et al., 2020; Petersen et al., 2019a). We refer the reader to Section 5.6 for further comparisons and discussion of methods for estimating the bar length.

For the potential's $R_{\rm Freq}$, we are always using particles extracted from the N-body model whose mass distribution is the basis of the potential. This is not necessarily true for the inferred $R_{\rm Freq}$. In the next section, we test how the inferred $R_{\rm Freq}$ changes from the potential's $R_{\rm Freq}$ as we change the potential, but fix the initial phase-space coordinates. It is reasonable to expect that inferred $R_{\rm Freq}$ is approximately the same as the potential's $R_{\rm Freq}$ when the potential is similar to the Model from which the initial positions and velocities are extracted. However, the power of our method comes from the fact that the inferred $R_{\rm Freq}$ and potential's $R_{\rm Freq}$ are approximately the same *only* when the

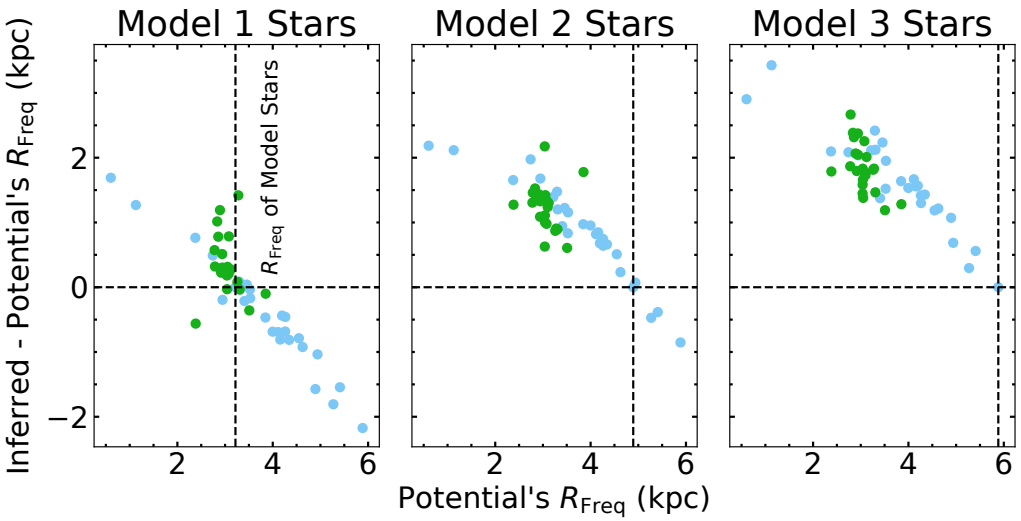

Figure 5.4: The change in the inferred R_{Freq} compared to the R_{Freq} of the potential. The inferred R_{Freq} is calculated from integrating 10,000 stars extracted from Model 1 (left), Model 2 (center) and Model 3 (right) for 1 Gyr in potentials with different bar lengths. Results using potentials based on the 29 Galaxy A snapshots are shown in light blue, while results using potentials based on the 29 Galaxy B snapshots are in green. The pattern speed is fixed to that of the model's bar from which the initial phase-space coordinates are extracted (Model 1, 2, or 3). The vertical black dashed line shows the R_{Freq} of Model 1, 2 or 3, respectively.

Note, we get a consistent result (y-axis value ≈ 0) only when the stars' 6D position and velocity data is consistent with the potential used.

potential is similar to the Model from which the initial positions and velocities are extracted as we show in Section 5.4.2.

5.4.2 Verifying the Method with Simulations

In this section, we perform three types of experiments. First, we test how the inferred R_{Freq} changes compared to the potential's R_{Freq} as we use potentials with varying bar length, but we fix the initial phase-space coordi-

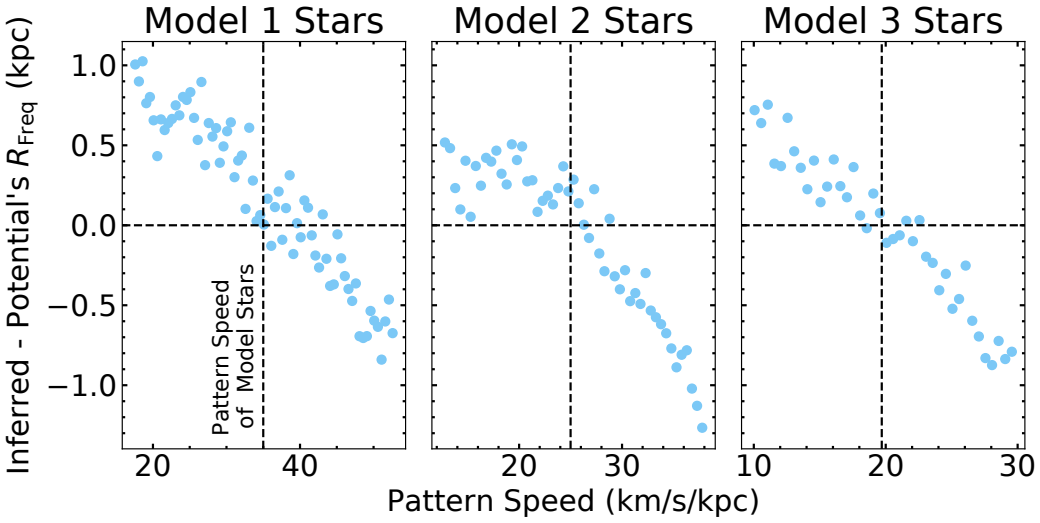

Figure 5.5: The effect of changing the potential's pattern speed on the inferred $R_{\rm Freq}$. In this plot, we use the same stars as in Figure 5.4, but we only use the corresponding Model's potential. We integrate 10,000 stars in the same potential for 1 Gyr using different pattern speeds each time and compare the inferred $R_{\rm Freq}$ from the orbits to the potential's $R_{\rm Freq}$. The vertical dashed line corresponds to the pattern speed calculated from the Model stars. In general, increasing the pattern speed at which the potential is rotated shortens the inferred $R_{\rm Freq}$. The inferred $R_{\rm Freq}$ is consistent with the potential's $R_{\rm Freq}$, only when the pattern speed is consistent with the Model stars.

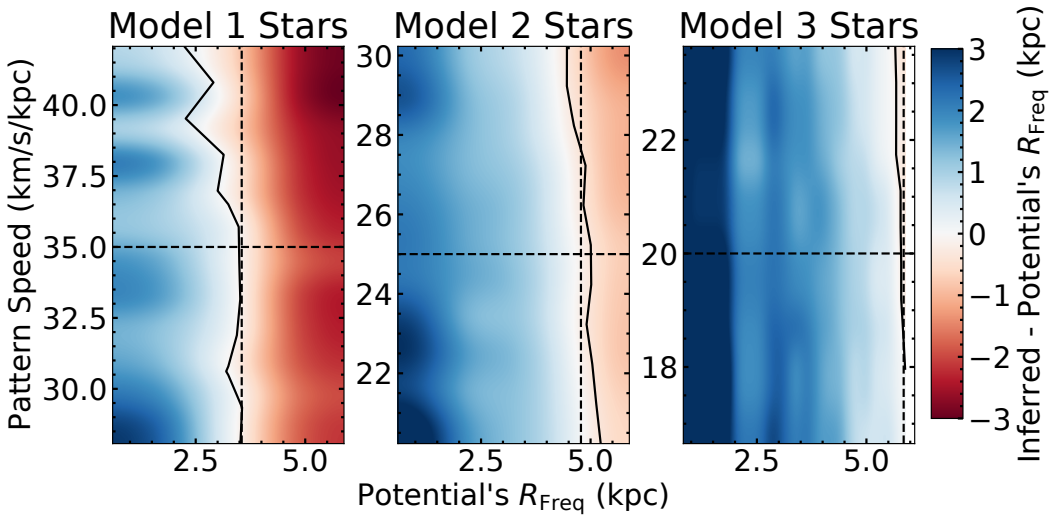

Figure 5.6: The difference between the inferred $R_{\rm Freq}$ and the potential's $R_{\rm Freq}$ as a function of the pattern speed and potential's $R_{\rm Freq}$. This figure is similar to Figure 5.4, except we also change the pattern speed (y-axis) by up to $\pm$ 20%. The color corresponds to the difference between the inferred $R_{\rm Freq}$ and the potential's $R_{\rm Freq}$, where red means the potential's $R_{\rm Freq}$ > the inferred $R_{\rm Freq}$ white is where the potential's $R_{\rm Freq}\approx$ the inferred $R_{\rm Freq}$ and blue means the potential's $R_{\rm Freq}$ < the inferred $R_{\rm Freq}$. The black line indicates where the potential's $R_{\rm Freq}$= the inferred $R_{\rm Freq}$. The black and grey vertical dashed lines mark the $R_{\rm Freq}$ and associated uncertainty of the model from which the stars' initial positions and velocities were extracted, while the horizontal black dashed line indicates its pattern speed. Even when the pattern speed is different than that of the stars by $\lesssim 20\%$, we still generally find a consistent inferred $R_{\rm Freq}$ only when the potential is consistent with the star's initial positions and velocities.

nates. We also hold the pattern speed of the potential constant at the value corresponding to the bar's pattern speed in the Model from which the initial phase-space coordinates are extracted. We show the results of these experiments for Model 1, 2 and 3 stars in Figure 5.4. In our next type of experiment, we hold the potential model and the initial phase-space coordinates constant but change the potential's pattern speed. The results of these experiments are shown in Figure 5.5. In our third type or experiment, which is shown in Figure 5.6, we vary both the pattern speed and the potential model, holding only the initial phase-space coordinates constant.

In Figure 5.4, we show the change in the inferred $R_{\rm Freq}$ for Model 1, 2, and 3 stars as they are integrated in potentials with different $R_{\rm Freq}$. On the y-axis, we show the inferred $R_{\rm Freq}$ compared to the $R_{\rm Freq}$ of the potential. We also show the potential's $R_{\rm Freq}$ on the x-axis. The left, center and right panels shows results for stars with initial positions and velocities extracted from Model 1, 2 and 3, respectively. We show the potential's $R_{\rm Freq}$ of Model 1, 2, and 3 as black vertical dashed lines with Models 1, 2 and 3 having a potential $R_{\rm Freq}$ of $\approx$3.22 kpc, 4.89 kpc, and 5.88 kpc, respectively (see Figure 5.3). It should be noted that here we assume the pattern speed is known and we rotate the potential with the pattern speed calculated from the corresponding Model stars.

We find that only when the potential's bar length is similar to the bar length of the model from which the initial positions and velocities are extracted do we measure a consistent inferred $R_{\rm Freq}$, i.e., the difference between the

inferred and potential's $R_{\rm Freq}$ is $\approx$0 kpc. That is to say, if the inferred $R_{\rm Freq}$ is significantly different from the $R_{\rm Freq}$ of the potential used to calculate the orbits, then we know that said potential is not representative of the initial 6D positions and velocities of the stars since it does not give a consistent result. Therefore, we can apply this to the Milky Way and constrain the Galactic bar's potential by testing which potential model provides an inferred $R_{\rm Freq}$ that is the same as the potential's $R_{\rm Freq}$ using APOGEE and *Gaia* data as our initial positions and velocities. However, first it is important to investigate the impact of different pattern speeds on these results given that the Milky Way's pattern speed is uncertain, although somewhat well-constrained.

In addition to the potential's bar length, we find that varying the potential's bar pattern speed also impacts the inferred $R_{\rm Freq}$. Similar to Figure 5.4, we recalculate the inferred $R_{\rm Freq}$ for Model 1, 2, and 3 stars, but instead of using potentials from different snapshots we assume the bar length is known. Specifically, we use the corresponding Model's potential and simply vary the pattern speed at which the potential is rotated as the orbits are integrated. We show the impact of varying the pattern speed on the inferred $R_{\rm Freq}$ in Figure 5.5. Similar to Figure 5.4, we have the difference between the inferred and potential's $R_{\rm Freq}$ on the y-axis. However, now we have the pattern speed on the x-axis. The vertical dashed line corresponds to the pattern speed of the bar in the respective Model 1, 2, and 3 snapshots (see Section 5.2 for calculation). In general, an increase in the pattern speed leads to a shorter inferred $R_{\rm Freq}$, while a decrease in the patter speed lengthens the inferred $R_{\rm Freq}$. However,

we need to determine how this behavior changes when the potential does not necessarily represent the model of the initial phase-space coordinates.

At this point, we have tested how the inferred $R_{\rm Freq}$ changes for a given set of initial phase-space coordinates when we vary either the potential's bar length or pattern speed. However, we have only varied one of these parameters at a time while we fixed the other to match that of the initial phase-space coordinate's model. Here, we test whether agreement between the potential and pattern speed will always lead to an inferred $R_{\rm Freq}$ consistent with the potential's, independent of the initial phase-space coordinates. Specifically, we perform the same experiment as in Figure 5.4, but instead of fixing the pattern speed to the value corresponding to the initial phase-space coordinate's models, we vary it so that it matches the potential model's bar pattern speed. We find that the initial phase-space coordinates play a major role in the inferred $R_{\rm Freq}$ and agreement between the potential and pattern speed does not always lead to an inferred $R_{\rm Freq}$ that matches the potential. Consistent with Figure 5.5, a faster or slower pattern speed can sometimes shorten or lengthen the inferred $R_{\rm Freq}$ to match the potential. Therefore, for each potential we could likely find a pattern speed that would shorten or length the inferred $R_{\rm Freq}$ to match that of the potential. Thus, it is crucial to have constraints on the pattern speed in order to determine the most consistent potential model.

In Figure 5.6, we test whether we can determine the correct potential model if the pattern speed is known to within 20%. Specifically, we recalculate the inferred $R_{\rm Freq}$ for Model 1, 2, and 3 stars using potentials with different

length bars *and* different bar pattern speeds. The pattern speed is shown on the y-axis, while the potential's $R_{\rm Freq}$ is on the x-axis. The color corresponds to the difference between the inferred and potential's $R_{\rm Freq}$ where blue means the inferred $R_{\rm Freq}$ > the potential's $R_{\rm Freq}$, white is where the inferred $R_{\rm Freq} \approx$ the potential's $R_{\rm Freq}$and red means the potential's $R_{\rm Freq}$> the inferred $R_{\rm Freq}$. The black line indicates where the inferred $R_{\rm Freq}$ = the potential's $R_{\rm Freq}$. The vertical black lines correspond to the $R_{\rm Freq}$ of the initial phase-space coordinates' Models. The horizontal black dashed lines correspond to the Model's bar pattern speed. As the difference in estimates for the Milky Way's pattern speed are ≈20% (Bovy et al., 2019), we wish to investigate the behavior of the inferred $R_{\rm Freq}$ when the assumed pattern speed is incorrect by up to 20%. We note that even the fastest pattern speed for a given Model does not decrease the corotation radius below the Model's A_2/A_0 bar length which would cause the bar to become ultrafast and violate our theoretical understanding of bars (Contopoulos, 1980, 1981; Buta & Zhang, 2009; Vasiliev & Athanassoula, 2015).

Even when the pattern speed does not match the initial positions and velocities of the stars, in general, we still find that we retrieve a consistent inferred $R_{\rm Freq}$ only when the assumed potential's bar length is similar to the bar length of the N-body snapshot from which the initial positions and velocities of the stars were taken. Consistent with Figure 5.5, we do see that at the highest pattern speeds, the inferred $R_{\rm Freq}$ begins to decrease. However, this effect is generally small compared to the uncertainties on $R_{\rm Freq}$ when the pattern speed

is within 20% of the Model's pattern speed. For the shorter bar in Model 1 (left panel), the faster pattern speed does lead to a potential model with a shorter bar being most consistent with the inferred $R_{\rm Freq}$. Therefore, we test a slow and fast bar model for the APOGEE data in Section 5.5. In general, it is possible to determine the bar length that corresponds to the initial positions and velocities of the stars if the bar's pattern speed is known to within 20%. As the Milky Way's bar pattern speed is known to within 20% (Bovy et al., 2019), we conclude that we can determine which bar potential is most consistent with the APOGEE and *Gaia* data.

5.5 Constraining the Milky Way's Bar Length

Currently, the gravitational potential in the center of the Milky Way is poorly understood, partly because the length of the Galactic bar is not well-constrained. However, several studies assume potentials and make conclusions about the Galactic bar based on the resulting stellar orbits (e.g., Queiroz et al., 2021; Lucey et al., 2021; Wylie et al., 2021). Furthermore, it is difficult to constrain exactly how the deviations of the assumed potential from the true underlying mass distribution will impact the stellar orbits and therefore the conclusions drawn from them. In this work, we have already discovered that $R_{\rm Freq}$ inferred from the stellar orbits changes when the assumed gravitational potential and pattern speed of the bar changes. This demonstrates that any conclusions from stellar orbits are greatly impacted by the assumed gravitational potential, but we can use this result to our advantage by finding which

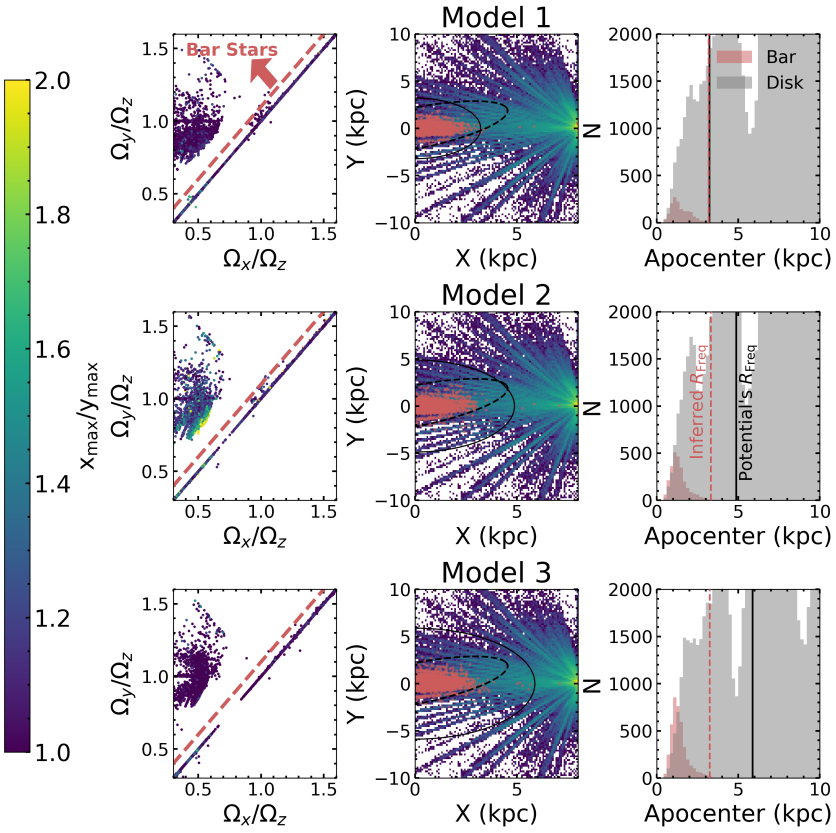

Figure 5.7: The selection and distribution of bar stars for the APOGEE/*Gaia* data integrated in three different potentials with different bar lengths. We assume a bar pattern speed of 41 km/s/kpc for the orbit calculation. The first column shows the orbital frequency map for ≈210,000 stars selected according to Figure 5.2 colored by the ratio of x_{max}/y_{max} where x is along the bar's major axis and y is along the minor axis. We also show a red dashed line corresponding to $\Omega_y/\Omega_z = \Omega_x/\Omega_z + 0.1$, as we select stars above this line as bar stars. The central column shows the spatial distribution of our selected bar stars (red points) compared to the rest of the stars. We also show the same bar model as in Figure 5.2 (dashed black line) as well as a circle with radius equivalent to the potential's $R_{\rm Freq}$ (solid black line). The last column shows the apocenter distribution from the orbits integrated in the corresponding model potential for 1 Gyr. The selected bar stars are shown in red and the rest of the stars are shown in grey. We also show the $R_{\rm Freq}$ of the potential as a black solid line. The red dashed line corresponds to the 99.5th percentile of the bar stars' apocenter distribution i.e., the inferred $R_{\rm Freq}$.

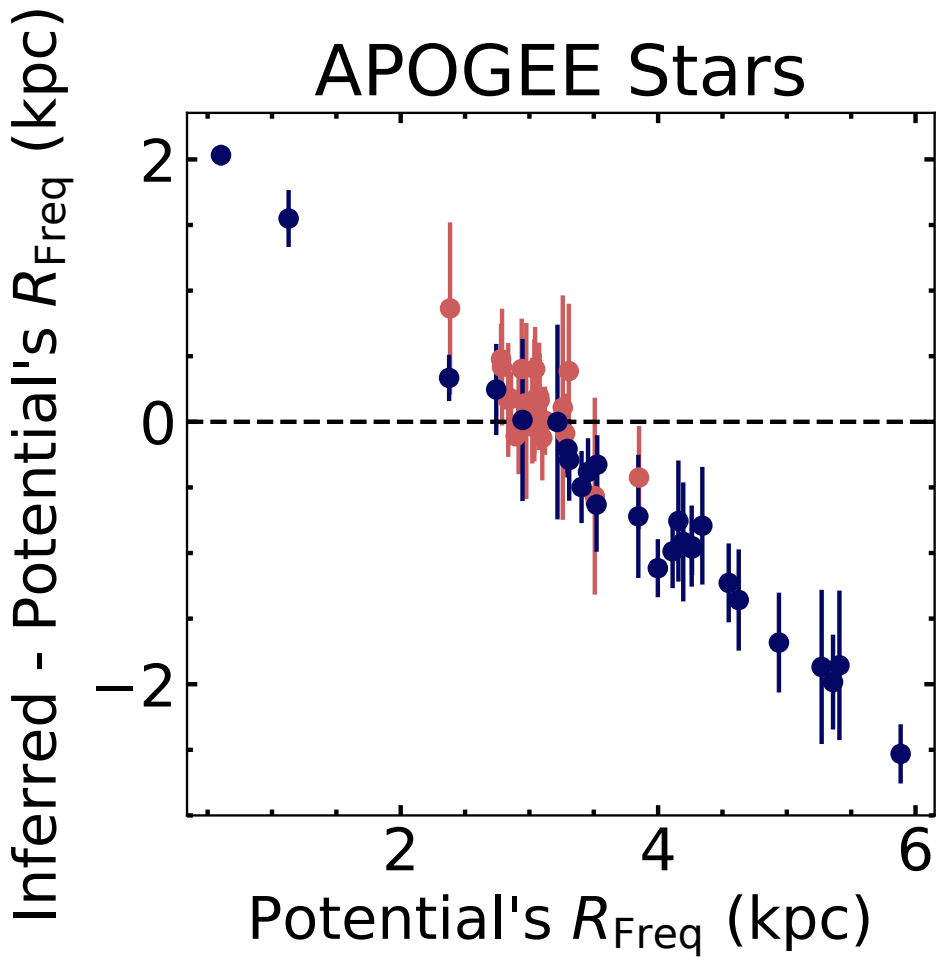

Figure 5.8: The comparison of the inferred $R_{\rm Freq}$ to the potential's $R_{\rm Freq}$ for APOGEE and *Gaia* stars that have been integrated in potentials with different bar lengths for 1 Gyr each, assuming a bar pattern speed of 41 km/s/kpc. Each point corresponds to the median inferred $R_{\rm Freq}$ of 10 random samples of ≈21,500 stars each with the error bar corresponding the standard deviation. The dark blue points correspond to potentials extracted from Galaxy A while the red points use potentials extracted from Galaxy B. We find potentials with $R_{\rm Freq}$ ≈3 kpc, which give the most self-consistent inferred $R_{\rm Freq}$s (i.e., the difference between the inferred and potential's $R_{\rm Freq}$ is ≈0 kpc). One of these potentials is Model 1.

potential gives a consistent result.

Using simulations, we have demonstrated that the inferred $R_{\rm Freq}$ from the apocenter distribution is only consistent with the $R_{\rm Freq}$ of the gravitational potential when that potential has a similar bar length to the snapshot from which the initial positions and velocities of the stars are extracted (see Figure 5.4). Therefore, we can determine which potential is consistent with observed positions and velocities of stars by determining which potential gives a consistent inferred $R_{\rm Freq}$ measurement. We apply this to the Milky Way by integrating APOGEE and *Gaia* stars in a variety of Milky Way-like potentials with different bar lengths.

Following the same methods as in Section 5.4, we integrate the orbits for 1 Gyr in a variety of potentials and report the 99.5th percentile of the apocenter distribution of stars in the bar as our inferred $R_{\rm Freq}$. At first, we assume a bar pattern speed of 41 km/s/kpc, consistent with previous estimates of the Milky Way's bar pattern speed (Portail et al., 2017; Sanders et al., 2019; Bovy et al., 2019). We calculate the orbits for the 215,869 stars shown in Figure 5.2. We divide this sample into 10 random samples so that we are computing ≈21,500 orbits at a time, which is the same order of magnitude of the simulation samples we used in Section 5.4. The final inferred $R_{\rm Freq}$ that we report is the median of the inferred $R_{\rm Freq}$s from the 10 random samples with the standard deviation as the corresponding uncertainty.

In Figure 5.7, we show the orbital frequency maps, galactic distribution and apocenter distributions of APOGEE/*Gaia* stars integrated in the Model 1,

2, and 3 potentials. The left column of Figure 5.7 is similar to the left column of Figure 5.3 with the selection of bar stars to the left of the red-dashed line. The middle panel shows the Galactic distribution of all of APOGEE/*Gaia* data with the selected bar stars shown in red. We show the same 5 kpc long bar as in Figure 5.2 rotated to 27° degrees in a dashed black line. In addition, we also show a circle with the radius equivalent to the potential's $R_{\rm Freq}$ derived from the apocenter distribution as a black solid line. We note that the Milky Way's bar angle is uncertain, thought estimates generally range from 25-27°. From visual inspection of the center panels of Figure 5.7, the stars selected as bar orbits appear to cluster closer to Y ≈0 kpc rather than higher Y values, suggesting the bar angle may be smaller than 27°. However, we defer determining whether the bar angle can be constrained from a similar method of checking for self-consistency until future work.

In the right column of Figure 5.7, we show the apocenter distribution of the disk stars in grey with the selected bar stars in red. The 99.5th percentile of the selected bar stars apocenter distribution (i.e., the inferred $R_{\rm Freq}$), is shown as a red dashed line with the potential's $R_{\rm Freq}$ as a black solid line. The inferred $R_{\rm Freq}$ and potential's $R_{\rm Freq}$ are similar for the APOGEE/*Gaia* data integrated in the Model 1 potential but are increasing different for the Model 2 and 3 potentials. This can also be seen from the Galactic distribution of the selected bar stars in the middle panel of Figure 5.7. For the APOGEE/*Gaia* data integrated in Model 1, the selected bar stars' Galactic distribution (red points) agrees with the potential's $R_{\rm Freq}$ (black dashed line). However, for the data

integrated in the Model 2 and 3 potentials, the selected bar stars' distribution mostly ends well within the potential's $R_{\rm Freq}$ indicating that the potential's $R_{\rm Freq}$ is likely larger than the data's true bar length. Based on our previous results from simulations, Model 1 is more consistent with the APOGEE/*Gaia* than Models 2 and 3 given that its potential leads to a more consistent $R_{\rm Freq}$ inference. However, it is important to test all of the 29 Galaxy A potentials and the 29 Galaxy B potentials to determine which of these potentials lead to the most consistent result.

In Figure 5.8, we show the difference between the inferred $R_{\rm Freq}$ and the potential's $R_{\rm Freq}$ for a variety of potentials with different bar lengths using APOGEE and *Gaia* stars. The dark blue points correspond to potentials extracted from Galaxy A (Bennett et al., 2021) while the red points correspond potentials from Galaxy B (Tepper-Garcia et al., 2021). Each point is calculated using the median inferred $R_{\rm Freq}$ of 10 samples of ≈21,500 APOGEE and *Gaia* stars with the uncertainty as the standard deviation. As demonstrated with simulations in Section 5.4, the gravitational potentials that are most consistent with the APOGEE and *Gaia* data will have a difference between the inferred $R_{\rm Freq}$ and the potential's $R_{\rm Freq}$ that is closest to zero kpc. From 5.8, we find that the potentials with a $R_{\rm Freq}$ of ≈3 kpc are most consistent with the APOGEE and *Gaia* data. Galaxy B has many potentials with $R_{\rm Freq}$ ≈3 kpc and are therefore consistent with the APOGEE and *Gaia* data. The Galaxy B potential that is most consistent with the APOGEE data has a potential $R_{\rm Freq}$ of 3.12 kpc. The inferred $R_{\rm Freq}$ from integrating the APOGEE data in this

potential is 3.13 kpc, 0.01 kpc higher than the potential's. On the other hand, the most consistent Galaxy A potential is Model 1 with $R_{\rm Freq}$ of 3.22 kpc, and the resulting APOGEE inferred $R_{\rm Freq}$is 3.22 kpc, only 0.002 kpc shorter than the potential's.

We also recalculate Figure 5.8 assuming a pattern speed of 60 km/s/kpc to match the estimate from Wang et al. (2012). With this pattern speed, we find that all of the Galaxy A potentials give an inferred $R_{\rm Freq}$ that is much shorter than the potential's $R_{\rm Freq}$. However, inferred $R_{\rm Freq}$s measured using Galaxy B potentials are less impacted by the faster pattern speed. We find that the Galaxy B potentials with $R_{\rm Freq}\approx$3 kpc are still the only potentials that give self-consistent inferred $R_{\rm Freq}$s.

In this work, we have only tested potentials based on N-body snapshots. However, the method presented here can be used to test any Milky Way potential model, including analytical potentials. One would need to sample initial phase-space coordinates from the analytical potential distribution in order to calculate the potential's $R_{\rm Freq}$.

It is important to note that our bar length estimate does **not** reclassify the Galactic bar as a 'fast' bar. The 'fast'/'slow' classification is based on the dimensionless ratio $\mathcal{R} = R_{CR}/R_{bar}$ where R_{CR} is the corotation radius and R_{bar} is the bar length. Historically, these classifications are performed using estimates of the bar length that are based on the number density counts (Debattista & Sellwood, 2000; Chiba & Schönrich, 2021) which is different than the dynamical $R_{\rm Freq}$ we measure above. For further discussion of the

Table 5.2: Bar Length Estimates for Model 1

	Model 1
Method	Bar Length Estimate (kpc)
$R_{\rm Fourier}$	4.84
Potential's R_Ω	3.22
Inferred R_Ω with APOGEE Stars	3.22
R_{x_1}	3.50

various methods for estimating and defining bar lengths see Section 5.6.

5.6 Methods of Measuring Bar Length

In this work, we define a quantity, $R_{\rm Freq}$, as a measure of bar length (see method described in Section 5.4). However, $R_{\rm Freq}$ is not a robust measurement of the bar length since it excludes x_1 orbits which have Ω_y/Ω_x=1 and are the backbone of most bars (Wang et al., 2016). There are a number of methods to measure bar lengths, but each method can lead to varying results. The dynamical length of a bar is defined by the maximal extent of trapped orbits. As x_1 orbits are the dominant bar orbits, especially at the ends, their maximal extent is the dynamical length of a bar. In this section, we determine the maximal extent of x_1 orbits for the Model 1 potential and compare it to other methods of measuring the length of bars. We focus on the Model 1 potential for this comparison, as it was the most consistent with the APOGEE/*Gaia* data. However, we note that the consistency of bar length measurements using different methods can be very dependent on the bar age and morphology (Petersen et al., 2019a; Hilmi et al., 2020).

One common method for measuring the bar length in external and model galaxies is Fourier decomposition using $A_{2,2}/A_0$ (see Section 6.2 for the calculation). For our Model 1 potential this leads to a bar length measurement of 4.84 kpc. However, the Fourier decomposition method has been shown to measure larger bar lengths than other methods (Petersen et al., 2019a). Similar to the method for measuring the bar length in external galaxies by fitting ellipses to the surface brightness, the Fourier decomposition method especially measures longer bar lengths when spiral arms are attached which is the case for most of the bars in external galaxies (Hilmi et al., 2020). Model 1 has weak spiral arms attached to the bar so it is possible that the measurement of bar length with this method is especially large. Interestingly, the $R_{\rm Fourier}$ of 4.84 kpc for this potential is similar to the Milky Way's bar length estimate (5 kpc) from number density counts (Wegg et al., 2015). However, Hilmi et al. (2020) suggest this measurement may be overestimated by 1-1.5 kpc given recent observations of spiral arms attached to the bar (Rezaei Kh. et al., 2018).

We also use another dynamical method of measuring the bar length from Petersen et al. (2021). For a complete description of the method we refer the reader to Petersen et al. (2016, 2021). In short, the method classifies bar stars based primarily on the angular distance between the apocenter positions of the star's orbit and the bar axis. Using this method we can cleanly select x_1 orbits which is the family of orbits associated with the inner Lindblad resonance ($2\Omega_\phi - \Omega_r = 1\Omega_{\rm b}$) and whose maximal extent provides a robust

estimate of the dynamical length of the bar (Petersen et al., 2019a). In similar models, Petersen et al. (2019b) found that the x_1 orbits are responsible for nearly all of the self-gravity of the $m = 2$ Fourier mode bar. With the x_1 orbits we measure R_{x_1}= 3.50 kpc for Model 1, which is slightly longer than the potential's $R_{\rm Freq}$, consistent with expectations that x_1 orbits make up the longest part of the bar (Wang et al., 2016).

Given the variation of measured bar lengths from the different methods, it is important to be careful when comparing reported bar length estimates in the literature. To avoid this, instead of emphasizing a specific bar length measurement, we emphasize Model 1 as the most consistent model for the Milky Way bar, for which we measure a *dynamical*[2] bar length of $R_{x_1}\approx$3.5 kpc with an overdensity that extends to $R_{\rm Fourier}\approx$4.8 kpc. We encourage a movement towards publicly available potential models that would allow for easier direct comparison between dynamical results for the inner Galaxy. We note our method can be used to check any potential for consistency with Milky Way data. However, it is important to test any potential model with simulated particles, as we have done in this work, to ensure a bias is not introduced by an incomplete selection of bar orbits with the orbital frequency method.

Another important thing to note is the dependence of the orbital structure of the inner Galaxy on the assumed potential model. This is apparent from looking at the orbital frequency maps in Figure 5.7. Using the three

[2]We define the dynamical bar length as R_{x_1}, the maximal extent of trapped x_1 orbits that participate in the solid-body rotation.

different potential models, we find the distribution of fundamental frequencies for the orbits are significantly different. The distribution of orbital frequencies for Model 1 and 2 are somewhat similar, but the ratios of the longest distance from the Galactic center along the bar's major axis to the bar's minor axis (x_{max}/y_{max}) are quite different. Although we have found that Model 1 leads to the most consistent result for the $R_{\rm Freq}$ determination, we are unsure if other parameters (e.g, the vertical structure and width) are accurate approximations for the Milky Way. Furthermore, we are unsure of how these other parameters may impact the orbital structure. Therefore, we caution the community to be wary when making conclusion about the inner Galaxy from orbits without doing a thorough investigation on the potential dependence.

5.7 Conclusions

In this work, we develop a new method to dynamically estimate the bar length directly from orbit integration. First, we verify this method using simulations. In short, we select a sample of bar stars using fundamental frequency maps of orbits and use the 99.5th percentile of the apocenter distribution as the $R_{\rm Freq}$. We find that when the initial position and velocity distribution of the star particles are extracted from the distribution of the potential model, then we achieve a consistent result in that the measured $R_{\rm Freq}$ from the orbits matches that of the potential. However, if the initial positions and velocities are extracted from a significantly different distribution than the potential's, then the measured $R_{\rm Freq}$ from the orbits is different than that of the potential

used to calculate said orbits. With this result, we can find the potential that matches the distribution from which the initial positions and velocities are taken by finding which potential leads to a self-consistent measured $R_{\rm Freq}$.

We then apply this new method to the Milky Way and find which potential leads to a sellf-consistent measured $R_{\rm Freq}$ for the APOGEE/*Gaia* data. We find our Model 1 (see Section 5.4 and Figure 5.1) is the most consistent potential. This model is derived from the `MWPotential2014-3` simulation in Bennett et al. (2021) and has a dynamical bar length of 3.50 kpc.

However, it is important to note that there are many methods of estimating the bar length, which can lead to biases dependent on bar age and morphology (Petersen et al., 2019a; Hilmi et al., 2020). For the Model 1 potential, we also measure a bar length of 4.84 kpc from the $m = 2$ mode of the Fourier decomposition. However, this method is known to give high estimates of bar lengths, especially in the case of connecting spiral arms. Given the inconsistency of bar length measures, we emphasize the importance of making gravitational potential models public for the Milky Way in order to make fair comparisons between results. Furthermore, we note that our method for checking consistency to constrain the bar length can be used with any potential and we encourage the community to test their favorite potential before using it to draw conclusions about the inner Milky Way. In future work, we plan to further investigate the orbital structure of the Milky Way's bar and its dependence on various potential model parameters.

Chapter 6

Carbon-Enhanced Metal-Poor star candidates from BP/RP Spectra in *Gaia* DR3

Abstract: Carbon-enhanced metal-poor (CEMP) stars make-up almost a third of stars with [Fe/H]<–2, although their origins are still poorly understood. It is highly likely that one sub-class (CEMP-*s* stars) is tied to mass-transfer events in binary stars, while another sub-class (CEMP-no stars) are enriched by the nucleosynthetic yields of the first generations of stars. Previous studies of CEMP stars have primarily concentrated on the Galactic halo, but more recently they have also been detected in the thick disk and bulge components of the Milky Way. *Gaia* DR3 has provided an unprecedented sample of over 200 million low-resolution ($R \approx 50$) spectra from the BP and RP photometers. Training on the CEMP catalog from the SDSS/SEGUE database, we use `XGBoost` to identify the largest all-sky sample of CEMP candidate stars to date. In total, we find 58,872 CEMP star candidates, with

[1] This chapter is based on Lucey M., Al Kharusi N., Hawkins K., Ting Y.S., Ramachandra N., Price-Whelan A.M., Beers T.C., Lee Y.S., Yoon J., 2022, Submitted to MNRAS. The author of this document, Madeline Reinke Lucey, completed most of the analysis and wrote the publication. The project was developed in collaboration with and supervised by K. Hawkins, Y.S. Ting, and N. Ramachandra. N. Al Kharusi and A.M. Price-Whelan assisted in part of the analysis. T.C. Beers provided crucial data for this work.

an estimated contamination rate of 12%. When comparing to literature high-resolution catalogs, we positively identify 60-68% of the CEMP stars in the data, validating our results and indicating a high completeness rate. Our final catalog of CEMP candidates spans from the inner to outer Milky Way, with distances as close as $r \sim 0.8$ kpc from the Galactic center, and as far as $r > 30$ kpc. Future higher-resolution spectroscopic follow-up of these candidates will provide validations of their classification and enable investigations of the frequency of CEMP-s and CEMP-no stars throughout the Galaxy, to further constrain the nature of their progenitors.

6.1 Introduction

Stellar chemical abundances act as a fossil record of the interstellar medium (ISM) from the time a star is formed, given that a star's atmospheric abundances generally do not change over its lifetime. Therefore, it is generally true that more metal-poor stars formed at earlier times when the Universe contained fewer metals. Furthermore, the detailed chemical composition of metal-poor stars can illuminate the early chemical evolution of the Universe that resulted from the lives and deaths of the first generations of stars.

Many studies of metal-poor stars have focused on the Galactic halo, where the metallicity distribution function is dominated by metal-poor stars (e.g., Beers & Christlieb, 2005; Frebel & Norris, 2015). These studies have found a significant fraction of metal-poor stars in the halo that exhibit high levels of carbon enhancement ([C/Fe] $> +0.7$), and are referred to as carbon-

enhanced metal-poor (CEMP) stars (e.g., Beers et al., 1992; Beers & Christlieb, 2005; Christlieb et al., 2008). This fraction increases with decreasing metallicity in the Galactic halo, with carbon-enhanced stars making up 10–30% of stars with [Fe/H]<–2 and ≈80% of stars with [Fe/H]<–4 (Lucatello et al., 2006; Lee et al., 2013; Placco et al., 2014; Yoon et al., 2018). However, as cautioned by Arentsen et al. (2022), it can be difficult to compare these fractions across different samples of CEMP stars, given the various selection effects and differences in the abundance analysis from study to study.

Further analysis of CEMP stars have identified a number of sub-classes (Beers & Christlieb, 2005). A significant fraction of CEMP stars exhibit enhancements of slow neutron-capture (s-process) elements (such as Ba), and are thus called CEMP-s stars. There also exist small numbers of CEMP-r stars, which show enhancements in rapid neutron-capture (r-process) elements (such as Eu), CEMP-r/s stars, which exhibit enhancements in both r- and s-process elements (Gull et al., 2018), and CEMP-i stars, which exhibit enhancements of intermediate neutron-capture (i-process) elements (Frebel, 2018). The CEMP-no sub-class of stars does not exhibit over-abundances of neutron-capture elements. The CEMP-r, CEMP-r/s, and CEMP-i sub-classes are sparsely populated in extant samples, while the CEMP-s and CEMP-no stars are the most common (see, e.g., Zepeda et al. 2022).

It is thought that CEMP-s stars, which are more common at [Fe/H] > –3.0, are the result of chemical enrichment by mass-transfer events from (post-)asymptotic giant branch (AGB) stars (Lugaro et al., 2012; Placco et al.,

2013). This hypothesis is strongly supported by the high rate of binarity among CEMP-*s* stars (McClure & Woodsworth, 1990; Preston & Sneden, 2001; Lucatello et al., 2005; Bisterzo et al., 2010; Abate et al., 2015; Hansen et al., 2016b; Jorissen et al., 2016). In fact, binarity rates as high as 82% have been reported for CEMP-*s* stars (Hansen et al., 2016b).

On the other hand, CEMP-no stars have a lower rate of binarity than CEMP-*s* stars and therefore are less likely to have experienced a mass-transfer event (Starkenburg et al., 2014; Hansen et al., 2016a; Arentsen et al., 2019). Hence, CEMP-no stars likely formed from an ISM that was already carbon enhanced. Given their low metallicity and increasing frequency at lower metallicities, it is thought that these stars are truly ancient stars, and were primarily enriched by the first generation of stars. It has been suggested that massive first stars may have had high rotation rates, which would lead to large carbon production (Chiappini et al., 2006; Meynet et al., 2006). Furthermore, it is possible that the first stars exploded as faint supernovae, which also overproduce carbon (Umeda & Nomoto, 2003; Nomoto et al., 2013; Tominaga et al., 2014). Yoon et al. (2016) have associated CEMP-no stars with their Morphological Groups III and II, respectively, corresponding to these two primary carbon-production sources.

Initial studies indicate that the frequency of CEMP-*s* and CEMP-no stars varies throughout the Galaxy. Specifically, the number of CEMP stars appears to increase with increasing distance from the Sun, although we note that these studies are mostly focused on the Galactic halo (Carollo et al.,

2012; Frebel et al., 2006; Lee et al., 2017; Yoon et al., 2018). Furthermore, the relative fraction of CEMP-no stars compared to CEMP-s stars also increases at larger distances (Carollo et al., 2014; Lee et al., 2019). Ultra-faint dwarf galaxies have shown similar fractions of CEMP-no stars as the Milky Way, but dwarf spheroidal galaxies have a clear deficit of CEMP-no stars (Norris et al., 2010; Lai et al., 2011; Frebel et al., 2014; Skúladóttir et al., 2015; Salvadori et al., 2015). In a comparative study between Galactic halo and dwarf galaxy CEMP stars, Yoon et al. (2019) suggests that the majority of Galactic halo CEMP-no stars have been accreted from dwarf galaxies. Furthermore, CEMP-no and CEMP-s stars have been discovered in the metal-weak thick disk (MWTD; Beers et al., 2017). Dietz et al. (2021) tentatively associated the retrograde MWTD CEMP-no population with the Gaia-Enceladus system, while suggesting that the equivalent prograde population has both in-situ and ex-situ origins.

There are fewer studies of metal-poor stars towards the center of the Galaxy compared to the Galactic halo. This is partly due to the difficulty of targeting metal-poor stars in a region of the Galaxy that is dense with metal-rich stars. Furthermore, high levels of extinction demand long exposure times and large-aperture telescopes in order to achieve sufficient signal-to-noise spectroscopic observations for metallicity measurements. Fortunately, the advent of metallicity-sensitive photometric surveys (e.g., Skymapper and Pristine; Bessell et al., 2011; Wolf et al., 2018; Starkenburg et al., 2017b) have led to studies of thousands of metal-poor inner Galaxy stars. Studies using

SkyMapper photometry have found a much lower fraction of CEMP stars in the inner Galaxy compared to the Galactic halo (Howes et al., 2014, 2015, 2016; Lucey et al., 2022). However, metallicity estimates from Skymapper photometry have proven to be biased against CEMP stars (Da Costa et al., 2019; Chiti et al., 2020). Targeting with Pristine photometry, Arentsen et al. (2021) found a CEMP frequency that is consistent with the Galactic halo for stars with [Fe/H] <-3, but also found that it is much lower than the halo at higher metallicities.

Measuring and understanding the frequency and relative rates of CEMP-no/CEMP-*s* stars throughout the Galaxy will be crucial for shedding new light on the origins and formation mechanisms of these stars, including whether or not CEMP-no stars are true inheritors of the elements created by the first stars. Given that the measured properties of CEMP samples have been shown to vary across different samples (Arentsen et al., 2022), creating a uniformly analyzed sample with limited selection effects across the Milky Way will be essential for achieving this goal. The release of the *Gaia* BP/RP spectra in DR3 presents a unique opportunity to identify the largest, all-sky sample of CEMP stars to date (Witten et al., 2022). However, the BP/RP spectra have quite low resolution ($R = \lambda/\Delta\lambda \approx 50$), and require unconventional methods for analysis.

In this work, we present a novel method for detecting CEMP stars in the *Gaia* BP/RP spectra with machine learning, specifically the `XGBoost` classification algorithm, and apply it to the spectra released in DR3. In Section

6.2 we describe the BP/RP spectra, along with other data used in our analysis. We introduce `XGBoost`, our chosen classification algorithm. in Section 6.3. We evaluate the accuracy and sensitivity (i.e., completeness) of our classification in Section 6.4. In Section 6.5, we interpret the `XGBoost` model. Finally, in Section 6.6 we present the sample of CEMP candidate stars, along with an investigation of their metallicity and Galactic distributions.

6.2 Data

The *Gaia* mission has revolutionised Milky Way astronomy and beyond, primarily by providing astrometric data for billions of stars (Gaia Collaboration et al., 2016a, 2022). Simultaneously, the *Gaia* mission has also been collecting low-resolution spectra ($R \approx 50$), with the blue photometer (BP) and red photometer (RP; De Angeli et al., 2022). These spectra have provided effective temperature (T_{eff}), surface gravity ($\log g$), and metallicity ([M/H]) estimates (Liu et al., 2012; Andrae et al., 2022), but have too low of a resolution to provide further elemental abundances (Gavel et al., 2021). Molecules, however, absorb large bands of light, and therefore may be easier to detect in the BP/RP spectra. Given the wavelength coverage of 3300–10500 Å (Carrasco et al., 2021), we expect to be able to detect carbon-enhanced stars from the plethora of carbon molecular bands in that range (e.g., C_2 Swan bands at $\approx$ 4500–6000 Å, and CN bands at $\approx$ 7000–10500 Å). The ability to measure carbon abundances from mock BP/RP spectra has been explored by Witten et al. (2022), but they make use of a different method than this work

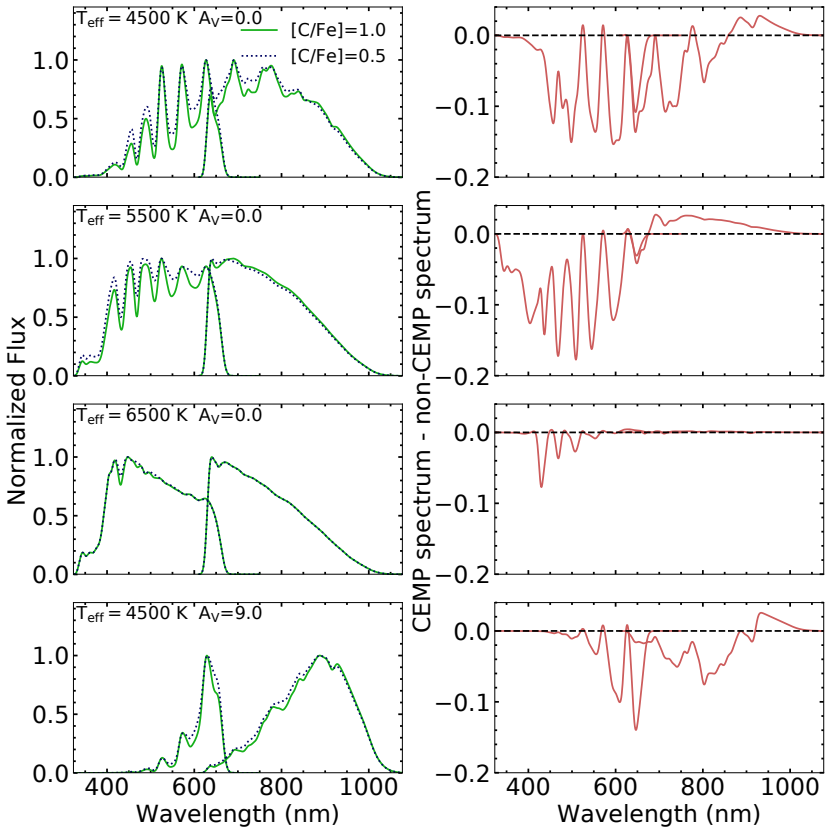

Figure 6.1: Examples of synthetic mock BP and RP spectra (left), and the impact of carbon enhancement on the spectra (right). Specifically, in the left panels, we compare stars of the same stellar parameters and reddening, except with different carbon abundances. The BP and RP spectra are plotted separately, with the BP spectra at lower wavelengths. The BP and RP spectra overlap at ≈650 nm. The blue dotted lines have [C/Fe] = +0.5, while the green solid lines have [C/Fe] = +1.0. Starting from the top, which has typical stellar parameters for a metal-poor giant (T_{eff}= 4500 K, log g = 2.5 and [Fe/H] = –2.0), we increase the T_{eff} to 5500 K in the second row and 6500 K in the third row. The fourth row has T_{eff}= 4500 K, but with increased extinction at A_V=9.0 mag. In the right panels, we have subtracted the dotted spectrum ([C/Fe] = +0.5) from the solid spectrum ([C/Fe] = +1.0) for each row. The impact of carbon on the spectra changes drastically with the stellar parameters with higher T_{eff}s having weaker signals and extinction erasing the signal in the bluest wavelengths. We, therefore, require a flexible classification model in order to achieve low contamination of our detected carbon-enhanced stars.

and also do not model the impact of dust extinction.

To explore the impact of carbon on the BP/RP spectra, we create mock synthetic spectra. We employ the MARCS carbon-enhanced model atmosphere grids (Gustafsson et al., 2008) and the TURBOSPECTRUM radiative transfer code (Alvarez & Plez, 1998; Plez, 2012) to construct these spectra. We also use the fifth version of the Gaia-ESO atomic linelist (Heiter et al., 2020) with the addition of molecular lines for CH (Masseron et al., 2014), CN, NH, OH, MgH, C_2 (T. Masseron, private communication), SiH (Kurucz linelists[2]), and TiO, ZrO, FeH, CaH (B. Plez, private communication). To apply the instrumental profile of the BP/RP photometers, we use the DR3 calibrated passbands (Riello et al., 2021). The true spectral resolution is a function of wavelength for both BP and RP spectra, with the BP spectra ranging from $R \approx 100$ at the blue edge to $R \approx 30$ at the red edge, and the RP spectra ranging from $R \approx 100$ at the blue edge to $R \approx 70$ at the red edge. To simplify the calculation, we assume a resolution of 50 for the BP spectra and 70 for the RP spectra. We also model the impact of dust extinction using the `DUST_EXTINCTION`[3] package with the extinction curve from Fitzpatrick (2004), assuming R_V=3.1.

Figure 6.1 shows examples of a number of synthetic mock spectra, along with the impact of carbon on the calculated flux. The left panels shows eight spectra, in sets of two with the same stellar parameters, except one spectrum

[2] `http://kurucz.harvard.edu`
[3] `https://github.com/karllark/dust_extinction`

has [C/Fe] = +0.5 (blue dotted line) and the other has [C/Fe] = +1.0 (green solid line). We start with the stellar parameters of a typical metal-poor giant star (T_{eff} = 4500 K, log g= 2.5 and [Fe/H] = –2.0) in the top row. We then increase the T_{eff} to 5500 K in the second row and T_{eff}=6500 K in the third row. The spectra in the bottom row have T_{eff}=4500 K but A_V=9.0 mag. This is a worst-case example, since we expect very few spectra released in *Gaia* DR3 to have $A_V \geq$9.0 mag, given that most stars have $G < 17.6$. In the right panels, we subtract the spectrum with [C/Fe] = +1.0 from the spectrum with the same stellar parameters, but with [C/Fe] = +0.5.

The impact of carbon enhancement on the BP/RP spectra (Fig. 6.1) is very dependent on the T_{eff} and reddening. Compared to the standard metal-poor giant (T_{eff} =4500 K), the hottest star (T_{eff} = 6500 K) has a significantly weaker signal. This is likely a consequence of the dissociation of carbon molecules in the atmospheres of hotter stars (T_{eff}>6000 K). This is consistent with results from Witten et al. (2022) which found that the T_{eff} must be <6000 K in order to achieve precision on the carbon abundance of <0.5 dex for stars with [Fe/H]=–2.0 with *Gaia* BP/RP spectra. Furthermore, reddening greatly reduces the flux, and therefore the strength of the carbon-enhancement signal in the bluest wavelengths. Fortunately, there are carbon molecules (e.g., CN bands at $\approx$ 7000–10500 Å) that impact the RP spectra so we are still able to detect reddened carbon-enhanced stars. These four combinations of T_{eff} and reddening values lead to significantly different results for the impact of carbon enhancement on the BP/RP spectra. As we hope to be

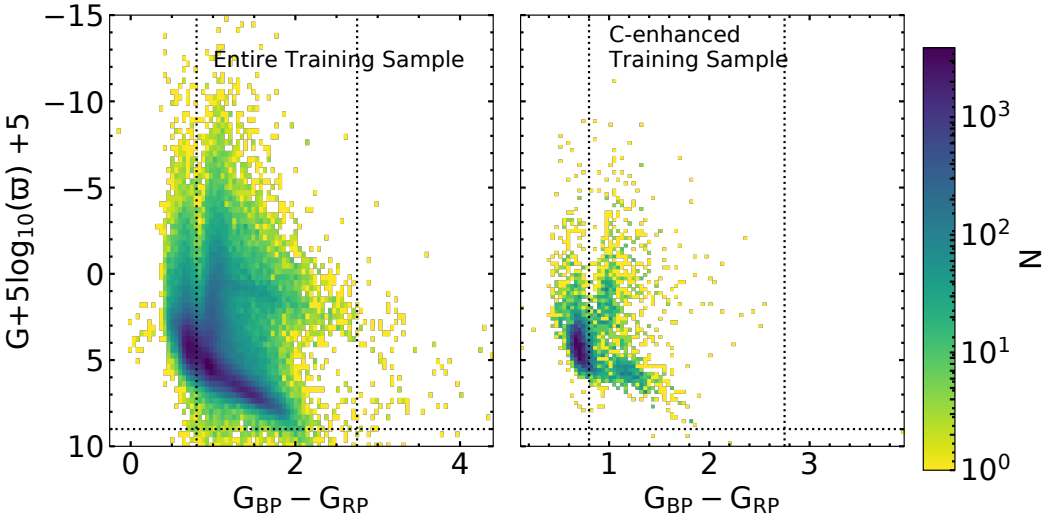

Figure 6.2: Color-magnitude diagram of our training sample from SDSS/SEGUE. The x-axis is the *Gaia* $G_{BP} - G_{RP}$ color; the y-axis is the absolute G magnitude, calculated from the distance modulus using the *Gaia* apparent G magnitude and parallax. The left panel shows the entire training set, while the right panel only shows stars with [C/Fe] $> +0.7$. The black dashed lines correspond to the color and magnitudes cuts made on our training/testing sample. The logarithmic color bar corresponds to the number of stars for each data point.

able to detect carbon-enhanced stars across a wide range of stellar parameters and reddenings, we require a complex model that can adapt to the different signals of carbon enhancement. To balance complexity with interpretability, we choose `XGBoost` as our algorithm for detecting carbon-enhanced stars.

6.2.1 Training and Testing Sample

In order to teach our model how to accurately detect carbon-enhanced stars, we require a sample of stars that are already classified. To acquire this,

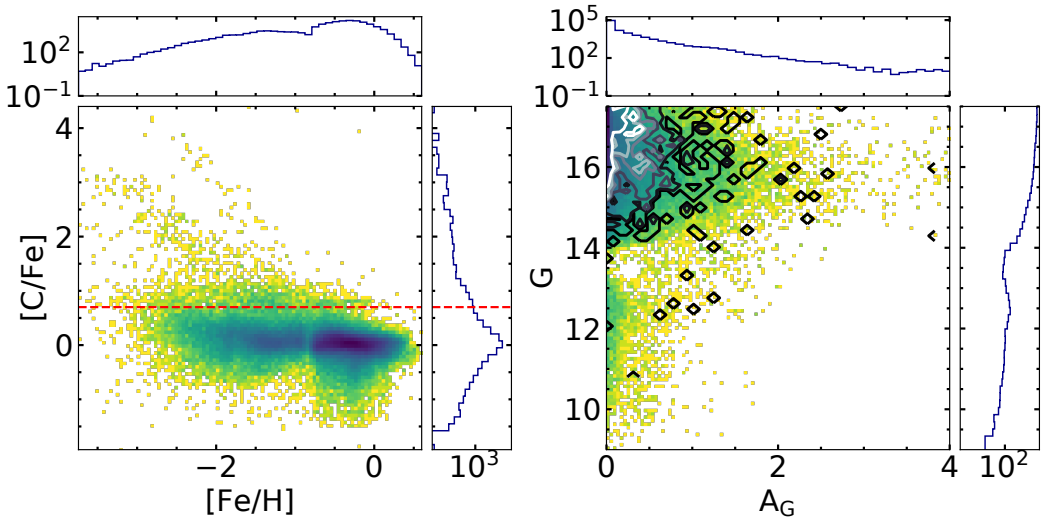

Figure 6.3: Relevant properties of the training/testing sample from the SDSS/SEGUE. The left panel shows the carbonicity ([C/Fe]), as a function of metallicity ([Fe/H]), with our definition of carbon-enhanced ([C/Fe] $> +0.7$) marked as a red dashed line. We also show the marginal histogram of each parameter on the corresponding axis. The right panel is a similar plot, but the axes are instead the extinction (A_G; Andrae et al., 2022) and apparent *Gaia G* magnitude. From inspection, the training/testing samples span a large range of parameters, similar to what we expect for the data we classify. In both plots the colors of the data points correspond to the logarithmic color bar shown in Fig.6.2. In the right panel, we also overlay the distribution of the CEMP stars in the training/testing sample as black/white contour lines.

we employ the spectroscopic catalogs of parameters for stars from the SDSS survey, and its various extensions, including the Sloan Extension for Galactic Understanding and Exploration (SEGUE; Yanny et al., 2009; Lee et al., 2013; Rockosi et al., 2022) , which obtained over 500,000 low-resolution ($R = 2000$) optical spectra. For simplicity, we refer to this collection of spectra as the SDSS/SEGUE sample.

The SEGUE Stellar Parameter Pipeline (SSPP; Allende Prieto et al. 2008b; Lee et al. 2008b,a, 2011; Smolinski et al. 2011; Lee et al. 2013) has continued to be refined since its introduction. In the process, additional calibration stars with available high-resolution spectroscopic analyses have been used to improve estimates of the stellar parameters from the SDSS/SEGUE spectra. The most recent version of the SSPP has been run through the stellar samples we employ. Note that, at this stage, the spectra include examples of objects originally targeted as QSO or candidate galaxy candidates, but that turned out to have spectra that were stellar in appearance. This is important, since numerous late-type CEMP stars turned out to be originally targeted as QSOs, based on their photometry (strong carbon absorption features can lead to colors that mimic quasars).

After removal of duplicates (retaining the parameter estimates for the highest signal-to-noise (S/N) spectrum among repeated objects), the full set of spectra were then inspected visually (by Beers), for the identification of defective spectra that could perturb the stellar parameter estimates, the identification and rejection of white dwarfs, some of which were missed by the flags

raised by the SSPP, as well as likely spectroscopic binaries, often comprising a white dwarf and a late-type star. For the recognized spectroscopic binaries that do not include a white dwarf, the estimated stellar parameters are not necessarily compromised, as the SSPP parameters primarily consider features in the bluer portion of the spectrum. Nevertheless, we conservatively dropped them from inclusion. Care is taken in order to evaluate the best available estimate of [Fe/H], based on consideration of the various techniques available in the SSPP.

Note that for the purpose of the present application, we use the measured carbon abundances, without corrections for evolutionary effects (e.g., the first and second dredge ups, see Placco et al. 2014). This means that there are stars that appear to have [C/Fe] estimates below our adopted CEMP cutoff, but would appear above this cutoff once corrections are applied. This is appropriate since, at this stage, we are primarily interested in identifying candidate CEMP stars in the *Gaia* DR3 sample, and this conservative choice ensures that we do not miss-classify stars due to uncertainties in the corrections.

After the culling procedure described above, we are left with 569,874 stars, of which 29,399 have [C/Fe] $> +0.7$. We find that 233,604 of the original 569,874 stars have BP/RP spectra released in *Gaia* DR3, of which 9,094 ($\approx$4%) have [C/Fe] $> +0.7$. In preliminary tests, we found that our algorithm is incapable of detecting carbon enhancement in warmer stars, due to the weakness of the molecular carbon bands, so we apply a cut in the $G_{BP} - G_{RP}$ color. Specifically, we only include stars with $G_{BP} - G_{RP} > 0.8$, which roughly corresponds

to T_{eff} ≈6000 K (Andrae et al., 2018). This cut is consistent with results from Witten et al. (2022), who found they could achieve a carbon-abundance precision of ≈0.5 dex for stars with [Fe/H] < -2 only if they restrict their analysis to stars with $T_{eff} < 6000$ K. This final trim leaves samples of 1,514 carbon-enhanced stars and 141,108 carbon-normal stars.

We randomly select ≈30% of these data as our testing sample, while the remaining ≈70% is used for training. Figure 6.2 shows color-magnitude diagrams of our training sample. The left panel shows the *Gaia* DR3 $G_{BP} - G_{RP}$ color on the x-axis and the absolute G magnitude calculated using the *Gaia* parallax and apparent G magnitude on the y-axis for the entire training/testing sample. The right panel shows the part of the sample that has [C/Fe] $>$ +0.7. To avoid extrapolation, we classify only stars that fall within this color-magnitude distribution (dotted black lines). However, note that our training sample is not uniformly distributed in this space, which may introduce a bias in our classification. We investigate this by evaluating the false positive and true positives rates of the classification as a function of color and absolute G magnitude (see Section 6.4).

Figure 6.3 shows the carbonicity as a function of metallicity (left panel), as well as the apparent G magnitude as a function of extinction (right panel) for the training/testing sample. In the left panel, we also show our definition for carbon enhancement as a red dashed line at [C/Fe] = +0.7. It is interesting to note the appearance of two sequences with different slopes in the carbonicity as a function of [Fe/H] plane for stars with [C/Fe]>+1. Most of the 1514

carbon-enhanced stars are metal-poor ([Fe/H] ≤ -1). However, there are 139 carbon-enhanced stars with [Fe/H] > -1, corresponding to 9% of the stars. We find that the classification algorithm identifies CEMP stars more accurately when these are included as positive cases in the training. We expect the metallicity distribution of carbon-enhanced stars in *Gaia* DR3 to be similar to our training/testing sample. Therefore, we call the stars positively classified by our algorithm as CEMP candidates, as we expect most of them to be metal-poor with only ≈9% to be metal-rich.

In the right panel of Fig. 6.3, the extinction values are from the *Gaia* DR3 GSP-Phot pipeline (Andrae et al., 2022). Our training/testing sample includes data with $A_V \approx 4$. Given that we constrain the data we wish to classify to $0.8 < G_{BP} - G_{RP} < 2.75$, it is unlikely we would include any data with $A_V > 4$. Therefore, our training/testing sample should sufficiently teach our algorithm to distinguish highly extincted stars from carbon-enhanced stars. In addition, we can use the apparent G magnitude distribution to investigate the signal-to-noise ratio (SNR) distribution of our testing/training sample. Given that the majority of the SDSS/SEGUE data is fainter than the apparent G magnitude cut for the BP/RP spectra released in DR3 ($G \leq 17.5$), we find the apparent G magnitude distribution of the SDSS/SEGUE data peaks at $G \approx 17.5$. Therefore, the G magnitude distribution of our training and testing data matches our expectations for the BP/RP spectra that we classify in that it peaks at the faintest magnitudes, but also includes stars as bright as $G \approx 10$.

6.2.2 Gaia BP/RP Spectra

The *Gaia* BP/RP spectra are a unique data set, not only due to their wide wavelength coverage, very low-resolution ($R \approx 50$), and an unprecedented number of stars, but also because the spectra have been released as a linear combination of basis functions, specifically as Hermite function coefficients (Carrasco et al., 2021). This was done because of the complexity of the *Gaia* instrument, which has two wide fields of view and 14 detectors. To create the calibrated mean spectra, multiple epochs of observations with different instrumental conditions needed to be combined. In this work, we use the coefficients as the input data for our model rather than convert them to sampled spectra, which results in some information loss (Carrasco et al., 2021).

In total, the BP and RP spectra comprise 55 coefficients each, but also come with a recommended truncation. This is possible because the coefficients have been rotated to an optimized basis so that the bulk of the spectral information is contained in the first few coefficients. A truncation is then recommended based on the magnitude of the coefficients compared to their corresponding uncertainties. For more details see Carrasco et al. (2021). As `XGBoost` requires the input data to be vectors of the same length, we apply the largest recommended truncation to avoid losing potentially useful information. The largest recommended truncation is 55 for both BP and RP spectra (i.e., all coefficients are relevant). Therefore, we do not truncate the coefficients. Because we do not want to include apparent magnitude information, we normalize the coefficients by the first BP coefficient. Furthermore, since

the coefficient values can span many orders of magnitude, we also divide the spectra by the mean normalized spectrum of the training sample. This decreases the orders of magnitudes spanned by the coefficients, which makes it easier for XGBoost to find the carbon-enhancement signal in the data.

The `XGBoost` algorithm cannot reliably extrapolate. Therefore, we ensure to only classify stars that are similar to our training sample. Specifically, we constrain our sample using the absolute G magnitude and $G_{BP} - G_{RP}$ color. As shown in the right panel of Figure 6.2 by the black dotted lines, we only classify stars that satisfy the following criteria:

1. $0.8 < G_{BP} - G_{RP} < 2.75$
2. $G + 5\log_{10}(\varpi) + 5 < 7.0$.

Although our training sample includes stars outside of this range, we chose to restrict to these values where most of the sample resides. Note that we do not place a lower limit on the absolute G magnitude, since stars with very low absolute G magnitudes likely have small, uncertain parallaxes that cause an overestimation in the brightness, and therefore underestimate the absolute G magnitude. As we do not want to introduce a selection bias by removing stars with uncertain parallaxes, we chose to include them. In Section 6.4, we investigate how the false positive rate and completeness (i.e., the true positive rate) of our classification behaves at the edges of this region where the training sample is less dense. In total, we find 182,815,672 BP/RP spectra in *Gaia* DR3 that are within our color and magnitude cuts.

6.3 XGBoost

In order to detect carbon-enhanced stars across a wide range of stellar parameters and reddenings, we require a flexible model. We chose to use `XGBoost`, which is powerful but still easy to interpret. Furthermore, `XGBoost` is optimized for efficiency, allowing fast training and inference. `XGBoost` is quickly becoming a popular machine learning algorithm in astronomy, with applications in a large variety of sub-fields (e.g., Hayden et al., 2020; Machado Poletti Valle et al., 2021; Li et al., 2021; He et al., 2022; Pham & Kaltenegger, 2022)

Figure 6.4 shows the general architecture of `XGBoost` used for classification. For a detailed description of the algorithm see Chen & Guestrin (2016). In short, `XGBoost` sequentially builds decision trees to fit the residuals from the previous tree. `XGBoost` continues to train trees until it reaches the maximum number of trees set by the user or the residuals stop consistently shrinking. The results from each tree are then summed together, weighted by the learning rate, η. This value is then plugged into the sigmoid function, $\sigma(x) = 1/(1 + e^{-x})$, to calculate the probability that the star is carbon enhanced ($\hat{y}$). We provide these probability values so that the reader can choose their own sample depending on the completeness and contamination rate required for their science. In this work, we choose to classify a star as carbon enhanced if its probability is $> 50\%$.

`XGBoost` does not allow for the direct inclusion of uncertainties for each input, but it is able to learn how to distinguish noise from signal sufficiently

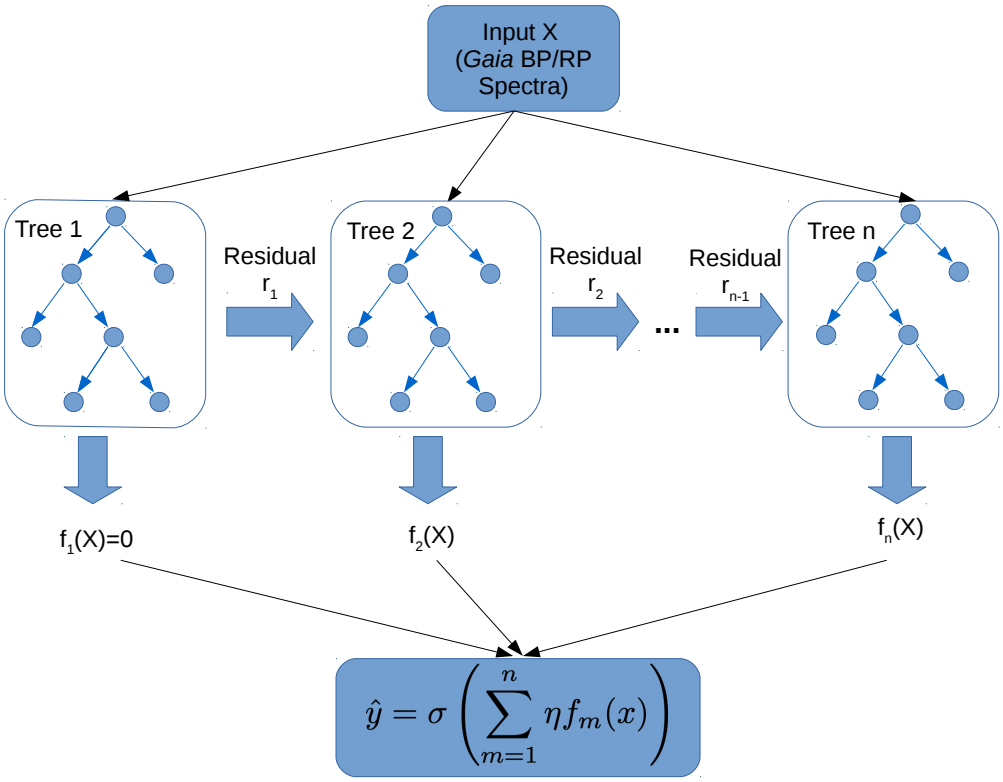

Figure 6.4: General architecture of `XGBoost` for classification. In short, `XGBoost` iteratively creates trees to fit the residuals from the prediction of the previous tree. The first tree provides a prediction of zero for each spectrum. For the final output, the predictions of each tree are summed after being multiplied by the learning rate, η. This value is then input into the sigmoid function, $\sigma(x) = 1/(1 + e^{-x})$, to calculate the final probability, $\hat{y}$. If $\hat{y} > 0.5$, the star is classified as carbon enhanced.

if the noise distribution of the training sample is representative of the data to which the model will be applied. Given that the apparent G magnitude distribution of our training sample is similar to what we expect for the BP/RP spectra we classify (see Figure 6.3), we conclude that the noise distribution of the training sample is representative and sufficient to train the `XGBoost` model.

To train the `XGBoost` algorithm, a number of hyperparameters need to be set. We can set the maximum number of trees, the learning rate (η), the percentage of the training sample and the percentage of input coefficients to use for each tree, as well as the maximum depth of each tree. We can also set limits on the purity of a sample for a given leaf to prevent overfitting. To explore the parameter space and find the optimal set of hyperparameters, we use `RandomSearchCV` from scikit-learn (Pedregosa et al., 2011).

6.4 Contamination and Completeness

In order to estimate the contamination and completeness (i.e., true positive rate) of our sample of newly identified CEMP candidates, we use our testing sample (described in Section 6.2.1), where we already know the observed carbon abundances. Specifically, we define contamination as the number of false positives divided by the sum of the true positives and false positives. In other words, the contamination estimates the rate of carbon normal stars in the sample we classify as CEMP. On the other hand, we define completeness as the number of true positives divided by the sum of the true positives

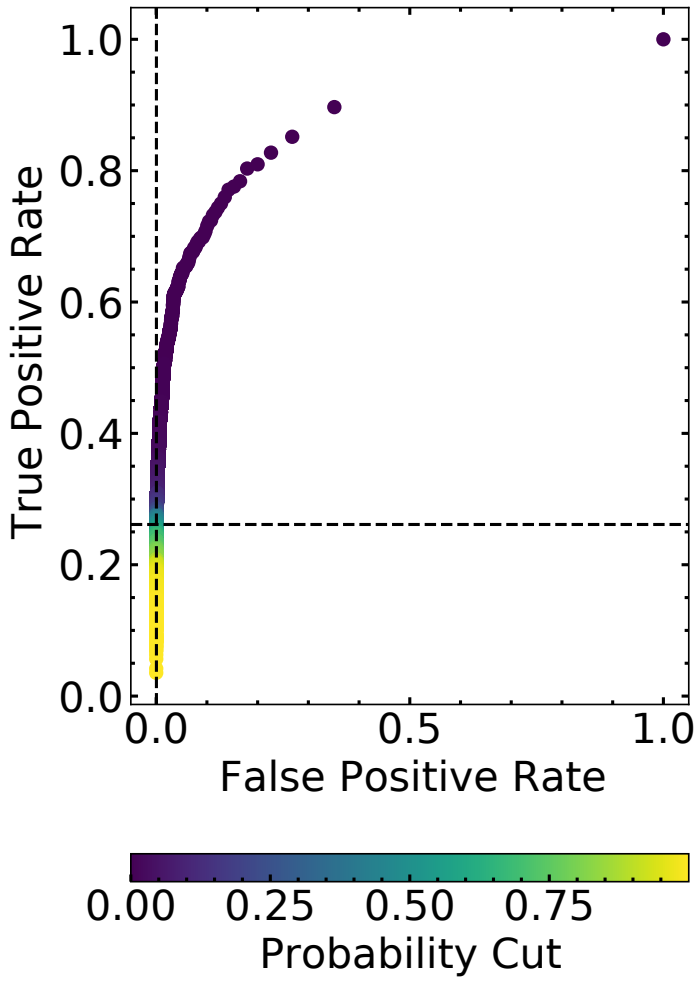

Figure 6.5: The receiver operating characteristic (ROC) describing the false positive (false positives divided by the sum of the true negatives and false positives) and true positive rates (true positives divided by the sum of the false negatives and true positives) of our classification for the testing sample. We calculate this curve by assuming different probability cuts for our classification, which are shown by the color of the points. We mark the point where the probability cut is $> 50\%$ with black dashed vertical and horizontal lines. Given that only $\approx 1\%$ of our training sample is carbon enhanced, the classification is very unbalanced. Therefore, the false positive rate is very small, even though the contamination rate (false positives divided by the sum of the true positives and false positives) is $\approx$12%. The true positive percentage or completeness is 26%.

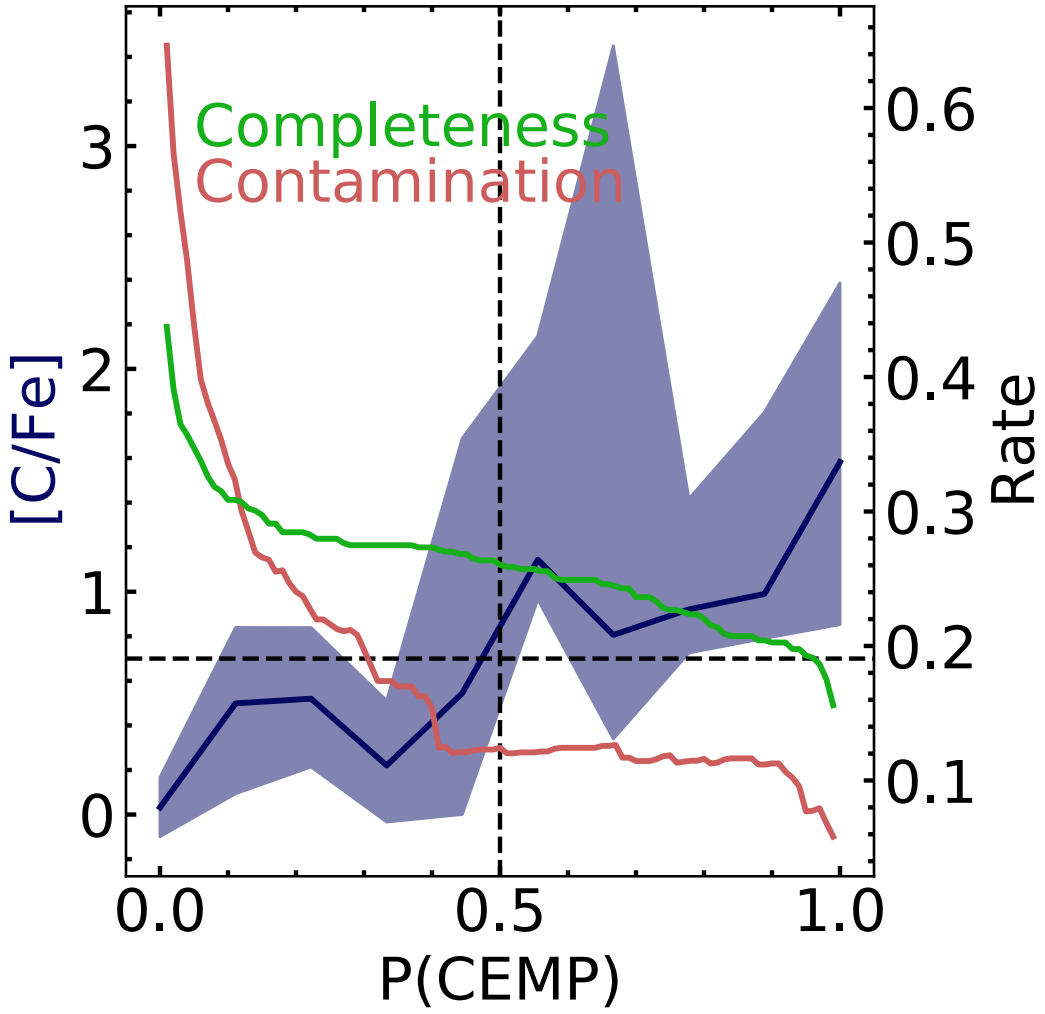

Figure 6.6: The median carbon abundance of the testing sample, as a function of the assigned probability of carbon enhancement, is shown by the dark blue line, with the 1σ percentiles shown in the blue shaded region. We also show the contamination rate as a red line, and the completeness as a green line, with the scaling shown on the right y-axis. The vertical dashed line corresponds to $p(\mathrm{CEMP}) = 0.5$ and the horizontal dashed line corresponds to [C/Fe] = +0.7, above which is our definition of a carbon-enhanced star. It is clear that the assigned $p(\mathrm{CEMP})$ is strongly correlated to carbon abundance. Furthermore, we find that the algorithm learns our definition of carbon-enhanced is [C/Fe] $> +0.7$, in that the median [C/Fe] for $p(\mathrm{CEMP}) \approx 0.5$ is $\approx +0.7$.

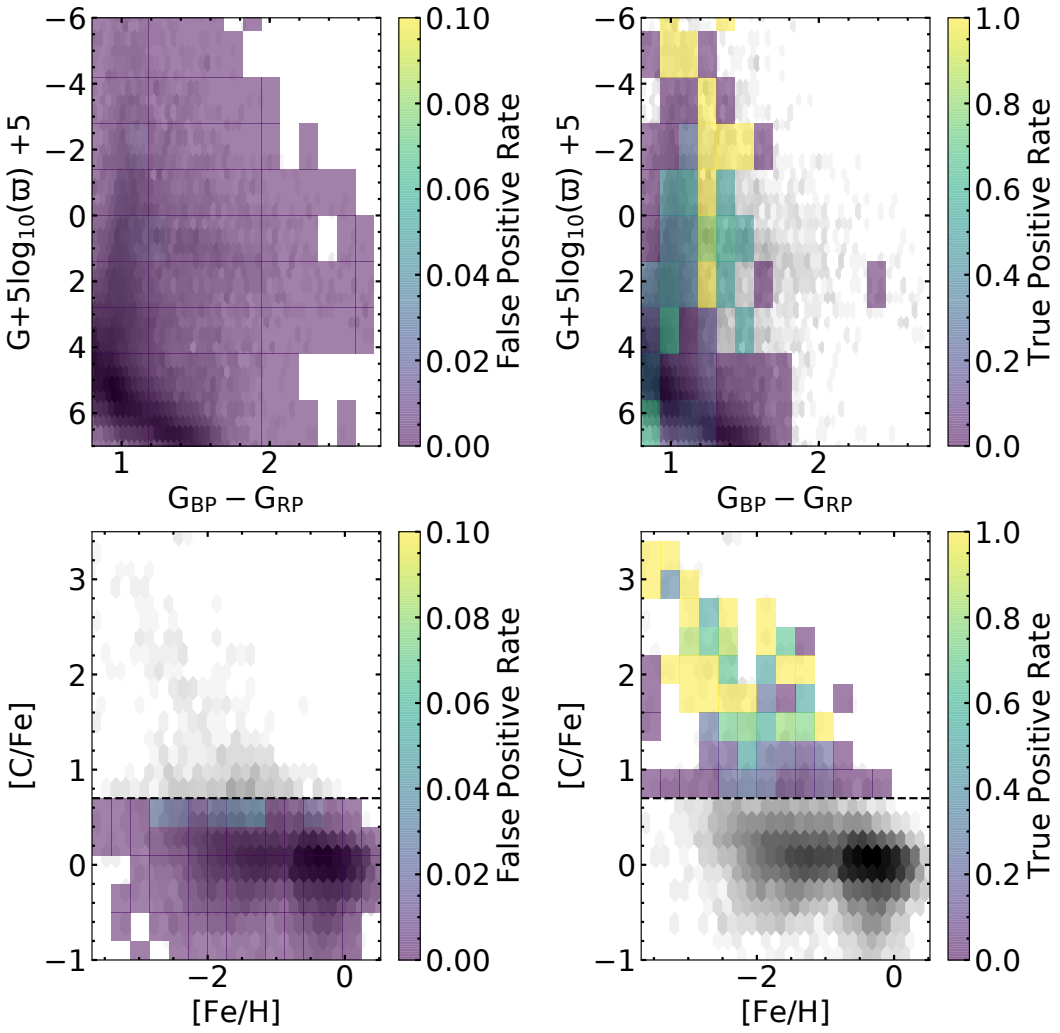

Figure 6.7: The false positive and true positive rates, as functions of absolute G magnitude, $G_{BP} - G_{RP}$ color, [C/Fe], and [Fe/H]. We show the distribution of stellar parameters for the testing sample in greyscale, with darker areas corresponding to more stars. In general, the model tends to struggle most with red dwarf stars and blue giant stars. Furthermore, the false positives tend to have $+0.5 \leq$ [C/Fe] $\leq +0.7$, while the false negatives tend to have $+0.7 \leq$[C/Fe] $\leq +1.0$. Therefore, our model likely only can interpret the carbon abundance to ≈ 0.5 dex for some stars.

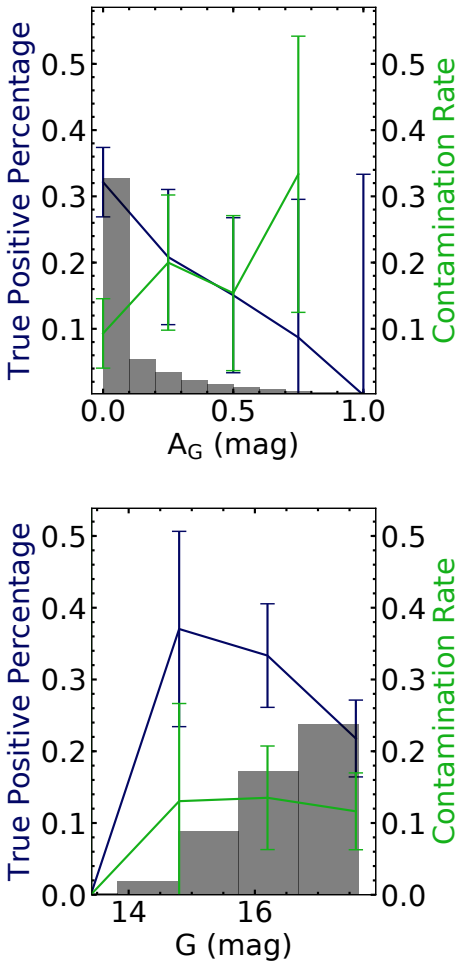

Figure 6.8: The contamination rate and true positive percentage, as a function of G magnitude and extinction (A_G). The grey bins show the arbitrarily scaled number density of stars in our training/testing sample. For each panel, the scale for the true positive percentage (dark blue) is on the left y-axis; the right y-axis shows the scale for the contamination rate (green). The error bars are $1/\sqrt{N}$ where N is the number of true positives. As expected, we find that our classification improves for bright stars, which likely have high signal-to-noise spectra, and for stars at low extinction.

and false negatives. Therefore, the completeness estimates the fraction of true CEMP stars that we expect to detect. There may be non-stellar objects that contaminate our sample (e.g., quasars), but we mitigate these effects by constraining the full set of spectra that we classify by the absolute G magnitude and $G_{BP} - G_{RP}$ color of the training/testing sample (see Section 6.2.2). Furthermore, stars hotter than our training/testing sample might mistakenly be included if high levels of extinction make them appear sufficiently red. However, we expect that this situation is rare, given that our training sample is representative of the full distribution in T_{eff} and extinction (see Figure 6.2 and 6.3). In addition, we have stellar parameters and carbon abundances for the testing sample, which allows us to study how the contamination and completeness behave as a function of various parameters, including observational effects.

Figure 6.5 shows the receiver operating characteristic (ROC) curve, which describes the false positive rate (false positives divided by the sum of the true negatives and false positives) and true positive rate (true positives divided by the sum of the false negatives and true positives) of the classification as a function of the probability cutoff assumed. As expected, the true positive percentage and false positive rate increase as the probability cut is decreased. The black dashed vertical and horizontal lines mark the true positive and false positive rates for a probability cut of $> 50\%$, which we use to define the CEMP candidate sample in this work. Specifically, for a probability cut of $> 50\%$ we find a false positive rate of 0.04% and a true positive rate of 26%. The false

positive rate is especially low because our classification is unbalanced, with only ≈1% of our sample being a positive case (i.e., carbon enhanced). On the other hand, the contamination rate (false positives divided by the sum of the false positives and the true positives) is ≈12%. In the final catalog, we provide the probability values for each star classified so that the reader can choose a probability cut best suited for their science case.

Figure 6.6 shows the median carbon abundance of the testing sample, as a function of the assigned probability of being carbon enhanced, as a dark blue line, with the 1σ percentiles as the shaded region. We also show the completeness (green line) and contamination rate (red line) for $p(\mathrm{CEMP}) > x$ with the scaling on the right y-axis. The vertical black dashed lines gives the p(CEMP) that above which a star is classified as CEMP ($p(\mathrm{CEMP}) = 0.5$). Therefore, where this line intersects the completeness (26%) and contamination rates (12%) gives those properties for our final sample. The horizontal dashed line indicates the [C/Fe] above which we define a star to be carbon-enhanced ([C/Fe] = +0.7). The median [C/Fe] becomes larger than this at ≈ $p(\mathrm{CEMP}) = 0.5$, indicating that our algorithm learns to assign a $p(\mathrm{CEMP}) > 0.5$ for stars with [C/Fe] > +0.7.

Figure 6.7 shows 2D maps of the false positive (left) and true positive rates (right), as a function of absolute G magnitude, and $G_{BP} - G_{RP}$ color (top), as well as for [C/Fe] and [Fe/H] (bottom). In these plots, we also show the underlying density distribution of stars as grey hexagonal bins. The left panels show the false positive rate, which is calculated by taking the number of

false positives divided by the number of true carbon-normal stars in that bin. The right panels show the true positive rate, which is calculated by dividing the number of true positives (i.e., correctly identified CEMP stars) by the total number of true CEMP stars in that bin.

In the top left panel of Figure 6.7, we do not see a trend in the false positive rate with the $G_{BP} - G_{RP}$ color or absolute G magnitude. In the top right panel, we see that at the true positive rate is lowest for dwarf stars and blue giant stars. We also find that the algorithm does not detect the most extincted, reddest giant stars in our testing sample.

In the bottom row of Figure 6.7, we see a slight trend in the false positive and true positive rates with the [C/Fe] abundance. Specifically, we see the false positive rate is higher for stars with $+0.5 <$ [C/Fe] $< +0.7$, and the true positive rate is lowest for stars with $+0.7 <$ [C/Fe] $< +1.0$. This indicates that our classification is most inaccurate for stars with [C/Fe] $\approx +0.7$, which is to be expected given that it is unlikely we could measure a [C/Fe] abundance from these very low-resolution ($R \approx$50) spectra that is more precise than $\approx$0.5 dex.

Figure 6.8 shows the true positive percentage and contamination rate, as a function of extinction (top panel) and apparent G magnitude (bottom panel). The grey histogram shows the arbitrarily scaled underlying distribution of the testing sample for these parameters. The green line shows the contamination rate, with the scaling provided by the right y-axis, while the dark blue lines show the true positive percentage, with corresponding scaling

on the left y-axis.

As expected, we find that the classification performs better at low extinction. Specifically, we see that the true positive percentage decreases from ≈30% at A_G=0 to ≈0% at A_G=1. We also see that the contamination rate increases from ≈10% to ≈30% over the same range. Of our final sample of CEMP candidates, 77% has $A_G < 0.5$. Furthermore, we find that the contamination rate also increases with fainter G magnitude, as expected, since the G magnitudes are directly related to the signal-to-noise for these spectra. We find that the false positive percentage increases from ≈5% at G magnitude of ≈ 13 to ≈ 12% at G =17.5. The true positive percentage is lowest for bright stars. This is likely because there are few bright CEMP stars in our training sample (see Figure 6.3), which may introduce a bias against detecting bright CEMP stars in the *Gaia* data. We also see that the true positive percentage decreases at $G > 15$. This is likely due to lower signal-to-noise for these data.

To further validate our sample, we also compare to large spectroscopic surveys. However, as CEMP stars are rare, large spectroscopic surveys generally do not correctly account for CEMP stars in their analysis pipelines. For example, APOGEE's ASPCAP pipeline does not account for stars with [C/Fe] $> +1$ (Abdurro'uf et al., 2022). When cross-matched against our SDSS training/testing sample, we find 1,765 stars in common with APOGEE DR17. Of these, only 26 are identified as CEMP in the SDSS/SEGUE catalog. However, the ASPCAP pipeline assigns only 1 of these stars an abundance of [C/Fe] $> +0.7$. This star has [C/Fe] = +2.28 from SDSS/SEGUE, while ASPCAP

measures [C/Fe]=+0.89. From this comparison, we expect ASPCAP to report [C/Fe] $< +0.7$ for as much as 96% of our final CEMP catalog. Of the stars we classify as CEMP, we find that 699 stars have a match in APOGEE DR17 without flags on the ASPCAP derived [C/Fe]. Of these, 389 have [C/Fe] $< +0.7$ as measured by ASPCAP, corresponding to 56%. As we found that ASPCAP measured [C/Fe] $< +0.7$ for 96% of our CEMP training sample, it is not unexpected that we find a high percentage of our final sample has [C/Fe] $< +0.7$ from ASPCAP as well.

To validate the completeness of our sample, we cross-match against a database of CEMP stars confirmed from high-resolution spectra (Yoon et al., 2016; Zepeda et al., 2022). Of the 253 stars that have [C/Fe]$>+0.7$ without including evolutionary corrections in Yoon et al. (2016), 108 of them have BP/RP spectra released in DR3 and fall inside our color and absolute magnitudes cuts. Of these 108, we classified 65 as CEMP in our catalog. This is a completeness percentage of 60%. Of the 382 stars from Zepeda et al. (2022) that have observed [C/Fe]$>+0.7$ (no evolutionary correction), 208 of them have BP/RP spectra within our color and absolute magnitude cuts. We correctly classify 143 of those as CEMP stars which gives a completeness rate of 69%. As both of these samples give similar completeness rates that are significantly higher than that estimated with our testing sample (26%) it is likely that our true completeness percentage is higher and 26% is a conservative estimate.

6.5 Model Interpretation

As we have used a data-driven method to classify stars in this work, we want to ensure that the final model matches our physical intuition. It is also important to ensure that the model is not using any confounding variables (e.g., extinction or metallicity) that could be correlated with carbon enhancement but are not a direct measurement of the true carbon abundance. Typically, model interpretation is done by determining the importance of each input feature for the final inference and comparing it to expectations from physical models. Here, we investigate the importance of four key Hermite coefficients and how they relate to true carbon abundance. Furthermore, we compare BP/RP spectra of CEMP stars from the training sample to newly classified stars in order to ensure they match expectations.

Figure 6.9 shows the average difference between CEMP spectra and carbon-normal stars for a subset of the training sample (green) and the newly classified data (black). We also show the difference between synthetic spectra (dark blue dashed line) with [C/Fe] = +1 and [C/Fe] = +0.5, assuming T_{eff} = 4500 K, log g = 2.5, and [Fe/H] = –2. This is the same line as shown in the top right panel of Figure 6.1. For the observed spectra, we chose to calculate the averages over a narrow color and absolute G magnitude range in order to isolate the effect of carbon from the effects of T_{eff}, log g, and extinction on the spectra. Specifically, we use stars with $1.20 < G_{BP} - G_{RP} < 1.25$ and $0 < G + 5\log_{10}(\varpi) + 5 < 3$, which is a narrow dense region of the red giant branch (RGB). For our training sample, this corresponds to a T_{eff} range of

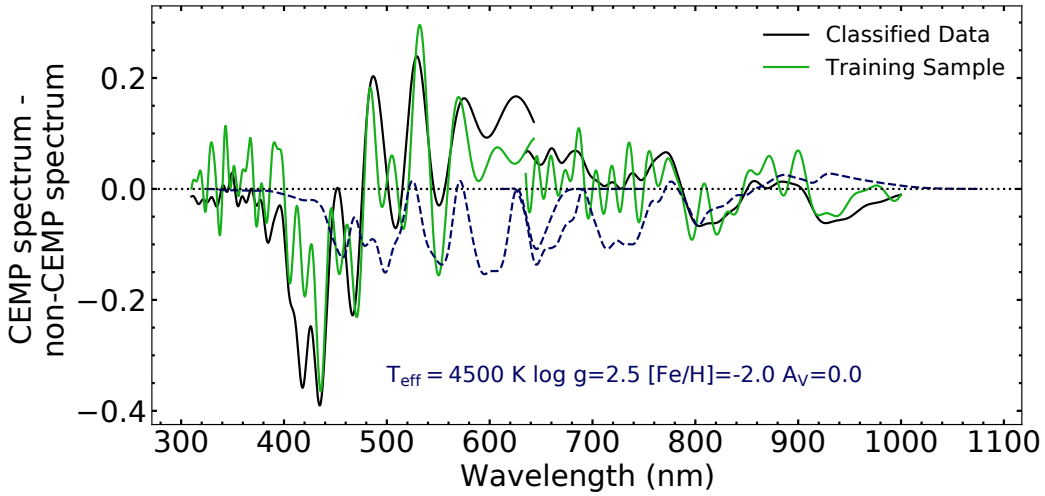

Figure 6.9: The average difference between CEMP spectra and carbon-normal spectra for a subset of the training sample (green) and newly classified data (black). We also include the difference between synthetic spectra (dark blue dashed line) with [C/Fe] = +1 and [C/Fe] = +0.5, assuming $T_{\rm eff}$ = 4500 K, log g = 2.5, and [Fe/H] = -2.0 , as described in Figure 6.1. The green and black lines are calculated by subtracting the average spectrum of carbon-normal stars from CEMP stars for stars in a narrow range of color ($1.20 < G_{BP} - G_{RP} < 1.25$) and absolute G magnitudes ($0 < \mathrm{G}+5\log_{10}(\varpi) + 5 < 3$) which corresponds to a small dense region of the red giant branch. We do this both for the training sample and the newly classified data in order to ensure that the classification has worked, and that the newly classified CEMP stars have the expected carbon features. Given that the difference between the CEMP stars and the carbon-normal stars is quite similar for both the training and newly classified samples. and that the features generally match expectations from synthetic spectra, we conclude that our classification has correctly selected candidate CEMP stars.

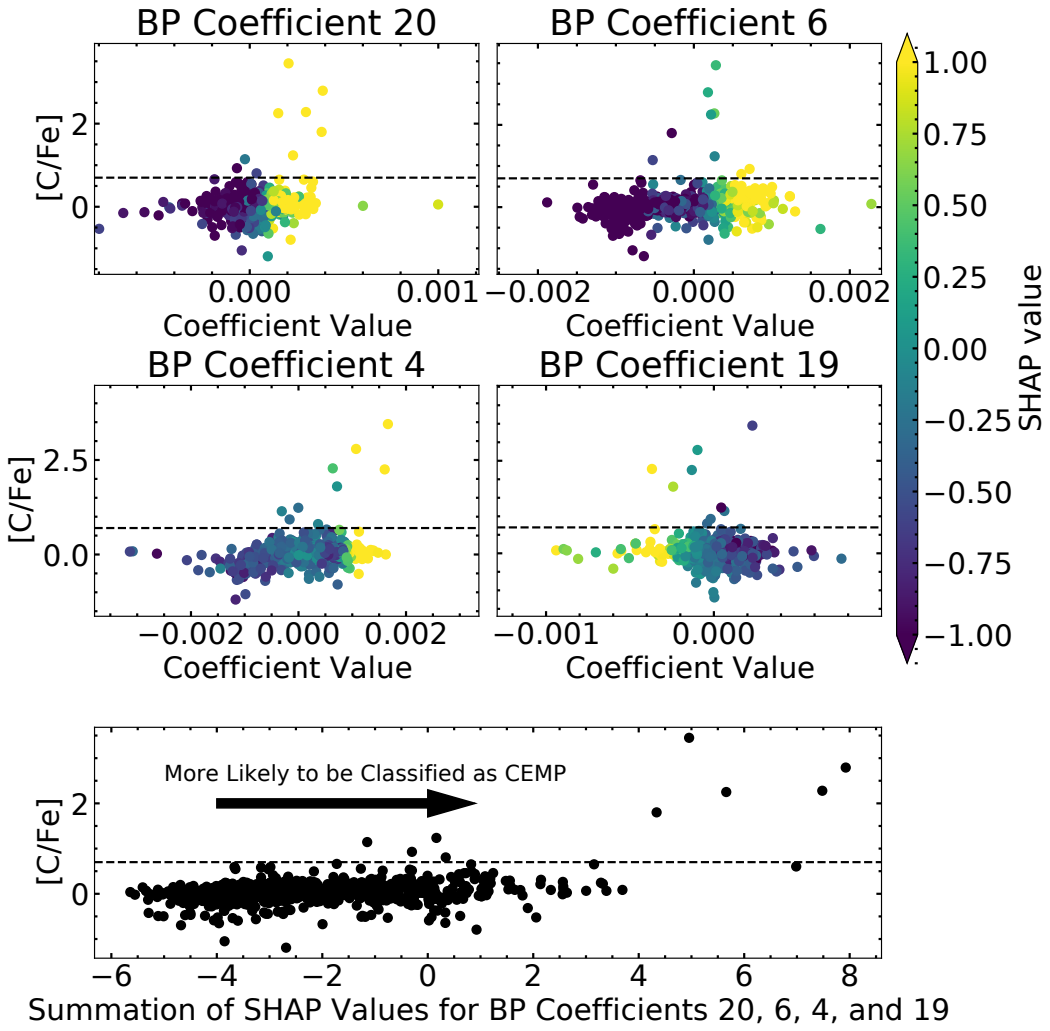

Figure 6.10: The relations between [C/Fe], the spectral coefficient value, and the SHAP value for the four spectral coefficients with the largest SHAP values. We show a horizontal black dashed line at [C/Fe] = +0.7. The bottom panel shows [C/Fe] as a function of the summation of the SHAP values of the four coefficients. Each point corresponds to an individual star in our testing sample. The SHAP values give the feature importance, in that large positive SHAP values indicate a large increase in the assigned probability of the star being carbon enhanced due to a given coefficient's value. Therefore, if the model uses the carbon information in the coefficients, we expect that stars with [C/Fe] > +0.7 to have high positive SHAP values.

$4500\,\mathrm{K} < \mathrm{T_{eff}} < 5500\,\mathrm{K}$. We calculate the average CEMP spectrum and carbon-normal spectrum in this region for both the training sample and the newly classified sample, in order to ensure that they look similar, which indicates that the classification algorithm successfully identified candidate CEMP stars. We also compare this to expectations from synthetic spectra. We find that the differences between CEMP and carbon-normal stars for the newly classified data matches the differences found in the training sample. Furthermore, the features seen in the subtracted spectra roughly match with expectations from mock spectra. The small discrepancies can likely be explained by the variation in $\mathrm{T_{eff}}$ and normalization procedure. The observed spectra are normalized in the *Gaia* BP/RP coefficient space following the procedure described in Section 6.2.2, while the synthetic spectrum is normalized by the maximum flux.

We measure the impact of each Hermite basis coefficient on the classification using SHAP (Shapley Additive exPlanations) values (Lundberg & Lee, 2017). The SHAP values allow us to explore the importance of individual features, as a function of various parameters, since each star's coefficients are assigned individual values. The SHAP values are defined so that their summation plus the average predicted value (ϕ_0) is equal to the predicted value ($\hat{y}$). Explicitly,

$$\hat{y} = \phi_0 + \sum_{i=1}^{M} \phi_i, \tag{6.1}$$

where ϕ_0 is the average value of $\hat{y}$ for all of the spectra, ϕ_i is the SHAP value for coefficient i, and M is the total number of coefficients per spectrum. Therefore, each SHAP value directly measures the impact of the selected coefficient on

the inference of $\hat{y}$ for a given star. We refer the interested reader to Lundberg & Lee (2017) for further details on the calculation of SHAP values.

We calculate the SHAP values for all of the spectra in our testing sample. Figure 6.10 shows how the SHAP values relate to the carbon abundance and coefficient value for four BP coefficients. These coefficients were selected because they have the largest SHAP values of all the BP and RP coefficients. Specifically, we have the [C/Fe] on the y-axis, and the coefficient value on the x-axis. The points are colored by the SHAP values. The bottom panel shows [C/Fe] as a function of the summation of the four SHAP values. As large positive SHAP values indicate that the given coefficient increased the probability that the star is carbon enhanced, it is expected that stars with [C/Fe] $> +0.7$ should have higher SHAP values than carbon-normal stars. We find that the `XGBoost` model is able to pick up this sensitivity, in that the SHAP values for these coefficients are generally large and positive for carbon-enhanced stars. Although there are some coefficients where the SHAP value is negative for a carbon-enhanced star, these stars may still be classified as carbon enhanced based on the value of other coefficients. Similarly, there are many carbon-normal stars that have individual positive SHAP values, but the combined effect of all of the other coefficients effectively decreases the probability of the star being carbon enhanced (see the bottom panel), so that the false positive rate is not exceedingly high. Given the positive correlation between [C/Fe] and the SHAP value, it is likely that `XGBoost` model is using the carbon information in the spectra to determine whether a given star is carbon enhanced

rather than using another confounding variable.

6.6 Properties of the CEMP Candidate Sample

Out of the ≈180 million stars that we classify, we find 58,872 CEMP candidate stars. This is the largest, homogeneously identified sample of CEMP candidate stars to date. In this section, we briefly investigate a few properties of this sample, including their metallicity distribution and Galactic distribution.

Figure 6.11 shows the color-magnitude diagram of our CEMP candidate sample compared to a random sample of stars classified as carbon-normal of the same size. We show the CEMP candidate sample in a gradient from dark blue to beige, where dark blue shows the densest area of stars. The carbon-normal sample is shown as contour lines, where the highest density is shown with white contour lines; lower density areas have black contour lines. In general, the color-magnitude distribution of the CEMP candidate and carbon-normal samples are similar, in that the highest density occurs where we expect bright dwarf and turn-off stars to reside (G ≈4-6). However, one key difference occurs on the giant branch ($G < 4$). In general, the CEMP candidate giant stars are bluer than the carbon-normal giant stars. There is a clear red clump feature in the carbon-normal giant star distribution (black contour) at $G \approx 1$ and $G_{BP} - G_{RP}$≈1.6, but this does not appear in the CEMP distribution. This is consistent with expectations that the CEMP candidate sample is more metal-poor than the carbon-normal sample, given that metal-poor stars will

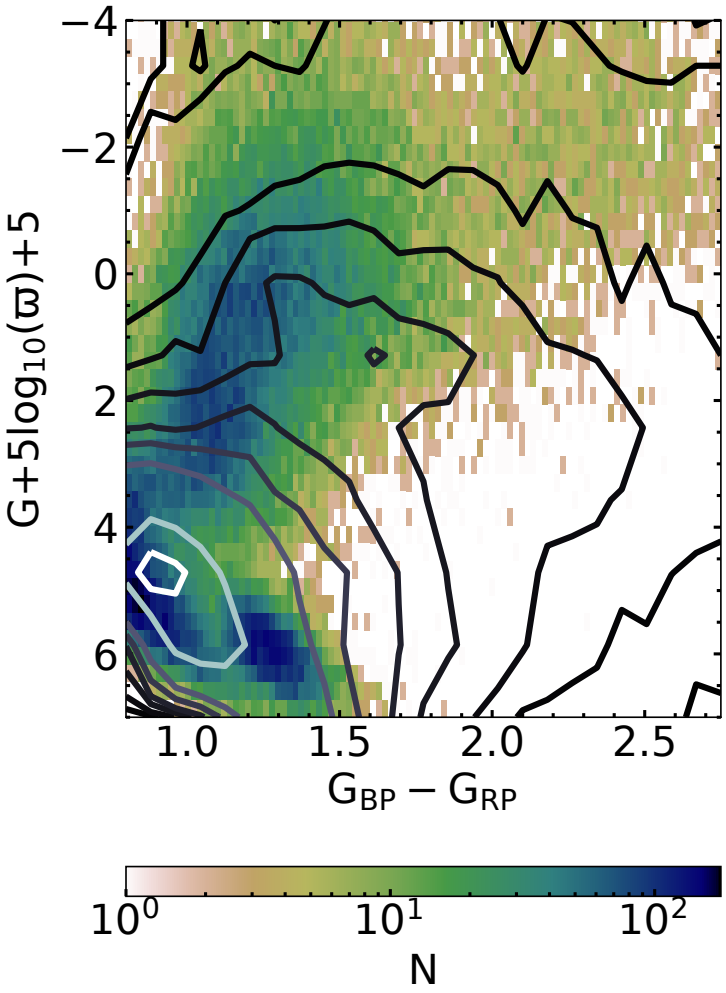

Figure 6.11: Color-magnitude diagram of the final sample of candidate carbon-enhanced stars (dark blue/beige gradient), compared to a random sample of stars classified as not carbon-enhanced in white (high density) to black (low density) gradient contour lines. In general, the color-magnitude distribution of our CEMP candidate sample is similar to the carbon-normal sample, in that the majority of stars are bright dwarf/turn-off stars. On the giant branch, however, the CEMP candidate sample tends to be bluer, while the carbon-normal sample shows a clear red clump at absolute $G \approx 1$. This indicates that the CEMP candidate sample is more metal-poor than the carbon-normal sample, as expected.

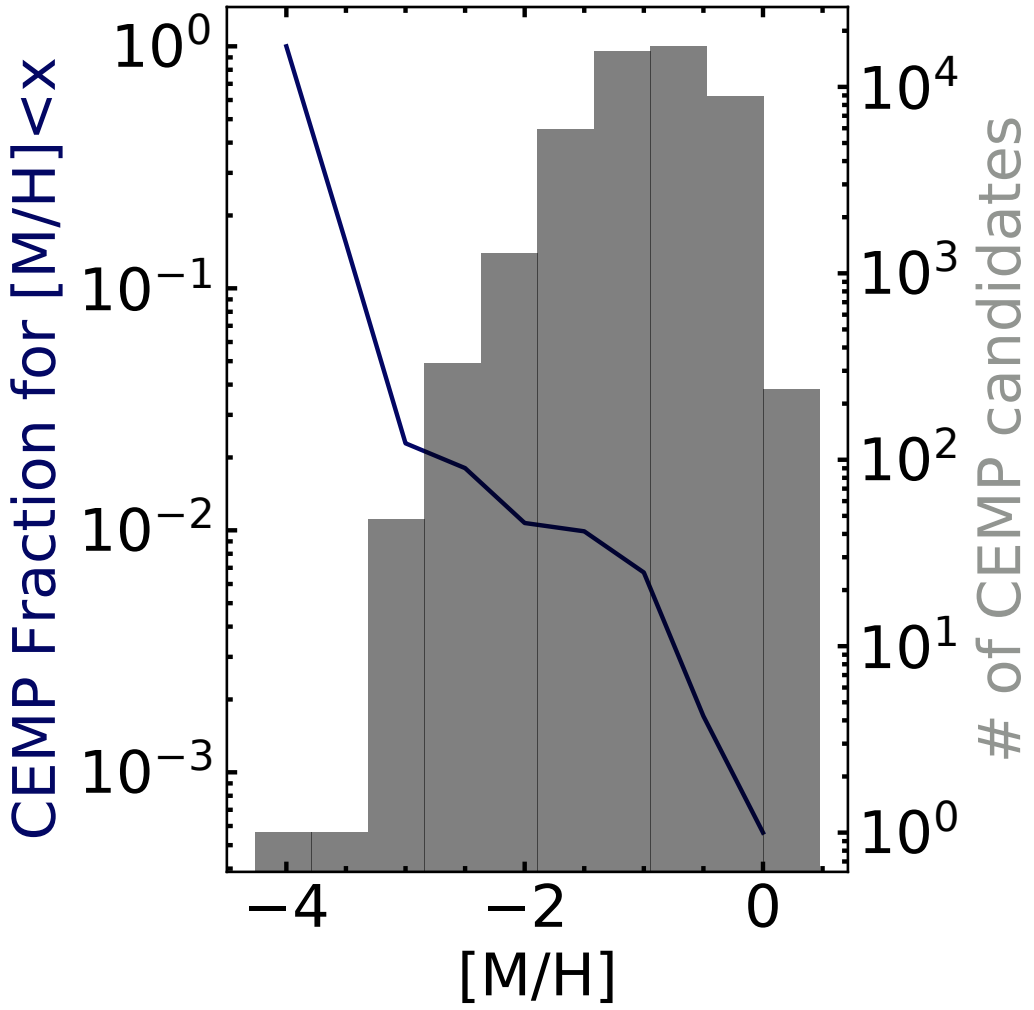

Figure 6.12: The behavior of the occurrence rate of our classified CEMP candidate stars, as a function of metallicity ([M/H]) provided by Andrae et al. (2023). Specifically, we show the fraction of stars with [M/H] $< x$ that are classified as CEMP out of the total number of BP/RP spectra that we classify in a given metallicity bin. We also plot the metallicity distribution of our CEMP candidate sample in grey. We note this plot is only to explore the properties of our sample, and is not meant as a measure of the true occurrence rate of CEMP stars. The CEMP fraction increases with decreasing metallicity, consistent with previous results from high-resolution samples.

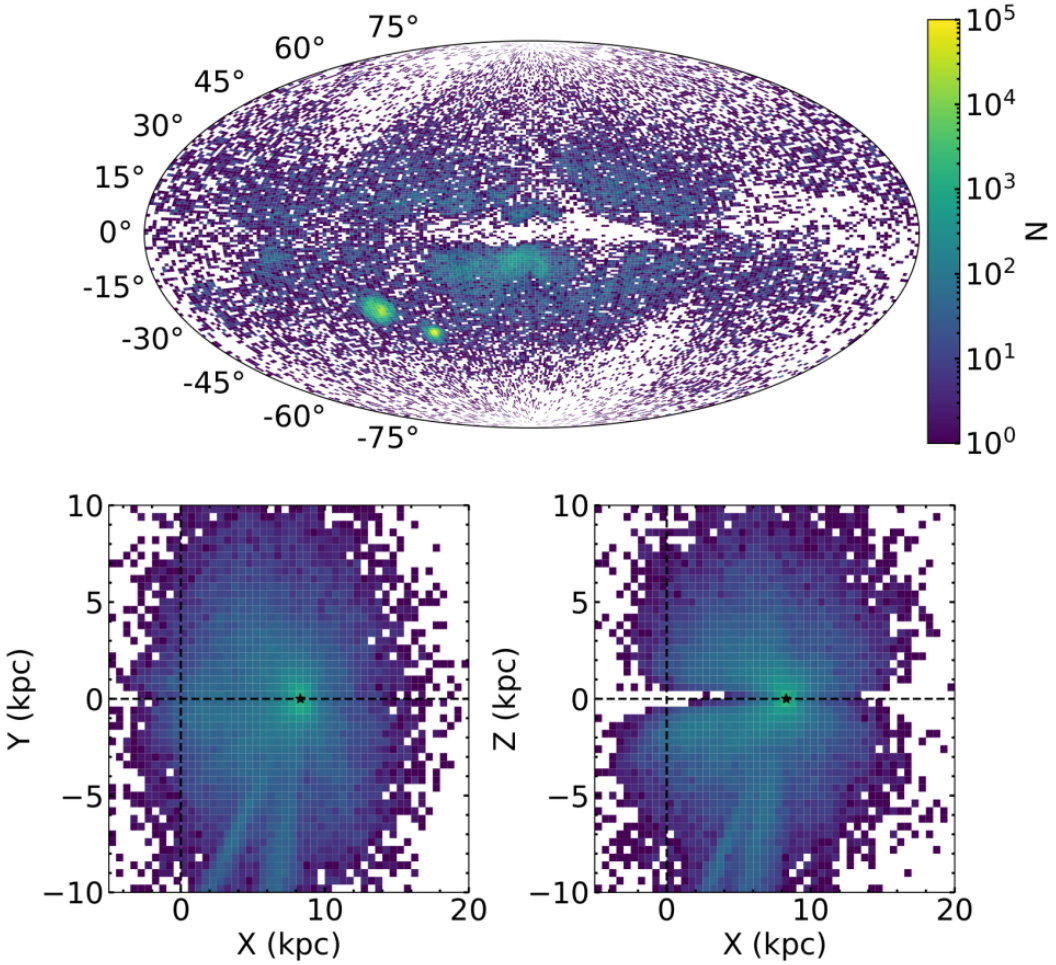

Figure 6.13: The Galactic distribution of our CEMP candidate sample. Specifically, in the top panel we show the sky projected distribution of the sample in Galactic coordinates, l and b, where $(l,b) = (0,0)^\circ$ is the line-of-sight towards the Galactic center. The bottom left panel shows the distribution of stars in the Galactic coordinates X and Y. The bottom right panel shows the distribution in the Galactic X and Z coordinates. The Galactic center is located at (0,0,0) kpc, while the Sun is at (8.3,0,0) kpc. The LMC and SMC are clear features in the sky projected distribution.

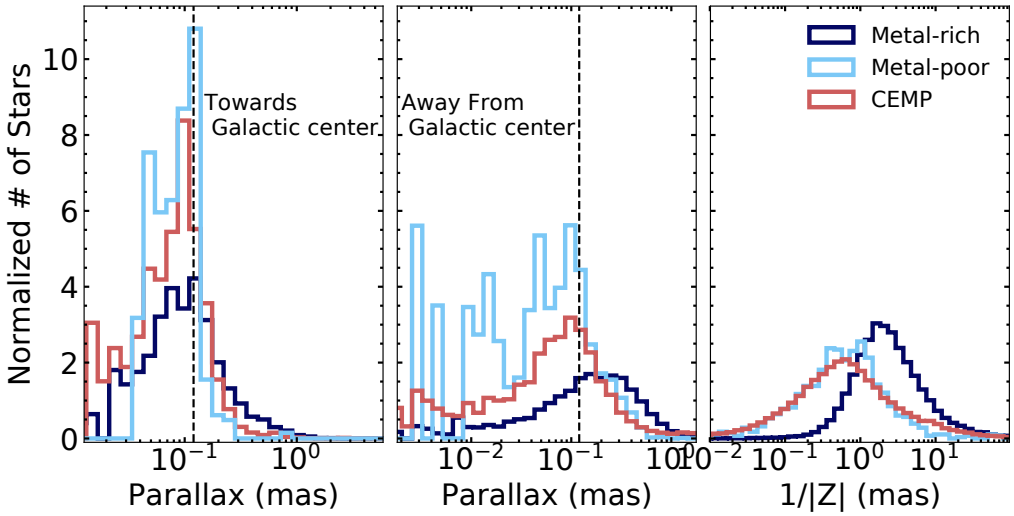

Figure 6.14: The parallax distribution of our CEMP candidate sample (red), compared to the metal-rich (dark blue) and metal-poor (light blue) carbon-normal sample. Specifically, in the left panel, we show the parallax distributions for stars towards the Galactic center with $|l|<10°$ (or $350°<l<10°$) and $|b|<10°$. The middle panel shows the parallax distributions for stars towards the Galactic anti-center with $170°<l<190°$ and $|b|<10°$. We also mark the parallax of the Galactic center (0.12 mas) with a black vertical dashed line in both the left and middle panels. The right panel shows the inverse distance from the Galactic plane (|Z|) calculated by dividing the parallax by sin(b). The CEMP candidate stars generally follow the distribution of metal-poor stars.

become blue-horizontal branch (BHB) after the RGB phase rather than red-clump stars like their more metal-rich counterparts.

Figure 6.12 shows the metallicity distribution of our sample of CEMP candidate stars in a grey histogram, using data-driven results from Andrae et al. (2023). In dark blue, we also show the ratio of the number of stars classified as CEMP to the total number of BP/RP spectra we analyzed for [M/H] $< x$. In other words, the dark blue line gives the fraction of CEMP candidate stars for stars with [M/H] $<$ x. It is important to note that this plot is only meant to explore the trends in our sample, and not meant as a measurement of the true occurrence rate of CEMP stars. With the uncertain metallicities, undefined selection function, and low completeness percentage, our sample currently cannot provide a robust estimate of the occurrence rate as a function of metallicity. However, the overall trend is consistent with previous work (Lucatello et al., 2006; Lee et al., 2013; Placco et al., 2014; Yoon et al., 2018; Arentsen et al., 2022) in that the occurrence rate increases with decreasing metallicity. Unexpectedly, we find that 57% of our CEMP candidate sample has [M/H] estimates from Andrae et al. (2023) higher than –1, indicating that they are not metal-poor. However, given that the [M/H] estimates are data-driven and CEMP stars are outliers, it is unlikely that the [M/H] values are robust for CEMP stars. It is likely that they are, in fact, overestimated given the carbon enhancement, and the true [Fe/H] would be much lower. However, higher resolution spectroscopic follow-up is required to confirm this.

Figure 6.13 shows the Galactic distribution of the CEMP candidate sample. Here we use the geometric distances from Bailer-Jones et al. (2021). We choose not to use distances that are calculated using photometry, since it is likely that the carbon enhancement will bias these results. The top panel simply shows the sky-projected distribution in Galactic coordinates, l and b, which is independent of the parallax. Here, the Galactic center is along the line-of-sight towards $(l,b) = (0,0)^{\circ}$. We also show the distribution of our CEMP candidate sample in Galactic X and Y coordinates in the bottom right panel, while the bottom left panel shows the distribution in Galactic X and Z coordinates. The Galactic center is located at (0,0,0) kpc with the Sun located at (8.3,0,0) kpc (Reid et al., 2014).

The CEMP candidate sample is spread throughout the Galaxy in a halo-like distribution. However, towards the inner Galaxy at low $|b|$ there is an underdensity of stars, likely caused by extinction. The Large and Small Magellanic Clouds (LMC and SMC) stand out as clear features in the sky projected distribution, with peaks in the number density of CEMP candidate stars. This is consistent with previous work that has identified thousands of carbon-rich (post-)AGB stars in the Magellanic clouds (Rebeirot et al., 1993; Kontizas et al., 2001). Similarly, the over-density of CEMP candidate stars towards the Galactic center at negative b is likely associated with the Sagittarius dwarf galaxy. However, further work on the dynamics of these stars is required to tag them to a specific Galactic component. Additionally, spectroscopic observations are required to calculate evolutionary corrections,

and determine which of these stars are potentially natal CEMP-no stars, rather than (post-)AGB carbon stars or CEMP-s stars. Impacts of the Gaia DR3 selection function can also be seen in the sky projected distribution at high $|b|$ with sweeping underdensity features (see Figure 29 in De Angeli et al., 2022).

Consistent with a kinematically hot Galactic population, our CEMP candidate sample is extended to large distances from the Galactic center (see Figure 6.13). It is important to note that some of the largest distances may be unreliable, given that the fractional parallax uncertainty for faint stars can be quite large. Given that the majority of BP/RP spectra released in DR3 have $G \approx 17.6$, and assuming an absolute G magnitude of -2.5 (roughly the tip of the RGB), we expect to have detected CEMP stars at distances of up to ≈ 30 kpc. We find that 8,707 stars in our CEMP sample that have parallaxes corresponding to distances from the Galactic center > 30 kpc. However, the Galactic prior used in Bailer-Jones et al. (2021) brings most of these to within ≈ 10 kpc.

We also investigate the relative parallax distribution of CEMP candidate stars (red), compared to carbon-normal metal-rich stars (dark blue) and carbon-normal metal-poor stars (light blue) in Figure 6.14. The left panel shows the parallax distribution of CEMP candidate stars towards the Galactic center by choosing stars with $|l|<10^\circ$ and $|b|<10^\circ$. We find that the distribution of CEMP candidate stars peaks at a parallax consistent with that of the Galactic center (0.12 mas). The distribution of metal-rich and metal-poor carbon-normal stars also peaks at this parallax, but the metal-rich stars have

a stronger tail towards large parallaxes, i.e., closer distances to the Sun. The middle panel shows the parallax distributions of CEMP candidate and carbon-normal stars towards the Galactic anti-center with $|l|<170^{\circ}$ and $|b|<10^{\circ}$. We find that the parallax distribution of CEMP candidate stars and carbon-normal metal-poor stars peaks at a parallax of ≈ 0.1 mas. Given that the average parallax precision for the faintest stars in our sample ($G \approx 17.5$) is $\approx$0.1 mas (Lindegren et al., 2021), this is consistent with CEMP stars peaking at distances $\geq$ 10 kpc. The carbon-normal metal-rich stars, on the other hand, peak at large parallaxes, indicating they are generally closer to the Sun than CEMP stars. This is consistent with previous work, which found the frequency of CEMP stars to increase with increasing distance from the Sun (Carollo et al., 2012; Frebel et al., 2006; Lee et al., 2013, 2017; Yoon et al., 2018). In the right panel, we show the inverse of the distance from the Galactic plane (1/|Z|), which is calculated by dividing the parallax by sin(b). Again, we find that the CEMP candidate and metal-poor carbon-normal stars follow the same trends, and are generally farther from the Galactic plane than the carbon-normal stars. In general, we find that the CEMP candidate stars are more distant from the Sun than the carbon-normal stars, consistent with a Galactic halo population. Further work looking at the rate of carbon-enhancement for metal-poor stars as a function of Galactic position is required to determine if CEMP stars have different origins than carbon-normal metal-poor stars.

6.7 Summary

The origins of CEMP stars are poorly understood, even though they comprise ≈30% of stars with [Fe/H] < –2 (Lucatello et al., 2006; Lee et al., 2013; Placco et al., 2014; Yoon et al., 2018; Arentsen et al., 2022). A significant fraction of CEMP stars have enhancements in *s*-process elements, and are called CEMP-s stars (Beers & Christlieb, 2005). These stars are thought to receive their over-abundant carbon and *s*-process elements from a mass-transfer event with their binary companion, which has evolved to or past the AGB (Lugaro et al., 2012; Placco et al., 2013). On the other hand, CEMP stars without neutron-capture enhancements are thought to have been primarily enriched by material from the first generations of stars (Umeda & Nomoto, 2003; Chiappini et al., 2006; Meynet et al., 2006; Nomoto et al., 2013; Tominaga et al., 2014). However, there are many remaining questions about these unique stars, including why they seem to be less frequent in the central regions of our Galaxy, where we expect the highest concentration of ancient stars to reside (Howes et al., 2014, 2015, 2016; Arentsen et al., 2021; Lucey et al., 2022). As suggested by Yoon et al. (2019), this dearth of CEMP stars may be caused by the dilution of CEMP stars in more massive subsystems (e.g., dwarf galaxies) with prolonged star-formation histories, which could be the origin of metal-poor stars in the inner Galaxy. However, given that the discrepancy in the CEMP fraction of the inner Galaxy is highest for [Fe/H]>-2.5, Arentsen et al. (2021) argue that it is due to a lower rate of CEMP-*s* stars caused by a lower binary fraction in the inner Galaxy.

In this work, we leverage the data from the all-sky *Gaia* survey to identify 58,872 CEMP candidates. Specifically, we use the ∼180 million BP/RP spectra made available in *Gaia* DR3. Using the `XGBoost` algorithm for classification, we achieve a completeness of 26% and a contamination rate of 12%. When comparing to high-resolution catalogs of CEMP stars (Yoon et al., 2016; Zepeda et al., 2022), we find that we positively identify 60-68% of the previously known CEMP stars in the *Gaia* DR3 BP/RP data. We ensure that the `XGBoost` algorithm matches our physical intuition and primarily performs the classification using spectral features that are correlated with the carbon abundance.

We briefly investigate a few of the properties of our CEMP candidate sample, including the metallicity distribution and the Galactic spatial distribution. As expected, the CEMP fraction increases with decreasing metallicity. In general, we find that the CEMP candidate stars tend to follow the distribution of metal-poor carbon-normal stars, and that they are farther from the Sun than metal-rich carbon-normal stars.

In future work, we plan to look at the orbital properties of a subset of these stars, as well as the rate of *s*-process enhancement. We plan to perform medium and high-resolution spectroscopic follow-ups of many of these targets in order to confirm our contamination rate, measure radial velocities where needed, derive their dynamical properties (see, e.g., Dietz et al. 2020, 2021), and identify chemo-dynamical groups (see, e.g., Zepeda et al. 2022), and determine their neutron-capture abundances. We plan to specifically follow-up

targets towards the central region of the Galaxy where the number of known CEMP stars is much lower. Following future *Gaia* releases, which will include many millions more BP/RP spectra, we expect to continue this work and again increase the number of CEMP candidate stars.

Chapter 7

Summary and Outlook

In this dissertation, I studied ancient stars and the inner Galaxy with the aim of illuminating properties of the first stars and the Milky Way's early formation history. Specifically, in Chapters 2, 3, and 4, I presented the COMBS survey which chemodynamically characterized metal-poor inner Galaxy stars using VLT/FLAMES spectra. In Chapter 5, I constrained the length of the Galactic bar using APOGEE and *Gaia* data. Lastly, in Chapter 6, I used low-resolution *Gaia* BP/RP spectra to detect and map CEMP stars. In Section 7.1, I summarize the conclusions of these chapters and this dissertation as a whole, starting with Table 7.1, which provides a condensed list of my findings. Finally, in Section 7.2, I suggest future avenues for building on this work, including plans to utilize upcoming surveys.

7.1 Summary of Conclusions

In Chapter 2 (COMBS I), I present detailed chemical abundance analysis of 26 stars observed with VLT/UVES high-resolution spectra. One of the major results from this work come from the α-element abundances. Specifically, I find they are enhanced relative to similar metallicity stars in the Milky

Table 7.1: Summary of Findings

Chapter	Question	Finding
2	What does the chemistry of metal-poor stars in the inner Galaxy tell us about star formation in the early universe?	Consistent with a top-heavy IMF for the first stars including a possible PISN signature.
3	What fraction of metal-poor stars in the inner Galaxy stay confined to it and to what Galactic structure do they belong?	≈50% of metal-poor stars in the inner Galaxy are halo interlopers. No evidence for a classical bulge structure amongst confined stars.
4	How does comparative analysis of the different dynamical populations of metal-poor inner Galaxy stars inform chemical evolution of the early universe?	Evidence for higher chemical complexity in early universe possibly from larger diversity in nucleosynthetic events or inhomogeneous mixing.
5	Is the length of the Milky Way's bar shorter when measured from the maximal extent of the last trapped bar star than from stellar number density?	The length of the Milky Way's bar from the maximal extent of the last trapped bar orbit is 3.5 kpc, which is shorter than number density estimates of 5 kpc.
6	What is the distribution of CEMP stars throughout the Galaxy?	Contrary to literature results, I find the distribution of CEMP stars follows the distribution of carbon-normal metal-poor stars, including having the highest density in the inner Galaxy.

Way's disk and halo, indicating the enriching population had a more top-heavy IMF (e.g., Johnson et al., 2013a). Although this result was discovered with a small sample of only 26 stars, other works have found similar results (Johnson et al., 2014; Duong et al., 2019a), including in Chapter 4 of this dissertation (COMBS III; Lucey et al., 2022). Given that the metal-poor inner Galaxy stars are thought to be some of the oldest stars in the Galaxy, their chemistry is thought to be indicative of the nucleosynthetic yields of the first generation of stars. Therefore, these results are consistent with predictions that the first generation of stars were massive (Bromm et al., 1999, 2002; Nakamura & Umemura, 2001; Abel et al., 2000, 2002).

In addition, a number of works have predicted that the metal-poor component of the inner Galaxy would be composed of dissipated globular clusters (Kruijssen, 2015; Shapiro et al., 2010; Bournaud, 2016). In Chapter 2 (COMBS I) and Chapter 4 (COMBS III), I found a total of 4 stars with the chemical signature of second-generation globular cluster stars. Specifically, they have enhanced aluminum abundances ([Al/Fe]$>+0.7$) and relatively low magnesium abundances ([Mg/Fe]$<+0.5$). This is consistent with previous works which have also found stars in the inner Galaxy with chemistry consistent with globular cluster stars (Schiavon et al., 2017; Fernández-Trincado et al., 2017; Horta et al., 2021).

In Chapter 3 (COMBS II), I performed dynamical analysis of ≈ 500 metal-poor inner Galaxy stars using VLT/FLAMES spectra. Specifically, I implement probabilistic orbit analysis in order to determine which metal-poor

inner Galaxy stars stay confined to the inner 3.5 kpc of the Galaxy versus which are Galactic halo stars just temporarily passing through the inner Galaxy. I find that ≈50% of the COMBS sample stays confined to the inner Galaxy, while the other half are halo interlopers. Furthermore, I find that the percentage of halo interlopers increases with decreasing metallicity.

Once the halo interlopers are removed from the COMBS sample, I study the dynamical structure of the confined inner Galaxy stars. Previous work which did not remove the halo interlopers found a high velocity dispersion and little to no net rotation in the metal-poor inner Galaxy stars (Ness et al., 2013b; Kunder et al., 2016; Arentsen et al., 2020a). To explain these observations, it was suggested that the Milky Way was host to a composite bulge with a metal-poor classical bulge component (Babusiaux et al., 2010; Hill et al., 2011; Zoccali et al., 2014). However, in Chapter 3 (COMBS II), when I remove the halo interloping population the velocity dispersion decreases and the net rotation increases so that there is no need to invoke a classical bulge to explain the observations. Furthermore, I find the kinematics of the confined metal-poor stars to be consistent with kinematic fractionation, which refers to the separation of stellar populations with different initial kinematics by a forming/growing bar (Debattista et al., 2017). Therefore, this results indicates that secular evolution may be more important early on in the Milky Way's formation rather than hierarchical accretion. This is consistent with initial results from JWST indicating that disks may form earlier in galaxies than previously thought (Kartaltepe et al., 2022).

In Chapter 4, I presented stellar parameter and chemical abundance analysis of ≈500 metal-poor inner Galaxy stars using VLT/GIRAFFE spectra. Consistent with results in Chapter 2 (COMBS I), I found high levels of α-element enhancement compared to other Milky Way populations of similar metallicity. Furthermore, two stars have such high calcium abundances ([Ca/Mg]$>+0.5$) that they are consistent with predictions for PISNe (Takahashi et al., 2018). However, their aluminum abundances are higher than expected. Given that they have [Fe/H]>-2, it is possible that they were enriched by more than one supernova, including a PISN.

Incorporating the dynamical results from Chapter 3 (COMBS II), I perform a comparative study between the chemical dimensionality of different inner Galaxy populations. Using PCA, I find that the metal-poor stellar population that is most confined (apocenter<3.5 kpc) to the inner Galaxy has the highest chemical dimensionality compared to the less confined populations. Simulations indicate stars that are more confined to the inner Galaxy are generally predicted to be older than similar metallicity stars that are less confined (Tumlinson, 2010). Therefore, these results indicate that the oldest metal-poor stars have higher chemical dimensionality than younger metal-poor stars. This may be because of inhomogeneous mixing of the ISM in the early universe, or a larger diversity of nucleosynthetic events. For example, this may be the case if the first generation of stars are more massive and explode in unusual supernova that are rare at later times (e.g., PISNe, faint supernovae, etc.).

In total, the COMBS survey provided the first detailed analysis of the

high-impact population of metal-poor inner Galaxy stars. With innovative dynamical methods, I demonstrated that halo interlopers comprise a large fraction of this population and when they are removed the evidence for a classical bulge in the Milky Way disappears. I also found chemical results that are consistent with predictions of the nucleosynthetic yields of the first stars, including high levels of α-element enhancement and a possible PISN signature.

In Chapter 5, I develop a new method to constrain the length of a galactic bar through direct orbit integration. Explicitly, I find that only gravitational potentials with a bar length consistent with that of the observational data will give a self-consistent measured bar length. In other words, the measured bar length from orbit integration will not match the assumed potential's bar length if the bar length of the observational data, which provide the initial phase-space coordinates of the orbit, is different than the assumed potential. Therefore, this method can be used to test any barred gravitational potential model for the Milky Way.

With this method, I find that APOGEE DR17 and *Gaia* DR3 data are only consistent with a gravitational potential that has a bar length of 3.5 kpc. This bar length estimate is based on the maximum extent of trapped orbits. The estimated bar length for the same potential is $\approx$5 kpc if measured from the the stellar number density counts. This is consistent with predictions that the Milky Way's bar length is overestimated at 5 kpc because of the attached spiral arms extending the number density counts past the trapped bar length (Hilmi et al., 2020). This work represent a first step towards more accurate

inner Galaxy dynamics by constraining a new parameter of the gravitational potential, the Galactic bar length.

One of the remaining mysteries about the chemistry of metal-poor inner galaxy stars is the rate of CEMP stars because photometric selection biases has thus far prevented a fair measurement (Howes et al., 2016; Lucey et al., 2022; Arentsen et al., 2021). To solve this problem, in Chapter 6, I develop a new method to detect candidate CEMP stars using *Gaia* DR3 BP/RP low-resolution spectra. With this method I identify 58,872 CEMP candidates, which is the largest homogeneously identified sample to date.

We briefly investigate a number of properties of this CEMP sample. Specifically, we find that the occurrence rate of CEMP stars increases with decreasing metallicity, consistent with previous work on CEMP stars (Lucatello et al., 2006; Lee et al., 2013; Placco et al., 2014; Yoon et al., 2018). Furthermore, this sample of CEMP candidates spans from the inner to outer Galaxy with distances as close as 0.8 kpc from the Galactic center and as far as >30 kpc. When we compare the CEMP candidates' parallax distribution to those of carbon-normal metal-rich and metal-poor stars, we find that the CEMP distribution closes follows that of the metal-poor carbon-normal stars, including peaking at the parallax of the Galactic center. By providing this sample of CEMP candidates, this work represents a crucial first step in constraining the occurrence rate of CEMP stars throughout the Galaxy and further constraining their origins.

7.2 Future Work

This dissertation has increased our understanding of the structure of the inner Galaxy, including the nature of the metal-poor component and its CEMP stars. There are a number of ways to build upon this dissertation and continue to advance our understanding of the ancient Milky Way. In Section 7.2.1, I discuss my plans to build on the results from the COMBS survey (Chapters 2, 3, and 4) and the dynamical methods from Chapter 5 using the upcoming Milky Way Mapper survey in SDSS-V. Section 7.2.2 outlines my plans for the near future to follow-up CEMP candidates (identified in Chapter 6) using McDonald Observatory's 2.7m telescope and IGRINS on Gemini South in order to perform detailed chemo-dynamical analysis and better understand their origins.

7.2.1 Inner Galaxy

In order to gain new insight into the Milky Way's formation history, I will chemo-dynamically characterize the stars in the inner Galaxy, using novel techniques to disentangle the complex mix of stellar populations. SDSS-V's Milky Way Mapper survey will provide stellar abundances of elements which are key to tracing nucleosynthetic pathways and illuminating the origins of a stellar population by tracing its star formation history. To better understand the powerful new inner Galaxy data from SDSS-V's Milky Way Mapper survey, I will use cutting edge simulations, including the FIRE-3 cosmological simulations. I will study the chemistry and orbital density of inner Galactic

halo stars as a function of orbital guiding radius to provide new insight into the Milky Way's early accretion history. I will also illuminate the Galactic bar and disk's formation and evolution by studying the distribution and chemistry of the bar's various orbit families.

- **Program 1: Tracing the Milky Way's early accretion history in the inner Galactic halo.** This program will focus on the pressure-supported component of the inner Milky Way, the inner Galactic halo, which informs the relative roles of secular and hierarchical accretion in early galaxy evolution. I will quantify the relationship between the orbital density and chemistry of the stars in the inner halo as a function of the accretion history, including merger rates and mass-ratios in FIRE-3 Milky Way-like galaxy simulations. Then, I will compare these results to data from SDSS-V in order to constrain the early Milky Way's merger rate. This program will maximize the impact of the SDSS-V survey by first quantifying expectations from simulations before diving into the Milky Way data.

- **Program 2: Testing theories of Galactic bar and disk formation with chemo-dynamics.** In contrast to Program 1, this program will focus on the rotationally-supported component of the inner Galaxy which is dominated by the Galactic bar. I will apply a novel dynamically method to the inner Galaxy SDSS-V data to deconstruct the orbital structure of the Galactic bar, fully taking into account the uncertainties

on the inner Galactic gravitational potential. I will then study the chemical distribution of each orbital family, comparing to simulations in order to illuminate the relationships between kinematics and chemistry in the Galactic disk before bar formation.

In total, this work will provide unprecedented insight into the formation of the inner Galaxy, using novel techniques and comparisons to simulations. By constraining the structure and dynamical properties of the inner Galaxy, my proposed programs lays crucial groundwork that will empower future studies with the upcoming Roman Galactic Bulge Time Domain Survey, which will measure proper motions of inner Galaxy stars with astrometric precision of $\approx$10 μas yr^{-1} (WFIRST Astrometry Working Group et al., 2019). In closing, this proposed work will maximize the inner Milky Way's constraints on our theories of cosmology and galaxy formation, yielding broad implications across the Universe.

7.2.2 CEMP Stars

It is crucial to follow-up the CEMP candidates identified in Chapter 6 with higher-resolution spectra to confirm the carbon abundance and determine the rate of *s*-process enhancement. Furthermore, in order to perform dynamical analysis and tag these stars to a Galactic structure, we must measure the radial velocities. Therefore, I will perform a spectroscopic survey to chemo-dynamically characterize the CEMP candidates.

Using the Tull spectrographon the 2.7m telescope at McDonald Observatory and IGRINS on Gemini South, I will observe CEMP candidates which do not already have radial velocities from the *Gaia* survey. With this data, I will also measure the carbon and *s*-process abundances in order to classify the stars as carbon-normal, CEMP-no or CEMP-*s*. I will also combine this with data from *Gaia* DR3. Specifically, stars that have been observed with *Gaia*'s Radial Velocity Spectrometer (RVS) instrument will have zirconium, cerium and neodymium abundance measurements and radial velocities in *Gaia* DR3. Combining these data, with the radial velocities measured from the spectra I will determine the orbits of the stars and investigate the relative frequency of CEMP-no/CEMP-*s* stars as a function of Galactic structure. In total, this survey will bring new insight into the origins of these mysterious, high-impact stars.

Bibliography

Abate C., Pols O. R., Karakas A. I., Izzard R. G., 2015, A&A, 576, A118

Abdurro'uf et al., 2021, arXiv e-prints, p. arXiv:2112.02026

Abdurro'uf et al., 2022, ApJS, 259, 35

Abel T., Bryan G. L., Norman M. L., 2000, ApJ, 540, 39

Abel T., Bryan G. L., Norman M. L., 2002, Science, 295, 93

Adibekyan V. Z., Sousa S. G., Santos N. C., Delgado Mena E., González Hernández J. I., Israelian G., Mayor M., Khachatryan G., 2012, A&A, 545, A32

Ahumada R., et al., 2020, ApJS, 249, 3

Allende Prieto C., 2004, Astronomische Nachrichten, 325, 604

Allende Prieto C., Beers T. C., Wilhelm R., Newberg H. J., Rockosi C. M., Yanny B., Lee Y. S., 2006, ApJ, 636, 804

Allende Prieto C., et al., 2008a, AJ, 136, 2070

Allende Prieto C., et al., 2008b, AJ, 136, 2070

Allende Prieto C., Hubeny I., Smith J. A., 2009, MNRAS, 396, 759

Alonso A., Arribas S., Martínez-Roger C., 1999, A&AS, 140, 261

Alvarez R., Plez B., 1998, A&A, 330, 1109

Amarante J. A. S., Beraldo e Silva L., Debattista V. P., Smith M. C., 2020, ApJLett, 891, L30

Amarsi A. M., Asplund M., 2017, MNRAS, 464, 264

Amarsi A. M., Asplund M., Collet R., Leenaarts J., 2016, MNRAS, 455, 3735

Anders F., et al., 2019, A&A, 628, A94

Andrae R., et al., 2018, preprint, (arXiv:1804.09374)

Andrae R., et al., 2022, arXiv e-prints, p. arXiv:2206.06138

Andrae R., Rix H.-W., Chandra V., 2023, arXiv e-prints, p. arXiv:2302.02611

Antoja T., et al., 2018, Nature, 561, 360

Arenou F., et al., 2018, A&A, 616, A17

Arentsen A., Starkenburg E., Shetrone M. D., Venn K. A., Depagne É., McConnachie A. W., 2019, A&A, 621, A108

Arentsen A., et al., 2020a, MNRAS, 491, L11

Arentsen A., et al., 2020b, MNRAS, 496, 4964

Arentsen A., et al., 2021, MNRAS, 505, 1239

Arentsen A., Placco V. M., Lee Y. S., Aguado D. S., Martin N. F., Starkenburg E., Yoon J., 2022, arXiv e-prints, p. arXiv:2206.04081

Armandroff T. E., Da Costa G. S., 1991, AJ, 101, 1329

Armandroff T. E., Zinn R., 1988, AJ, 96, 92

Arnett W. D., 1978, ApJ, 219, 1008

Arp H., 1962, ApJ, 135, 311

Asplund M., Grevesse N., Sauval A. J., 2005, in Barnes III T. G., Bash F. N., eds, Astronomical Society of the Pacific Conference Series Vol. 336, Cosmic Abundances as Records of Stellar Evolution and Nucleosynthesis. p. 25

Athanassoula E., 2005, MNRAS, 358, 1477

Athanassoula E., Misiriotis A., 2002, MNRAS, 330, 35

Baade W., 1946, PASP, 58, 249

Babusiaux C., et al., 2010, A&A, 519, A77

Babusiaux C., et al., 2014, A&A, 563, A15

Bailer-Jones C. A. L., Rybizki J., Fouesneau M., Mantelet G., Andrae R., 2018, AJ, 156, 58

Bailer-Jones C. A. L., Rybizki J., Fouesneau M., Demleitner M., Andrae R., 2021, AJ, 161, 147

Banik N., Bovy J., 2019, MNRAS, 484, 2009

Barbuy B., Zoccali M., Ortolani S., Hill V., Minniti D., Bica E., Renzini A., Gómez A., 2009, A&A, 507, 405

Barkat Z., Rakavy G., Sack N., 1967, Phys. Rev. Lett., 18, 379

Battaglia G., Irwin M., Tolstoy E., Hill V., Helmi A., Letarte B., Jablonka P., 2008, MNRAS, 383, 183

Battistini C., Bensby T., 2015, A&A, 577, A9

Battistini C., Bensby T., 2016, A&A, 586, A49

Beers T. C., Christlieb N., 2005, ARA&A, 43, 531

Beers T. C., Preston G. W., Shectman S. A., 1992, AJ, 103, 1987

Beers T. C., Norris J. E., Placco V. M., Lee Y. S., Rossi S., Carollo D., Masseron T., 2014, ApJ, 794, 58

Beers T. C., et al., 2017, ApJ, 835, 81

Bekki K., 2019, MNRAS, 490, 4007

Belokurov V., Erkal D., Evans N. W., Koposov S. E., Deason A. J., 2018, MNRAS, 478, 611

Bennett M., Bovy J., 2021, MNRAS, 503, 376

Bennett M., Bovy J., Hunt J. A. S., 2021, arXiv e-prints, p. arXiv:2107.08055

Bensby T., et al., 2013, A&A, 549, A147

Bensby T., Feltzing S., Oey M. S., 2014, A&A, 562, A71

Bensby T., et al., 2017, A&A, 605, A89

Bergemann M., Gehren T., 2008, A&A, 492, 823

Bergemann M., Pickering J. C., Gehren T., 2010, MNRAS, 401, 1334

Bergemann M., Lind K., Collet R., Asplund M., 2011, in Journal of Physics Conference Series. p. 012002 (arXiv:1109.2601), doi:10.1088/1742-6596/328/1/012002

Bergemann M., Kudritzki R.-P., Würl M., Plez B., Davies B., Gazak Z., 2013, ApJ, 764, 115

Bergemann M., Kudritzki R.-P., Gazak Z., Davies B., Plez B., 2015, ApJ, 804, 113

Bessell M. S., Castelli F., Plez B., 1998, A&A, 333, 231

Bessell M., Bloxham G., Schmidt B., Keller S., Tisserand P., Francis P., 2011, Publications of the Astronomical Society of the Pacific, 123, 789

Binney J., 2020, MNRAS, 495, 895

Binney J., Spergel D., 1982, ApJ, 252, 308

Binney J., Gerhard O. E., Stark A. A., Bally J., Uchida K. I., 1991, MNRAS, 252, 210

Binney J., Gerhard O., Spergel D., 1997, MNRAS, 288, 365

Bisterzo S., Gallino R., Straniero O., Cristallo S., Käppeler F., 2010, MNRAS, 404, 1529

Bisterzo S., Gallino R., Straniero O., Cristallo S., Käppeler F., 2011, MNRAS, 418, 284

Blanco-Cuaresma S., Soubiran C., Heiter U., Jofré P., 2014, A&A, 569, A111

Bland-Hawthorn J., Gerhard O., 2016, preprint, (arXiv:1602.07702)

Blitz L., Spergel D. N., 1991, ApJ, 379, 631

Bonaca A., et al., 2020, ApJ, 889, 70

Bournaud F., 2016, in Laurikainen E., Peletier R., Gadotti D., eds, Astrophysics and Space Science Library Vol. 418, Galactic Bulges. p. 355 (arXiv:1503.07660), doi:10.1007/978-3-319-19378-6˙13

Bovy J., 2015, ApJS, 216, 29

Bovy J., et al., 2012, ApJ, 759, 131

Bovy J., Leung H. W., Hunt J. A. S., Mackereth J. T., García-Hernández D. A., Roman-Lopes A., 2019, MNRAS, 490, 4740

Bowen I. S., Vaughan A. H. J., 1973, Appl. Opt., 12, 1430

Bromm V., 2013, Reports on Progress in Physics, 76, 112901

Bromm V., Loeb A., 2003, Nature, 425, 812

Bromm V., Coppi P. S., Larson R. B., 1999, ApJLett, 527, L5

Bromm V., Coppi P. S., Larson R. B., 2002, ApJ, 564, 23

Brook C. B., Kawata D., Scannapieco E., Martel H., Gibson B. K., 2007, ApJ, 661, 10

Brown T. M., et al., 2010, ApJLett, 725, L19

Buder S., et al., 2018, preprint, (arXiv:1804.06041)

Burbidge E. M., Burbidge G. R., Fowler W. A., Hoyle F., 1957, Reviews of Modern Physics, 29, 547

Bureau M., Athanassoula E., 2005, ApJ, 626, 159

Bureau M., Aronica G., Athanassoula E., Dettmar R. J., Bosma A., Freeman K. C., 2006, MNRAS, 370, 753

Buta R. J., Zhang X., 2009, ApJS, 182, 559

Cabrera-Lavers A., Hammersley P. L., González-Fernández C., López-Corredoira M., Garzón F., Mahoney T. J., 2007, A&A, 465, 825

Cabrera-Lavers A., González-Fernández C., Garzón F., Hammersley P. L., López-Corredoira M., 2008, A&A, 491, 781

Calamida A., et al., 2014, ApJ, 790, 164

Carlberg R. G., Dawson P. C., Hsu T., Vandenberg D. A., 1985, ApJ, 294, 674

Carollo D., et al., 2007, Nature, 450, 1020

Carollo D., et al., 2012, ApJ, 744, 195

Carollo D., Freeman K., Beers T. C., Placco V. M., Tumlinson J., Martell S. L., 2014, ApJ, 788, 180

Carollo D., et al., 2019, ApJ, 887, 22

Carrasco J. M., et al., 2021, A&A, 652, A86

Carrera R., Pancino E., Gallart C., del Pino A., 2013, MNRAS, 434, 1681

Carretta E., Gratton R. G., Bragaglia A., Bonifacio P., Pasquini L., 2004, A&A, 416, 925

Carrillo A., Hawkins K., Bowler B. P., Cochran W., Vanderburg A., 2020, MNRAS, 491, 4365

Carroll J. A., 1933a, MNRAS, 93, 478

Carroll J. A., 1933b, MNRAS, 93, 680

Casagrande L., Wolf C., Mackey A. D., Nordlander T., Yong D., Bessell M., 2019, MNRAS, 482, 2770

Cescutti G., Chiappini C., 2014, A&A, 565, A51

Cescutti G., Chiappini C., Hirschi R., Meynet G., Frischknecht U., 2013, A&A, 553, A51

Cescutti G., Chiappini C., Hirschi R., 2018, in Chiappini C., Minchev I., Starkenburg E., Valentini M., eds, IAU Symposium Vol. 334, Rediscovering Our Galaxy. pp 94–97 (arXiv:1710.11014), doi:10.1017/S1743921317008183

Chen T., Guestrin C., 2016, arXiv e-prints, p. arXiv:1603.02754

Cherchneff I., Dwek E., 2010, ApJ, 713, 1

Chiappini C., Hirschi R., Meynet G., Ekström S., Maeder A., Matteucci F., 2006, A&A, 449, L27

Chiappini C., Frischknecht U., Meynet G., Hirschi R., Barbuy B., Pignatari M., Decressin T., Maeder A., 2011, Nature, 472, 454

Chiba R., Schönrich R., 2021, MNRAS, 505, 2412

Chiti A., Frebel A., Jerjen H., Kim D., Norris J. E., 2020, ApJ, 891, 8

Choi J., Dotter A., Conroy C., Cantiello M., Paxton B., Johnson B. D., 2016, ApJ, 823, 102

Christlieb N., Schörck T., Frebel A., Beers T. C., Wisotzki L., Reimers D., 2008, A&A, 484, 721

Clark P. C., Glover S. C. O., Smith R. J., Greif T. H., Klessen R. S., Bromm V., 2011, Science, 331, 1040

Clarkson W., et al., 2008, ApJ, 684, 1110

Clarkson W. I., et al., 2011, ApJ, 735, 37

Coşkunoğlu B., et al., 2011, MNRAS, 412, 1237

Cohen J. G., 1978, ApJ, 221, 788

Cole A. A., Smecker-Hane T. A., Tolstoy E., Bosler T. L., Gallagher J. S., 2004, MNRAS, 347, 367

Cole D. R., Debattista V. P., Erwin P., Earp S. W. F., Roškar R., 2014, MNRAS, 445, 3352

Collier A., Madigan A.-M., 2021, ApJ, 915, 23

Combes F., Sanders R. H., 1981, A&A, 96, 164

Combes F., Debbasch F., Friedli D., Pfenniger D., 1990, A&A, 233, 82

Conroy C., Naidu R. P., Zaritsky D., Bonaca A., Cargile P., Johnson B. D., Caldwell N., 2019, ApJ, 887, 237

Contopoulos G., 1980, A&A, 81, 198

Contopoulos G., 1981, A&A, 102, 265

Cooke R. J., Madau P., 2014, ApJ, 791, 116

Couchman H. M. P., Rees M. J., 1986, MNRAS, 221, 53

Cowan J. J., Thielemann F.-K., Truran J. W., 1991, Phys. Rep., 208, 267

Cristallo S., et al., 2011, The Astrophysical Journal Supplement Series, 197, 17

Da Costa G. S., et al., 2019, MNRAS, 489, 5900

De Angeli F., et al., 2022, arXiv e-prints, p. arXiv:2206.06143

Debattista V. P., Sellwood J. A., 2000, ApJ, 543, 704

Debattista V. P., Carollo C. M., Mayer L., Moore B., 2004, ApJLett, 604, L93

Debattista V. P., Mayer L., Carollo C. M., Moore B., Wadsley J., Quinn T., 2006, ApJ, 645, 209

Debattista V. P., Ness M., Gonzalez O. A., Freeman K., Zoccali M., Minniti D., 2017, MNRAS, 469, 1587

Debattista V. P., Gonzalez O. A., Sand erson R. E., El-Badry K., Garrison-Kimmel S., Wetzel A., Faucher-Giguère C.-A., Hopkins P. F., 2019, MNRAS, 485, 5073

Dehnen W., 2000, AJ, 119, 800

Dekker H., D'Odorico S., Kaufer A., Delabre B., Kotzlowski H., 2000, in Iye M., Moorwood A. F., eds, Proc. SPIEVol. 4008, Optical and IR Telescope Instrumentation and Detectors. pp 534–545

Di Matteo P., Haywood M., Lehnert M. D., Katz D., Khoperskov S., Snaith O. N., Gómez A., Robichon N., 2019, A&A, 632, A4

Diemand J., Madau P., Moore B., 2005, MNRAS, 364, 367

Diemand J., Kuhlen M., Madau P., Zemp M., Moore B., Potter D., Stadel J., 2008, Nature, 454, 735

Dietz S. E., Yoon J., Beers T. C., Placco V. M., 2020, ApJ, 894, 34

Dietz S. E., Yoon J., Beers T. C., Placco V. M., Lee Y. S., 2021, ApJ, 914, 100

Dotter A., 2016, ApJS, 222, 8

Duong L., Asplund M., Nataf D. M., Freeman K. C., Ness M., Howes L. M., 2019a, MNRAS, 486, 3586

Duong L., Asplund M., Nataf D. M., Freeman K. C., Ness M., 2019b, MNRAS, 486, 5349

Edvardsson B., Andersen J., Gustafsson B., Lambert D. L., Nissen P. E., Tomkin J., 1993, A&A, 275, 101

Eggen O. J., 1969, PASP, 81, 553

Eggen O. J., Lynden-Bell D., Sandage A. R., 1962, ApJ, 136, 748

El-Badry K., Rix H.-W., Ting Y.-S., Weisz D. R., Bergemann M., Cargile P., Conroy C., Eilers A.-C., 2018a, MNRAS, 473, 5043

El-Badry K., et al., 2018b, MNRAS, 480, 652

Englmaier P., Gerhard O., 1999, MNRAS, 304, 512

Erkal D., Koposov S. E., Belokurov V., 2017, MNRAS, 470, 60

Erwin P., et al., 2015, MNRAS, 446, 4039

Fasano G., Franceschini A., 1987, MNRAS, 225, 155

Feltzing S., Holmberg J., Hurley J. R., 2001, A&A, 377, 911

Fernández-Trincado J. G., et al., 2017, ApJ, 846, L2

Fisher D. B., Drory N., 2016, in Laurikainen E., Peletier R., Gadotti D., eds, Astrophysics and Space Science Library Vol. 418, Galactic Bulges. p. 41 (arXiv:1512.02230), doi:10.1007/978-3-319-19378-6˙3

Fitzpatrick E. L., 2004, in Witt A. N., Clayton G. C., Draine B. T., eds, Astronomical Society of the Pacific Conference Series Vol. 309, Astrophysics of Dust. p. 33 (arXiv:astro-ph/0401344)

Fragkoudi F., Grand R. J. J., Pakmor R., Springel V., White S. D. M., Marinacci F., Gomez F. A., Navarro J. F., 2021, A&A, 650, L16

Frebel A., 2018, Annual Review of Nuclear and Particle Science, 68, 237

Frebel A., Norris J. E., 2015, ARA&A, 53, 631

Frebel A., et al., 2006, ApJ, 652, 1585

Frebel A., Simon J. D., Kirby E. N., 2014, ApJ, 786, 74

Freeman K., Bland-Hawthorn J., 2002, ARA&A, 40, 487

Freeman K., et al., 2013, MNRAS, 428, 3660

Friel E. D., 1995, ARA&A, 33, 381

Frogel J. A., Whitford A. E., 1987, ApJ, 320, 199

Fryer C. L., Woosley S. E., Heger A., 2001, ApJ, 550, 372

Fujii M. S., Bédorf J., Baba J., Portegies Zwart S., 2019, MNRAS, 482, 1983

Fukugita M., Ichikawa T., Gunn J. E., Doi M., Shimasaku K., Schneider D. P., 1996, AJ, 111, 1748

Fulbright J. P., McWilliam A., Rich R. M., 2006, ApJ, 636, 821

Fulbright J. P., McWilliam A., Rich R. M., 2007, ApJ, 661, 1152

Fux R., 1999, A&A, 345, 787

Gadotti D. A., 2009, MNRAS, 393, 1531

Gaia Collaboration et al., 2016a, A&A, 595, A1

Gaia Collaboration et al., 2016b, A&A, 595, A2

Gaia Collaboration Brown A. G. A., Vallenari A., Prusti T., de Bruijne J. H. J., Babusiaux C., Bailer-Jones C. A. L., 2018a, preprint, (arXiv:1804.09365)

Gaia Collaboration et al., 2018b, A&A, 616, A1

Gaia Collaboration et al., 2021a, A&A, 649, A1

Gaia Collaboration et al., 2021b, A&A, 649, A1

Gaia Collaboration Vallenari A., Brown A. G. A., Prusti T., et al. 2022, A&A

García Pérez A. E., et al., 2013, ApJ, 767, L9

García Pérez A. E., et al., 2016, AJ, 151, 144

García Pérez A. E., et al., 2018, ApJ, 852, 91

Gardner J. P., et al., 2006, Space Sci. Rev., 123, 485

Gavazzi G., et al., 2015, A&A, 580, A116

Gavel A., Andrae R., Fouesneau M., Korn A. J., Sordo R., 2021, A&A, 656, A93

Gilmore G., Wyse R. F. G., Kuijken K., 1989, ARA&A, 27, 555

Gilmore G., et al., 2012, The Messenger, 147, 25

Gómez A., Di Matteo P., Schultheis M., Fragkoudi F., Haywood M., Combes F., 2018, A&A, 615, A100

Gonzalez O. A., Gadotti D., 2016, in Laurikainen E., Peletier R., Gadotti D., eds, Astrophysics and Space Science Library Vol. 418, Galactic Bulges. p. 199 (arXiv:1503.07252), doi:10.1007/978-3-319-19378-6_9

Gonzalez O. A., et al., 2011, A&A, 530, A54

Gonzalez O. A., Rejkuba M., Zoccali M., Valent E., Minniti D., Tobar R., 2013, A&A, 552, A110

Gonzalez O. A., et al., 2015, A&A, 584, A46

Gratton R. G., et al., 2001, A&A, 369, 87

Gratton R., Sneden C., Carretta E., 2004, Annual Review of Astronomy and Astrophysics, 42, 385

Greif T. H., Johnson J. L., Klessen R. S., Bromm V., 2008, MNRAS, 387, 1021

Greif T. H., Glover S. C. O., Bromm V., Klessen R. S., 2010, ApJ, 716, 510

Greif T. H., Bromm V., Clark P. C., Glover S. C. O., Smith R. J., Klessen R. S., Yoshida N., Springel V., 2012, MNRAS, 424, 399

Grevesse N., Asplund M., Sauval A. J., 2007, Space Sci. Rev., 130, 105

Griffith E. J., Johnson J. A., Weinberg D. H., Ilyin I., Johnson J. W., Rodriguez-Martinez R., Strassmeier K. G., 2023, ApJ, 944, 47

Guedes J., Mayer L., Carollo M., Madau P., 2013, ApJ, 772, 36

Gull M., et al., 2018, ApJ, 862, 174

Gunn J. E., et al., 2006, AJ, 131, 2332

Gustafsson B., Edvardsson B., Eriksson K., Jørgensen U. G., Nordlund Å., Plez B., 2008, A&A, 486, 951

Hammersley P. L., Garzon F., Mahoney T., Calbet X., 1994, MNRAS, 269, 753

Hammersley P. L., Garzón F., Mahoney T. J., López-Corredoira M., Torres M. A. P., 2000, MNRAS, 317, L45

Hansen T. T., Andersen J., Nordström B., Beers T. C., Placco V. M., Yoon J., Buchhave L. A., 2016a, A&A, 586, A160

Hansen T. T., Andersen J., Nordström B., Beers T. C., Placco V. M., Yoon J., Buchhave L. A., 2016b, A&A, 588, A3

Hattori K., Erkal D., Sanders J. L., 2016, MNRAS, 460, 497

Hawkins K., Wyse R. F. G., 2018, MNRAS,

Hawkins K., et al., 2015, MNRAS, 447, 2046

Hawkins K., et al., 2016, A&A, 592, A70

Hawkins K., Leistedt B., Bovy J., Hogg D. W., 2017, MNRAS, 471, 722

Hayden M. R., et al., 2020, arXiv e-prints, p. arXiv:2011.13745

He X.-J., Luo A. L., Chen Y.-Q., 2022, MNRAS, 512, 1710

Heger A., Woosley S. E., 2002, ApJ, 567, 532

Heger A., Woosley S. E., 2010, ApJ, 724, 341

Heger A., Fryer C. L., Woosley S. E., Langer N., Hartmann D. H., 2003, ApJ, 591, 288

Heiter U., Jofré P., Gustafsson B., Korn A. J., Soubiran C., Thévenin F., 2015, A&A, 582, A49, Paper I

Heiter U., et al., 2020, arXiv e-prints, p. arXiv:2011.02049

Helmi A., 2008, A&A Rev., 15, 145

Hill V., et al., 2011, A&A, 534, A80

Hilmi T., et al., 2020, MNRAS, 497, 933

Hirano S., Hosokawa T., Yoshida N., Umeda H., Omukai K., Chiaki G., Yorke H. W., 2014, ApJ, 781, 60

Hirano S., Hosokawa T., Yoshida N., Omukai K., Yorke H. W., 2015, MNRAS, 448, 568

Hirshfeld A., McClure R. D., Twarog B. A., 1978, in Philip A. G. D., Hayes D. S., eds, Vol. 80, The HR Diagram - The 100th Anniversary of Henry Norris Russell. p. 163

Horta D., et al., 2020, arXiv e-prints, p. arXiv:2007.10374

Horta D., et al., 2021, MNRAS, 500, 5462

Howard C. D., Rich R. M., Reitzel D. B., Koch A., De Propris R., Zhao H., 2008, ApJ, 688, 1060

Howard C. D., et al., 2009, ApJLett, 702, L153

Howes L. M., et al., 2014, MNRAS, 445, 4241

Howes L. M., et al., 2015, Nature, 527, 484

Howes L. M., et al., 2016, MNRAS, 460, 884

Hunt J. A. S., Bovy J., 2018, MNRAS, 477, 3945

Iwamoto K., Brachwitz F., Nomoto K., Kishimoto N., Umeda H., Hix W. R., Thielemann F.-K., 1999, ApJS, 125, 439

Jeon M., Pawlik A. H., Bromm V., Milosavljević M., 2014, MNRAS, 444, 3288

Jofré P., et al., 2014, A&A, 564, A133, Paper III

Johnson J. L., Bromm V., 2006, MNRAS, 366, 247

Johnson C. I., Rich R. M., Fulbright J. P., Valenti E., McWilliam A., 2011, ApJ, 732, 108

Johnson C. I., Rich R. M., Kobayashi C., Fulbright J. P., 2012, ApJ, 749, 175

Johnson C. I., Rich R. M., Kobayashi C., Kunder A., Pilachowski C. A., Koch A., de Propris R., 2013a, ApJ, 765, 157

Johnson C. I., McWilliam A., Rich R. M., 2013b, ApJ, 775, L27

Johnson C. I., Rich R. M., Kobayashi C., Kunder A., Koch A., 2014, AJ, 148, 67

Johnson C. I., et al., 2020, MNRAS,

Jones J. E., Alloin D. M., Jones B. J. T., 1984, ApJ, 283, 457

Jorissen A., et al., 2016, A&A, 586, A158

Karlsson T., Johnson J. L., Bromm V., 2008, ApJ, 679, 6

Kartaltepe J. S., et al., 2022, arXiv e-prints, p. arXiv:2210.14713

Kauffmann G., White S. D. M., Guiderdoni B., 1993, MNRAS, 264, 201

Keller S. C., et al., 2007, , 24, 1

Keller S. C., et al., 2014, Nature, 506, 463

Kerr F. J., Lynden-Bell D., 1986, MNRAS, 221, 1023

Kitayama T., Yoshida N., Susa H., Umemura M., 2004, ApJ, 613, 631

Kobayashi C., Nakasato N., 2011, ApJ, 729, 16

Kobayashi C., Umeda H., Nomoto K., Tominaga N., Ohkubo T., 2006, ApJ, 653, 1145

Kobayashi C., Karakas A. I., Umeda H., 2011a, MNRAS, 414, 3231

Kobayashi C., Tominaga N., Nomoto K., 2011b, ApJ, 730, L14

Kobayashi C., Ishigaki M. N., Tominaga N., Nomoto K., 2014, ApJLett, 785, L5

Kobayashi C., Nomoto K., Hachisu I., 2015, ApJ, 804, L24

Kobayashi C., Karakas A. I., Lugaro M., 2020, ApJ, 900, 179

Koch A., McWilliam A., Preston G. W., Thompson I. B., 2016, A&A, 587, A124

Koch A., Reichert M., Hansen C. J., Hampel M., Stancliffe R. J., Karakas A., Arcones A., 2019, A&A, 622, A159

Kontizas E., Dapergolas A., Morgan D. H., Kontizas M., 2001, A&A, 369, 932

Koposov S. E., Belokurov V., Torrealba G., Evans N. W., 2015, ApJ, 805, 130

Koppelman H. H., Hagen J. H. J., Helmi A., 2021, A&A, 647, A37

Kormendy J., Illingworth G., 1982, ApJ, 256, 460

Kormendy J., Kennicutt Robert C. J., 2004, Annual Review of Astronomy and Astrophysics, 42, 603

Kruijssen J. M. D., 2015, MNRAS, 454, 1658

Kuijken K., Rich R. M., 2002, AJ, 124, 2054

Kunder A., et al., 2016, ApJLett, 821, L25

Kunder A., et al., 2020, AJ, 159, 270

Lai D. K., Lee Y. S., Bolte M., Lucatello S., Beers T. C., Johnson J. A., Sivarani T., Rockosi C. M., 2011, ApJ, 738, 51

Larson R. B., 1998, MNRAS, 301, 569

Laskar J., 1993, Celestial Mechanics and Dynamical Astronomy, 56, 191

Lattimer J. M., Schramm D. N., 1974, ApJ, 192, L145

Laurikainen E., Salo H., Athanassoula E., Bosma A., Herrera-Endoqui M., 2014, MNRAS, 444, L80

Lecureur A., Hill V., Zoccali M., Barbuy B., Gómez A., Minniti D., Ortolani S., Renzini A., 2007, A&A, 465, 799

Lee Y. S., et al., 2008a, AJ, 136, 2050

Lee Y. S., et al., 2008b, AJ, 136, 2022

Lee Y. S., et al., 2011, AJ, 141, 90

Lee Y. S., et al., 2013, AJ, 146, 132

Lee Y. S., Beers T. C., Kim Y. K., Placco V., Yoon J., Carollo D., Masseron T., Jung J., 2017, ApJ, 836, 91

Lee Y. S., Beers T. C., Kim Y. K., 2019, ApJ, 885, 102

Leung H. W., Bovy J., 2019, MNRAS, 489, 2079

Leung H. W., Bovy J., Mackereth J. T., Hunt J. A. S., Lane R. R., Wilson J. C., 2022, arXiv e-prints, p. arXiv:2204.12551

Leung H. W., Bovy J., Mackereth J. T., Hunt J. A. S., Lane R. R., Wilson J. C., 2023, MNRAS, 519, 948

Li T. S., et al., 2017, ApJ, 838, 8

Li C., et al., 2021, MNRAS, 506, 1651

Lind K., Asplund M., Barklem P. S., 2009, A&A, 503, 541

Lind K., Asplund M., Barklem P. S., Belyaev A. K., 2011, A&A, 528, A103

Lind K., et al., 2015, A&A, 575, L12

Lindegren L., 2018, Technical report, Re-normalising the astrometric chi-square in Gaia DR2

Lindegren L., et al., 2018, A&A, 616, A2

Lindegren L., et al., 2021, A&A, 649, A2

Lippuner J., Fernández R., Roberts L. F., Foucart F., Kasen D., Metzger B. D., Ott C. D., 2017, MNRAS, 472, 904

Liu C., Bailer-Jones C. A. L., Sordo R., Vallenari A., Borrachero R., Luri X., Sartoretti P., 2012, MNRAS, 426, 2463

López-Corredoira M., Cabrera-Lavers A., Mahoney T. J., Hammersley P. L., Garzón F., González-Fernández C., 2007, AJ, 133, 154

Lucatello S., Tsangarides S., Beers T. C., Carretta E., Gratton R. G., Ryan S. G., 2005, ApJ, 625, 825

Lucatello S., Beers T. C., Christlieb N., Barklem P. S., Rossi S., Marsteller B., Sivarani T., Lee Y. S., 2006, ApJLett, 652, L37

Lucey M., et al., 2019, MNRAS, 488, 2283

Lucey M., Ting Y.-S., Ramachandra N. S., Hawkins K., 2020, MNRAS, 495, 3087

Lucey M., et al., 2021, MNRAS, 501, 5981

Lucey M., et al., 2022, MNRAS, 509, 122

Lucey M., Pearson S., Hunt J. A. S., Hawkins K., Ness M., Petersen M. S., Price-Whelan A. M., Weinberg M. D., 2023, MNRAS, 520, 4779

Lugaro M., Karakas A. I., Stancliffe R. J., Rijs C., 2012, ApJ, 747, 2

Lundberg S. M., Lee S.-I., 2017, Advances in neural information processing systems, 30

Machado Poletti Valle L. F., Avestruz C., Barnes D. J., Farahi A., Lau E. T., Nagai D., 2021, MNRAS, 507, 1468

Madau P., Ferrara A., Rees M. J., 2001, ApJ, 555, 92

Majewski S. R., et al., 2017, AJ, 154, 94

Marino A. F., Villanova S., Piotto G., Milone A. P., Momany Y., Bedin L. R., Medling A. M., 2008, A&A, 490, 625

Marino A. F., et al., 2011, ApJ, 731, 64

Martinez-Valpuesta I., Gerhard O., 2011, ApJLett, 734, L20

Martinez-Valpuesta I., Shlosman I., Heller C., 2006, ApJ, 637, 214

Mashonkina L., et al., 2008, A&A, 478, 529

Massari D., et al., 2014, ApJ, 791, 101

Masseron T., Johnson J. A., Plez B., van Eck S., Primas F., Goriely S., Jorissen A., 2010, A&A, 509, A93

Masseron T., et al., 2014, A&A, 571, A47

Masseron T., Merle T., Hawkins K., 2016, BACCHUS: Brussels Automatic Code for Characterizing High accUracy Spectra, Astrophysics Source Code Library (ascl:1605.004), doi:10.20356/C4TG6R

Masters K. L., et al., 2011, MNRAS, 411, 2026

Matteucci F., Greggio L., 1986, A&A, 154, 279

Mayor M., et al., 2003, The Messenger, 114, 20

McClure R. D., Woodsworth A. W., 1990, ApJ, 352, 709

McWilliam A., 2016, , 33, e040

McWilliam A., Rich R. M., 1994, ApJS, 91, 749

McWilliam A., Rich R. M., 2004, in McWilliam A., Rauch M., eds, Origin and Evolution of the Elements. p. 38 (arXiv:astro-ph/0312628)

McWilliam A., Zoccali M., 2010, ApJ, 724, 1491

McWilliam A., Fulbright J., Rich R. M., 2010, in Cunha K., Spite M., Barbuy B., eds, IAU Symposium Vol. 265, Chemical Abundances in the Universe: Connecting First Stars to Planets. pp 279–284, doi:10.1017/S1743921310000748

Merritt D., Sellwood J. A., 1994, ApJ, 425, 551

Meusinger H., Reimann H. G., Stecklum B., 1991, A&A, 245, 57

Meynet G., Ekström S., Maeder A., 2006, A&A, 447, 623

Meynet G., Hirschi R., Ekstrom S., Maeder A., Georgy C., Eggenberger P., Chiappini C., 2010, A&A, 521, A30

Minchev I., Famaey B., 2010, ApJ, 722, 112

Minniti D., et al., 2010, NewA, 15, 433

Monari G., Famaey B., Siebert A., Grand R. J. J., Kawata D., Boily C., 2016, MNRAS, 461, 3835

Moore B., Diemand J., Madau P., Zemp M., Stadel J., 2006, MNRAS, 368, 563

Mori M., Ferrara A., Madau P., 2002, ApJ, 571, 40

Mucciarelli A., Lapenna E., Ferraro F. R., Lanzoni B., 2018, ApJ, 859, 75

Myeong G. C., Evans N. W., Belokurov V., Sanders J. L., Koposov S. E., 2018, ApJLett, 863, L28

Nakamura F., Umemura M., 2001, ApJ, 548, 19

Nakamura F., Umemura M., 2002, ApJ, 569, 549

Nakasato N., Nomoto K., 2003, ApJ, 588, 842

Nassau J. J., Blanco V. M., 1958, ApJ, 128, 46

Nataf D. M., Udalski A., Gould A., Fouqué P., Stanek K. Z., 2010, ApJ, 721, L28

Nataf D. M., et al., 2013, ApJ, 769, 88

Ness M., Freeman K., 2016, Publications of the Astronomical Society of Australia, 33, e022

Ness M., Lang D., 2016, AJ, 152, 14

Ness M., et al., 2012, ApJ, 756, 22

Ness M., et al., 2013a, MNRAS, 430, 836

Ness M., et al., 2013b, MNRAS, 432, 2092

Ness M., Debattista V. P., Bensby T., Feltzing S., Roškar R., Cole D. R., Johnson J. A., Freeman K., 2014, ApJLett, 787, L19

Nidever D. L., et al., 2015, AJ, 150, 173

Nishimura N., Takiwaki T., Thielemann F.-K., 2015, ApJ, 810, 109

Nomoto K., 1984, ApJ, 277, 791

Nomoto K., Kobayashi C., Tominaga N., 2013, ARA&A, 51, 457

Nordlander T., Lind K., 2017, A&A, 607, A75

Norris J. E., Christlieb N., Korn A. J., Eriksson K., Bessell M. S., Beers T. C., Wisotzki L., Reimers D., 2007, ApJ, 670, 774

Norris J. E., Wyse R. F. G., Gilmore G., Yong D., Frebel A., Wilkinson M. I., Belokurov V., Zucker D. B., 2010, ApJ, 723, 1632

Norris J. E., et al., 2013, ApJ, 762, 28

Nozawa T., Kozasa T., Umeda H., Maeda K., Nomoto K., 2003, ApJ, 598, 785

Oh S. P., Haiman Z., 2002, ApJ, 569, 558

Olszewski E. W., Schommer R. A., Suntzeff N. B., Harris H. C., 1991, AJ, 101, 515

Omukai K., Palla F., 2003, ApJ, 589, 677

Omukai K., Tsuribe T., Schneider R., Ferrara A., 2005, ApJ, 626, 627

Ortolani S., Renzini A., Gilmozzi R., Marconi G., Barbuy B., Bica E., Rich R. M., 1995, Nature, 377, 701

Osorio Y., Barklem P. S., Lind K., Belyaev A. K., Spielfiedel A., Guitou M., Feautrier N., 2015, A&A, 579, A53

Pancino E., et al., 2017, A&A, 601, A112

Pasquini L., et al., 2000, in Iye M., Moorwood A. F., eds, Society of Photo-Optical Instrumentation Engineers (SPIE) Conference Series Vol. 4008, Proc. SPIE. pp 129–140, doi:10.1117/12.395491

Pasquini L., et al., 2002, The Messenger, 110, 1

Paxton B., Bildsten L., Dotter A., Herwig F., Lesaffre P., Timmes F., 2011, ApJS, 192, 3

Paxton B., et al., 2013, ApJS, 208, 4

Paxton B., et al., 2015, ApJS, 220, 15

Peacock J. A., 1983, MNRAS, 202, 615

Pearson S., Price-Whelan A. M., Johnston K. V., 2017, Nature Astronomy, 1, 633

Pedregosa F., et al., 2011, Journal of Machine Learning Research, 12, 2825

Peebles P. J. E., Dicke R. H., 1968, ApJ, 154, 891

Peters W. L. I., 1975, ApJ, 195, 617

Petersen M. S., Weinberg M. D., Katz N., 2016, MNRAS, 463, 1952

Petersen M. S., Weinberg M. D., Katz N., 2019a, arXiv e-prints, p. arXiv:1903.08203

Petersen M. S., Weinberg M. D., Katz N., 2019b, MNRAS, 490, 3616

Petersen M. S., Weinberg M. D., Katz N., 2021, MNRAS, 500, 838

Pham D., Kaltenegger L., 2022, MNRAS,

Pignatari M., Gallino R., Meynet G., Hirschi R., Herwig F., Wiescher M., 2008, ApJ, 687, L95

Piskunov N., Valenti J. A., 2017, A&A, 597, A16

Placco V. M., Frebel A., Beers T. C., Karakas A. I., Kennedy C. R., Rossi S., Christlieb N., Stancliffe R. J., 2013, ApJ, 770, 104

Placco V. M., Frebel A., Beers T. C., Stancliffe R. J., 2014, ApJ, 797, 21

Planck Collaboration et al., 2014, A&A, 571, A11

Plez B., 2012, Turbospectrum: Code for spectral synthesis, Astrophysics Source Code Library (ascl:1205.004)

Portail M., Gerhard O., Wegg C., Ness M., 2017, MNRAS, 465, 1621

Preston G. W., Sneden C., 2001, AJ, 122, 1545

Price-Whelan A. M., 2015a, SuperFreq, doi:10.5281/zenodo.18787

Price-Whelan A. M., 2015b, SuperFreq: Numerical determination of fundamental frequencies of an orbit (ascl:1511.001)

Price-Whelan A. M., Johnston K. V., Valluri M., Pearson S., Küpper A. H. W., Hogg D. W., 2016a, MNRAS, 455, 1079

Price-Whelan A. M., Sesar B., Johnston K. V., Rix H.-W., 2016b, ApJ, 824, 104

Queiroz A. B. A., et al., 2020, A&A, 638, A76

Queiroz A. B. A., et al., 2021, A&A, 656, A156

Quillen A. C., 2002, AJ, 124, 722

Quillen A. C., Minchev I., Sharma S., Qin Y.-J., Di Matteo P., 2014, MNRAS, 437, 1284

Raha N., Sellwood J. A., James R. A., Kahn F. D., 1991, Nature, 352, 411

Rakavy G., Shaviv G., Zinamon Z., 1967, ApJ, 150, 131

Ramírez S. V., Cohen J. G., 2002, AJ, 123, 3277

Ramírez S. V., Cohen J. G., 2003, AJ, 125, 224

Randich S., Gilmore G., Gaia-ESO Consortium 2013, The Messenger, 154, 47

Rebeirot E., Azzopardi M., Westerlund B. E., 1993, A&AS, 97, 603

Reddy B. E., Tomkin J., Lambert D. L., Allende Prieto C., 2003, MNRAS, 340, 304

Rees M. J., 1999, in Holt S., Smith E., eds, American Institute of Physics Conference Series Vol. 470, After the Dark Ages: When Galaxies were Young (the Universe at 2 Z 5). pp 13–23, doi:10.1063/1.58643

Reggiani H., Schlaufman K. C., Casey A. R., Ji A. P., 2020, arXiv e-prints, p. arXiv:2007.12728

Reid M. J., et al., 2014, ApJ, 783, 130

Rezaei Kh. S., Bailer-Jones C. A. L., Hogg D. W., Schultheis M., 2018, A&A, 618, A168

Rich R. M., 1990, ApJ, 362, 604

Rich R. M., McWilliam A., 2000, in Bergeron J., ed., Society of Photo-Optical Instrumentation Engineers (SPIE) Conference Series Vol. 4005, Discoveries and Research Prospects from 8- to 10-Meter-Class Telescopes. pp 150–161 (arXiv:astro-ph/0005113), doi:10.1117/12.390138

Rich R. M., Reitzel D. B., Howard C. D., Zhao H., 2007, ApJ, 658, L29

Riello M., et al., 2021, A&A, 649, A3

Robin A. C., Marshall D. J., Schultheis M., Reylé C., 2012, A&A, 538, A106

Rockosi C. M., et al., 2022, ApJS, 259, 60

Roederer I. U., Preston G. W., Thompson I. B., Shectman S. A., Sneden C., Burley G. S., Kelson D. D., 2014, AJ, 147, 136

Rojas-Arriagada A., et al., 2014a, A&A, 569, A103

Rojas-Arriagada A., et al., 2014b, A&A, 569, A103

Rojas-Arriagada A., et al., 2017, A&A, 601, A140

Rojas-Arriagada A., et al., 2020, arXiv e-prints, p. arXiv:2007.13967

Rosas-Guevara Y., et al., 2020, MNRAS, 491, 2547

Rosas-Guevara Y., et al., 2021, arXiv e-prints, p. arXiv:2110.04537

Rosswog S., Liebendörfer M., Thielemann F. K., Davies M. B., Benz W., Piran T., 1999, A&A, 341, 499

Rosswog S., Korobkin O., Arcones A., Thielemann F. K., Piran T., 2014, MNRAS, 439, 744

Rybizki J., Demleitner M., Fouesneau M., Bailer-Jones C., Rix H.-W., Andrae R., 2018, PASP, 130, 074101

Safranek-Shrader C., Milosavljević M., Bromm V., 2014, MNRAS, 438, 1669

Saito R. K., Zoccali M., McWilliam A., Minniti D., Gonzalez O. A., Hill V., 2011, AJ, 142, 76

Saito R. K., et al., 2012a, A&A, 537, A107

Saito R. K., et al., 2012b, A&A, 544, A147

Sakari C. M., et al., 2018, ApJ, 868, 110

Salvadori S., Ferrara A., Schneider R., Scannapieco E., Kawata D., 2010, MNRAS, 401, L5

Salvadori S., Skúladóttir Á., Tolstoy E., 2015, MNRAS, 454, 1320

Sanders J. L., Smith L., Evans N. W., 2019, MNRAS, 488, 4552

Santistevan I. B., Wetzel A., El-Badry K., Bland-Hawthorn J., Boylan-Kolchin M., Bailin J., Faucher-Giguère C.-A., Benincasa S., 2020a, MNRAS, 497, 747

Santistevan I. B., Wetzel A., El-Badry K., Bland-Hawthorn J., Boylan-Kolchin M., Bailin J., Faucher-Giguère C.-A., Benincasa S., 2020b, MNRAS, 497, 747

Saslaw W. C., Zipoy D., 1967, Nature, 216, 976

Schauer A. T. P., Drory N., Bromm V., 2020, ApJ, 904, 145

Schiavon R. P., et al., 2017, MNRAS, 466, 1010

Schlaufman K. C., Casey A. R., 2014, ApJ, 797, 13

Schneider R., Ferrara A., Salvaterra R., Omukai K., Bromm V., 2003, Nature, 422, 869

Schneider R., Ferrara A., Salvaterra R., 2004, MNRAS, 351, 1379

Schneider R., Omukai K., Bianchi S., Valiante R., 2012, MNRAS, 419, 1566

Schultheis M., et al., 2017, A&A, 600, A14

Searle L., Zinn R., 1978, ApJ, 225, 357

Sellwood J. A., Gerhard O., 2020, MNRAS, 495, 3175

Sellwood J. A., Wilkinson A., 1993, Reports on Progress in Physics, 56, 173

Sestito F., et al., 2020, MNRAS, 497, L7

Shapiro K. L., Genzel R., Förster Schreiber N. M., 2010, MNRAS, 403, L36

Sharples R., Walker A., Cropper M., 1990, MNRAS, 246, 54

Shen J., Rich R. M., Kormendy J., Howard C. D., De Propris R., Kunder A., 2010, ApJLett, 720, L72

Simmerer J., Sneden C., Cowan J. J., Collier J., Woolf V. M., Lawler J. E., 2004, ApJ, 617, 1091

Siqueira-Mello C., et al., 2016, A&A, 593, A79

Sitnova T. M., Yakovleva S. A., Belyaev A. K., Mashonkina L. I., 2020, Astronomy Letters, 46, 120

Skrutskie M. F., et al., 2006, AJ, 131, 1163

Skúladóttir Á., Tolstoy E., Salvadori S., Hill V., Pettini M., Shetrone M. D., Starkenburg E., 2015, A&A, 574, A129

Smiljanic R., et al., 2014, A&A, 570, A122

Smith V. V., et al., 2021, AJ, 161, 254

Smolinski J. P., et al., 2011, AJ, 141, 89

Sneden C., Cowan J. J., Lawler J. E., Burles S., Beers T. C., Fuller G. M., 2002, ApJ, 566, L25

Soto M., Rich R. M., Kuijken K., 2007, ApJ, 665, L31

Spinrad H., Taylor B. J., 1969, ApJ, 157, 1279

Spinrad H., Taylor B. J., 1971, ApJ, 163, 303

Stanek K. Z., Mateo M., Udalski A., Szymanski M., Kaluzny J., Kubiak M., 1994, ApJLett, 429, L73

Stanek K. Z., Zaritsky D., Harris J., 1998, ApJLett, 500, L141

Starkenburg E., et al., 2010, A&A, 513, A34

Starkenburg E., Shetrone M. D., McConnachie A. W., Venn K. A., 2014, MNRAS, 441, 1217

Starkenburg E., Oman K. A., Navarro J. F., Crain R. A., Fattahi A., Frenk C. S., Sawala T., Schaye J., 2017a, MNRAS, 465, 2212

Starkenburg E., et al., 2017b, MNRAS, 471, 2587

Starkenburg E., et al., 2017c, MNRAS, 471, 2587

Stebbins J., Whitford A. E., 1947, ApJ, 106, 235

Steinmetz M., et al., 2020a, arXiv e-prints, p. arXiv:2002.04377

Steinmetz M., et al., 2020b, arXiv e-prints, p. arXiv:2002.04512

Susa H., Hasegawa K., Tominaga N., 2014, ApJ, 792, 32

Takahashi K., Yoshida T., Umeda H., 2018, ApJ, 857, 111

Tegmark M., Silk J., Rees M. J., Blanchard A., Abel T., Palla F., 1997, ApJ, 474, 1

Tepper-Garcia T., et al., 2021, arXiv e-prints, p. arXiv:2111.05466

Terndrup D. M., 1988, AJ, 96, 884

Tinsley B. M., 1979, ApJ, 229, 1046

Todini P., Ferrara A., 2001, MNRAS, 325, 726

Tominaga N., Iwamoto N., Nomoto K., 2014, ApJ, 785, 98

Tremaine S., Weinberg M. D., 1984, ApJLett, 282, L5

Truran J. W., 1981, A&A, 97, 391

Tumlinson J., 2006, ApJ, 641, 1

Tumlinson J., 2010, ApJ, 708, 1398

Twarog B. A., 1980, ApJ, 242, 242

Udalski A., et al., 2002, AcA, 52, 217

Umeda H., Nomoto K., 2003, Nature, 422, 871

Valenti J. A., Piskunov N., 1996, A&AS, 118, 595

Valenti E., Zoccali M., Renzini A., Brown T. M., Gonzalez O. A., Minniti D., Debattista V. P., Mayer L., 2013, A&A, 559, A98

Valluri M., 1999, in Merritt D. R., Valluri M., Sellwood J. A., eds, Astronomical Society of the Pacific Conference Series Vol. 182, Galaxy Dynamics - A Rutgers Symposium. p. 195

Valluri M., Merritt D., 1998, ApJ, 506, 686

Valluri M., Debattista V. P., Quinn T., Moore B., 2010, MNRAS, 403, 525

Valluri M., Shen J., Abbott C., Debattista V. P., 2016, ApJ, 818, 141

Van der Swaelmen M., Hill V., Primas F., Cole A. A., 2013, A&A, 560, A44

Vasiliev E., 2019, MNRAS, 482, 1525

Vasiliev E., Athanassoula E., 2015, MNRAS, 450, 2842

Vincenzo F., Kobayashi C., 2018, A&A, 610, L16

WFIRST Astrometry Working Group et al., 2019, Journal of Astronomical Telescopes, Instruments, and Systems, 5, 044005

Wada K., Venkatesan A., 2003, ApJ, 591, 38

Wang Y., Zhao H., Mao S., Rich R. M., 2012, MNRAS, 427, 1429

Wang Y., Mao S., Long R. J., Shen J., 2013, MNRAS, 435, 3437

Wang Y., Athanassoula E., Mao S., 2016, MNRAS, 463, 3499

Wegg C., Gerhard O., 2013, MNRAS, 435, 1874

Wegg C., Gerhard O., Portail M., 2015, MNRAS, 450, 4050

Weiland J. L., et al., 1994, ApJLett, 425, L81

Whalen D., Abel T., Norman M. L., 2004, ApJ, 610, 14

White S. D. M., Rees M. J., 1978, MNRAS, 183, 341

White S. D. M., Springel V., 2000, in Weiss A., Abel T. G., Hill V., eds, The First Stars. p. 327 (arXiv:astro-ph/9911378), doi:10.1007/10719504˙62

Whitford A. E., Rich R. M., 1983, ApJ, 274, 723

Wilson J. C., et al., 2019, PASP, 131, 055001

Winteler C., Käppeli R., Perego A., Arcones A., Vasset N., Nishimura N., Liebendörfer M., Thielemann F. K., 2012, ApJLett, 750, L22

Wise J. H., Abel T., 2007, ApJ, 665, 899

Wise J. H., Abel T., 2008, ApJ, 684, 1

Wise J. H., Turk M. J., Norman M. L., Abel T., 2012, ApJ, 745, 50

Witten C. E. C., et al., 2022, arXiv e-prints, p. arXiv:2205.12271

Wolf C., et al., 2018, Publications of the Astronomical Society of Australia, 35, e010

Woosley S. E., Heger A., 2006, ApJ, 637, 914

Woosley S. E., Weaver T. A., 1995, ApJS, 101, 181

Woosley S. E., Heger A., Weaver T. A., 2002, Reviews of Modern Physics, 74, 1015

Wylie S. M., Gerhard O. E., Ness M. K., Clarke J. P., Freeman K. C., Bland-Hawthorn J., 2021, arXiv e-prints, p. arXiv:2106.14298

Yanny B., et al., 2009, AJ, 137, 4377

Yavetz T. D., Johnston K. V., Pearson S., Price-Whelan A. M., Weinberg M. D., 2021, MNRAS, 501, 1791

Yong D., et al., 2013, ApJ, 762, 26

Yoon J., et al., 2016, ApJ, 833, 20

Yoon J., et al., 2018, ApJ, 861, 146

Yoon J., Beers T. C., Tian D., Whitten D. D., 2019, ApJ, 878, 97

Yoshida N., Abel T., Hernquist L., Sugiyama N., 2003, ApJ, 592, 645

Yoshida N., Omukai K., Hernquist L., 2007, ApJLett, 667, L117

Yoshii Y., Saio H., 1986, ApJ, 301, 587

Yurin D., Springel V., 2014, GALIC: Galaxy initial conditions construction (ascl:1408.008)

Zana T., Dotti M., Capelo P. R., Bonoli S., Haardt F., Mayer L., Spinoso D., 2018, MNRAS, 473, 2608

Zasowski G., et al., 2017, AJ, 154, 198

Zepeda J., et al., 2022, arXiv e-prints, p. arXiv:2209.12224

Zhao H., Spergel D. N., Rich R. M., 1994, AJ, 108, 2154

Zoccali M., et al., 2003, A&A, 399, 931

Zoccali M., et al., 2006, A&A, 457, L1

Zoccali M., Hill V., Lecureur A., Barbuy B., Renzini A., Minniti D., Gómez A., Ortolani S., 2008, A&A, 486, 177

Zoccali M., et al., 2014, A&A, 562, A66

Zoccali M., et al., 2017, A&A, 599, A12

de Vaucouleurs G., 1964, in Kerr F. J., ed., Vol. 20, The Galaxy and the Magellanic Clouds. p. 195